Integration and study of a MOEMS-based endomicroscopic system for early detection of gastrointestinal cancers by SS-OCT

Fernando Eleazar Garcia Ramirez

THÈSE DE DOCTORAT DE L'ETABLISSEMENT UNIVERSITÉ BOURGOGNE FRANCHE-COMTÉ

PREPARÉE À L'UNIVERSITÉ DE FRANCHE-COMTÉ

École doctorale nº 37

SPIM

Doctorat de Sciences pour l'Ingénieur

Par

Fernando Eleazar García Ramírez

Intégration et étude d'un système endomicroscopique basé sur MOEMS pour la détection précoce des cancers gastro-intestinaux par SS-OCT

Thèse présentée et soutenue á Besançon, le 21 juin 2022

Composition du Jury:

M. Franck Chollet	Professeur, Université de Franche-Comté, France	Président
M. Frédéric Zamkotsian	Directeur de Recherche CNRS, Université Aix & Marseille, France	Rapporteur
M. Maciej Wojtkowski	Professeur, Institut de Chimie Physique, Académie Polonaise des Sciences, Pologne	Rapporteur
Mme. Michalina Gora	Chargée de Recherche, Centre Wyss de Bio et Neuroingénierie, Suisse	Examinatrice
M. Philippe Lutz	Professeur, Université de Franche-Comté, France	Directeur de thèse
M. Sylwester Bargiel	Ingénieur de Recherche, Institut FEMTO-ST, France	Codirecteur de thèse

Acknowledgements

I would like to start by thanking my parents Guadalupe Ramírez Vázquez and Juan Onofre García Mejía (†) and my brother Alberto Onofre García Ramírez for their total support during, not only my studies, but all my life.

I thank my thesis director Dr. Philippe Lutz (†) for their advices and teachings in all the meetings we had during my PhD and my co-director Dr. Sylwester Bargiel for his teachings in micro fabrication processes and considerable help in the integration of the probe in the clean room.

Special thanks to Dr. Olivier Gaiffe for his teachings in OCT data processing and Lissajous scanning as well as his significant help, advices, talks, observations and much much more. I will never be able to pay back his unconditional support.

I would like to thank my former thesis director Dr. Christophe Gorecki who invited me to work in this first-class research institute. Also, I thank Dr. Przemyslaw Struk who, with the members of the MOEMS group, developed the Mirau micro-interferometer and worked on the first version of the SS-OCT system.

Many thanks to Jean-Marc Cote for his substantial help in the development of the softwares in LabView.

I specially thank Dr. Quentin Tanguy who, under the supervision of Dr. Huikai Xie at the University of Florida, developed the electrothermal micro scanner and thought me the requirements to drive it. I thank him much more for his valuable help on my arrival in France and the university (incsription, getting bank account, showing fundamental aspects of the life in France, initial French lessons and much more).

I also address my thanks to Dr. Nicolas Pasilly for his essential help at the beginning of my PhD. I also kindly thank Dr. Magali Barthès, Dr. Michel De Labachelerie and Sophie Marguier for the friendly conversations in the institute and for sharing ideas and advices in the meetings of the MOEMS group.

My sincerely thanks to Dr. Claude Humbert for his friendship and major help during all my PhD and to his wife, Dr. Souha Khadraoui with whom I could also share wonderful moments like their wedding.

I warmly thank all my office mates during all my PhD with whom I could always have friendly conversations, meals and coffe breaks: Jean Kovchar, Jean-Loup Skora, Dr. Alpha Diallo, Victoria Duval, Marvin Tresse and Guillaume Ozout.

I express my gratitude to the head of the MOSAIC group Dr. Frédérick Cherioux and the head of the MN2S department, Dr. Vincent Laude for letting me work in the teams under their

supervision and their support during the confinement.

I kindly thank the head of the doctoral school Dr. Thérèse Leblois for her absolute help during all my PhD.

I also express my gratitude to the collaborators of the ROBOT project Dr. Nicolas Andreff, Dr. Michalina Gora, Dr. Florent Nageotte and Dr. Bassem Dahroug.

I kindly thank Dr. Maciej Wojtkowski for letting me work at ICTER in Warsaw.

I thank the MIMENTO staff for their teachings in the clean room.

I would like to thank to my mexican friends Jesús Brito and Julio Iglesias with whom I could always laugh and talk in mexican spanish.

Finally, I thank all the wonderful people with whom I could share a nice talk, a meal, a drink and, in general, great moments: Sylvain Midrouet, Florian Jouy, Alexandra Mérienne, Dr. Toky Rabenimanana, Dr. Svenja Hermann, Mark Anisimov, Ophélie Bourgeois, Geetika Raizada, Paresh Mahapatra, Dr. Agathe Figarol, Axelle Rabbe, Sandrine Chatrenet, Jocelyne Renaut, Lucie Connétable, Thibaut Zwingelstein, Reinaldo Chacon, Dr. Charles-Louis Azzopardi, Dr. Aleksandr Oseev, Dr. Anne Frelet-Barrand, Alain Rouleau, Pauline Bourgeois, Phoölan Roman, Daniel Guneysu, Olivia Ben M'Barek, Dr. Juliana Chawich, Dr. Raya EI Beainou, Dr. Maya Geagea, Dr. Aymen Jallouli, Dr. Balasubramaniam Namasivayam, Achraf El Mohajir, Charalampos Sakkas, Dr. Julien Dufourmantelle, Yida Yang, Dr. Mengjia Wang, Dr. Laetitia Raguin, Dr. Asma Chargui, Dr. Jesús Toledo, Yucely Beb, Daniel Garzon, Nelson Cisneros, Nahashon Osinde, Dr. Vladimir Semenov, Souhaila Boublouh, Kirthanaa Indumathi, Ria Talukder, Adriá Grabulosa, Dr. Benoît Morel and Dr. Hugo Delahaye.

This work was supported by the Labex Action program, the INSERM Plan Cancer program (ROBOT project), the French RENATECH network and its FEMTO-ST technological facility and by the Collegium SMYLE.

Résumé de la thèse en français

En 2018, les cancers gastro-intestinaux (GI) reprśentaient 26,3 % de tous les cancers dans le monde. De nombreuses modalités d'imagerie sont utilisés pour la détection et le diagnostic des cancers gastro-intestinaux, mais certaines sont invasives, lentes, coûteuses ou ne fournissent pas une résolution et une profondeur de pénétration suffisantes pour une détection précoce. Une technique d'imagerie prometteuse pour la détection des cancers gastro-intestinaux aux premiers stades est la tomographie par cohérence optique (OCT), en raison de son caractère non invasif, de sa haute résolution axiale et de sa capacité à produire des images en coupe transversale. En outre, l'OCT est compatible avec les bras endoscopiques robotisés mais nécessite l'insertion de sondes miniaturisées dans l'endoscope. Les systèmes micro-opto-électro-mécaniques (MOEMS) permettent de répondre à ce besoin, et offre la possibilité de fabrication en série des composants clés de la sonde. Un micro scanner électrothermique à 2 axes et un micro-interféromètre de Mirau on été développé a l'Institut FEMTO-ST pour des applications endoscopiques.

Les principaux objectifs de cette thèse sont de fabriquer la sonde OCT endoscopique miniature par l'intégration de tous les composants MOEMS, de caractériser ses performances de balayage, de développer le système expérimental OCT pour l'acquisition des signaux OCT et le contrôle du scanner pour effectuer un balayage de Lissajous et la production d'images 2D et 3D.

Dans un premier temps, la capacité du micro-interféromètre Mirau à produire des images OCT a été testée. Il a été connecté à une source balayée avec une longueur d'onde centrale de 840 nm, une bande passante de 60 nm et une fréquence de balayage de 110 kHz. Ensuite, un échantillon constitué de deux couches de photorésist a été balayé latéralement avec le micro-interféromètre en déplaççant l'échantillon avec une platine motorisée. Les signaux d'interférence ont ensuite été traités pour produire une image correspondant à la vue en coupe de l'échantillon avec des résolutions axiale et latérale calculées de 5,18 μm et 9,73 μm, respectivement, où les couches de résine photosensible pouvaient être observées.

Des dispositifs supplémentaires ont été couplés dans la première génération du système SS-OCT, à savoir un détecteur à double balance pour supprimer le bruit causé par les fluctuations d'intensité de la source balayée et un atténuateur optique variable pour diminuer la composante continue des signaux d'interférence. Avec cette nouvelle version du système SS-OCT, une carte avec une surface lisse réfléchissante et une surface rugueuse diffusante a été scannée en déplaçant l'échantillon avec la platine motorisée. Dans ce cas, des images OCT avec les balayages avant et arrière de la source ont été obtenues. Une diminution du rapport signal/bruit de 4,4 dB a été constatée dans les images produites avec les balayages arrière par rapport à celles produites avec

les balayages avant.

Comme nous avions montré la capacité du micro-interféromètre à produire des images OCT, il a été intégré au micro-scanner électrothermique. Après, la sonde OCT intégrée a été connectée au système SS-OCT avec les composants correspondants pour piloter le micro scanner et le caractériser. La fréquence de résonance mesurée du micro scanner était de 943 Hz et 945 Hz pour l'axe x et l'axe y respectivement.

Ensuite, un motif de balayage de Lissajous à 33 fps et un champ de vision de 169,7 x 136,5 m^2 ont été obtenus avec le micro scanner en utilisant des signaux sinusoïdaux avec une tension continue de 2 V, des amplitudes $V_x = 90$ mV et $V_y = 106$ mV et des fréquences $f_x = 957$ Hz et $f_y = 924$ Hz. Au final, des images OCT 3D ont été produites avec la sonde entièrement intégrée. Un échantillon composé de 3 couches de verre a été scanné avec le modèle de balayage de Lissajous et un image 3D correspondante a été reconstruite où les 3 couches de verre sont clairement visibles.

Summary of the thesis in English

In 2018, gastrointestinal (GI) cancers represented the 26.3 % of all the cases worldwide. Many imaging modalities are used for detection and diagnosis of GI cancers, but some are invasive, slow, expensive or they do not provide enough resolution and penetration depth for early detection. A promising imaging technique for GI cancers detection at initial stages is Optical Coherence Tomography (OCT) due to its non-invasiveness, high axial resolution and capacity to produce cross-sectional images. Furthermore, OCT is compatible with robotic endoscopic arms but requires the insertion of miniaturized probes through the endoscope. This demand has been addressed through Micro-Opto-Electro-Mechanical Systems (MOEMS) technology which enables batch fabrication of the key components of these probes. A 2-axis electrothermal micro scanner and a Mirau micro-interferometer were developed at the FEMTO-ST Institute for OCT endoscopic applications

The main objectives of this thesis are to fabricate the miniature endoscopic OCT probe by the integration of all the MOEMS components, to characterize its scanning performances and to develop the OCT experimental system for OCT signals acquisition, scanner control to perform Lissajous scanning and 2D and 3D image production.

The capacity of the Mirau micro-interferometer to produce OCT images was tested as a first task. It was connected to a swept source with a central wavelength of 840 nm, a bandwidth of 60 nm and a sweeping rate of 110 kHz. Then, a sample made of two layers of photoresist was scanned laterally with the micro-interferometer by moving the sample with a motorized stage. The interfence signals were processed to produce an image corresponding to the cross-sectional view of the sample with calculated axial and lateral resolutions of 5.18 μm and 9.73 μm, respectively, where the layers of photoresist could be observed.

Additional devices were coupled in the first generation of the SS-OCT system, namely, a dual balance detector, to suppress the noise caused by intensity fluctuations of the swept source, and a variable optical attenuator to decrease the DC component of the interference signals. With this new version of the SS-OCT system, a card with a reflective smooth and a diffusive rough surface (Thorlabs VRC2) was scanned by moving the sample with the motorized stage. In this case, OCT images with the forward and backward sweeps of the source were obtained. A decrease in SNR of 4.4 dB was found in the images produced with the backward sweeps with respect to those ones produced with the forward sweeps.

After the micro interferometer showed its capacity to produce OCT images, it was integrated with the micro scanner. Then, the integrated OCT probe was connected to the SS-OCT system with the corresponding components to drive the micro scanner and characterize it. The measured

resonance frequency of the micro scanner were 943 Hz and 945 Hz for the x-axis and y-axis respectively.

Then, a Lissajous scanning pattern at 33 fps and a field of view of 169.7 x 136.5 μm^2 was achieved with the micro scanner using sinusoidal signals with a DC voltage of 2 V, amplitudes $V_x = 90$ mV and $V_y = 106$ mV and frequencies $f_x = 957$ Hz and $f_y = 924$ Hz. Finally, 3D OCT images were produced with the fully integrated probe. A sample made of 3 layers of cover glass was scanned with this Lissajous scanning pattern and a 3D images was reconstructed where the 3 layers are clearly visible.

Contents

General introduction

Motivation

Gastrointestinal (GI) cancers represented 26.3 % (4.8 million) of all the cancer cases worldwide in 2018 and were responsible of the 35 % (3.4 million) of all deaths related to this disease (Fig. 1) [1]. Besides, it has been predicted that these percentages of incidence and mortality will increase by 58 % (to 7.5 million) and 73 % (to 5.6 million), respectively, by 2040. Stomach, liver, esophageal, and pancreatic cancer are the 5th (1 million cases), 6th (841 000), 7th (572 000) and 12th (432 000) most common between all types, respectively, and they occupy the 3rd (800 000 deaths), 4th (782 000), 6th (508 000) and 7th (459 000) place in cause of death because of cancer. These values of incidence and mortality are related directly to the absence of specific symptoms at initial stages of cancer development that results in a delayed diagnosis, when this disease is already at an advanced stage. However, more options of treatment are available if tumors are detected at an early curable stage.

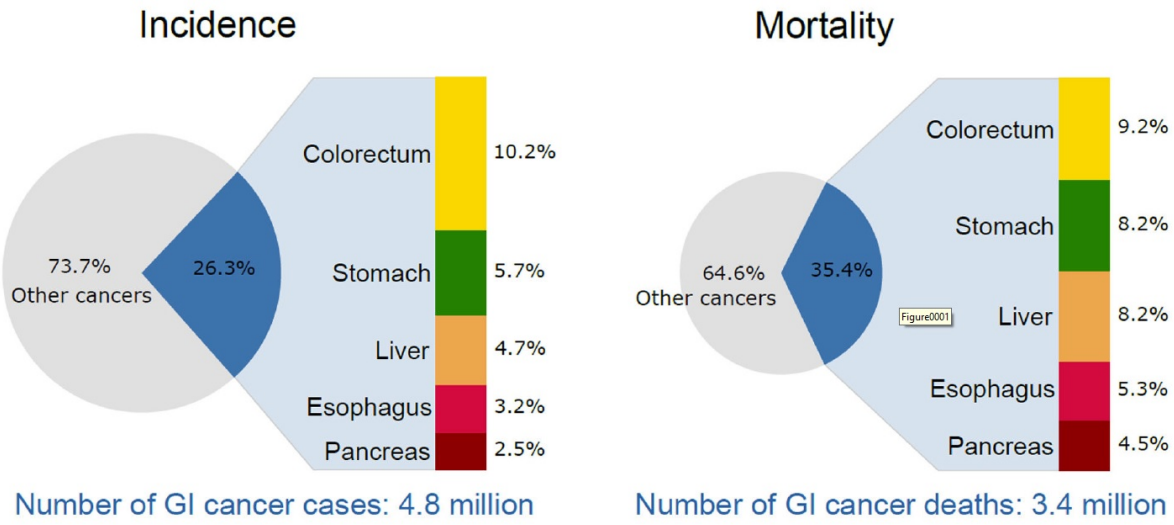

Figure 1: Incidence and mortality of GI cancers worldwide in 2018. Image taken from [1].

Table 1 presents the stages of esophageal, gastric and colorectal cancer according to the "T stage" of the TNM (tumour, node, metastasis) classification that refers to the size of the

primary tumor. T0 indicates no evidence of tumor while the values T1 to T4 indicate the degree of progressive extension from the outermost layers of the organs until invading all the layers and adjacent structures [3]. Figure 2 shows these stages for esophageal cancer where the N and M stages are also illustrated. The "N stage" refers to the degree of extension of the cancer to the lymph nodes that can spread it to other organs. N0 indicates no regional lymph node metastasis while the values N1 to N3 indicate the level of spreading of the tumor to a higher number of lymph nodes. The "M stage" specifies if distant metastases have occurred (M1) or not (M0).

Table 1: T stages for esophageal, gastric and colorectal cancer. Table taken from tables 1-3 in [2]

Stage	Esophageal cancer	Gastric cancer	Colorectal cancer
T0	No evidence of primary tumor	No evidence of primary tumor	No evidence of primary tumor
T1	**T1a:** Tumor invades mucosa – T1a-EP: Carcinoma in situ (Tis) – T1a-LPM: Tumor invades lamina propria mucosa – T1a-MM: Tumor invades muscularis mucosa **T1b:** Tumor invades submucosa – SM1: Tumor invades the upper third of the submucosal layer – SM2: Tumor invades the middle third of the submucosal layer – SM3: Tumor invades the lower third of the submucosal layer	**T1a:** Tumor confined to the mucosa **T1b:** Tumor confined to the submucosa – SM1: Tumor invasion within 0.5 mm of muscularis mucosae – SM2: Tumor invasion is 0.5 mm or more deep into the muscularis mucosae	Tumor invades submucosa
T2	Tumor invades muscularis propria	Tumor invades the muscularis propria	Tumor invades muscularis propria
T3	Tumor invades adventitia	Tumor invades the sudserosa	Tumor invades through the muscularis propria into the subserosa, or into non-peritonealized pericolic or perirectal tissues
T4	Tumor invades adjacent structures	**T4a:** Tumor invasion is contiguous to the serosa or penetrated the serosa and is exposed to the peritoneal cavity **T4b:** Tumor invades adjacent structures	Tumor directly invades organs or structures, and/or perforates visceral peritoneum

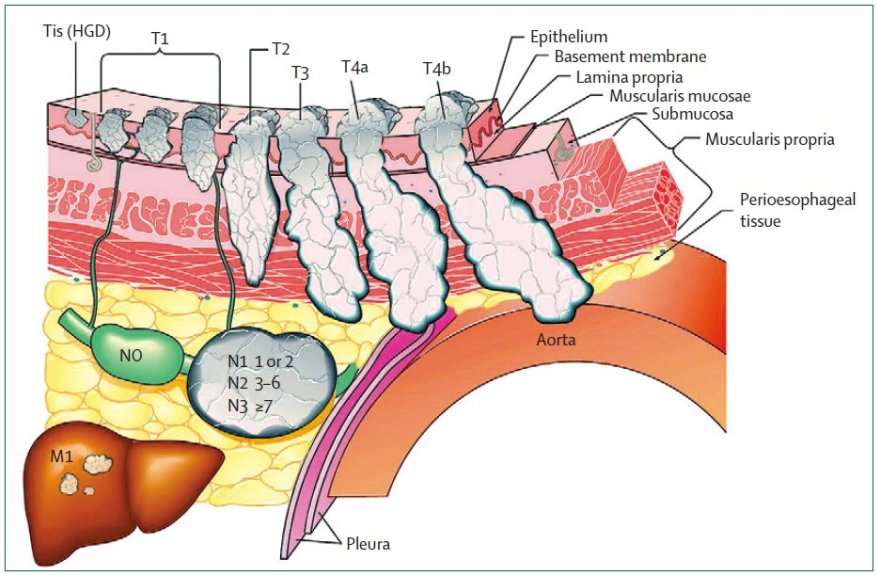

Figure 2: T stages in esophageal cancer. T4a and T4b refer to resectable and unresectable respectively. Labels: intraepithelial neoplasia (Tis), high-grade dysplasia (HGD). Image taken from [4].

Early cancer is defined by Eleftheriadis *et al.* as "*local lesion which has no risk of lymph node metastasis*" [2]. It has been observed that the rate of this metastasis is much lower in mucosal cancers (2% - 3% for esophageal, 2% - 4% for gastric and 0% for colorectal carcinomas) compared to submucosal ones (37% - 53% for esophageal, 14 % - 20 % for gastric and 3% - 18% for colorectal carcinomas). The defined stages for early cancer are highlighted in blue in table 1 when lymph node metastasis is still not produced [2].

There are several imaging techniques for GI cancer diagnosis such as computerized tomography (CT), magnetic resonance imaging (MRI), positron emission tomography (PET), endoscopic ultrasound (EUS), fluorescence endoscopy (FE), confocal microscopy (CM), chromoendoscopy (CE) and narrow band imaging (NBI) ([6]-[8]). The principles of operation of each modality as well as their correspondent advantages and disadvantages are summarized in table 2. Those techniques that need the use of endoscopes are highlighted in green. The axial resolution and penetration depth of each image modality are presented in table 3.

Table 2: Imaging techniques for GI cancers diagnosis. This table is composed from table 1 in [6], tables 1 and 2 in [7], table 1 in [8] and table 1 in [9].

Modality	**Principles**	**Advantages**	**Disadvantages**
CT	– X-ray beams traverse patient from multiple directions to generate images based on the relative attenuation of different tissues. – Images are acquired rapidly with overlapping helical slices (spiral computed tomography) with multiple slices obtained at the same time.	– Rapid assessment – High spatial resolution – Large field of view – Excellent penetration depth	– Ionizing radiation – Limited physiologic and viability data – Low contrast
MRI	– Magnetic resonance imaging exposes protons with unpaired electrons (predominantly hydrogen atoms) to	– Excellent tissue contrast – Physiologic data obtainable	– Time consuming – Limited evaluation of lungs

Continuation of Table 2			
Modality	**Principles**	**Advantages**	**Disadvantages**
	different magnetic fields and radiofrequency pulses. – The behavior of these protons, which are used to generate the image, is influenced not only by what magnetic fields and radiofrequency pulses they are exposed to but also the local tissue milieu.	– No ionizing radiation – Diffusion-weighted imaging – High-quality biliary and pancreatic ductal anatomy – High spatial resolution – No tissue penetrating limit	– Relatively low sensitivity and low contrast – High cost
PET	– Fluorodeoxyglucose (FDG) is a radioactive compound taken up by the cells to enter the glucose pathway. Once acted upon by hexokinase, it becomes trapped in the cell. – Acts as a surrogate marker for glucose utilization in the cell and, therefore, metabolic activity.	– Assesses metabolic activity – Functional assessment – High sensitivity – Excellent penetration depth – Whole-body imaging	– Low spatial resolution – High cost of cyclotron needed – Radiation risk
EUS	– High-frequency sound waves provide real-time information of the anatomy and pathology of the interrogated structure. – The vast majority of malignancies are relatively less echoic (hypoechoic) compared with normal tissue	– Better characterization of early hollow viscera wall invasion – No ionizing radiation – Useful for image guidance – Vascularity – High temporal resolution – Inexpensive	– Limited field of view – Bowel and bone can obscure structures – Low resolution – Poor penetration depth – Low contrast
FE	Sensitizers accumulate selectively in malignant lesions and induce fluorescence upon illumination with light of the appropriate wavelength.	– High sensitivity – No radiation – Inexpensive – Activatable	– Low spatial resolution – Attenuation by overlying tissues – Poor penetration depth
CM	Fluorescent agents are absorbed by tissue and provide cellular and histological details.	– Cellular resolution – Point and view	– Limited imaging depth – Limited field of view – Contrast required
CE	It uses dyes to differentiate between normal and malignant tissue by highlighting changes in the mucosa related to dysplasia.	– Enhanced endoscopic imaging contrast	– Superficial imaging – Large volume dye required
NBI	It uses 3 wavelengths of light that have different penetration depths to increase the contrast between superficial capillaries and the mucosa.	– Enhanced endoscopic imaging contrast – No contrast agent required	– Superficial imaging

Depending on the organ and the stage of cancer, a different technique should be used for diagnosis as it is indicated in table 4. PET is employed to detect distant metastases (M stage)

Table 3: Resolution and penetration depth of the different imaging techniques for GI cancer diagnosis. N/A = not applicable. Data taken from table 1 in [8] and table 1 in [9].

Modality	**CT**	**MRI**	**PET**	**EUS**	**FE**	**CM**	**CE**	**NBI**
Resolution (μm)	50 - 200	25 - 100	1000 - 2000	50 - 500	2000 - 3000	1 - 5	N/A	N/A
Depth (mm)	Limitless	Limitless	Limitless	10 - 100	< 10	< 0.250	N/A	N/A

and to monitor response to treatments but it does not provide tumor size information or local invasion because of its low resolution [7]. Besides, it requires the use of ionizing radiation as CT imaging. MRI is utilized for monitoring low and high T stages in the liver, pancreas and biliary but it requires long acquisition time (a few minutes per scan) which makes it sensitive to body movement. Moreover, its high cost of operation makes it unaffordable for many hospitals. EUS is the most used imaging modality for the diagnosis of GI malignancies at low early cancer T stages where, according to table 1, the mucosa and submucosa are invaded. Huh *et al.* measured the thickness of the stomach and rectal mucosa using EUS in 18 patients (10 in the stomach and 8 in the rectum) [10]. In the case of the stomach mucosa, the thickness was measured to range from 1030 ± 130 μm to 1640 ± 80 μm and the total stomach wall from 2.80 ± 0.12 to 4.23 ± 0.03 mm. Regarding the rectal mucosa, the range is from 660 ± 50 μm to 1130 ± 250 μm and the total rectal wall from 2.28 ± 0.05 to 3.55 ± 0.43 mm. The penetration depth of EUS is appropriate to scan the stomach and rectal mucosa but the low resolution can make difficult to detect structural changes indicating carcinogenesis (as FE that has much less resolution). CM possesses the highest resolution but the low penetration depth does not allow a complete scanning of the mucosa while CE and NBI only provide superficial images.

Table 4: Imaging modality used at different stages of cancer. Table taken from [6].

	T stage		**N stage**		**M stage**
Cancer	**Low**	**High**	**Local**	**Distant**	
Esophagus	EUS	PET-CT	PET/EUS	PET	PET
Stomach	EUS	PET-CT	PET/EUS	PET	PET
Small bowel	EUS/capsule	PET-CT	PET/EUS	PET	PET
Colon	EUS	PET-CT	PET/EUS	PET	PET
Rectum	EUS	MRI	MRI	PET	PET
Liver	MRI/CT	MRI/CT	MRI/CT	MRI/CT	
Pancreas	MRI/CT	MRI/CT	MRI/CT	CT	
Biliary	MRI	MRI	MRI/CT	CT	

Another technique that has been used for cancer detection in gastroenterology is optical coherence tomography (OCT) that is based on low coherence interferometry and provide cross-sectional images of tissue microstructures using their endogenous scattering properties [11]. This modality has become very attractive for endomicroscopy technology due to the use of non-invasive radiation (low power NIR), high axial resolution from 5 to 30 μm (ten times higher than high-frequency US [7]), very high acquisition speed and a penetration depth of 3 mm [8]. These characteristics allow in-situ revealing of early carcinogenic changes on the cellular level. The relatively small scanning depth of this method is not an obstacle in the case of the implementation of OCT in the optical-fiber endoscopic probes since (1) imaging is performed in direct proximity of the internal organs and (2) the penetration depth is in the same order of magnitude of the thickness of

the mucosa layer where cancer cells start to proliferate. Moreover, the high acquisition speed is beneficial to avoid image deterioration in the presence of physiological movements of the human body. Hence, the combination of OCT and endoscopy makes it a powerful tool for early cancer detection (low T stage) [12]. This malignant tissue is characterized by irregular shapes that have different optical scattering properties than healthy tissue and, hence, can be detected by OCT [13]. Moreover, optical biopsies open the possibility of in-situ endoscopic treatments, such as endoscopic submucosal dissection (ESD).

One of the basic difficulties in the imaging of internal organs is to realize fast lateral scans at the tip of small endoscopes that must be able to fit into narrow lumens whose diameters typically are only a few millimeters. Several research groups have attempted to solve this problem by use of micro-opto-electro-mechanical systems (MOEMS) technology. Indeed, MOEMS technology is a key enabling technology for biomedical applications, playing an important role in the development of a new generation of medical instruments, not only to decrease their size and manufacturing costs, but also to improve their performances. The potential of MOEMS to manipulate the light beam by mm-sized devices, operating with high speed and at very small power consumption, has strongly influenced the development of lower-cost, portable optical OCT imaging systems, e.g. for early detection of skin pathologies in dermatology [15] as well as the development of a large number of endoscopic probes with MOEMS components, mainly micromirrors/microlens scanners, to allow optical imaging using different imaging techniques [16]. A review of OCT-based MOEMS probes will be presented later in section 2.2.

Context

The implementation of the MOEMS technology in an OCT endoscopic system is an exciting research activity that is carried out since a decade at the FEMTO-ST (Franche-Comté Électronique Mécanique Thermique et Optique - Sciences et Technologies) institute (MN2S (Micro Nano Sciences and Systems) department), by the MOEMS Group led by Christophe Gorecki (Research Director of CNRS), in strong collaboration with the MIMENTO (MIcrofabrication for MEcanics, Nanosciences, Thermal and Optics) technological platform. This activity resulted in the elaboration of some technical concepts as well as the fabrication of MOEMS devices that have been used in this work.

In particular, a concept of a common-path OCT endoscopic probe based on a Mirau micro-interferometer was proposed by Struk *et al.* [17], as shown in Fig. 3a. A first-generation probe (with capacity of scanning only in depth, A-scan) with a silicon-glass monolithically integrated Mirau micro-interferometer was then fabricated in the frame of the DEMO4 project (LabEx Action program), using a multi-wafer vertical integration technology presented by Bargiel *et al.* in 2015 [18]. Moreover, a first version of a Swept Source OCT measurement setup was built, allowing a successful proof-of-concept demonstration of the OCT imaging capability.

A further development of this concept resulted in the implementation of a MOEMS micro-mirror scanner with a 45°-tilted micromirror in order to perform fast 2-D scanning of a tissue sample, and hence, to be capable of generating cross-sectional (B-scan) or even 3D (C-scan) OCT images (Fig. 3b). For this purpose, a 2-axis electro-thermally driven micro-mirror scanner was developed and fabricated by Dr. Quentin Tanguy (thesis 2014-2018), in the frame of the DEMO4 project (LabEx Action program, ANR-11-LABX-0001-01) in a strong cooperation with the University of Florida and the group of Prof. Huikai Xie [19].

Nevertheless, at the beginning of this work, the fully integrated probe with all the above men-

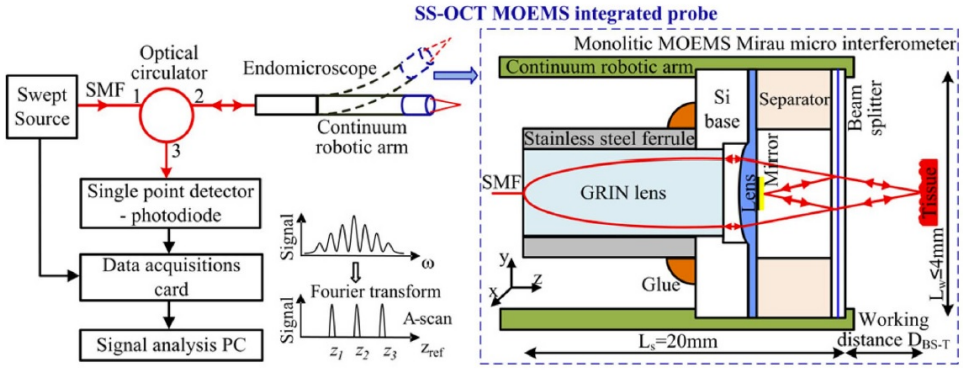

(a)

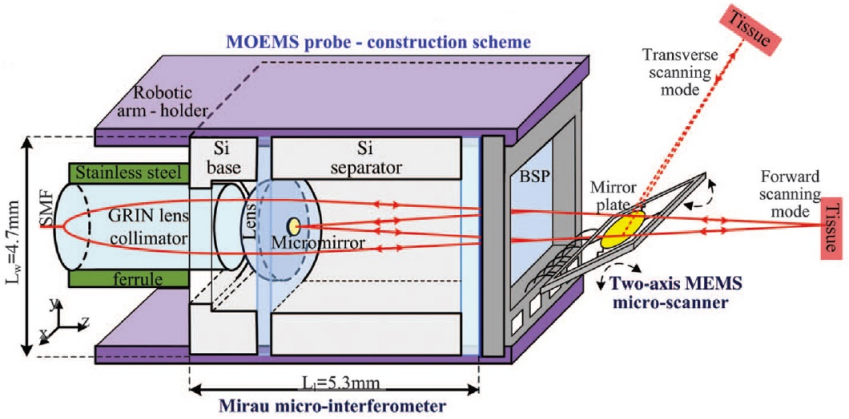

(b)

Figure 3: (*a*) Scheme of the first generation of the swept source OCT system with a "passive" probe with the integrated Mirau micro-interferometer. Image taken from [17]. (*b*) Scheme of the "active" probe equipped with a Mirau micro-interferometer and a micro-mirror scanner. Image taken from [147].

tioned components was not available. The main reasons were the lack of an appropriate chip-level assembly method and some technical issues related to the scanner fabrication (e.g. inappropriate mirror angle) that will be described later in section 4.2.2. As a consequence, the OCT imaging performances of the MOEMS probe with the scanning micromirror were unknown. Moreover, the available SS-OCT measurement setup was not interfaced to such active scanning probe, neither from hardware nor software point of view, since it requires an electronics for the generation of the scanner driving signals as well as a synchronization between the OCT signals acquisition and the well-controlled movement of the scanning micromirror. In the frame of this work, all these missing aspects were addressed leading to a development of a second generation of the swept source OCT system, fully cooperated with an integrated MOEMS scanning probe.

The application of OCT-based endoscopy is a growing field with strong interest in real-time diagnosing and in-situ treatment of digestive diseases but also in the characterization of medical materials (ceramic, polymer) or in control of arterial plaques during stent placement [20]. However, most of the technology development for the GI tract is focused on imaging of the human esophagus that has a relatively simple geometry and easy access [21]. Extending applications of OCT for other types of cancer in the digestive system, e.g. colorectal or pancreas cancer, is challenging due to the complex geometry and difficult access. Currently available passive OCT catheters are not

suitable to significantly improve the management of patients with such diseases. To address this issue, a new type of "active" endoscopic probes were proposed that combine OCT-based imaging with other optical imaging modalities as well as with micro robotic solutions to guide and stabilize an endoscope during medical procedures.

This work was carried out in the context of ROBOT collaborative project which aimed at developing a robotized endoscope equipped with a dexterous flexible robotic micromanipulator and a white-light camera for OCT-based optical biopsy in the digestive tract. This project was financed by INSERM (Institut National de la Santé et de la Recherche Médicale) under the grant OPE-2017-0123 in the frame of the "Plan Cancer 2014-2019" program. The project involved three research groups having complementary expertise in microrobotics (FEMTO-ST, AS2M (Automatique et Systémes Micro-Mécatroniques) department, Besançon), MOEMS technology (FEMTO-ST, MN2S department, Besançon) and endoscopic robotics (ICube, Strasbourg).

Objectives

The overall goal of this work is to address the difficulties of early detection of cancer in the human gastrointestinal tract and to develop a complete endoscopic-based system for real-time, high-resolution and not-invasive OCT imaging (optical biopsy), using MOEMS technology. The main objectives of this work, directly linked to the above mentioned ROBOT project, are:

1. To complete the fabrication of an optical-fiber miniature OCT probe by elaborating appropriate methods of integration of the previously fabricated building blocks (i.e. GRIN-lens collimator, a Mirau micro-interferometer and a 2-axis electrothermal micro-mirror scanner), ensuring reliable optical, mechanical and electrical interconnections.

2. To characterize the scanning performances of the fully integrated probe.

3. To complete the development of a Swept Source OCT measurement system in order to ensure a full compatibility with the MOEMS OCT probe and to enhance the OCT image quality.

4. To develop software blocks to control the crucial processes of OCT imaging: (1) data acquisition of the interference signals from the OCT probe, (2) control of the movement of the micro-mirror, (3) real-time synchronization between these two processes, (4) OCT image reconstruction in 3D.

5. To implement an advanced Lissajous scanning method in the SS-OCT system to allow a real-time 3D OCT imaging of biological samples.

Scope of the thesis

This thesis is composed of 5 chapters:

- **Chapter 1:** A review of the development of the OCT technology is given. Additionally, we present the mathematical theory that shows that the depth profile of a sample is obtained by applying the inverse Fourier transform to an interference signal.
- **Chapter 2:** A brief review of OCT in gastroenterology is provided. After, several endoscopic probes based on MOEMS scanners with different types of actuation (electrostatic, electromagnetic, piezoelectric and electrothermal) are presented. We justify why an electrothermal micro scanner is preferable to perform OCT endoscopy. At the end, we introduce the 2-axis electrothermal scanner used in this work.
- **Chapter 3:** The construction of the single-axis probe (A-scan only) based on a Mirau micro-interferometer is presented. We describe the first version of the SS-OCT measurement system and then we explain the basic data processing procedure to reconstruct an image from the registered interference signals. We show 2D and 3D OCT images obtained with this probe by moving of the sample by a motorized stage in order to validate the proper functioning of the whole OCT system. Then, we describe several improvements to this setup and to the data treatment algorithms towards an improved OCT image quality, followed by a demonstration of B-scans of biological samples.
- **Chapter 4:** The fabrication process of the complete probe is presented. A chip-level 3D microassembly procedure is explained in details to achieve mechanical and electrical connections between the previously fabricated building blocks, i.e. an optical-fiber GRIN lens collimator, the Mirau micro interferometer, the 2-axis electrothermal micro-scanner and a flexible PCB. The method for post-fabrication correction of the micromirror angle of the scanner is explained as well. At the end, the fully integrated OCT probe is presented.
- **Chapter 5:** We describe the final version of the SS-OCT system that is fully interfaced with the fabricated MOEMS scanning probe in order to monitor in-situ the movement of the micromirror and synchronize it with the OCT image acquisition. Then, the frequency response of the 2-axis electrothermal mico-scanner is determined. Subsequently, the Lissajous scanning method is described and implemented in the probe taking into account the resonance bandwidth of each scanner axis. The selection of the driving signal parameters to achieve an effective Lissajous scanning is explained. At the end, we present 3D OCT images of a multilayer glass structure (highly reflective sample) and an onion (biological diffusive sample) obtained with the Lissajous trajectory.

1 Introduction to Optical Coherence Tomography

Optical Coherence Tomography (OCT) is a high speed non-invasive technique which allows to produce cross-sectional images of biological tissue with micrometer resolution and a depth scan distance of 3 mm. As ultrasound, this technique uses the magnitude and time delays of the optical echoes reflected back by the internal structures of biological tissues to produce images. Sound waves do not travel too fast (500 m/s) and the back reflected waves can be detected without problems in ultrasound. However, the velocity of light is extremely high (3 x 10^8 m/s) and the back reflected light beams should be detected almost instantly after being sent. Therefore, low-coherence interferometry has been used to detect the optical echoes when they interfere with the light beam reflected from the reference mirror. By measuring this interference pattern, a depth profile of the sample can be retrieved. In this chapter, the development of the OCT technique is reviewed. At the end, the mathematical theory of one faster and more sensitive mode of OCT, called Fourier Domain OCT (FD-OCT), is provided.

1.1 Development of OCT

The idea of using optical echoes to see internal structures of biological tissues was proposed by Duguay and Mattick in 1971 [22]. They were able to photograph a picosecond pulse of light displacing through a scattering media (a suspension of milk particles) using a camera with a framing rate of 10 ps. With this camera, they could detect the laser pulses back reflected by the drawing of a bell under a slide of tissue paper (Fig. 1.1a). Using the framing rate of 10 ps, they made that the shutter of the camera (Kerr type shutter) only opened when just the pulses reflected by the drawing reached the camera. Figure 1.1b (up and left) shows the drawing of the bell without the slide of paper covering it. When the camera is under normal illumination conditions, only the tissue paper can be observed (Fig.1.1b (up and right)). However, the bell can be appreciated using the 10 ps of framing rate (Fig.1.1b (both pictures below)). With these results, Duguay and Mattick suggested to use this method to see under the human skin and proposed to use it as a diagnosis tool. In 1978, Bruckner used the Kerr type shutter to measure cataracts in the eyes of one rabbit *in vivo* [23]. On his experiment, he sent picopulses of light to one eye of the rabbit and used one arrange of optical fibers at different angles to detect the pulses back scattered by the cataract. The detection system was coupled with the ultrafast Kerr type shutter that opened only when the pulses were back scattered by the cataract, blocking those ones coming from other layers in the eye. Bruckner could study the structure of the cataract analyzing the intensity and the angular position measurements.

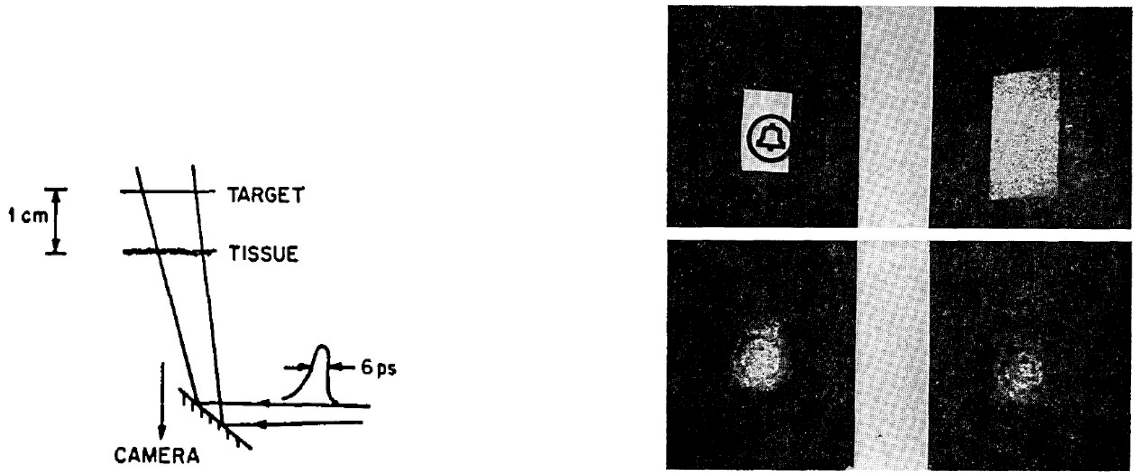

(a) (b)

Figure 1.1: (*a*) Pulse of light sent to a slide of tissue paper and the drawing of a bell (target). The light is reflected to a camera. (*b*) Images of the bell without the slide of paper covering it (up and left), the slide of paper under normal illumination conditions (up and right) and the images of the bell obtained with the ultrafast camera (both images below). Images taken from [22].

The use of interference of light picopulses to produce images of biological tissues was suggested by Park *et al.* in 1981 [24]. They described a system to detect the back reflection from a mirror immersed in an opaque media (a mixture of milk and water) using the interference of two picosecond pulses (Fig. 1.2). One of the pulses was directed to the mirror in the opaque media (container) and then reflected back to a photomultiplier (PMT). The other pulse was directed to one movable prism in order to produce a time delay on it. This pulse was used as a reference since the PMT only detected when both pulses overlapped, in other words, when the optical path lengths (OPL) of both pulses were equal. In this way, they showed that their system was able to detect an object in an opaque media and suggested that it could be used to produce images of structures in scattering media like biological tissue. In 1986, Fujimoto *et al.* used femtosecond laser pulses to measure the cornea (transparent tissue) of a rabbit eye *in vivo* and to study the internal structure of the human skin (non-transparent tissue) *in vitro* [25]. They showed that the use of femtosecond pulses can be used as a non-invasive technique to analyze the internal structures of biological tissue.

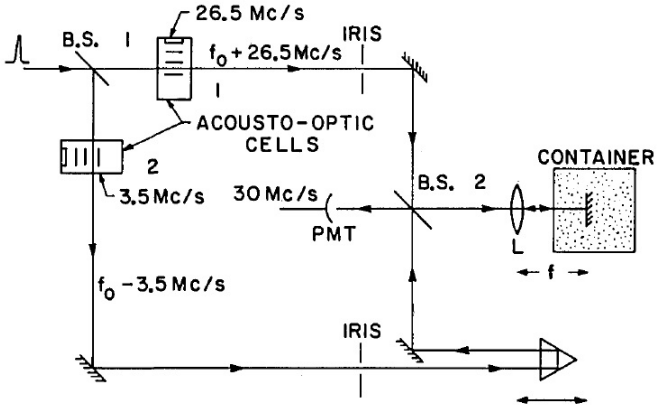

Figure 1.2: System used by Park *et al.*. Image taken from [24].

In 1987, Youngquist *et al.* described a technique called Optical Coherence-Domain Reflectometry (OCDR) to determine the positions and magnitudes of the reflections produced by the internal structures of small optical components with a resolution of 10 μm [26]. This technique used a Michelson interferometer but the component to analyze (device under evaluation (DUE)) was placed instead of one of the mirrors (Fig. 1.3). The light which goes to the DUE penetrates in it and is reflected back not only by the surface but also by internal structures of the sample. In this way, if the reference mirror is moved back, constructive interference can be observed if the distance between the beam splitter and the reference mirror (reference arm) matches the distance between the beam splitter and one of the internal structures of the sample (sample arm). This can only be observed using a light source with a short coherent length since the interference is observed only if the difference between the distances of the reference and sample arms is small compared with the coherence length of the light source. Therefore, information about the structure of the sample can be obtained by moving the reference mirror back and fort and analyzing the interference signals. The next year, Fercher *et al.* were able to measure the optical length of the human eye *in vivo* using low coherence interferometry [27]. This technique started to be used in measurements of biological structures.

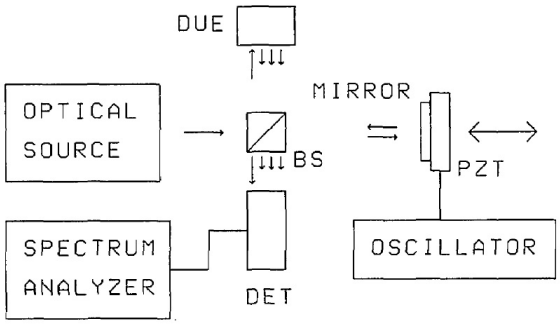

Figure 1.3: System used by Youngquist *et al.* to study the reflections produced by the internal structure of small optical components. DUE (device under evaluation), BS (beam splitter), DET (detector), PZT (piezoelectric transducer). Image taken from [26].

In 1991, Huang *et al.* used OCDR to analyse the internal structure of a calf eye *ex vivo* [28]. Figure 1.4a (top) shows the interference measurements when the beam was directed on an excision made in the cornea. They could detect the back reflections produced by the interfaces air-cornea and cornea-aqueous humor in the anterior chamber. This depth profile of the sample is referred as **A-scan**. The units of the horizontal axes of these graphs represent the free space delays. To convert these units into real distances, the optical delay units must be divided by the indexes of refraction (n) of the different internal structures. In this way, the measured thickness of the cornea ($n = 1.38$) with the excision was 371 μm. Figure 1.4b (bottom) shows the interference measurements produced when the light beam was directed to the region of the cornea next to the excision. In this case, the thickness was 745 μm. The authors also measured the thickness of the cornea (without the excision) with a light microscope and found a value of 765 μm, close to the value obtained with OCDR. Also, they measured the thickness of the anterior chamber with respect to the lens of the eye (2.88 mm) (Fig. 1.4b, top) and with respect to the iris (2.62 mm) (Fig. 1.4b, bottom). In this article, Huang *et al.* suggested the use of OCDR to study the structure of the eye since it offers a resolution of 10 μm, which is necessary to observe the cornea and the retina, and allows to detect diffusive tissue as the iris. Besides, OCDR does not need to be in contact with the sample which is an important advantage over ultrasound. Later that year,

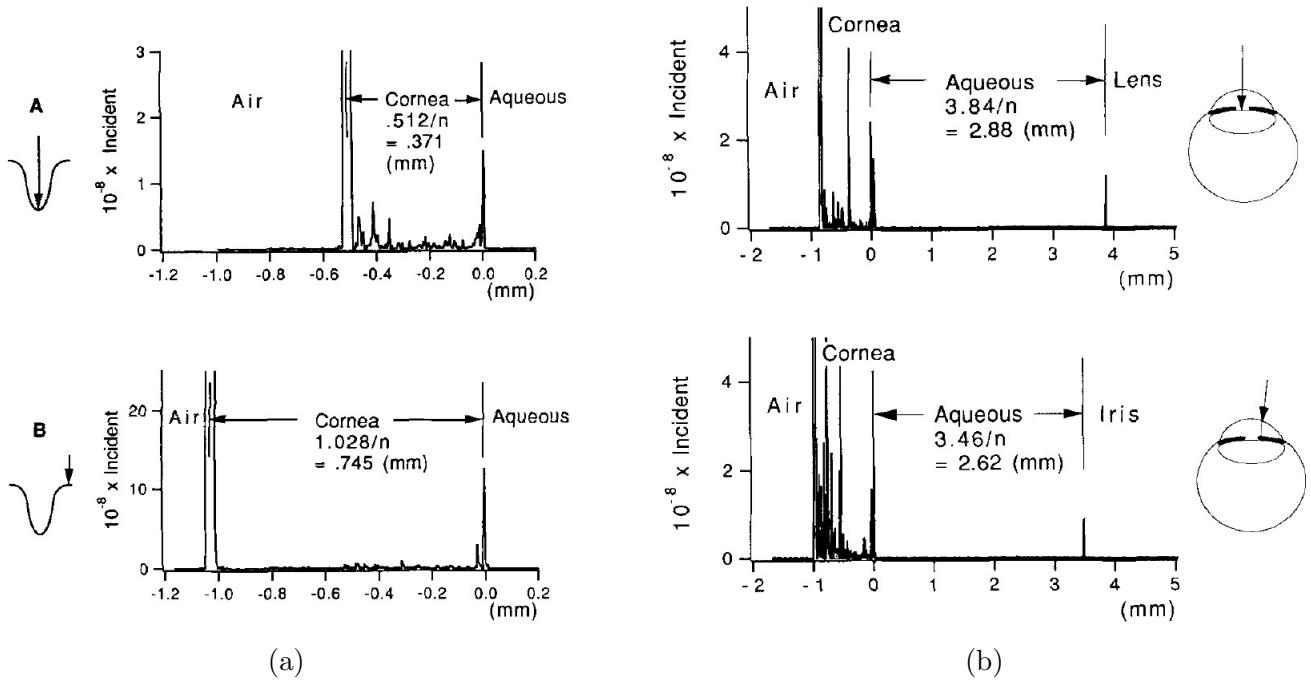

(a) (b)

Figure 1.4: Experiment performed by Huang *et al.* in 1991. (*a*) Interference measurements corresponding to the thickness of the cornea with an excision (top) and without it (bottom). The *x-axis* indicate the free space delays and the *y-axis* the reflected power. (*b*) Interference measurements corresponding to the thickness of the aqueous humor (anterior chamber) with respect to the lens of the eye (top) and respect to the iris (bottom). Images taken from [28].

Huang *et al.* used OCDR to produce cross sectional images of biological tissues [11]. They took multiple A-scans along a human retina and a human coronary artery *ex vivo* using the optical fiber based system which is shown in Fig. 1.5. The authors named this technique **Optical Coherence Tomography (OCT)** and obtained the images shown in Fig. 1.6. This scanning along one direction in the sample is known as **B-scan**. Different types of tissues were well distinguished in the images due to the differences in the light scattering properties between them. Consequently, OCT was proposed for research and clinical purposes.

In 1993, Fercher *et al.* obtained the first OCT image *in vivo* [29]. They scanned a human eye (at 830 nm) at the the optic disk and could observe the retina, the pigment epithelium and the lamina cribrosa. The same year, Swanson *et al.* produced OCT images of a human retina *in vivo* [30]. They could observe different parts of this region in the eye like the vitreous, retinal nerve fiber layer, photoreceptor layer, fovea and sclera. They suggested the use of OCT to diagnose and monitor glaucoma and retinal diseases like macular degeneration, macular hole and macular edema. In 1995, Puliafito *et al.* obtained OCT images with an axial resolution (a.r.) of 10 μm *in vivo* of the macula in persons with macular diseases like macular hole, epiretinal membrane, macular edema, diabetic retinopathy and detachments of the retinal pigment epithelium [31]. In this way, it was probed that OCT can be used as a diagnostic and monitoring tool for macular diseases.

In 1996, Brezinksi *et al.* obtained OCT images of aortic atherosclerotic plaques *ex vivo* from a human aorta with an a.r. of less than 20 μm and a lateral resolution (l.r.) of 30 μm [32]. Unlike the tissues in the eye, the aorta is nontransparent and it requires the use of a low coherence laser of 1300 nm (50 nm bandwidth) since infrared light is less absorbed by most of the tissues and can

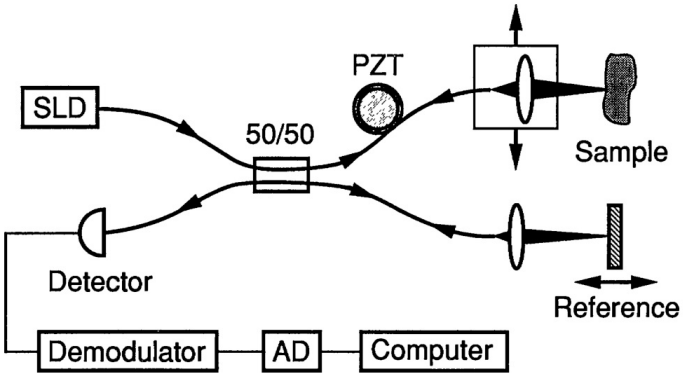

Figure 1.5: Optical fiber based system used by Huang *et al.* to produce cross-sectional images of a human retina and a human coronary artery *ex vivo*. The reference mirror is moved back and forth to detect the reflections sites in the sample. SLD (superluminescent diode, 830 nm), PZT (Piezoelectric transducer), AD (analog-digital converter). Image taken from [11].

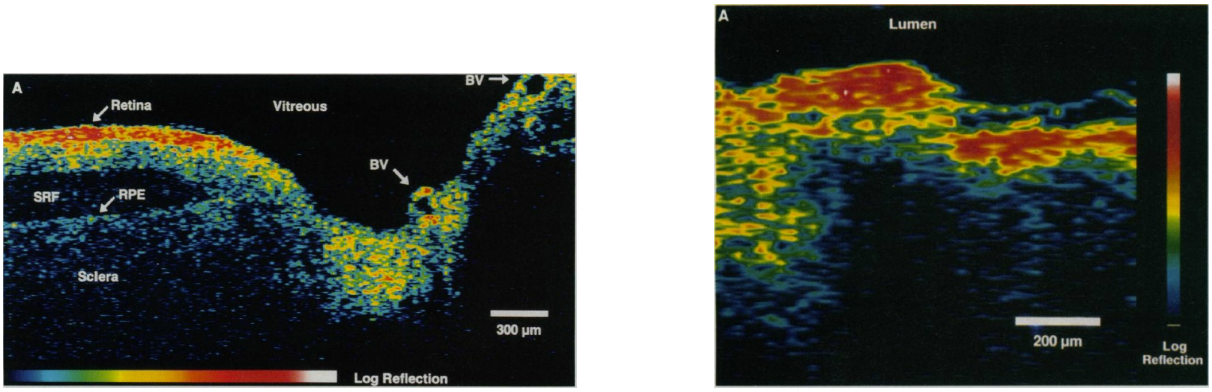

(a) (b)

Figure 1.6: Images obtained by Huang *et al.* in 1991. (*a*) OCT image of a human retina *ex vivo*. Labels: subretinal fluid (SRF), retinal pigment epithelium (RPE), blood vessels (BV). (*b*) OCT image of a human coronary artery *ex vivo*. Images taken from [11].

penetrate deeper. Figure 1.7a shows an OCT image of cardiac muscle next to adipose tissue. Both tissues can be well differentiated in the image since light is reflected much less by adipose tissue than muscle. Also, they published two OCT images of a human epiglottis *ex vivo* using two low coherence lasers at different wavelengths (λ), 1300 μm and 850 μm (Fig. 1.7b). The image with higher deepness is produced by the laser with longer λ (1300 μm). Because of the high resolution and its ability to differentiate different types of tissues, the authors proposed the use OCT for intravascular imaging. The same year, Tearney *et al.* created a rotatory catheter with a diameter of 1.1 mm to scan the internal wall of a human saphenous vein *in vitro* [33]. The probe had a microprism to reflect the light beam (λ = 1300 nm) out of it at 90° from the optical axis (see Fig. 2.1a in the next chapter). Then, it was inserted in the lumen and rotated to scan the internal wall. They could obtain an OCT image (a.r. = 20 μm) of the vessel wall (see Fig. 2.1c in the next chapter), probing that OCT is suitable to obtain images of the internal walls of tubular organs like in the vascular system as well as the gastrointestinal, urinary and respiratory tracts.

The first ophthalmic OCT commercial system was released in 1996 by the company Humphrey Zeiss [34]. The second and third commercial systems were released in 2000 and 2002 respectively,

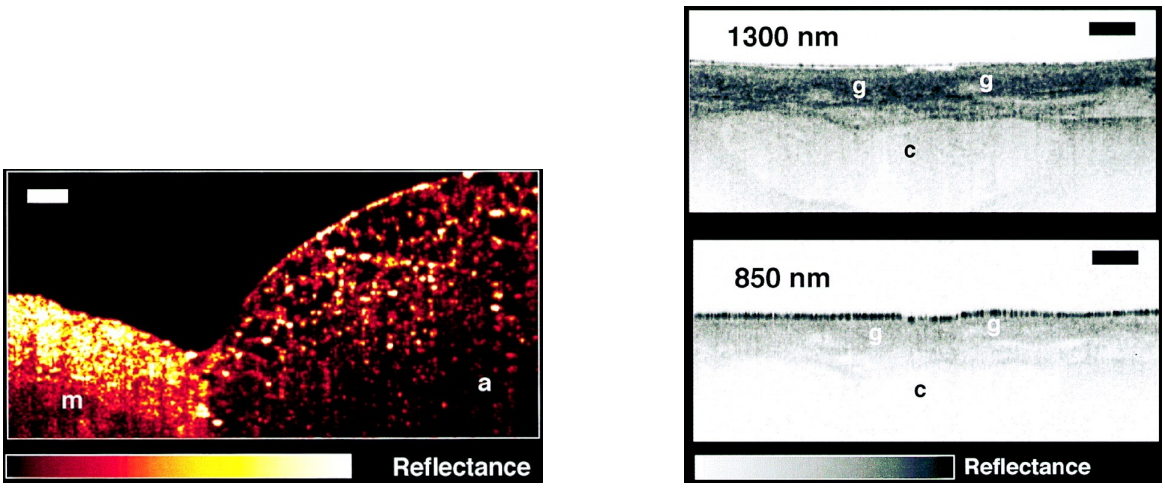

(a) (b)

Figure 1.7: (*a*) OCT image of cardiac muscle (m) next to adipose tissue (a) obtained by Brezinski *et al.* in 1996. (*b*) OCT images of a human epiglottis *ex vivo*. Labels: cartilage (c), superficial secretory glands (g). The length of the black bars is 500 μm. Images taken from [32].

having this last one an increase in the scanning velocity (400 A-scans per second). Images of these three systems are shown in Fig. 1.8. OCT also proved to be promising for neurosurgical imaging. Boppart *et al.* obtained 3D images of an intracortical metastatic melanoma in a human cerebral cortex (*ex vivo*) in 1998 [35]. The tumor showed an increase in optical backscattering in comparison with the surrounding healthy tissue and it could be differentiated in the image. Besides, the authors also produced an OCT image of one cerebral artery where the lumen is clearly visible. This work showed the capacity of OCT to detect tumors, delineate its margins and detect (and avoid) vascular structures, which is essential for resection procedures. OCT also was tested for applications in dermatology. The same year, Pan and Farkas obtained OCT images of a human fingertip, hand, forearm and nail *in vivo*, using a superluminescence diode with a λ of 1285 nm (to increase the penetration depth to around 2 mm) [36].

Figure 1.8: The first three OCT commercial systems. Image taken from [34].

OCT had started to be used as diagnostic tool. These systems that scan the internal layers by scanning the reference mirror are referred as time domain OCT (TD-OCT). However, the image rate was still limited by the speed of scanning of the reference mirror. A faster and more sensitive mode of OCT was required to develop clinical imaging systems. The next section introduces Fourier domain OCT (FD-OCT), the mode that fulfilled these requirements.

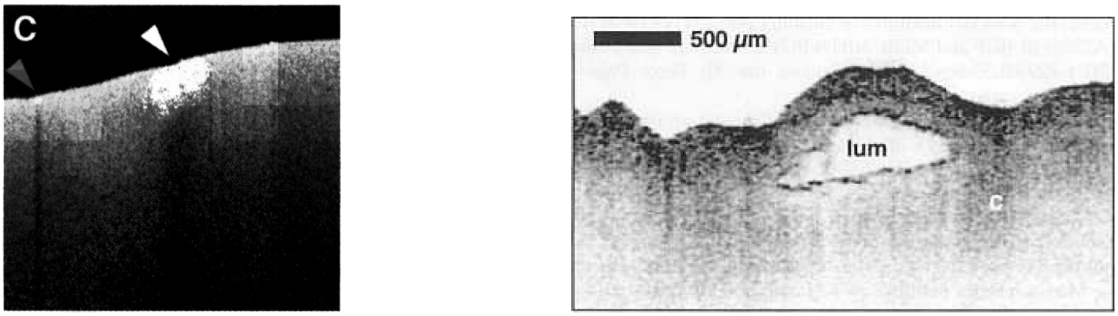

(a) (b)

Figure 1.9: Images obtained by Boppart *et al.* in 1998. (*a*) OCT image of an intracortical melanoma in a human cerebral cortex (a.r. = 16 μm, λ of the laser = 1300 nm, tumor size $<$ 1 mm). (*b*) OCT image of a cerebral artery *ex vivo*. Labels: artery lumen (lum), normal cortex (c). Images taken from [35].

1.2 Fourier Domain OCT

FD-OCT was described by Fercher *et al.* in 1995 [38]. They proved that the distances between layers in one sample can be obtained from the inverse Fourier transform of the interference spectrum between the reference mirror and the different layers in the sample. Therefore, it is not necessary to move the reference mirror as in TD-OCT. There are two ways to obtain the interference spectrum in FD-OCT. The first one is by using a spectrometer and a detector array at the output of the interferometer as shown in Fig. 1.10a. This spectrometer splits the interference signal in its different component frequencies that are detected simultaneously by a linear photodetector. This method is called spectral-domain OCT (SD-OCT). The second way is by sweeping the wavelength of the laser source along its spectrum while recording sequentially the component frequencies of the interference spectrum with a single detector (Fig. 1.10b). This technique is called swept-source OCT (SS-OCT).

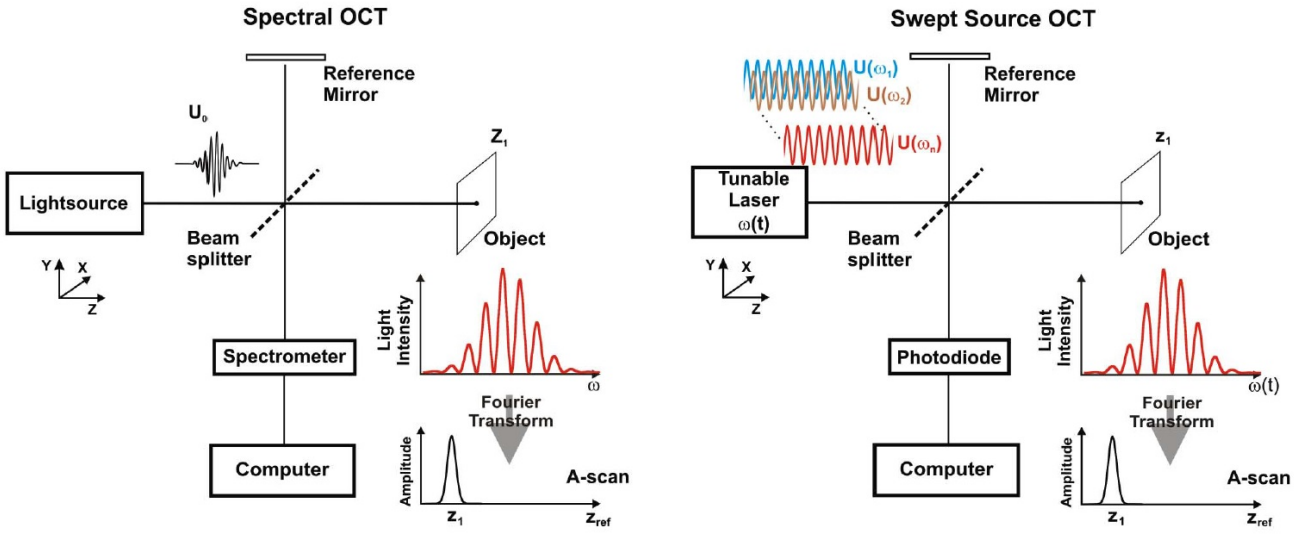

(a) (b)

Figure 1.10: (*a*) SD-OCT. (*b*) SS-OCT. Images taken from [40].

In 1998, Häusler *et al.* produced OCT images of human skin using SD-OCT [41]. They scanned

a hand *in vivo* and could measure the thickness of the different internal layers (stratum corneum, stratum germinativum and the stratum papilare). Besides, they also scanned a melanoma *in vitro* and could differentiate in the image from healthy tissue because of a thicker epidermis and a higher backscattering resulting from the increase in melanin in cancer cells. In 2002, Wojtkowski *et al.* got the first SD-OCT images of the human retina *in vivo* and could observe the inner limiting membrane, the retinal pigment epithelium and the choroid [42]. They could measure the thickness of the retina in the image (160 μm in the fovea, 215 μm out the fovea). Additionally, they presented images of the optic disc where blood vessels are also visible. Yun *et al.* also showed the use of SD-OCT for biological tissue imaging and an important increase in framing rate respect to TD-OCT [43]. The authors presented images of a finger at 38 frames per second (fps) of similar characteristis as others obtained with a TD-OCT system that provided only 4 fps. In 2004, Nassif *et al.* also presented images of the human retina *in vivo* and could observe its different layers as well. They also showed high speed in the scanning rate (29,300 A-scans/s) and an increase of 21.7 dB in sensivity compared to a TD-OCT system.

Regarding SS-OCT, Chinn *et al.* used an external cavity laser tuned with a grating and a mirror scanned with a galvanometer to produce OCT images of layers of glass [45]. The same year, Lexer *et al.* succeeded in obtaining A-scans of human eyes *in vivo* using a tunable laser diode [46]. They observed two peaks in the A-scan corresponding to the positions of the posterior layer of the lens and the retina and could measure the optical distances of the anterior segment (10.5 mm) and the vitreous body (24.8 mm). Golubovic *et al.* used a laser tuned by an array of prisms and, as Chinn *et al.*, a mirror scanned by a galvanometer to produce a 3D structure of the surface of a coin with an a. r. of 15 μm at 2000 A-scans/s [47]. In 2003, Yun *et al.* presented OCT images of a human finger with an a.r. of 13.5 μm using a swept laser at 15.7 kHz [48]. As with SD-OCT [43] (see last paragraph), they compared the characteristics of the image obtained with the SS-OCT system with a TD-OCT system and found the same sensitivity (110 dB) but an increase in speed from 4 fps (TD-OCT) to 30 fps (SS-OCT), 1.5 times higher depth range and 3 times less source power. SS-OCT showed to be suitable for medical imaging because of its high scanning speed and sensitivity. In 2005, Choma *et al.* succeeded in producing images of a human cornea and a fingerpad *in vivo* using SS-OCT with a sensitivity of 119 dB [49]. The same year, Huber *et al.* could increase slightly the A-scan rate to 16 kHz (32 fps) with a laser tuned with a grating and resonant scanner and achieved 3D images of a tadpole (sensitivity = 109 dB, a.r. $\approx$ 10 μm, acquisition time = 25 s) [51]. They also increased the field of depth to 600 μm approximately by changing the position of the focal point in the axial direction and fusing the resulting images. In 2006, Huber *et al.* achieved an A-scan rate of 370 kHz by removing the forward sweeps of the swept source and replacing them by the correspondent copies of the backward sweeps to have equal dynamic range in both directions (a difference in dynamic range is produced because of the high sweep rate) [52].

During the next years, the speed of FD-OCT continued increasing and it was utilized in more fields of medicine. Figure 1.11a shows a 2D and 3D SS-OCT image of the retina obtained at 1.37 MHz by Klein *et al.* where the macula and the optic disc can be observed clearly [53]. The scanning of the sample in two directions is known as **C-scan**. Commercial systems were also developed for dermatology applications. Figure 1.11b shows an image of a basal cell carcinoma in the right check of a 33-year-old woman obtained with a SS-OCT commercial system (Vivosight) [54]. Besides ophthalmology and dermatology, FD-OCT has also been used in cardiology ([55], [56]), neurology ([57] - [59]), pneumology ([60] - [62]) and urology ([63], [64]). Figures 1.11 and 1.12 provide some examples of the applications in these different fields. The mathematical theory of FD-OCT is presented in the next section.

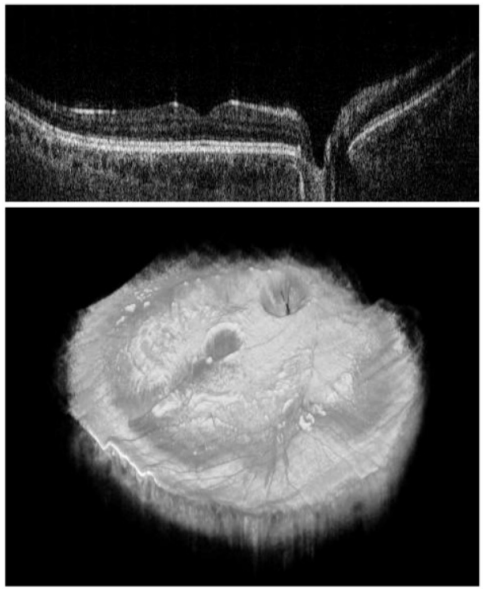

(a)

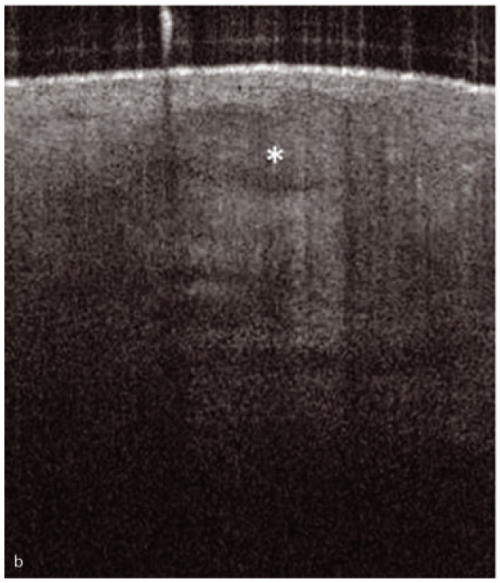

(b)

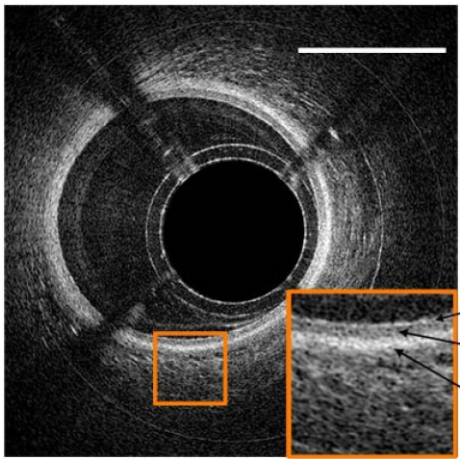

(c)

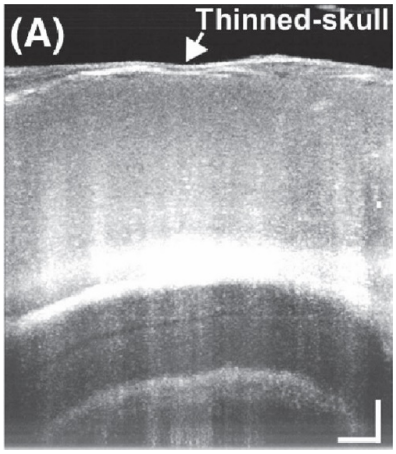

(d)

Figure 1.11: (*a*) B-scan (up) and C-scan (down) of a retina (a.r. = 19 μm) obtained with a SS-OCT system (λ = 1050 nm, acquisition time = 3 s). Images taken from [53]. (*b*) Basal cell carcinoma (a.r. < 10 μm, a.l. < 7.5 μm) obtained with a commercial SS-OCT system (Vivosight, λ = 1305 nm, A-scan rate = 20 kHz). (*) indicates basal cell nests. Image taken from [54]. (*c*) Left anterior descending artery of a swine (a.r. = 13 μm, l.r. = 29 μm, white line length = 1 mm). Image obtained *in vivo* with a rotatory catheter tip and a SS-OCT system (λ = 1310 nm) with an A-scan rate of 2.88 MHz (4000 fps). The internal elastic lamina, media and adventitia can be observed. Image taken from [55]. (*d*) Mice brain *in vivo* obtained with a SD-OCT system at λ = 1.7 μm (a.r. = 5.6 μm, l.r. = 15 μm). This wavelength proved to have the smallest attenuation coefficient for brain tissue imaging compared with 570 nm and 1.3 μm. The brightest part in the middle corresponds to the corpus callosum that presents an increased reflectivity due to its higher quantity of myelin. Under this structure, some layers of the hippocampus can be differentiated: stratum oriens, stratum pyramidale (the thinnest less reflective structure), stratum radiatum and the stratum lacunosum-moleculare at the bottom. White lines length = 0.5 mm. Image taken from [57].

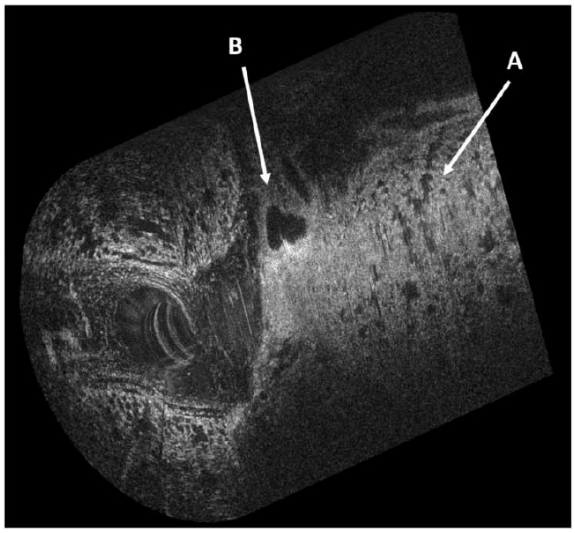

(a)

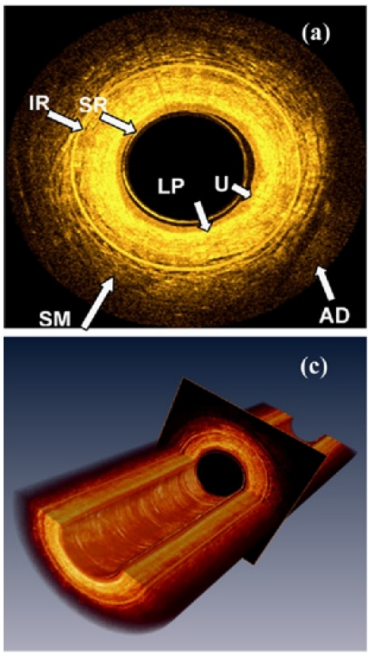

(b)

Figure 1.12: (*a*) 3D image composed of 400 radial B-scans of a lamb lung *ex vivo* (length of the volume = 2 mm, a.r. = 9.3 μm) obtained with an endoscopic needle probe with an outer diamter of only 0.31 mm and a SD-OCT system ($\lambda = 840$ nm). Bronchiole (B) and alveoli (A) structures can be observed. Image taken from [60]. (*b*) Radial B-scan of a porcine ureter *ex vivo* (up) and 3D reconstruction using 900 radial B-scans along 20 mm at 10 fps (down)(a.r. = 12 μm, l.r. = 8 μm). The images were obtained with a rotatory scanning fiber catheter and a SD-OCT system ($\lambda = 1.3$ μm) with an acquisition time of less than 90 s. Labels: catheter surface reflection (SR), lamina propria (LP), urothelium (U), internal reflection artifact (IR), smooth muscle (SM), adventitia (AD). Image taken from [63]

1.3 Mathematical theory of FD-OCT

The mathematical analysis of FD-OCT presented here was taken from [65]. Figure 1.13 presents the interferometer system used for this analysis. The electrical field of the input beam (coming from the light source) is given by:

$$E_i = S(k, \omega) \exp[i(kz - \omega t)] \tag{1.1}$$

where $S(k, w)$ is the amplitude as a function of the wavenumber $k = 2\pi/\lambda$ and the angular temporal frequency $\omega = 2\pi\nu$, λ is the wavelength and ν is the temporal frequency. The variable z denotes the distance traveled by the electric field and the variable t denotes time. It is assumed that all the distances are in free space for simplicity, therefore, the free space delays must be divided by the refractive index of the sample to obtain the real distances between the internal layers. The electrical field E_i is directed to the beam splitter (assumed achromatic with a power splitting ratio of 0.5) which divides it in two half-power beams, one goes to the reference reflector (reference arm) and the other one to the sample (sample arm). The reference reflector has an electric field reflectivity r_R whose power reflectivity is given by $R_R =\mid r_R \mid^2$. The distance between the beam splitter and the reference reflector is denoted as z_R.

The electrical field reflectivities of the different internal layers in the sample are $r_{s1}, r_{s2}, r_{s3}, \ldots r_{sN}$ and the distances between the beam splitter and each layer are $z_{s1}, z_{s2}, z_{s3} \ldots z_{sN}$, where N is the

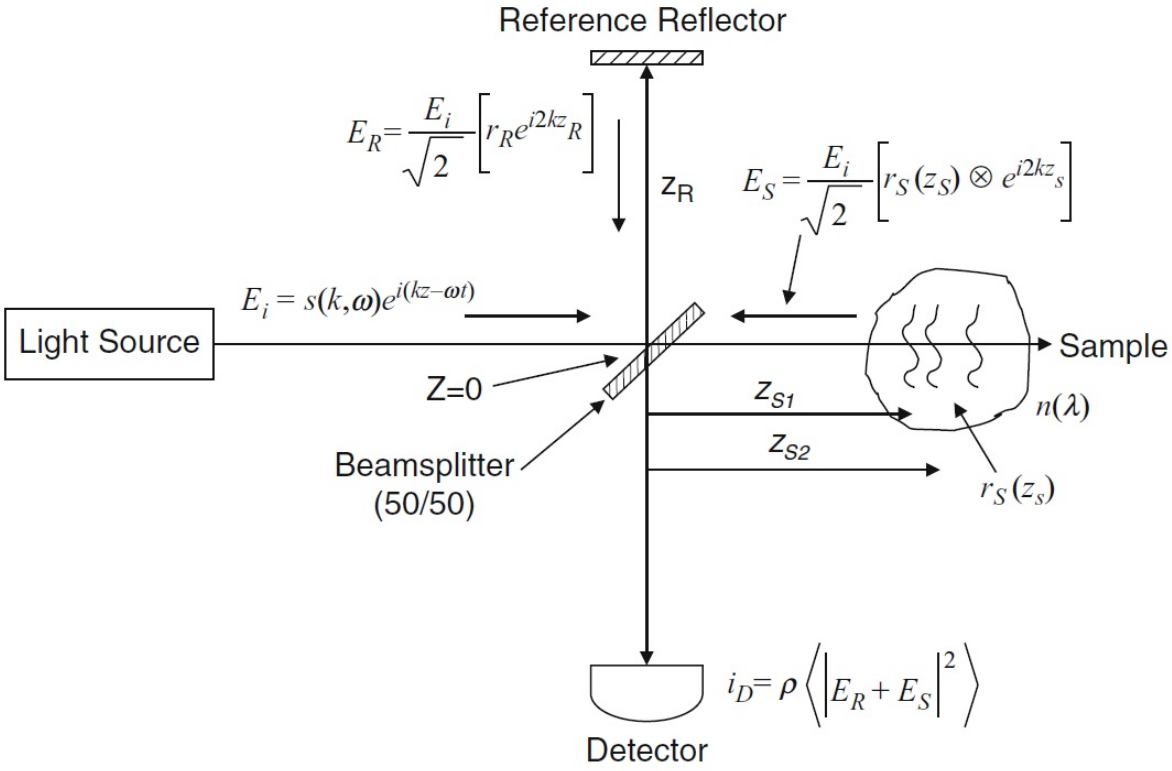

Figure 1.13: FD-OCT diagram. Image taken from [65].

total number of layers. The discrete depth-dependent electric field reflectivity profile of the sample is expressed as:

$$r_S(z_S) = \sum_{n=1}^{N} r_{Sn}\delta(z_S - z_{Sn}) \tag{1.2}$$

where δ is the delta function (see Fig. 1.14). The power reflectivity of each layer is $R_{Sn} = \mid r_{Sn} \mid^2$.

The electric field reflected back from the sample is:

$$E_S = \frac{E_i}{\sqrt{2}} \sum_{n=1}^{N} r_{Sn} \exp(i2kz_{Sn}) \tag{1.3}$$

On the other hand, the electric field reflected back by the reference reflector is given by:

$$E_R = \frac{E_i}{\sqrt{2}} r_R \exp(i2kz_R) \tag{1.4}$$

These electric fields reflected back by the sample and the reference reflector produce an interference pattern in the detector whose intensity is:

$$I_D(k,\omega) = \frac{\rho}{2}\langle \mid E_R + E_S \mid^2 \rangle = \frac{\rho}{2}\langle (E_R + E_S)(E_R + E_S)^* \rangle \tag{1.5}$$

where ρ is the responsivity of the detector (in amperes/watt), the angular brackets indicate integration over its response time and the symbol" * " denotes the complex conjugate. Substituting

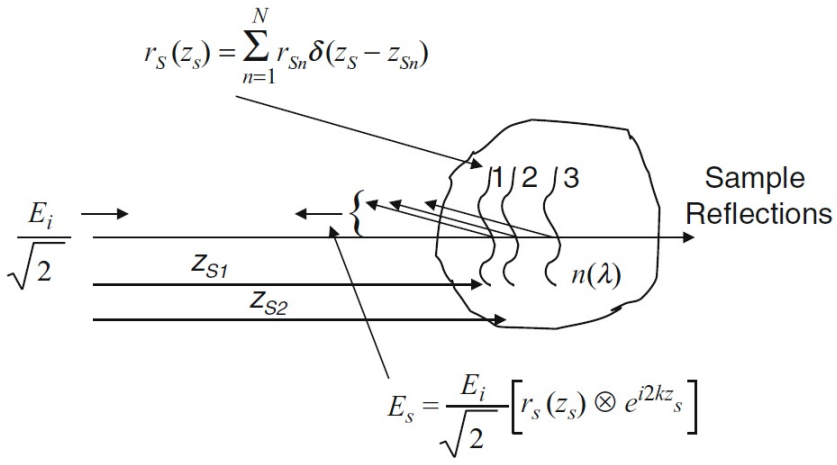

Figure 1.14: The internal layers of the sample, at different distances from the beam splitter, reflecting back the input light beam. Image taken from [65].

1.3 and 1.4 (and 1.1) in the last equation, it is obtained:

$$I_D(k,\omega) = \frac{\rho}{2}\left\langle \left| \frac{S(k,\omega)}{\sqrt{2}} r_R \exp[i(kz - \omega t + 2kz_R)] + \frac{S(k,\omega)}{\sqrt{2}} \sum_{n=1}^{N} r_{Sn} \exp[i(kz - \omega t + 2kz_{Sn})] \right|^2 \right\rangle \tag{1.6}$$

In Fig. 1.13, we can see that $z = 0$ in this reference system (where the beam splitter is placed). Therefore:

$$I_D(k,\omega) = \frac{\rho}{2}\left\langle \left\{ \frac{S(k,\omega)}{\sqrt{2}} r_R \exp[i(2kz_R - \omega t)] + \frac{S(k,\omega)}{\sqrt{2}} \sum_{n=1}^{N} r_{Sn} \exp[i(2kz_{Sn} - \omega t)] \right\} \left\{ \frac{S(k,\omega)}{\sqrt{2}} r_R \exp[-i(2kz_R - \omega t)] + \frac{S(k,\omega)}{\sqrt{2}} \sum_{n=1}^{N} r_{Sn} \exp[-i(2kz_{Sn} - \omega t)] \right\} \right\rangle \tag{1.7}$$

The second term of the multiplication is the complex conjugate term (equation 1.5). After performing the multiplication, we have:

$$I_D(k,\omega) = \frac{\rho}{2}\left\langle \left\{ \frac{[S(k,\omega)]^2}{2} \right\} \left\{ (r_R)^2 + \sum_{n=1}^{N} r_R r_{Sn} \exp[i2k(z_R - z_{Sn})] + \sum_{n=1}^{N} r_R r_{Sn} \exp[-i2k(z_R - z_{Sn})] + \left\{ \sum_{n=1}^{N} r_{Sn} \exp[i(2kz_{Sn} - \omega t)] \right\} \left\{ \sum_{n=1}^{N} r_{Sn} \exp[-i(2kz_{Sn} - \omega t)] \right\} \right\} \right\rangle \tag{1.8}$$

The first two sums sequences can be joined in one term. It can be shown that:

$$\begin{aligned}&\sum_{n=1}^{N} r_R r_{Sn} \exp[i2k(z_R - z_{Sn})] + \sum_{n=1}^{N} r_R r_{Sn} \exp[-i2k(z_R - z_{Sn})] = \\ &\sum_{n=1}^{N} r_R r_{Sn} \{\exp[i2k(z_R - z_{Sn})] + \exp[-i2k(z_R - z_{Sn})]\}\end{aligned} \tag{1.9}$$

and also that:

$$\begin{aligned}&\left\{\sum_{n=1}^{N} r_{Sn} \exp[i(2kz_{Sn} - \omega t)]\right\}\left\{\sum_{n=1}^{N} r_{Sn} \exp[-i(2kz_{Sn} - \omega t)]\right\} = \\ &\sum_{n=1}^{N}(r_{Sn})^2 + \sum_{n\neq m=1}^{N} r_{Sn} r_{Sm} \{\exp[i2k(z_{Sn} - z_{Sm})] + \exp[-i2k(z_{Sn} - z_{Sm})]\}\end{aligned} \tag{1.10}$$

Substituting the equations 1.9 and 1.10 in 1.8, we have:

$$\begin{aligned}I_D(k,\omega) = \frac{\rho}{2}\Bigg\langle &\left\{\frac{[S(k,\omega)]^2}{2}\right\}\Bigg\{R_R + \sum_{n=1}^{N} R_{Sn} \\ &+ \sum_{n=1}^{N} \sqrt{R_R R_{Sn}}\,\{\exp[i2k(z_R - z_{Sn})] + \exp[-i2k(z_R - z_{Sn})]\} \\ &+ \sum_{n\neq m=1}^{N} \sqrt{R_{Sn} R_{Sm}}\,\{\exp[i2k(z_{Sn} - z_{Sm})] + \exp[-i2k(z_{Sn} - z_{Sm})]\}\Bigg\}\Bigg\rangle\end{aligned} \tag{1.11}$$

The angular brackets denote time average:

$$\langle \ldots \rangle = \lim_{T\to\infty} \frac{1}{T} \int_{-\frac{1}{2}T}^{\frac{1}{2}T} \ldots \, \mathrm{d}\tau \tag{1.12}$$

In equation 1.11, only the term $[S(k,\omega)]^2$ depends upon the temporal angular frequency $\omega = 2\pi\nu$ (the temporal frequency ν is related to the temporal period τ by: $\nu \equiv 1/\tau$). This term averaged in time is referred as $S(k)$ and corresponds to the light source spectrum:

$$S(k) = \left\langle [S(k,\omega)]^2 \right\rangle = \lim_{T\to\infty} \frac{1}{T} \int_{-\frac{1}{2}T}^{\frac{1}{2}T} \left[S\left(k, \frac{2\pi}{\tau}\right)\right]^2 \mathrm{d}\tau \tag{1.13}$$

Hence, the equation 1.11 can be expressed as:

$$\begin{aligned}I_D(k) = &\left(\frac{\rho}{4}\right)\left[S(k)\left(R_R + \sum_{n=1}^{N} R_{Sn}\right)\right] \\ &+ \left(\frac{\rho}{4}\right)\left\{S(k)\sum_{n=1}^{N} \sqrt{R_R R_{Sn}}\,\{\exp[i2k(z_R - z_{Sn})] + \exp[-i2k(z_R - z_{Sn})]\}\right\} \\ &+ \left(\frac{\rho}{4}\right)\left\{S(k)\sum_{n\neq m=1}^{N} \sqrt{R_{Sn} R_{Sm}}\,\{\exp[i2k(z_{Sn} - z_{Sm})] + \exp[-i2k(z_{Sn} - z_{Sm})]\}\right\}\end{aligned} \tag{1.14}$$

Then, the Euler's formula:

$$2\cos(x) = \exp(ix) + \exp(-ix) \tag{1.15}$$

can be used to have:

$$\begin{aligned} I_D(k) = &\left(\frac{\rho}{4}\right)\left[S(k)\left(R_R + \sum_{n=1}^{N} R_{Sn}\right)\right] \quad \text{“DC Terms”} \\ &+ \left(\frac{\rho}{2}\right)\left\{S(k)\sum_{n=1}^{N}\sqrt{R_R R_{Sn}}\cos[2k(z_R - z_{Sn})]\right\} \quad \text{“Cross} - \text{correlation Terms”} \\ &+ \left(\frac{\rho}{2}\right)\left\{S(k)\sum_{n\neq m=1}^{N}\sqrt{R_{Sn}R_{Sm}}\cos[2k(z_{Sn} - z_{Sm})]\right\} \quad \text{“Auto} - \text{correlation Terms”} \end{aligned} \tag{1.16}$$

The “Cross-correlation terms” have the differences between the distances of the reference reflector and the internal layers of the sample. These are the terms we are interested in. The “Auto-correlation terms” represent the interference between the light back reflected by the different internal layers of the sample and appear as artifacts in the OCT systems. Equation 1.16 provides the intensity distribution measured by the detector and it is known as “spectral interferogram”. The spectral components of $I_D(k)$ can be obtained by SD-OCT (diffraction grating) or SS-OCT (sweeping the wavelength of the light source). The inverse Fourier transform of the equation 1.16 must be calculated in order to obtain the reflectivity profile of the sample $\sqrt{R_s(z_s)}$ (to pass the equation from the k-space to the space domain (z)):

$$i_D(z) = \mathcal{F}^{-1}\{I_D(k)\} \tag{1.17}$$

The operator $\mathcal{F}^{-1}\{\}$ indicates the inverse Fourier transform.

The linearity theorem of the Fourier transform states that:

$$\mathcal{F}\{\alpha f(z) + \beta g(z)\} = \alpha\mathcal{F}\{f(z)\} + \beta\mathcal{F}\{g(z)\} \tag{1.18}$$

where α and β are constants. Therefore, the inverse Fourier transform of $I_D(k)$ is expressed as:

$$\begin{aligned} i_D(z) = &\left(\frac{\rho}{4}\right)\left(R_R + \sum_{n=1}^{N} R_{Sn}\right)\mathcal{F}^{-1}\{S(k)\} \\ &+ \left(\frac{\rho}{2}\right)\mathcal{F}^{-1}\left\{S(k)\sum_{n=1}^{N}\sqrt{R_R R_{Sn}}\cos[2k(z_R - z_{Sn})]\right\} \\ &+ \left(\frac{\rho}{2}\right)\mathcal{F}^{-1}\left\{S(k)\sum_{n\neq m=1}^{N}\sqrt{R_{Sn}R_{Sm}}\cos[2k(z_{Sn} - z_{Sm})]\right\} \end{aligned} \tag{1.19}$$

Then, the convolution theorem (see pag. 117 in [66]):

$$\mathcal{F}\{f(z)\,g(z)\} = \mathcal{F}\{f(z)\} \circledast \mathcal{F}\{g(z)\} \tag{1.20}$$

is used to write the equation 1.19 as:

$$\begin{aligned} i_D(z) = &\left(\frac{\rho}{4}\right)\left(R_R + \sum_{n=1}^{N} R_{Sn}\right)\mathcal{F}^{-1}\{S(k)\} \\ &+ \left(\frac{\rho}{2}\right)\left\{\mathcal{F}^{-1}\{S(k)\} \circledast \mathcal{F}^{-1}\left\{\sum_{n=1}^{N}\sqrt{R_R R_{Sn}}\cos[2k(z_R - z_{Sn})]\right\}\right\} \\ &+ \left(\frac{\rho}{2}\right)\left\{\mathcal{F}^{-1}\{S(k)\} \circledast \mathcal{F}^{-1}\left\{\sum_{n\neq m=1}^{N}\sqrt{R_{Sn} R_{Sm}}\cos[2k(z_{Sn} - z_{Sm})]\right\}\right\} \end{aligned} \tag{1.21}$$

Now, the inverse Fourier transforms of the light source spectrum function $S(k)$ and the cosine functions must be obtained.

The spectrum of the light sources are Gaussian-shaped, hence, the light source spectrum is expressed as a Gaussian function:

$$S(k) = \frac{1}{\Delta k\sqrt{\pi}}\exp\left[-\left(\frac{k - k_0}{\Delta k}\right)^2\right] \tag{1.22}$$

where Δk is the spectral bandwidth (half-width of the spectrum at $1/e$ of its maximum) (Fig. 1.15, *right*). The inverse Fourier transform of a Gaussian function is also Gaussian:

$$\mathcal{F}^{-1}\{S(k)\} = \exp(-z^2\Delta k^2) = \gamma(z) \tag{1.23}$$

The term $\gamma(z)$ is called "coherence function" and it is shown in Fig. 1.15 (*left*) where l_c is the free-space coherence length that corresponds to the light source bandwidth:

$$l_c = \frac{2\sqrt{\ln(2)}}{\Delta k} = \frac{2\,\ln(2)}{\pi}\frac{\lambda_0^2}{\Delta\lambda} \tag{1.24}$$

where λ_0 is the central wavelength of the light source:

$$\lambda_0 = \frac{2\pi}{k_0} \tag{1.25}$$

and $\Delta\lambda$ is the wavelength bandwidth.

On the other hand, the inverse Fourier transform of a cosine function is given by:

$$\mathcal{F}^{-1}\{\cos(kz_0)\} = \frac{1}{2}[\delta(z + z_0) + \delta(z - z_0)] \tag{1.26}$$

Using this equation, it can be shown that:

$$\mathcal{F}^{-1}\left\{\sum_{n=1}^{N}\sqrt{R_R R_{Sn}}\cos[2k(z_R - z_{Sn})]\right\} = \sum_{n=1}^{N}\frac{\sqrt{R_R R_{Sn}}}{2}\{\delta[z \pm 2(z_R - z_{Sn})]\} \tag{1.27}$$

$$\mathcal{F}^{-1}\left\{\sum_{n\neq m=1}^{N}\sqrt{R_{Sn} R_{Sm}}\cos[2k(z_{Sn} - z_{Sm})]\right\} = \sum_{n\neq m=1}^{N}\frac{\sqrt{R_{Sn} R_{Sm}}}{2}\{\delta[z \pm 2(z_{Sn} - z_{Sm})]\} \tag{1.28}$$

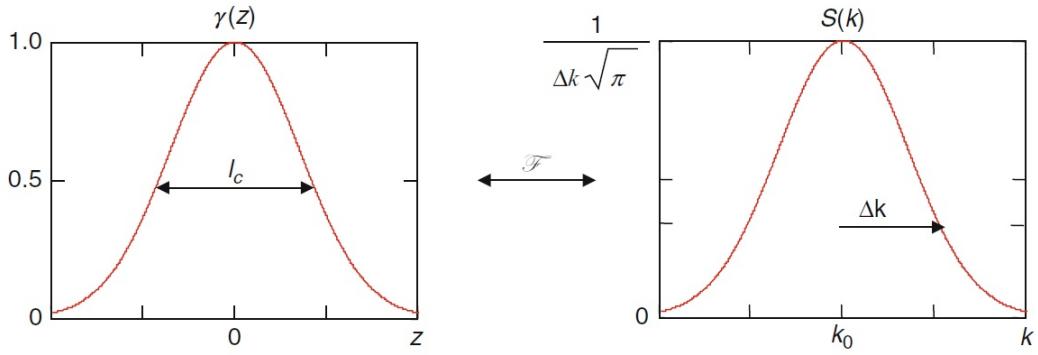

Figure 1.15: Light source spectrum $S(k)$ (*right*) and its inverse Fourier transform $\gamma(z)$ (*left*). Image taken from [65].

Substituting 1.23, 1.27 and 1.28 in 1.21, we obtain:

$$\begin{aligned} i_D(z) = &\left(\frac{\rho}{4}\right)\left[\gamma(z)\left(R_R + \sum_{n=1}^{N} R_{Sn}\right)\right] \quad \text{“DC Terms”} \\ &+ \left(\frac{\rho}{4}\right)\left\{\gamma(z) \circledast \sum_{n=1}^{N} \sqrt{R_R R_{Sn}}\left\{\delta[z \pm 2(z_R - z_{Sn})]\right\}\right\} \quad \text{“Cross} - \text{correlation Terms”} \\ &+ \left(\frac{\rho}{4}\right)\left\{\gamma(z) \circledast \sum_{n\neq m=1}^{N} \sqrt{R_{Sn} R_{Sm}}\left\{\delta[z \pm 2(z_{Sn} - z_{Sm})]\right\}\right\} \quad \text{“Auto} - \text{correlation Terms”} \end{aligned} \tag{1.29}$$

To simplify this equation, we can use the distributive property of the convolution:

$$f(z) \circledast [g(z) + h(z)] = f(z) \circledast g(z) + f(z) \circledast h(z) \tag{1.30}$$

Hence, the equation 1.29 can be expressed as:

$$\begin{aligned} i_D(z) = &\left(\frac{\rho}{4}\right)\left[\gamma(z)\left(R_R + \sum_{n=1}^{N} R_{Sn}\right)\right] \\ &+ \left(\frac{\rho}{4}\right)\left\{\sum_{n=1}^{N} \sqrt{R_R R_{Sn}}\left\{\gamma(z) \circledast \delta[z + 2(z_R - z_{Sn})] + \gamma(z) \circledast \delta[z - 2(z_R - z_{Sn})]\right\}\right\} \\ &+ \left(\frac{\rho}{4}\right)\left\{\sum_{n\neq m=1}^{N} \sqrt{R_{Sn} R_{Sm}}\left\{\gamma(z) \circledast \delta[z + 2(z_{Sn} - z_{Sm})] + \gamma(z) \circledast \delta[z - 2(z_{Sn} - z_{Sm})]\right\}\right\} \end{aligned} \tag{1.31}$$

The convolution of two functions is defined as:

$$f(z) \circledast g(z) = \int_{-\infty}^{\infty} f(u)\, g(z-u)\mathrm{d}u \tag{1.32}$$

Therefore, the convolution of one of the terms of the equation 1.31 (from the second sum for example) is expressed as:

$$\gamma(z) \circledast \delta[z + 2(z_R - z_{S1})] = \int_{-\infty}^{\infty} \gamma(u)\, \delta[(z-u) + 2(z_R - z_{S1})]\mathrm{d}u \tag{1.33}$$

Using this property of the delta function:

$$\delta(x) = \delta(-x) \tag{1.34}$$

the convolution can be written as:

$$\gamma(z) \circledast \delta[z + 2(z_R - z_{S1})] = \int_{-\infty}^{\infty} \gamma(u)\, \delta\{u - [z + 2(z_R - z_{S1})]\}\mathrm{d}u \tag{1.35}$$

On the other hand, the sifting property of the delta function states that:

$$\int_{-\infty}^{\infty} f(x)\delta(x - a)\mathrm{d}x = f(a) \tag{1.36}$$

Using this property and making $a = [z + 2(z_R - z_{S1})]$:

$$\int_{-\infty}^{\infty} \gamma(u)\, \delta\{u - [z + 2(z_R - z_{S1})]\}\mathrm{d}u = \gamma(z + 2(z_R - z_{S1})) \tag{1.37}$$

and finally, the convolution results in:

$$\gamma(z) \circledast \delta[z + 2(z_R - z_{S1})] = \gamma(z + 2(z_R - z_{S1})) \tag{1.38}$$

It can be proved that all the convolutions in the equation 1.31 can be expressed in the same way. Finally, the expression for $i_D(z)$ that corresponds to the "A-scan" of the sample is:

$$\begin{aligned} i_D(z) = &\left(\frac{\rho}{4}\right)\left[\gamma(z)\left(R_R + \sum_{n=1}^{N} R_{Sn}\right)\right] \\ &+ \left(\frac{\rho}{4}\right)\left\{\sum_{n=1}^{N} \sqrt{R_R R_{Sn}}\,\{\gamma[z + 2(z_R - z_{Sn})] + \gamma[z - 2(z_R - z_{Sn})]\}\right\} \\ &+ \left(\frac{\rho}{4}\right)\left\{\sum_{n\neq m=1}^{N} \sqrt{R_{Sn} R_{Sm}}\,\{\gamma[z + 2(z_{Sn} - z_{Sm})] + \gamma[z - 2(z_{Sn} - z_{Sm})]\}\right\} \end{aligned} \tag{1.39}$$

Figure 1.16 shows the graph of this function. It is observed that the different layers of the sample are given by the cross-correlation terms. Besides, a mirror image is also produced since the cross-correlation terms are complex conjugates of each other. Notice that the amplitude of the DC term (produced mainly by the reflectivity of the reference mirror) is much bigger than the amplitudes of the cross-correlation terms. One way to decrease this amplitude is to record the spectral interferogram but without a sample (to have only the contribution from the reference mirror) and then subtract it from the interferograms measured with the sample. In this way, the amplitudes of the cross-correlation terms increase significantly and the layers of the sample are better appreciated. The auto-correlation terms also appear as artifacts in the image as the DC term. They are close to $z = 0$ since the distances between the layers of the sample are much smaller than the distances between these layers and the reference mirror. The amplitudes of these terms are smaller than the amplitudes of the cross-correlation terms as soon as the reflectivity of the reference mirror is much bigger than the reflectivities of the layers of the sample (as it is usually). These terms are not only produced by the interference between the back reflections coming from the different layers of the sample but also by the interference between the many back reflections coming from the internal reflecting surfaces of the different devices of the OCT system (connections of optical fibers mainly).

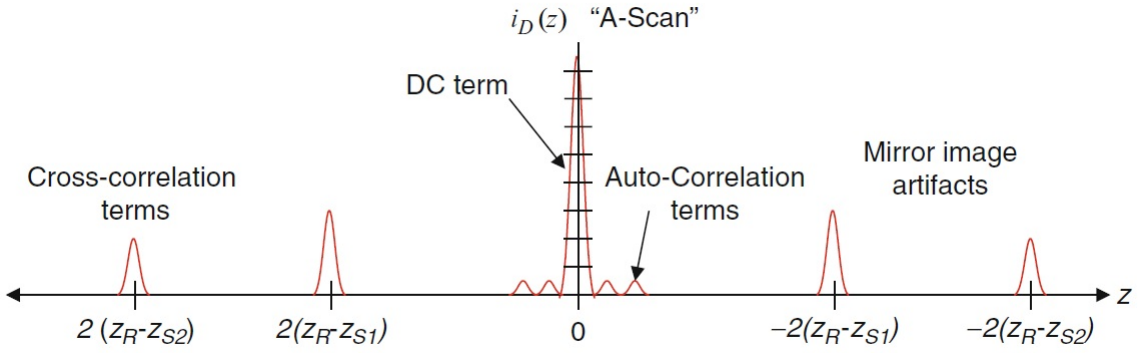

Figure 1.16: Graph of the function $i_D(z)$ ("A-scan"). Image taken from [65]

1.3.1 Sampling effects in FD-OCT

In real world applications, FD-OCT is limited by the optical and electronic characteristics of the equipment that is used in the system. In SD-OCT, the spectral resolution $\delta_r k$ of the acquisition equipment is limited by the resolution of the spectrometer and the distance between the pixels of the linear photodetector. The finite spectral resolution can be modeled by convolving an ideal interferogram with the Gaussian function:

$$\exp\left[-\frac{4\ln(2)k^2}{\delta_r k^2}\right]$$

as shown in Fig. 1.17a. When taking the inverse Fourier transform to obtain the A-scan, the convolution becomes a multiplication and the inverse Fourier transform of the Gaussian function is given by:

$$\exp\left[-\frac{\hat{z}^2\,\delta_r k^2}{4\ln(2)}\right]$$

where $\hat{z} = 2z$. This term, which is also a Gaussian function, gives the sensitivity decay in the A-scan since it is multiplying the function $i_D(\hat{z})$ as shown in Fig. 1.17b. Hence, this exponential describes the decrease of visibility of the deeper layers of the sample that correspond to the higher frequencies of the spectral interferograms. The exponential equals 0.5 if:

$$\hat{z}_{6dB} = \frac{2\ln(2)}{\delta_r k} = \frac{\ln(2)\lambda_0^2}{\pi\,\delta_r \lambda} \tag{1.40}$$

So, the sensitivity decreases at the half (6 dB) at this value of $\hat{z}$, that corresponds to the half of the free-space coherence length.

Other limitation in real applications is that the spectral interferograms must be resampled as in usual electrical signals acquisition. The sampling interval is referred as $\delta_s k$ and the total number of acquisitions as M (see Fig. 1.17a). Therefore, the total wave number range is:

$$\Delta k = M\,\delta_s k \tag{1.41}$$

that provides the sampling interval in the z-space:

$$\delta_s \hat{z} = \frac{2\pi}{2\Delta k} \tag{1.42}$$

Finally, the maximum range in the z-space is given by:

$$\pm\, z_{max} = \pm\frac{\pi}{2\,\delta_s k} = \pm\frac{n_0\lambda_0^2}{4\,\delta_s \lambda} \tag{1.43}$$

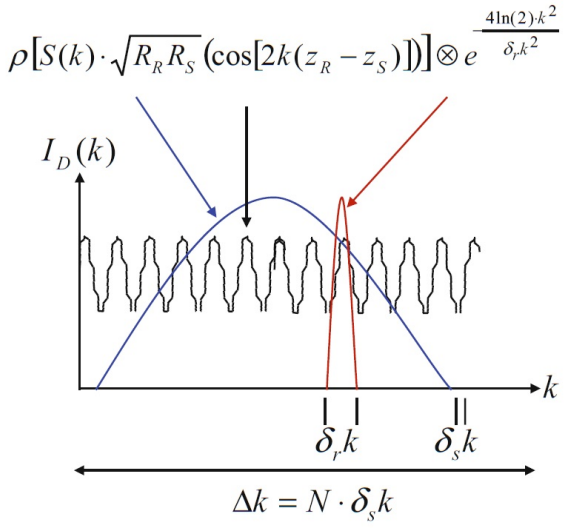

(a)

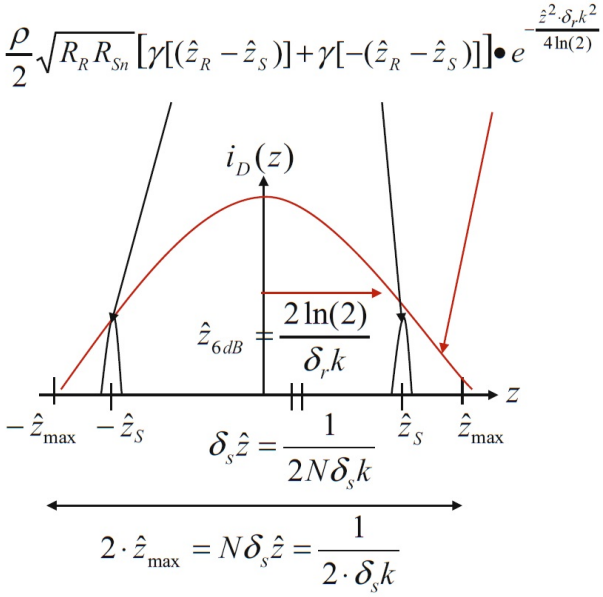

(b)

Figure 1.17: (*a*) Ideal interferogram convolved with a Gaussian function that models the finite spectral resolution. (*b*) Inverse Fourier transform. Images taken from [65].

1.3.2 Sensitivity in FD-OCT

The analysis of the sensitivity of FD-OCT was published in 2003 in three different articles ([69], [70], [71]). The sensitivity of one OCT system is defined as "*the minimal sample arm reflectivity, at which the signal to noise ratio (SNR) equals one*" [69], in other words, the SNR for a perfect reflector. Hence, an expression for the SNR must be obtained. The SNR is defined as "*the signal power divided by the noise process variance*" [65]. The OCT signal (interferogram) is given by the equation 1.16. For simplicity, only one layer in the sample with reflectivity R_S at the distance z_S is considered and the auto-correlations terms are neglected. With these considerations, the discrete

version of the equation 1.16 is:

$$I_D(k_m) = \frac{\rho}{2} S_{FDOCT}(k_m) \left\{ R_R + R_S + 2\sqrt{R_R R_S} \cos[2k_m(z_R - z_S)] \right\} \tag{1.44}$$

where:

$$S_{FDOCT}(k_m) = \frac{S(k)|_{k=k_m}}{2} \tag{1.45}$$

As before, the inverse Fourier transform (discrete in this case) of $I_D(k_m)$ is taken to pass this function to the space domain (z):

$$i_D(z_m) = \sum_{m=1}^{M} I_D(k_m) \exp\left(\frac{ik_m z_m}{M}\right) \tag{1.46}$$

For the case that the distance between the sample (one layer) and the beam splitter equals the distance between the reference mirror and the beam splitter ($z_R = z_S$), the cross-correlation term of the equation 1.44 is:

$$i_D(z_m = z_R - z_S = 0) = \frac{\rho}{2}\sqrt{R_R R_S} \sum_{m=1}^{M} S_{FDOCT}(k_m) \tag{1.47}$$

Assuming a rectangular shape of the light source spectrum, in order to have the same power throughout the spectrum, the last equation can be expressed as:

$$i_D(z_m = z_R - z_S = 0) = \frac{\rho}{2}\sqrt{R_R R_S}\, S_{FDOCT}(k_m)\, M \tag{1.48}$$

For the case of a light source spectrum with a Gaussian shape centered at $M/2$, we have:

$$S_{FDOCT}(k_m) = S_{FDOCT}(k_{M/2}) \exp\left[\frac{-2\,(k_m - k_{M/2})^2}{(k_{M/2})^2}\right] \tag{1.49}$$

and $i_D(z_m = 0)$ turns to:

$$i_D(z_m = z_R - z_S = 0) = \frac{\rho}{2}\sqrt{R_R R_S}\, S_{FDOCT}(k_{M/2})\, M\,(0.598) \tag{1.50}$$

Therefore, the mean-square peak signal power of i_D (for a rectangular shape of the light source spectrum) is:

$$\langle i_D \rangle^2_{FDOCT} = \frac{\rho^2 S^2_{FDOCT}(k_m)}{4} R_R R_S\, M^2 \tag{1.51}$$

Regarding the noise variance, we must consider how the white noise $\alpha(k_m)$ of the OCT signal is transformed from the k-space to the z-space. It has a mean of zero, a standard deviation $\sigma(k_m)$ and it is limited by shot noise. In OCT, the reflectivity from the reference mirror is bigger than the reflectivity from the sample ($R_R \gg R_S$). So, the noise variance in the shot noise limit is given by:

$$\sigma^2 = e\rho S_{FDOCT}(k_m) R_R B_{FDOCT} \tag{1.52}$$

where e is the electronic charge ($e = 1.6021x10^{-19}C$) and B_{FDOCT} is the bandwidth of the system. The noise in each component of k_m is not correlated, so, the noise variances can be added incoherently in the inverse discrete Fourier transform:

$$\sigma^2_{FDOCT}(z_m) = \sum_{m=1}^{M} \sigma^2_{FDOCT}(k_m) = e\rho S_{FDOCT}(k_m) R_R B_{FDOCT} M \tag{1.53}$$

Finally, the SNR in FD-OCT is given by:

$$SNR_{FDOCT} = \frac{\langle i_D \rangle^2_{FDOCT}}{\sigma^2_{FDOCT}} = \frac{\rho\, S_{FDOCT}(k_m)\, R_S}{4\, e\, B_{FDOCT}}\, M \tag{1.54}$$

1.4 Conclusion

In this chapter, we reviewed the development of OCT since the first experiments about detection of laser pulses reflected from internal layers of biological samples until recent applications in different fields of medicine such as ophthalmology, dermatology, cardiology, neurology, pneumology and urology. OCT has shown to be a proper technique for monitoring and diagnosis due to its high resolution and depth scanning, tissue differentiation and tumor detection capacities. With the development of FD-OCT, the scanning rate and the sensitivity could be increased making this technique suitable for medical real time imaging. It was probed that the depth profile of the sample is retrieved by applying the inverse Fourier transform to the interference pattern, produced by the internal layers of the sample and the reference mirror. In this work, we present an endoscopic FD - OCT probe for early cancer detection in gastroenterology. These type of devices will be discussed in the next chapter.

2

OCT in gastroenterology based on endoscopic probes

Since the OCT systems can be assembled with optical fibers (see Fig. 1.5 in the previous chapter), endoscopic imaging is feasible by coupling the fiber of the sample arm in an endoscope or a cathether. Some examples were already introduced in the previous chapter where images of internal organs (vein [33], ureter [63], lung [60], coronary artery [55]) were obtained with rotatory scanning probes as the one in Fig. 2.1a. They were coupled in the sample arm fiber where, at the distal end, there is a GRIN lens that focuses the light beam towards a micro reflective surface (as the right angle prism in Fig. 2.1a) that then reflects it out of the probe at 90° (side-viewing probes). Afterwards, the probe is inserted in the tubular organ and rotated with external motors (proximal-end scanning probes) or integrated micro motors (distal-end scanning probes, Fig. 2.1b) to perform radial B-scans as in Fig. 2.1c. Besides, the probe can be pull forth and back to combine radial and lateral scanning and produce 3D tubular OCT images as those ones showed in the previous chapter in Fig. 1.12. Gora *et al.* have reviewed the applications of these endoscopic probes in several fields of medicine such as cardiology, pneumology, urology, gynecology and otolaryngology where they also describe forward-viewing probes as in Fig 2.1d [73]. In these type of probes, the sample arm fiber is mounted in the actuator (PZT tube in this example) that moves it vertically and horizontally and then, the light beam is focused to the sample by a micro lens. In this chapter, we present some examples of the use of these type of endoscopic OCT probes in gastroenterology during the last years. In other probes (as in the one presented here), the laser scanning is not performed with motors but with MOEMS micro scanners. We provide the state of the art of these types of scanners designed for endoscopic OCT and discuss the difference between them according to their actuation principle. At the end, we describe the micro scanner based on electrothermal actuation of the probe presented in this thesis.

2.1 Application of OCT in gastroenterology

Optical Coherence Tomography endoscopic probes have been widely used in gastroenterology during the last decades. In 1997, Tearney *et al.* performed OCT imaging *in vivo* of the esophagus (and trachea) of a rabbit with a rotatory probe of 1 mm of diameter at 4 fps (2000 axial scans per second) [75]. The different layers of the esophagus (as mucosa, inner muscular layer, serosa) were well differentiated in the radial image with a resolution of 10 μm. The same year, Sergeev *et al.* performed OCT imaging (at 1 fps) of healthy and cancered mucous membranes *in vivo* of the esophagus and the stomach (larynx, urinary bladder and uterinve cervix as well) in humans by coupling a forward-viewing probe in the biopsy channel of an endoscope [76]. In healthy tissues,

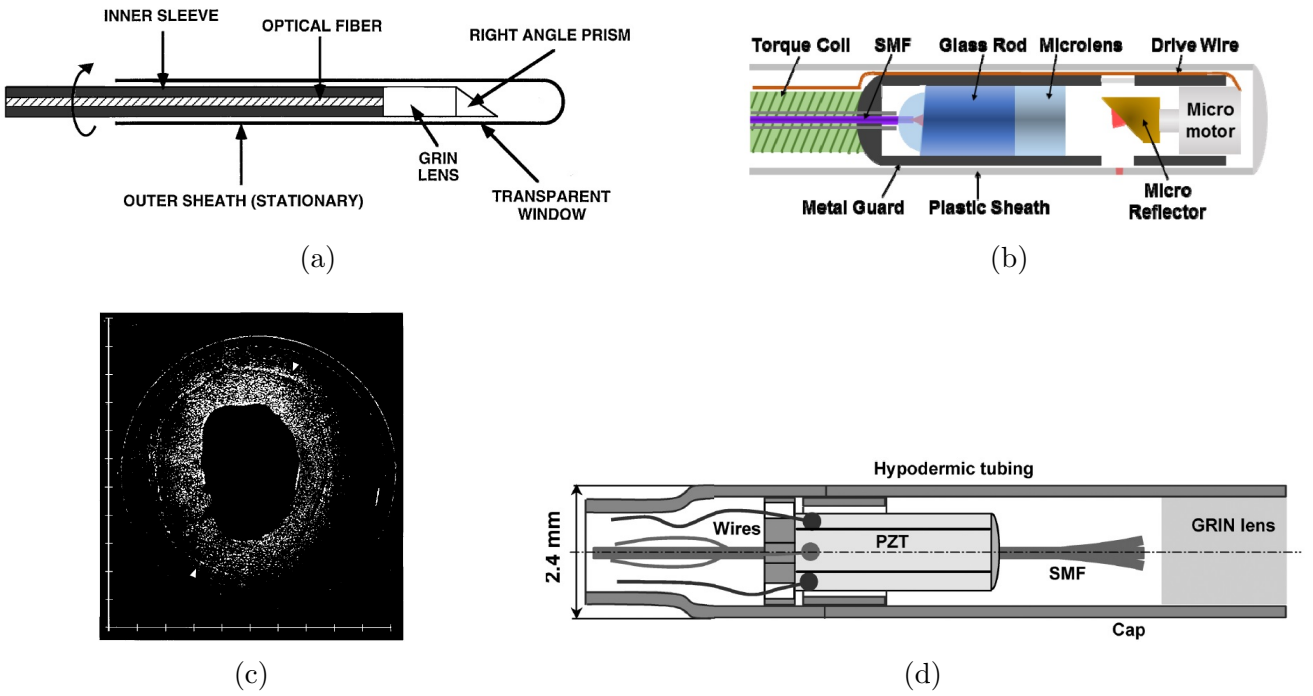

Figure 2.1: (*a*) Rotatory side-viewing probe with an external diameter of 1.1 mm for endoscopic OCT. It is rotated with an external mechanism (proximal-end scanning probe). Image taken from [33]. (*b*) Rotatory side-viewing probe with an integrated micro motor (distal-end scanning probe). Image taken from [73]. (*c*) Radial OCT image of a human saphenous vein *in vitro* scanned with the endoscopic probe of Fig. 2.1a. The space between the marks in the axes is 500 μm. This was the first radial B-scan reported in OCT. Image taken from [33]. (*d*) Forward-viewing probe with a tubular piezoelectric actuator. Image taken from [74].

they could identify different layers such as the epithelium, lamina propria, muscularis mucosa and the submucosa. Even blood vessels and pyloric glands (in the stomach) are well detected in the images. However, these layers suffer from structural changes in cancered tissues where, in addition, the quantity of blood vessels tend to increase (Fig. 2.2a). Kobayashi *et al.* also obtained OCT images of human gastrointestinal tissues (*in vitro*) such as the esophagus, stomach, small intestine and colon [77]. They could observe these different layers in the images as well and, besides, villi in the small intestine and crypts in the colon. In 1999, Rollins *et al.* performed real-time endoscopic OCT imaging in humans by coupling a rotatory endoscopic probe of 2.4 mm of diameter in an endoscope [78]. Figure 2.2b shows the image of the esophagus *in vivo* where the different layers of the mucosa and blood vessels in the submucosa can be distinguished. Furthermore, the authors could identify gastric pits in the stomach, villi in the douodenum and the ileum, and crypts in the colon. The next year, Pitris *et al.* compared healthy and neoplastic tissues *ex vivo* of the esophagus and colon [79]. Images of Barrett's esophagus, esophageal cancer, ulcerative colitis and adenocarcinoma of the colon were presented. They observed (as Sergeev *et al.*) that the well defined layers in healthy tissues become non-uniform in the neoplastic ones because of the growth of tumors. Figures 2.2c and 2.2d show images of a normal and Barrett's esophagus, respectively, where this can be appreciated. These and other more publications showed that OCT is a technique with capacity and enough resolution to observe the different layers of gastrointestinal tissues and microstructures such as blood vessels, glands and colonic crypts in them. This makes it a suitable tool to monitor structural changes, small lesions or an increase in vascularization, which could be

an indication of beginning of cancer.

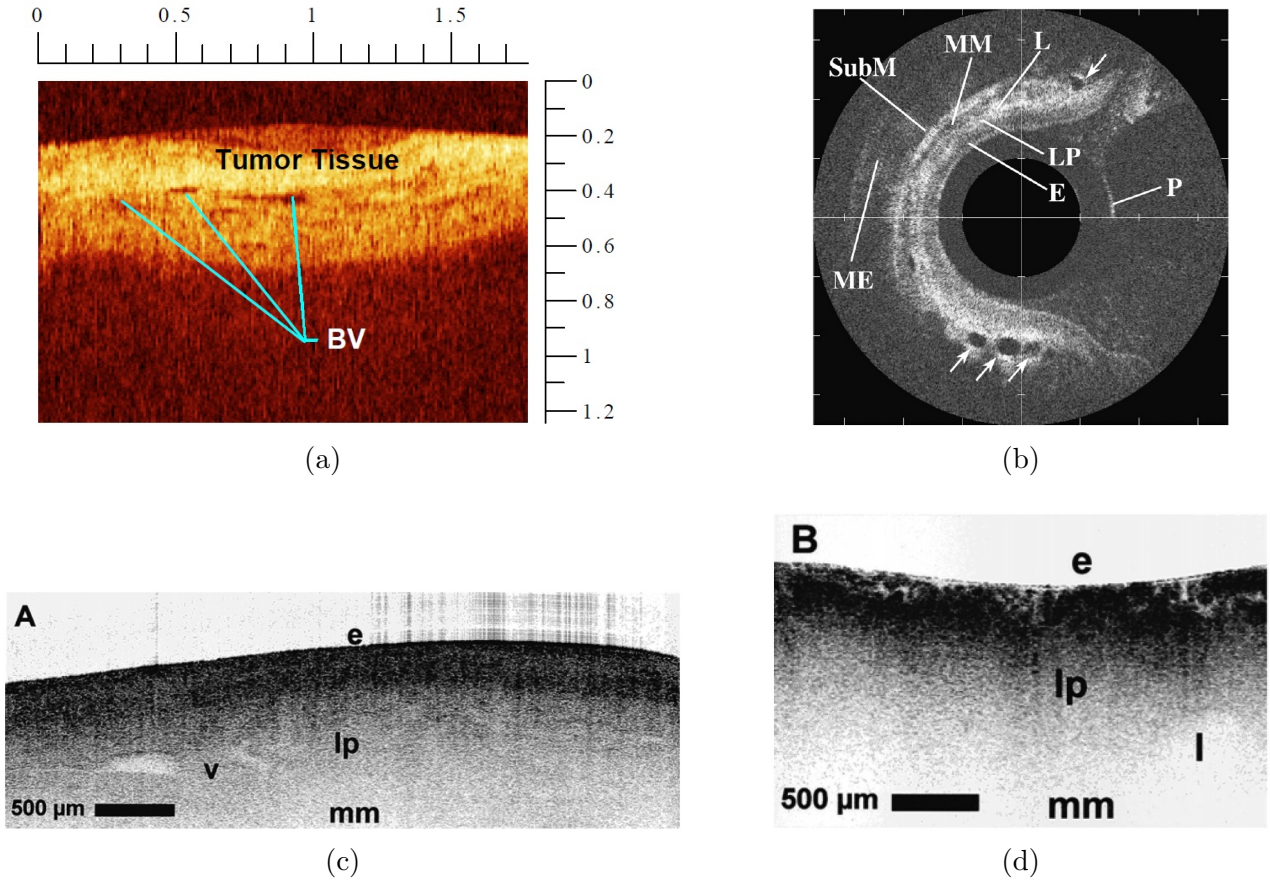

Figure 2.2: (*a*) OCT image of a tumor in a human stomach *in vivo*. Label: blood vessels (BV). The units of the axes are in mm. Image taken from [76]. (*b*) OCT image of a healthy human esophagus *in vivo* with an axial resolution of 8 μm and scanned at 4 revolutions per second. Labels: squamous epithelium (E), lamina propria (LP), muscularis mucosae (MM), submucosa (SubM), lymph nodule (L), surface of the probe (P), muscularis externa (ME). The arrows indicate blood vessels and glands. The image depth is 2.5 mm and the distance between the white marks is 1 mm. Image taken from [78]. (*c*) Normal and (*d*) Barrett's human esophagus *ex vivo*. Labels: epithelium (e), lamina propria (lp), musculares mucosae (mm), lymphoid aggregates (l).

This endoscopic OCT technology have evolved rapidly during the last years. In 2008, Fu *et al.* described a side-viewing probe with a diameter of 1.3 mm inside a double lumen ballon of 18 mm of diameter (when inflated) to scan big tubular organs such as the esophagus [80]. Once inside the organ, the ballon inflates flattening the non-uniform lumen and placing the probe exactly in the middle where it can finally rotate and achieve uniform radial scanning due to its large working distance of 9 mm. They achieved 3D OCT images (a.r. = 12 μm, circumferential resolution = 39 μm) of a pig esophagus *in vivo* with a scanning rate of 4 fps. In 2013, Gora *et al.* presented a tethered capsule with a proximal-end scanning probe inside (Fig. 2.3a) that is swallowed by the patient without anesthesia requirements [21]. Once it has reached the section of interest, the capsule is pulled back by the tether while the probe is scanning. The authors showed the proficency of the capsule producing radial 3D images of the stomach, Barrett's and normal esophagus *in vivo* at 20 fps with a l.r. of 30 μm and a.r. of 7 μm. Another capsule but with a distal-end scanning probe was described by Liang *et al.* in 2015 [81]. Additionally, a pneumatic

actuator was integrated in the capsule as shown in Fig. 2.3b for precise lateral scanning over 3.5 mm. The motor carriage displaces laterally by the expansion and contraction of the bellows. A micro lens is also integrated to focus the beam towards the sample. The capsule was coupled to a SS-OCT system ($\lambda = 1300$ nm, $\Delta\lambda = 115$ nm) with and axial scan rate of 1 MHz that allowed to obtain 2D radial OCT images of the esophagus and rectum of a swine (*in vivo*) at 250 fps with an a.r. of 8.5 μm. Futhermore, manual lateral scanning of the probe (no pneumatic actuator) was also possible by pulling and advandcing the capulse by the tether to achieve larger field of view of 80 mm. High speed endoscopic scanning was also demostrated by Lee *et al.* in 2016 with a distal-end ballon catheter (outer diameter = 2.6 mm, length = 16 mm) coupled to a SS-OCT system (almost the same than Liang *et al.*) with an axial scanning rate of 1.2 MHz [82]. 3D images of the esophagus of a swing *in vivo* were produced at 240 fps with an axial resolution of 8.5 μm.

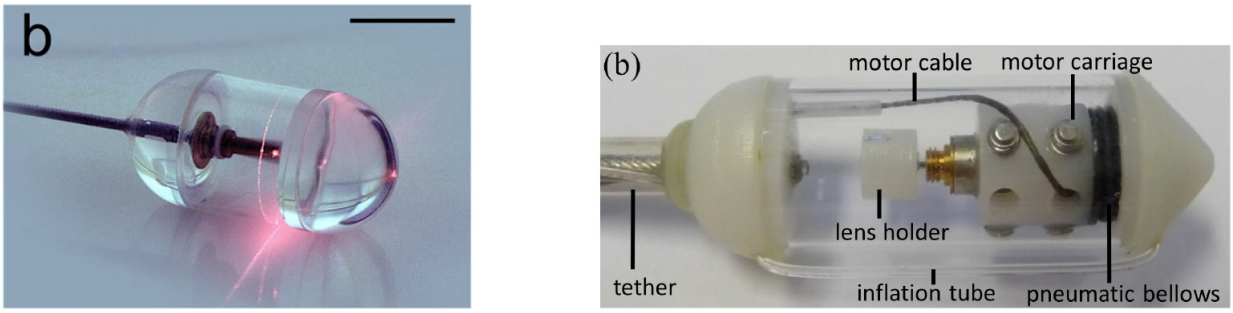

(a) (b)

Figure 2.3: (*a*) Endoscopic tethered capsule presented by Gora *et al.* in 2013. The diameter and the length of the capsule are 12.8 mm and 24.8 mm, respectively. Image taken from [21]. (*b*). Endoscopic tethered capsule presented by Liang *et al.* in 2015. The diameter and the length of the capsule are 12 mm and 35 mm, respectively. Image taken from [81].

At the same time, OCT probes with integrated MOEMS scanners have been developed as a promising and complementary endoscopic imaging technology with suitable characteristics for clinical applications such as small size, real-time scanning in 2-axis, distal-end scanning that provides better stability and lower cost of fabrication (batch fabrication processes). These OCT probes are presented in the next section.

2.2 Overview of MOEMS scanners for OCT endoscopic probes

Several MOEMS scanners for OCT imaging (sample scanning) have been developed since 2001 [83]. They are based on electrostatic, electromagnetic, piezoelectric and electrothermal actuation and, most of them, have two scanning axes for 3D OCT imaging as the scanner shown in Fig. 2.4a. The scanning in one axis ("x direction") is performed by driving two opposite actuators with two electrical signals dephased 180°. In the same way, the scanning in two axes ("x and y directions") is achieved by driving the four of the actuators with the same input signal for opposite actuators (dephased 180°). Different scanning patterns as raster or Lissajous can be produced by scanning in two axes at specific frequencies. Some of these scanners have been integrated in endoscopic probes (as in Fig. 2.4b) that, at the same time, are coupled to the sample arm of a fiber optic based OCT system as shown in Fig. 2.4c. These probes have a GRIN lens at the end of the optical fiber that focuses the light beam to the scanner than, then, reflects it to the sample. They also

have electrical connections (copper wires in Fig. 2.4b) to send signals to the actuators from an external control system.

In this section, some MOEMS scanners that have been developed for OCT imaging are presented. It is divided in five subsections, the first four (from 2.2.4 to 2.2.3) present the scanners with each actuation principle and, in the last one (2.3), some of their characteristics are discussed. In each subsection, we show images of some scanners, probes and OCT images as examples. After, we present a table (except for scanners with piezoelectric actuation) that give some characteristics of the scanners (as its size and resonance frequency), the OCT systems (as the wavelength and A-scan rate) and the obtained images (as resolution and size). The information given in each column is explained next.

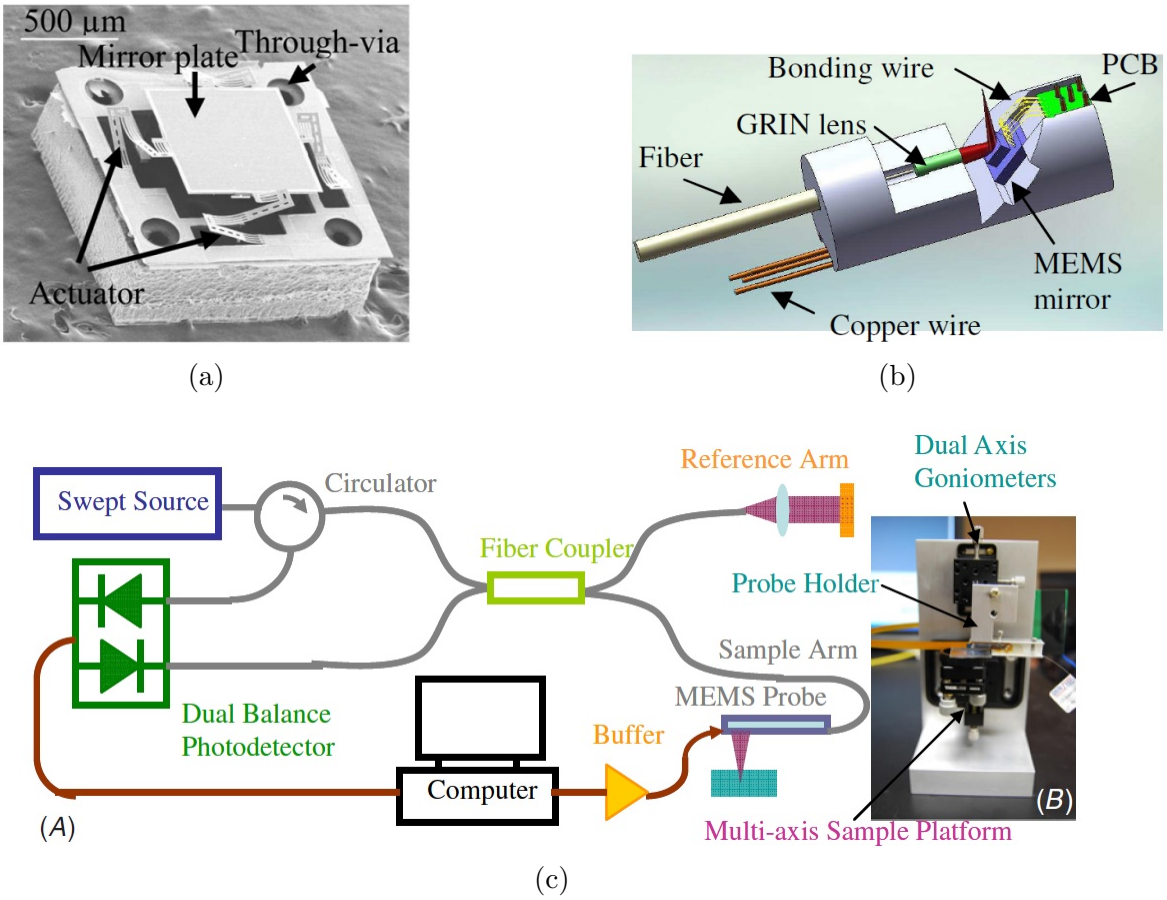

Figure 2.4: (*a*) MOEMS scanner presented by Liu *et al.* in 2011. Image taken from [84]. (*b*) Scheme of an endoscopic probe with a MOEMS scanner presented by Sun *et al.* in 2010. Image taken from [85]. (*c*) SS-OCT system with an endoscopic probe in the sample arm used by Xu *et al.* in 2008. Image taken from [86].

Columns

- **Authors and year:** Authors and year of the publication (and the corresponding reference). There are table footnotes that provide extra information that we consider is important to mention.

- **Size:** Size of the MOEMS scanner and the probe. The symbol ⓜ refers to the size of only the micro mirror in the scanner. The symbol ⊡ gives the size of the complete scanner including the

actuators, the frame and the connections. When both of these parameters are given, we estimate the fill factor (**ff**) of the scanner that is the ratio between the size of the mirror and the size of the complete scanner. The symbol △ specifies the size of the fully integrated OCT probe (GRIN lens, silicon optical bench (SiOB) package, scanner, electric wires, encapsulation, etc.). "D" indicates "Diameter" and "L" indicates "Length". Some of the scanners were not integrated in a probe, however, we still present them in the tables since they were fabricated and used for OCT imaging and have future applications in endoscopy. They are indicated as "NCP" (Not Coupled in a Probe). Some of the scanners have only one scanning axis and are signalized in this column as "(one-axis)".

- **Driving V/I:** The driving voltage (V) and (or) current (I) applied to the actuators of the scanners. We have divided this column in two sub rows. **Max:** the maximum values used in the tests described in each publication. **Image:** the values used to get the OCT images. In some publications, the authors specify the voltages (or currents) applied to the actuators that make the mirror to scan in the x-axis or y-axis. We indicate them as "(x)", "(y)" for the x-axis and y-axis, respectively. The indication "(both)" refers to both scanning axes. The assignment of "x" and "y" for the scanning direction depends on the authors, there is no any standard for this. Some authors (like Kim *et al.* (2007) [87]) refer them as "inner-axis" and "outer-axis" (see Fig. 2.7b) and they are indicated as "(inn)" and "(out)". It is important to clarify that some authors could have used the maximum values to obtain the images but it is not specified in the publications.

- **Scan angle:** The corresponding scan angles achieved with the values in the column "Driving voltage/current". The maximum scanning angles do not correspond to the resonance frequency except in the publications of Jung *et al.* in 2005 [88] and Chong *et al.* in 2006 [89] in the subsection of scanners with electromagnetic actuation (see the table footnotes).

- **Frequency:** This column specifies the scan frequency of the scanner and it is divided in two subrows. **S. rate:** the scan rate used to obtain the images. Some authors specify it in Hz and others in frames per second (fps). In some publications, the authors specify the scanning frequency in each axis and we present them with the notations "(x)" and "(y)" as in the column "Driving V/I". $\mathbf{F_r}$: the resonance frequency of the scanner in each axis.

- **OCT System:** Some characteristics of the OCT system are given in this column. **Mode:** the type of system. TD = Time Domain (axial scanning performed by an optical path length variation in the reference arm), SD = Spectral Domain (with an spectrometer at the output of the interfeomter), SS = Swept source (with a wavelength-swept laser as in Fig. 2.4c). **WL:** the wavelength of the laser in nanometers. λ indicates the central wavelength and $\Delta\lambda$ the bandwidth. **As/s:** axial scanning rate (A-scans per second).

- **Images:** In this column, the resolution of the images is given in the subrow **Res.** (l.r. = lateral resolution, a.r. = axial resolution) and the scanned samples in the subrow **Samples**. Not all the authors cited in this work presented images.

- **Image size:** Some authors present 2D images, others 3D and others both. The size of each image is presented in the subrows **2D** and **3D**. The value that corresponds to the imaging depth is indicated as "(Z)". Some authors specify that they used raster scanning to obtain 3D images. This is also specified in the subrow **3D**. The others authors do not mention the scanning pattern.

The abbreviation "Np" indicates "Not presented". As mentioned before, images of some scanners, probes and OCT images are shown as examples. The numbers of the correspondent figures are highlighted in orange in the tables.

2.2.1 Scanners with electrostatic actuation

The actuators in this type of scanners are micro electrodes that move the mirror through electrostatic forces. Some examples of scanners are shown in Fig. 2.7. One of the electrodes is fixed and the other is movable as in Fig. 2.5d (up and right). These actuators with comb shape are common in these type of scanners. Figure 2.6 shows some OCT images obtained with scanners with electrostatic actuation.

The scanners and probes presented by Piyawattanametha *et al.* in 2004 and Aguirre *et al.* in 2007 are similar and we have highlighted in blue their correspondent rows in the table. In the same way, the scanners and probes presented by Jung *et al.* in 2006 and in 2007 are also similar and we have highlighted in green their correspondent rows.

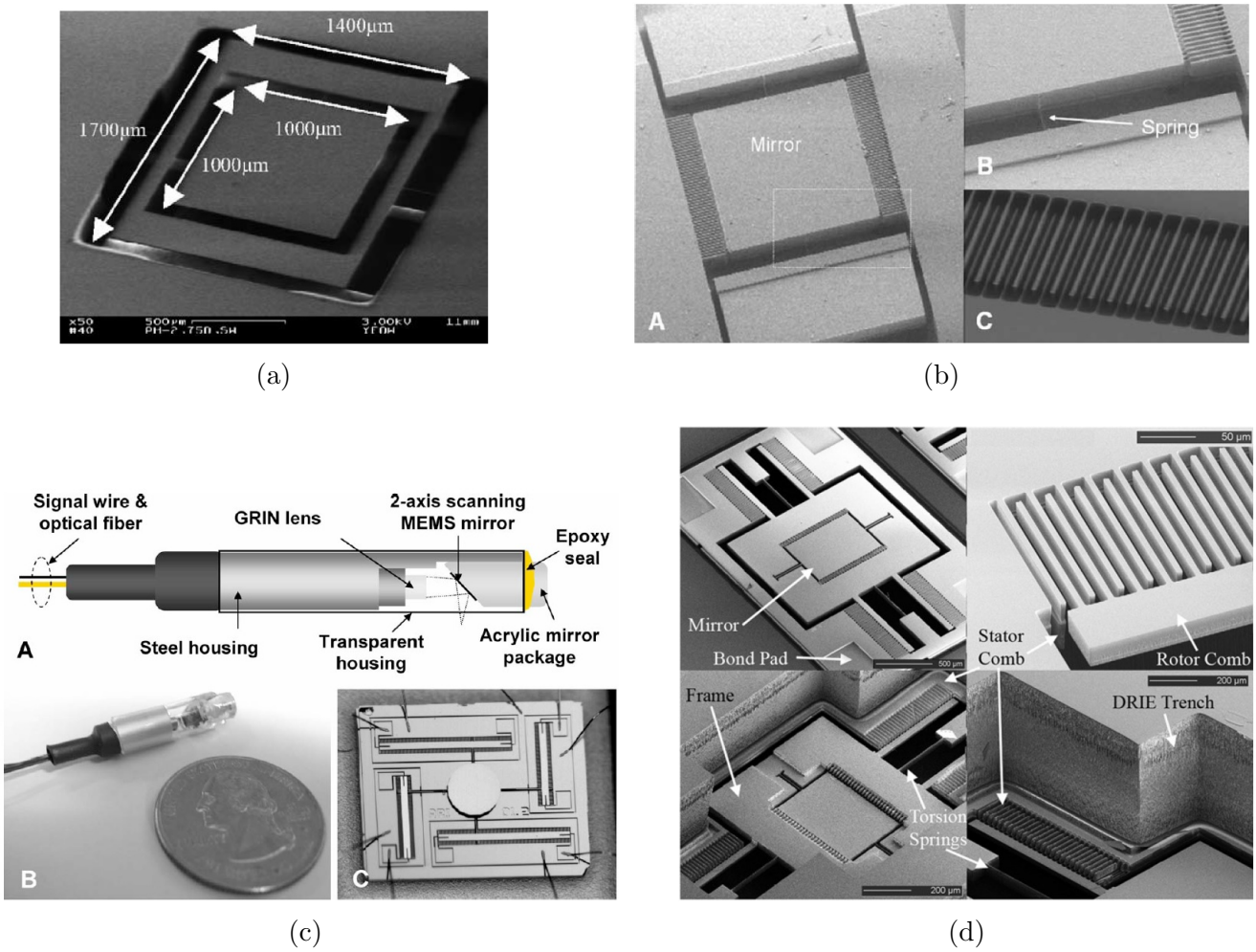

Figure 2.5: Examples of MOEMS scanners with electrostatic actuation for OCT imaging. (*a*) Scanner presented by Yeow *et al.* in 2005. There are four electrodes under the mirror, two for scanning in the x-axis and two in the y-axis. When there is a voltage between the mirror plate and the electrodes, electrostatic fields are generated that can rotate the mirror through torsion beams to scan in a specific direction. Image taken from [102]. (*b*) Scanner presented by Jung *et al.* in 2005. Voltages are applied in the comb actuators to move the scanner through the spring. Image taken from [88]. (*c*) Probe and scanner presented by Jung *et al.* in 2007. This probe is similar to that one presented by Jung *et al.* in 2006. Image taken from [103]. (*d*) Scanner presented by Kumar *et al.* in 2008. Image taken form [104]. The scanners in (*c*) and (*d*) also have comb array actuators that scan the mirrors in two axes (through torsion springs) by electrostatic forces.

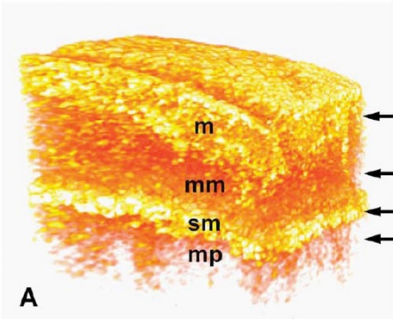

(a)

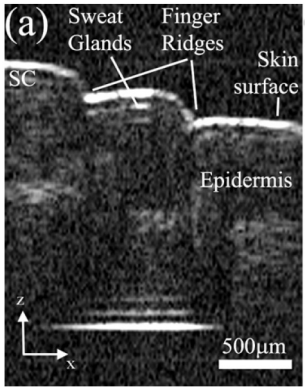

(b)

Figure 2.6: Examples of OCT images obtained with MEMS scanners with electrostatic actuation. (*a*) 3D OCT image of a rabbit rectum *in vivo* presented by Jung *et al.* in 2007. Labels: muscosa (m), muscularis mucosa (mm), submucosa (sm), muscularis propria (mp). Image taken from [103]. (*b*) 2D OCT image of a human finger *in vivo* presented by Kumar *el al.* in 2008. "SC" indicates stratum corenum. Image taken from [104].

Table 2.1: Scanners with electrostatic actuation.

Authors, year	**Size (mm)**	**Driving V/I**	**Scan angle (°)**	**Frequency**	**OCT system**	**Images**	**Image size (mm)**
Zara *et al.*[13] 2003 [105]	ⓜ 1.5x1.5 ⊡ Np △ Np (one-axis)	**Max:** ≈100V **Image:** Np	**Max:** ≈50 **Image:** Np	**S. rate:** 4Hz **F_r (Hz):** 20.6(1st) 41.2(2nd)	**Mode:** TD **WL:** λ=1290 $\Delta\lambda$=28 **As/s** 4k	**Res.(μm):** Np **Samples:** -Ruler -Porcine colon tissue and eyeball -Human finger	**2D:** 3xNp(Z) **3D:** Np
Piyawattanametha *et al.* 2004 [107]	ⓜ 1(D) ⊡ Np △ 6(D)	**Max:** Np **Image:** 30-70V (both)	**Max/ Image:** Np	**S. rate:** 20fps **F_r (Hz):** 855(x) 1394(y)	**Mode:** Np **WL:** λ=1250 $\Delta\lambda$=180 **As/s** Np	**Res.(μm):** l.r.=13 a.r.≈4 **Samples:** -Human skin -Human nailfold	**2D:** ≈ 0.2xNp(Z) ≈ 0.4xNp(Z) **3D:** Np
Yeow *et al.* 2005 [102]	ⓜ 1x1 ⊡ 1.4x1.7 **(2.5a)** **ff:** 42% △ NCP	**Max:** 55V (both) **Image:** Np	**Max:** ±0.23(x) ±0.33(y) **Image:** Np	**S. rate:** 56Hz(x) 0.5Hz(y) **F_r (Hz):** 181(x) 45(y)	**Mode:** TD **WL:** λ=1300 $\Delta\lambda$=63 **As/s** 8k	**Res.(μm):** Np **Samples:** -*Drosophila melanogaster* and its larva	**2D:** Np **3D:** 0.7x0.2 x1(Z) (raster)
Jung *et al.*[14] 2005 [88]	ⓜ 0.6x0.6 x0.002 ⊡ 2.5x3	**Max:** 100V (both)	**Max:** 30 (both)	**S. rate:** 3-5fps **F_r (Hz):**	**Mode:** TD **WL:**	**Res.(μm):** l.r.=10 a.r.=10	**2D:** 2x1.4(Z) **3D:**

Continuation of Table 2.1

Authors, year	Size (mm)	Driving V/I	Scan angle (°)	Frequency	OCT system	Images	Image size (mm)
	x0.5 **(2.5b)** **ff:** 4.8% △ NCP	**Image:** Np	**Image:** Np	8000(x) 3500(y)	λ=1310 $\Delta\lambda$=80 **As/s** 500	**Samples:** -Normal and cancerous hamster cheek	2x2 x1.4(Z) (raster)
Chong *et al.*[15] 2006 [89]	ⓜ 1x2 ⊡ Np △ 5(D) (one-axis)	**Max:** 5V **Image:** Np	**Max:** 8 **Image:** Np	**S. rate:** 350Hz **F_r (Hz):** 350	**Mode:** Np **WL:** λ=1310 $\Delta\lambda$: Np **As/s** Np	**Res.(μm):** Np **Samples:** Np	Np
Jung *et al.*[16] 2006 [108]	ⓜ 1.2(D) ⊡ Np △ <4(D)	**Max:** 100V **Image:** Np	**Max:** 20(both) **Image:** Np	**S. rate:** 3fps **F_r (Hz):** 1800(x) 2400(y)	**Mode:** TD **WL:** λ=1310 $\Delta\lambda$=80 **As/s** 500	**Res.(μm):** l.r.: Np a.r.=10 **Samples:** -Rabbit trachea -Normal and cancerous hamster cheek	**2D:** Np **3D:** 1x1x1.4(Z) (raster)
Aguirre *et al.*[17] 2007 [109]	ⓜ 1(D) ⊡ 3x3 **ff:** 8.7% △ ≈5(D) x25(L)	**Max:** ≈100V (both) **Image:** Np	**Max:** ±6 (both) **Image:** Np	**S. rate:** 4fps **F_r (Hz):** 463(x) 140(y)	**Mode:** TD **WL:** λ=1060 $\Delta\lambda$ >200 **As/s** 2k	**Res.(μm):** l.r.≈12 a.r.<4 **Samples:** -Human skin -Lime pulp -Hamster cheek	**2D:** 1.8x1.3(Z) **3D:** 1.8x1x1.3(Z)
Jung *et al.*[18] 2007 [103]	ⓜ Np ⊡ Np △ 5.5(D) x2000(L) **(2.5c)**	**Max:** Np **Image:** Np	**Max:** 20(both) **Image:** Np	**S. rate:** 8fps **F_r (Hz):** 1800(x) 2400(y)	**Mode:** SD **WL:** λ=1310 $\Delta\lambda$=95 **As/s** 7.7k	**Res.(μm):** l.r.=20 a.r.=10 **Samples:** -Rabbit rectum **(2.6a)** -Human finger -Human vocal cord	**2D:** Np **3D:** 1x1x1.4(Z) (raster)
Kumar *et al.*[19] 2008 [104]	ⓜ 0.5x0.7 ⊡ Np **(2.5d)** △ NCP	**Max:** 150V (both) **Image:** Np	**Max:** ±9 (both) **Image:** Np	**S. rate:** 40fps **F_r (Hz):** 2280(inn) 385(out)	**Mode:** SS **WL:** λ=1310 $\Delta\lambda$=100 **As/s** 20k	**Res.(μm):** l.r.=12.5 a.r.=8.6 **Samples:** -Scanner -Onion peels -Pickle slices -Human finger	**2D:** 2x4(Z) **3D:** 2x1x4(Z) (raster)

Continuation of Table 2.1							
Authors, year	**Size (mm)**	**Driving V/I**	**Scan angle (°)**	**Frequency**	**OCT system**	**Images**	**Image size (mm)**
						(2.6b)	
Strathman *et al.*[20] 2014 [110]	ⓜ 0.8(D) ⊡ <2x2 **ff:** 12.5% △ NCP	**Max:** ≈130V **Image:** Np	**Max:** ≈4.5 **Image:** Np	**S. rate:** 16Hz **F_r (Hz):** 472(inn) 399(out)	**Mode:** SD **WL:** λ=1310 $\Delta\lambda$=83 **As/s** 16k	**Res.(μm):** l.r.=50 **Samples:** -Mouse ear	**2D:** Npx≈0.6(Z) **3D:** Np

[13] The fabrication of this scanner and the resonance frequencies are presented in [106]. This scanner has only one scanning axis and two resonance frequencies, one at 20.6 Hz and the other at 41.2 Hz with scan angles of 77° and 142° respectively (using a voltage of ±40 V).

[14] The scan angle of 30° is achieved at the resonance frequency in both axes.

[15] This probe was designed to work at the resonance frequency. The scan angle of 8° is achieved at the resonance. A laser at 1550 nm is used to control the movement of the mirror through electrostatic actuators. No OCT images were presented in this publication.

[16] The OCT system in this publication is the same as that one presented by Jung *et al.* 2005 [88] but the scanner is different (and coupled in a probe).

[17] The probe presented here is very similar as that one presented by Piyawattanametha *et al.* in 2004 [107]. However, the characteristics (as the resonance frquency of the scanner) are different.

[18] This probe (Fig. 2.5c) is very similar as that one presented by Jung *et al.* 2006 [108]. Both scanners resemble and the resonance frequencies and the scan angles are the same. However, the OCT systems and the scanned samples are not.

[19] The scan angle of the inner and outer axis at the resonance are ≈ 17° and ≈ 8° respectively (for the input signal: $V = 18.0 + 9.0\sin(2\pi ft)$ V, per axis). See Fig. 2 in this publication.

[20] The driving voltage and the scan angle presented in the table correspond to DC actuation. This scanner was also tested with a TD-OCT system (scan rate = 2 mHz, λ = 1325 nm, $\Delta\lambda > 100$ nm). The scanned sample was cover glass (Image size (2D) ≈ 600 μm x Np(Z)). We present in the table the data correspondent to the SD-OCT system since it is faster.

2.2.2 Scanners with electromagnetic actuation

The actuators in this type of scanners are coils and magnets that scan the mirror by the Lorentz force that is produced by the interaction between the electrical current that flows through the coils and the static field of the magnet. Figure 2.7 shows scanners and one probe with this type of actuation. Figure 2.8 shows some OCT images obtained with the scanners.

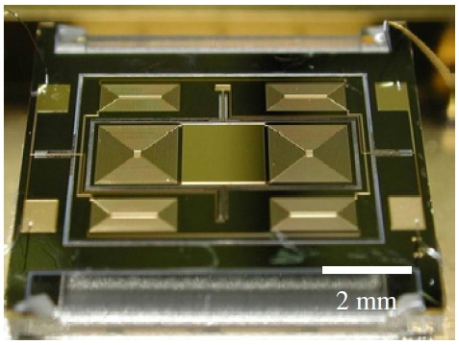

(a)

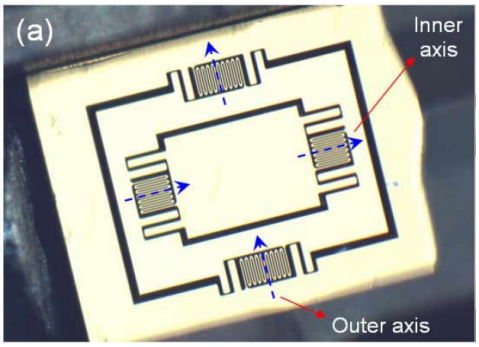

(b)

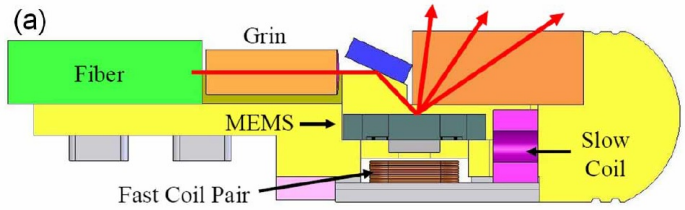

(c)

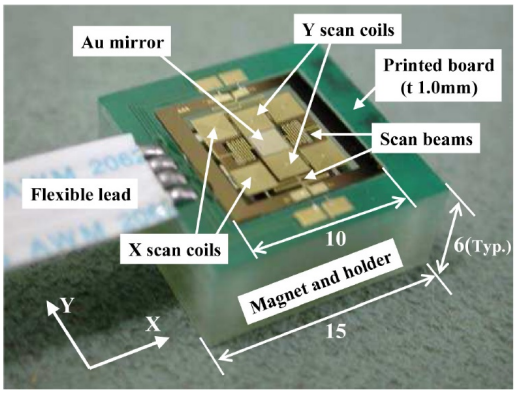

(d)

Figure 2.7: Examples of MOEMS scanners with electromagnetic actuation for OCT imaging. (*a*) Scanner presented by Mitsui *et al.* in 2006. The mirror is rotated in two axes by the forces between the current in the planar coils (Au/Cr) in the frame of the scanner (with 4 torsion beams) and the magnetic field of a magnet placed under it. Image taken from [111]. (*b*) Scanner and (*c*) probe presented by Kim *et al.* in 2007. A magnet is glued in the back side of the mirror to move it through two coils that are coupled in the probe. The mirror has four flexible structures that allow it to rotate in both axes. Images taken from [87]. (*d*) Probe presented by Watanabe *et al.* in 2011. As the scanner in (*a*), this mirror is also rotated through planar coils in the frame (with 4 torsion beams as well) and a manget under the Au mirror. Image taken from [112].

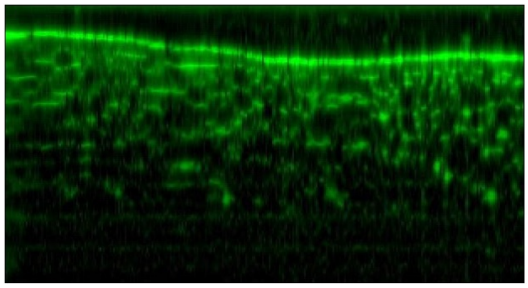

(a)

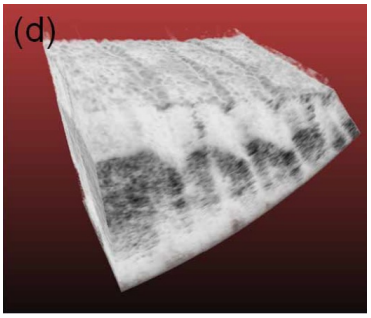

(b)

Figure 2.8: Examples of OCT images obtained with MEMS scanners with electromagnetic actuation. (*a*) 2D OCT image of an onion presented by Mitsui *et al.* in 2006. Image taken from [111]. (*b*) 3D OCT image of a human fingertip *in vivo* presented by Kim *et al.* in 2007. The epithelium and dermis can be observed. Image taken from [87].

Table 2.2: Scanners with electromagnetic actuation.

Authors, year	Size (mm)	Driving V/I	Scan angle (°)	Frequency	OCT system	Images	Image size (mm)
Mitsui *et al.*[21] 2006 [111]	ⓜ 2x2 ⊡ Np **(2.7a)** △ NCP	**Max/ Image:** ±4.6mA(x) ±10.3mA(y)	**Max/ Image:** ±8 (both)	**S. rate:** 14Hz **F_r (Hz):** 106(x) 80.5(y)	**Mode:** SD **WL:** λ=1300 $\Delta\lambda$=44 **As/s:** Np	**Res.(μm):** l.r.=17 a.r.=10 **Samples:** -Onion **(2.8a)**	**2D:** 8x1.4(Z) **3D:** Np
Kim *et al.*[22] 2007 [87]	ⓜ 0.6x0.8 ⊡ 2.4x2.9 **(2.7b)** **ff:** 6.9% △ 2.8(D) x12(L) **(2.7c)**	**Max:** ≈ ±1.2V(inn) ≈ ±4V(out) **Image:** ±0.8V(inn) ±2.8V(out)	**Max:** ≈ ±30 (both) **Image:** Np	**S. rate:** 0.09Hz(inn) 18.5Hz(out) **F_r (Hz):** 450(inn) 350(out)	**Mode:** SD **WL:** λ=1300 $\Delta\lambda$=68 **As/s:** 18.5k	**Res.(μm):** l.r.=25 a.r.: Np **Samples:** -Fingertips **(2.8b)** -Oral cavity	**2D:** 1.5xNp(Z) **3D:** 1.5x1 xNp(Z) (raster)
Watanabe *et al.*[23] 2011 [112]	ⓜ 1.8x1.8 ⊡ 10x10 x0.2 **ff:** 3.2% △ 15x15 x6 **(2.7d)**	**Max:** ≈2.8mA(x) ≈2.3mA(y) **Image:** Np	**Max:** ≈2.8(x) ≈2.3(y) **Image:** Np	**S. rate:** Np **F_r (Hz):** 70(x) 90(y)	**Mode:** SD **WL:** λ=1550 $\Delta\lambda$: Np **As/s:** Np	**Res.(μm):** Np **Samples:** -Human finger	**2D:** 3xNp(Z) **3D:** 3x3 xNp(Z)

[21] The authors presented two types of MOEMS scanners based on torsion beams; one type has straight ones and the other, meandering ones. The data presented in the table correspond to the scanner with meandering torsion beams that showed higher scanning angles. For the scanner with straight torsion beams, the maximum scan angle was ±4.4° at ± 20mA for the x-axis and ±2.7° at ±2.7 mA for the y-axis. The resonance frequencies were 322 Hz and 236 Hz for the x and y axes respectively.

[22] The authors also present images for the case when the inner-axis is used as the fast axis (18.5 Hz) and the outer-axis as the slow one (0.09Hz). The driving voltage in the inner-axis was ±0.8V resulting in a scanning angle of ±20° and a scanning distance on the sample of 1 mm. The outer-axis was driven with a voltage of ±1V (scanning angle not mentioned) resulting in a scanning distance on the sample of 0.55 mm. The image depth was not neither mentioned in this publication. The power required to drive both axes is 150 mW.

[23] The authors tested different magnets shapes (cubic, cylindrical and spherical) with different sizes. The data presented in the columns "Driving V/C" and "Scan angle" correspond to a cubic magnet whose size is 8 mm^2 (used to obtain the images). See Fig. 7 in this publication.

2.2.3 Scanners with piezoelectric actuation

Gilchrist *et al.* reported MOEMS scanners based on piezoelectric actuation (bending by an electric field) for endoscopic OCT imaging in 2009 [113]. They presented the design of a probe with two scanners (one per scanning axis) (Fig. 2.9a) where each scanner is composed of a rectangular micro mirror and a piezoelectric cantilever made of lead zirconate titanate (PZT) (Fig. 2.9b). Several scanners with different sizes of the mirror (500 x 500 μm, 600 x 840 μm, 700 x 1300 μm and 840 x 1600 μm) and the cantilever (200 μm and 400 μm) were fabricated and characterized

to study how the scan angle and the resonance frequency change. For scanners with cantilevers of length 400 μm, high fill factors of 68% and 76% were achieved for small and big mirrors, respectively. The authors reported a scan angle of 14° for a scanner with a mirror size of 600 x 840 μm and a cantilever length of 400 μm when it was driven with an electric signal with Vpp of 20 V and offset of 6 V. The maximum current was 50 μA for a power consumption of 1 mW. Table 2.3 presents the measured scan angles and resonance frequencies (ω_r) for this and other scanners with different sizes.

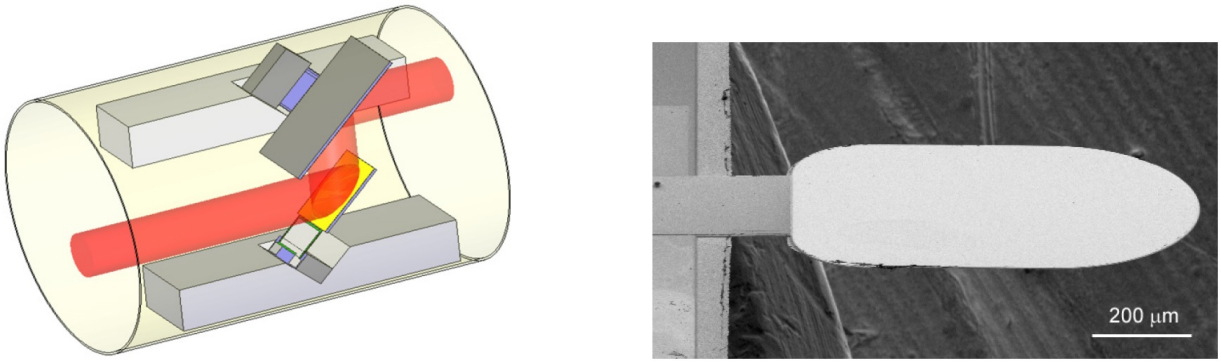

(a) (b)

Figure 2.9: (*a*) Design of an OCT probe with two piezoelectric scanners proposed by Gilchrist *et al.* in 2009. (*b*) MOEMS scanner with a mirror size of 600 x 840 μm and a cantilever length of 200 μm. Images taken from [113].

Table 2.3: Scan angle and resonance frequency of some scanners fabricated and tested by Gilchrist *et al.* in 2009. Data taken from table 1 in [113].

Cantilever length (μm)	**Mirror size (μm)**	**Scan angle (°)**	**F_r (Hz)**
200	600 x 840	6.8	1210
400	600 x 840	14	650
200	700 x 1300	5.2	650
400	700 x 1300	8.5	240

One of the scanners (mirror size of 600 x 840 μm) was used to produce an OCT image. It was coupled in the sample arm of a SD-OCT system where the central wavelength and bandwidth of the laser were 840 nm and 87 nm, respectively. For the imaging, the scanner was driven with a sawtooth signal with a Vpp of 10 V and offset of 3V at 1 Hz for one-axis scanning. The scanned sample was an infrared (IR) card and the 2D image is shown in Fig. 2.10 where the plastic and photosensitive layers are clearly distinguished. The axial scanning rate was 10 000 lines/s and the image size is 1 mm x 2.09 mm (Z). The scanners were still not coupled in a probe as in Fig. 2.9a for 3D imaging, they were just tested individually.

2.2.4 Scanners with electrothermal actuation

The actuators of these type of scanners are based on bimorph cantilevers composed of two layers of different materials that have a big difference between their coefficient of thermal expansion

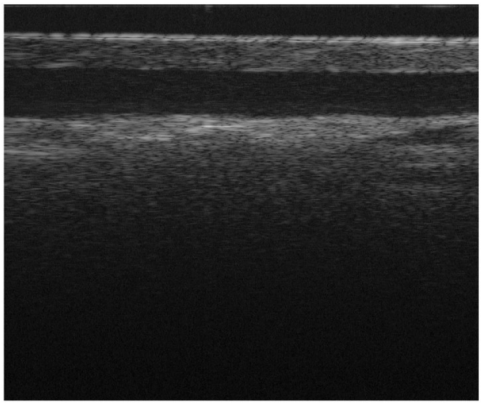

Figure 2.10: OCT image of an IR card obtained with a scanner with pizeoelectric actuation. Image taken from [113].

(Fig. 2.11a). When the bimorph is heated by an electrical current, the material with higher coefficient expands more than the material with lower coefficient, making the bimorph to bend. These structures also have an extra layer between the two others that acts as a heater where the input signal is applied. The materials used in some of the bimorphs are aluminim (Al) and silicon dioxide (SiO_2) that have coefficients of thermal expansion of $23x10^{-16}$ (K^{-1}) and $0.4x10^{-16}$ (K^{-1}) respectively [91]. The bimorphs used in the scanners presented by Pan *et al.* in 2001, Xie *et al.* in 2003 and Jain *et al.* in 2004 (table 2.4) have a layer of silicon sandwiched between the two others that acts as a heater. The bimorphs in the scanners presented by Sun *et al.* in 2010, Liu *et al.* in 2011, Wang *et al.* in 2013, Duan *et al.* in 2016 and Tanguy *et al.* in 2017 have a layer of Platinum (Pt) as the heater. On the other hand, the bimorphs in the scanners presented by Singh *et al.* in 2007, Singh *et al.* in 2008, Xu *et al.* in 2008 and Mu *et al.* in 2011 are made of aluminium and silicon (coefficient of $2.6x10^{-16}$ (K^{-1})) with a layer of SiO_2 beteween them as the heater. These bimorph cantilevers are arranged in different configurations to form the actuators of the scanners. Figure 2.11b shows an actuator conformed of two structures known as "folded dual S-shaped bimorphs (FDSB)". These type of actuators were used in the scanners presented by Samuelson *et al.* in 2012, Wang *et al.* in 2013 and Duan *et al.* in 2016 (Fig. 2.12d).

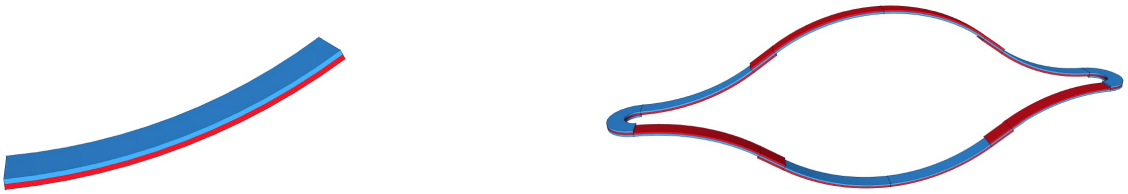

(a) (b)

Figure 2.11: (*a*) A bimorph cantilever. (*b*) Actuator composed of several bimorphs. Images taken from [90].

Some of the scanners presented in the table 2.4 have the same design but with different sizes and we have identified them with different colors. The rows of the table that describe the scanners with the design of Fig. 2.12b (with linear actuators) are colored in blue. Other design is shown in Fig. 2.12c where each actuator is composed of three bimorphs arrays and two static frames in series. The rows that describe scanners with this design are colored in green. Finally, the rows corresponding to the scanners with the design of Fig. 2.12d (with the actuators of Fig. 2.11b) are

colored in beige. Some examples of probes with scanners based on electrothermal actuation and images obtained with this type of scanners are shown in Fig. 2.13 and Fig. 2.14, respectively.

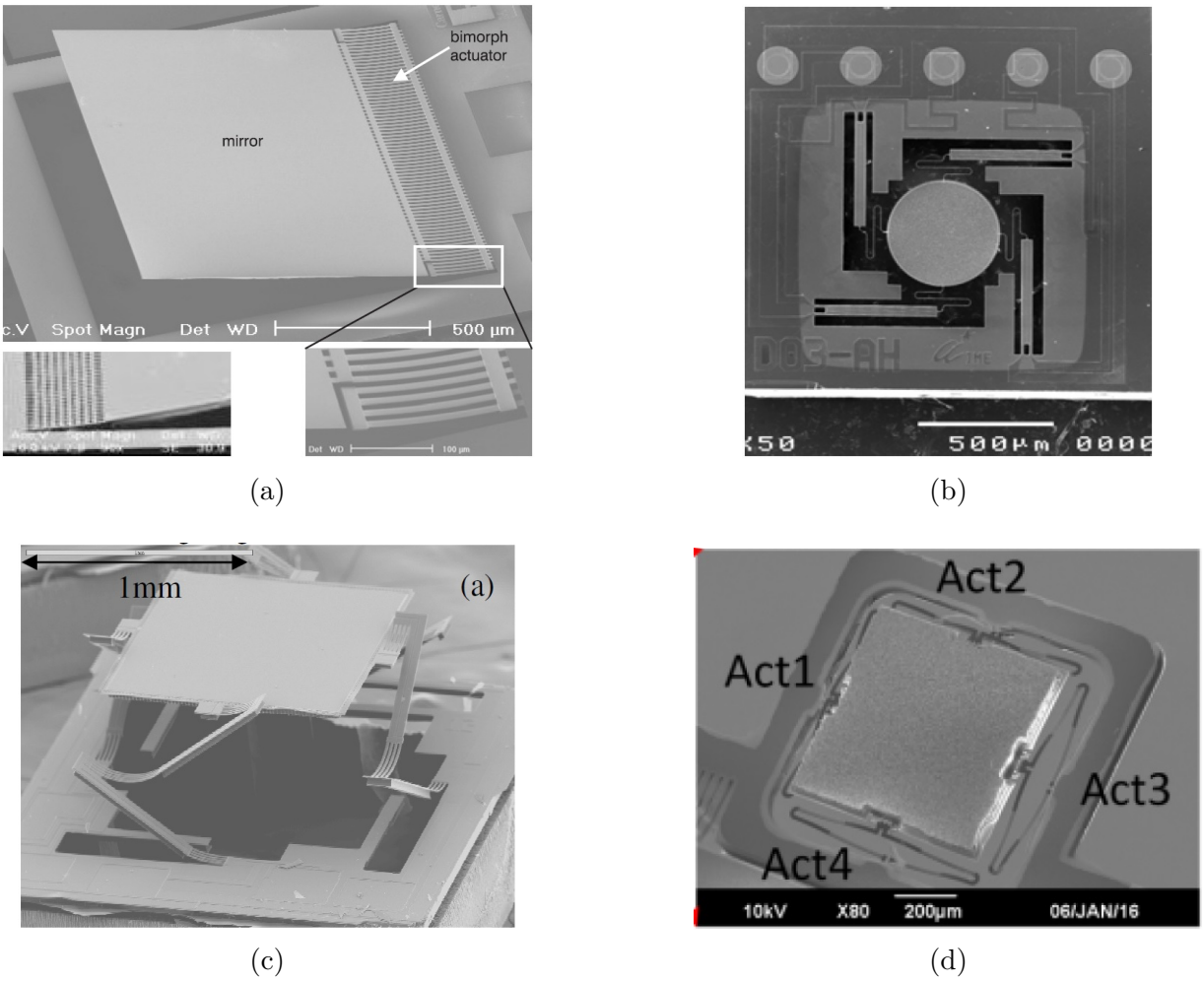

(a) (b) (c) (d)

Figure 2.12: Examples of MOEMS scanners with electrothermal actuation for OCT imaging. (*a*) Scanner presented by Xie *et al.* in 2003. Left down image: actuators array with mesh shape used by Pan *et al.* in 2001 (previous version of this scanner). Image taken from [92]. (*b*) Scanner presented by Singh *et al.* in 2008. Image taken from [91]. (*c*) Scanner presented by Sun *et al.* in 2010. Image taken from [85]. (*d*) Scanner presented by Duan *et al.* in 2016. Image taken from [93].

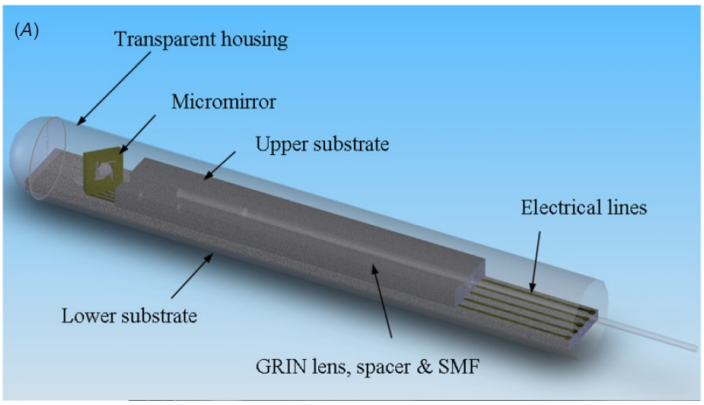

(a)

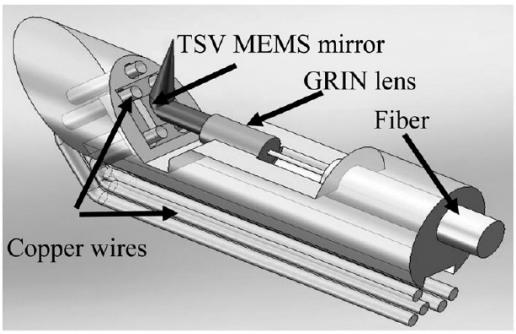

(b)

Figure 2.13: Examples of probes with MOEMS scanners with electrothermal actuation. (*a*) Diagram of the Probe presented by Xu *et al.* in 2008. The lower substrate was fabricated with precise slots for the scanner, the GRIN lens and the optical fiber in order to be aligned. Another version of this probe is presented by Mu et al. in 2011. Image taken from [86]. (*b*) Diagram of the probe presented by Liu *et al.* in 2011. This probe is similar to those ones presented by Sun *et al.* in 2010 (Fig. 2.4b), Samuelson *et al.* in 2012, Wang *et al.* in 2013 and Duan *et al.* in 2016. Image taken from [84].

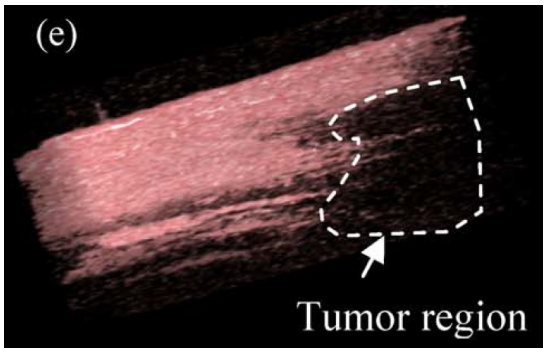

(a)

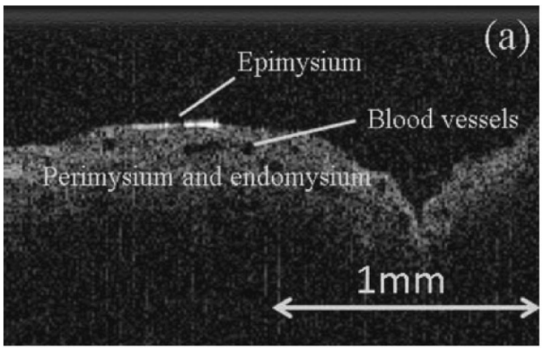

(b)

Figure 2.14: Examples of OCT images obtained with MOEMS scanners with electrothermal actuation. (*a*) 3D OCT image of a tumor in mouse *in vivo* obtained by Samuelson *et al.* in 2012. There is a difference between the structures of the tumor and the healthy tissue, besides, light is more absorbed by the tumor. Image taken from [99]. (*b*) 2D OCT image of mouse muscle *ex vivo* obtained by Mu *et al.* in 2011. Image taken from [94].

Table 2.4: Scanners with electrothermal actuation.

Authors, year	**Size (mm)**	**Driving V/I**	**Scan angle (°)**	**Frequency**	**OCT system**	**Images**	**Image size (mm)**
Pan *et al.*[1] 2001 [83]	ⓜ 1x1 ⊡ Np △ Np (one-axis)	**Max:** 15mA 33V **Image:** Np	**Max:** ±15 **Image:** Np	**S. rate:** 5fps **F_r (Hz):** 165	**Mode:** TD **WL:** λ=1320 $\Delta\lambda$=77 **As/s**	**Res.(μm):** l.r.=20 a.r.=10.2 **Samples:** -Glass slides -Porcine	**2D:** 2.9x2.8(Z) **3D:** Np

Continuation of Table 2.4

Authors, year	Size (mm)	Driving V/I	Scan angle (°)	Frequency	OCT system	Images	Image size (mm)
					2.4k	bladder	
Xie *et al.*[2] 2003 [92]	ⓜ 1x1 ⊡ Np **(2.12a)** △ Np (one-axis)	**Max:** ≈7.5mA **Image:** Np	**Max:** ≈37 **Image:** Np	**S. rate:** 5fps **F_r (Hz):** 165	**Mode:** TD **WL:** λ=1320 $\Delta\lambda$=77 **As/s** 2.4k	**Res.(μm):** l.r.=20 a.r.=10 **Samples:** -Rabbit bladder	**2D:** 4.3x2(Z) **3D:** Np
Jain *et al.*[3] 2004 [96]	ⓜ 1x1 ⊡ Np △ NCP	**Max:** 8mA (both) **Image:** Np	**Max:** 50(mirror) 25(frame) **Image:** Np	**S. rate:** 10fps **F_r (Hz):** 445(mirror) 259(frame)	**Mode:** Np **WL:** Np **As/s** Np	**Res.(μm):** Np **Samples:** Np	**2D:** Np **3D:** Np
Singh *et al.*[4] 2007 [97]	ⓜ 0.4(D) ⊡ 2.5x2.5 **ff:** 2% △ > 5 x1.5(L)	Np	**Max:** 10 **Image:** Np	**S. rate:** 12fps **F_r (Hz):** Np	**Mode:** TD **WL:** λ=1550 $\Delta\lambda$: Np **As/s** Np	**Res.(μm):** Np **Samples:** -Onion -Glass	**2D:** 0.12x6(Z) (glass) 0.07x2.5(Z) (onion) **3D:** Np
Singh *et al.*[5] 2008 [91]	ⓜ 0.4(D) ⊡ 1x1 **(2.12b)** **ff:** 12.5% △ Np	**Max:** 1.4V **Image:** Np	**Max:** 17 **Image:** Np	**S. rate:** Np **F_r (Hz):** Np	**Mode:** TD **WL:** λ=1550 $\Delta\lambda$: Np **As/s** Np	**Res.(μm):** Np **Samples:** Np	Np
Xu *et al.*[6] 2008 [86]	ⓜ 0.5(D) ⊡ 1.5x1.5 **ff:** 8.7% △ < 4(D) x25(L) **(2.13a)**	**Max:** ≈1.3V **Image:** Np	**Max:** 17 **Image:** Np	**S. rate:** 21.5fps **F_r (Hz):** Np	**Mode:** SS **WL:** λ=1325 $\Delta\lambda$=110 **As/s** 16k	**Res.(μm):** l.r.=20 a.r.=12 **Samples:** -Infrared viewing card	**2D:** 0.55x1(Z) **3D:** 0.55x0.55 x1(Z) (raster)
Sun *et al.*[7] 2010 [85]	ⓜ 1x1 ⊡ 2x2 **(2.12c)** **ff:** 25% △ 5.8(D) x12(L) **(2.4b)**	**Max:** 5.5V 15.5mA **Image:** 0-4V (fast) 0.5-3.5V (slow)	**Max:** ±31 **Image:** Np	**S. rate:** 1.25Hz (fast) 0.0125Hz (slow) 2.5fps **F_r (Hz):** Np	**Mode:** TD **WL:** λ=1310 $\Delta\lambda$=75 **As/s** 1k	**Res.(μm):** l.r.: Np a.r.=10 **Samples:** -Mouse ear -Mouse tongue	**2D:** 2.3x1.6(Z) **3D:** 2.3x2.3 x1.6(Z) (raster)

Continuation of Table 2.4

Authors, year	Size (mm)	Driving V/I	Scan angle (°)	Frequency	OCT system	Images	Image size (mm)
Liu *et al.*[8] 2011 [84]	ⓜ 0.8x0.8 ⊡ 1.5x1.5 **(2.4a)** **ff:** 28.4% △ 2.6(D) x10.7(L) **(2.13b)**	**Pres.:** 3.6V **Image:** 0-4V (fast) 0-4V (slow)	**Pres.:** ±16 **Image:** Np	**S. rate:** 1.25Hz (fast) 2mHz (slow) 2.5fps **F_r (Hz):** 659	**Mode:** TD **WL:** λ=1310 $\Delta\lambda$=75 **As/s** 1k	**Res.(μm):** l.r.: Np a.r.=10 **Samples:** -Microspheres in PDMS -Rat brain tissue	**2D:** 0.8x1.6(Z) (spheres) 0.4x1.6(Z) (rat brain) **3D:**
Mu *et al.*[9] 2011 [94]	ⓜ 1(D) ⊡ Np △ 3(D)	**Max:** 1.4V 35mA **Image:** 1.2V	**Max:** 11 **Image:** Np	**S. rate:** 8.9Hz **F_r (Hz):** Np	**Mode:** SD **WL:** λ=930 $\Delta\lambda$=110 **As/s** Np	**Res.(μm):** l.r.: Np a.r.≈10 **Samples:** -Glass -Mouse muscle **(2.14b)** -Mouse skin	**2D:** 2x1(Z) **3D:** Np
Samuelson *et al.*[10] 2012 [99]	ⓜ 1x1 ⊡ 1.55 x1.7x0.5 **ff:** 32% △ 2.8(D)	**Max:** 4.8V **Image:** 0-4V (fast) 0-4.5V (slow)	**Max:** ±23 **Image:** Np	**S. rate:** 1.25Hz (fast) 0.0125Hz (slow) 2.5fps **F_r (Hz):** 406	**Mode:** TD **WL:** λ=1310 $\Delta\lambda$=75 **As/s** 1k	**Res.(μm):** l.r.: Np a.r.=10 **Samples:** -Mouse ear -Tumor in mouse **(2.14a)**	**2D:** 1.6x1.6(Z) **3D:** 1.6x1.6 x1.6(Z)
Wang *et al.* 2013 [100]	ⓜ 0.8x0.8 ⊡ 1.6x1.4 **ff:** 28.5% △ 3.5(D) x15(L)	**Max:** 4.5V <23mA **Image:** 0-4V (both)	**Max:** Np **Image:** 28(fast) 28(slow)	**S. rate:** 50Hz (fast) 450mHz (slow) 50fps **F_r (Hz):** Np	**Mode:** SS **WL:** λ=1310 $\Delta\lambda$=80 **As/s** 50k	**Res.(μm):** l.r.=17.5 a.r.=10.6 **Samples:** -Human finger -Normal buccal mucosa -Leukoplakia mucosa	**2D:** 2x1.5(Z) **3D:** 2x2 x1.5(Z) (raster)
Duan *et al.* 2016 [101]	ⓜ 0.72 0.72x0.06 ⊡ 2.22 x6.78x0.85 **(2.12d)** **ff:** 3.4% △ 2.7(D) x≈25(L)	**Max:** 5.5V (both) **Image:** 5V (both)	**Max:** 40 (both) **Image:** ±16.3 (both)	**S. rate:** 1.25Hz (fast) 0.005Hz (slow) **F_r (Hz):** 750 (both)	**Mode:** TD **WL:** λ=1310 $\Delta\lambda$=75 **As/s** 500	**Res.(μm):** l.r.=23 a.r.=10 **Samples:** -Infrared viewing card -Human finger -Human nail -Rat brain	**2D:** 2.5x1.75(Z) **3D:** 2.5x2.5 x1.75(Z) (raster)

Continuation of Table 2.4

Authors, year	Size (mm)	Driving V/I	Scan angle (°)	Frequency	OCT system	Images	Image size (mm)
						slices -Canine meniscus	
Tanguy *et al.* 2017 [90]	ⓜ 1(D) ⊡ Np △ NCP	**Max:** 17V (pitch) 16.5V (roll) **Image:** Np	**Max:** 38 (pitch) 22 (roll) **Image:** Np	**S. rate:** Np **F_r (Hz):** 205(pitch) 1286(roll)	**Mode:** Np **WL:** Np **As/s** Np	**Res.(μm):** Np **Samples:** Np	**2D:** Np **3D:** Np

[1] The dynamic range of this system is ≈ 100 dB.

[2] This publication presents an improved scanner version of that one presented by Pan *et al.* in 2001 (last row). The OCT system is the same. The bimorph actuators array was changed from a mesh shape (Fig. 2.12a, left down) to a parallel beams array (Fig. 2.12a, right down) in this improved version. With this modification, the buckling in the bimorph structure (mesh shape) present in the previous version was removed and the scanning distance was increased over 6.6 mm. Artifacts in the images caused by the buckling were also removed with this improved scanner. The authors also present images of rat bladder cancer *ex vivo* using this scanner in [95]. The resonance frequency is presented in this last publication (that is the same as the previous version).

[3] The scanning axes of this scanner are denoted as "mirror"and "frame" since the scanning in one axis is produced by the movement of the mirror and, in the other one, by the movement of the frame. The scan rate of 10 fps corresponds to lateral scanning (surface of a screen) and not for OCT imaging (scan in depth). No OCT images were presented in this publication.

[4] The values for the size of the probe correspond to the cross section. This scanner has four linear actuators for two scanning axes but the maximum scan angle is just specified for one. In this publication, the authors also present a similar scanner with curved actuators and size is 1.5 x 1.5 mm but no OCT images were produced with it. A smaller version of this design was presented by Singh *et al.* in 2008 (next row).

[5] This scanner is shown in Fig. 2.12b. The OCT system is the same than that one used by Singh *et al.* in 2007 (previous row). OCT images were not presented in this publication.

[6] The design of this scanner is the same to that one presented by Singh *et al.* in 2007 (linear actuators) but the size is different (see two rows before). The values in maximum driving voltage and scanning angle correspond to the driving of only one bimorph array (actuator) (see Fig. 3b in this publication).

[7] In this publication, the scanning axes were not refered with any specific name. We have presented them as "fast" and "slow". The measured sensitivity of this OCT system is 53 dB. A smaller version of this probe (same scanner) is presented in [98]. The diameter is only 2.7 mm and, besides images of ear and tongue of a mouse, a 3D image of a human fingerip are also shown.

[8] The scanner and the probe in this publication (Fig. 2.13b) are very similar to those ones presented by Sun *et al.* in 2010 (previous row) but smaller. The actuators design (based on three bimorphs cantilevers) and the OCT system are the same. The authors mention that the scan angle is ±16° at 3.6V but they do not specify if these values are per bimorph array (actuator) or per scanning axes (see Fig. 3 in this publication). Besides, these values are not the maximum since they used 4 V for imaging. Therefore, we refer them as "Presented (Pres.)" in the table. Also, it is not specified for which scanning axis (or if for both) the resonance frequency is. 3D images were presented but not its size.

[9] This scanner is similar to that one presented by Singh *et al.* in 2008 [91] but with a bigger mirror to improve light collection. The probe is very similar to that one presented by Xu et al. in 2008 (Fig. 2.13a).

[10] It is not specified for which scanning axis (or if for both) the resonance frequency is. The OCT system is the same as that one used by Sun *et al.* in 2010 and Liu *et al.* in 2011. The measured sensitivity of the system is 74 dB.

2.3 Discussion on MOEMS scanners with different types of actuation

For endoscopic OCT imaging, one proper scanner should be small enough to fit in endoscopes, to scan at high angles (that translates in bigger image sizes), to be able to scan at high frequencies for real-time imaging and to operate at low driving voltages for patient's safety [114]. High fill factors are also desirable, or what is the same, the size of the mirror should be big in relation to the size of the scanner. Hence, the space required by the actuators in the MOEMS should be the minimum possible to make easier the miniaturization of the fully integrated probes.

Electrostatic scanners have relatively lower fill factors (4.8%, 8.7%, 12.5%) since the actuators require more space around the mirror (see Fig. 2.5). Yeow *et al.* reported one device with a high fill factor of 42% but it required a driving voltage up to 55 V to produce scan angles of ± 0.23° (x-axis) and ± 0.33° (y-axis). The main disadvantage of these type of scanners is the requirement of high driving voltages which is not desirable for endoscopic applications. Most of them operate at 100 V in average and achieve scan angles comparables to those ones obtained with electrothermal scanners that demand less than 10 V. The exception is the MOEMS presented by Chong *et al.* in 2006 that achieved a scan angle of 8° at only 5 V although it has only one scanning axis. In most of the cases, the scanning rates for image acquisition are also comparable to those ones achieved with electrothermal scanners, less than 10 fps. However, Piyawattanametha *et al.* and Kumar *et al.* reported scanning rates of 20 fps and even 40 fps, respectively, where this last one was reached with a SS-OCT system (20 k As/s). Again, the speed of some scanners (those ones presented by Jung *et al.* (2006) and Aguirre *et al.* (2007)) was limited by the TD-OCT system.

Electromagnetic scanners also have low fill factors (6.9%, 3.2%) because of the considerable space needed for the coils (see Fig. 2.7), although they can operate at low driving voltages of less than 4 V and reach high scan angles of ±30° (Kim *et al.*, 2007). They showed a linear response between the scan angle and the input voltage (current) and, in addition, satisfactory scanning rates of 14 Hz and 18.5 Hz were also achieved due to the use of SD-OCT systems. Nevertheless, the power consumption can be high as in the scanner of Kim *et al.* that required 150 mW for driving both axes. These scanners require that magnets or coils (not part of them) be coupled externally in the probes which can make difficult its miniaturization. Moreover, they are also susceptible to external electromagnetic interference.

Piezoelectric scanners have very high fill factors of 68% and 76% but they only have one scanning axis. Two of them are required for 3D OCT imaging. Nonetheless, good scan angles (14°) can be achieved at not very high voltages (20 V) and with very low power consumption (1 mW).

On the other hand, some electrothermal scanners can have higher fill factors like 25% (Sun *et al.*), 28.4% (Liu *et al.*), 32% (Samuelson *et al.*) and 28.5% (Wang *et al.*) due to the small size of the actuators and also because they can be fabricated and placed almost under the mirror as in Figures 2.12c and 2.12d. These type of scanners require low driving voltages of around 5 V to achieve large scan angles of even ±31° (Sun *et al.*). Additionally, some of them show almost a linear response between the scan angle and the input voltage (scanners presented by Xie *et al.* in 2003, Singh *et al.* in 2008, Xu *et al.* in 2008, Sun *et al.* in 2010, Liu *et al.* in 2011, Samuelson *et al.* in 2012 and Duan *et al.* in 2016). Most of these scanners were driven at scanning rates equal to or less than 10 fps for image acquisition. However, Xu *et al.* (2008) and Wang *et al.* (2013) reported scanning rates of up to 21.5 fps and 50 fps respectively. Notice that in these two publications, the authors used SS-OCT systems that have higher axial scanning rates (16 kHz and 50 kHz, respectively) compared with the TD-OCT systems (1 kHz and 2.4 kHz) and this allowed faster image acquisition. It is important to mention that in some of the publications cited here (as

Sun *et al.* and Duan *et al.* specified), the scanning rates were limited by the OCT system and not for the scanner capacity.

As a conclusion of this section, we can say that electrothermal scanners seem to be specially well suited for endoscopic applications due to its high fill factors, high scan angles, low driving voltages, two scanning axes and high scanning rates when they are coupled to SS-OCT systems. In the next section, we briefly describe the electrothermal scanner integrated in the OCT probe presented in this thesis.

2.4 Description of the 2-axis electrothermal micro-scanner

The scanner is batch fabricated and a total of 279 chips are produced at 4" wafer level [19]. A picture of one structure is shown in Fig. 2.15a after dicing of the SOI wafer and the releasing process. The 30-μm-thick silicon mirror is coated with an Cr/Al/Cr layer on both sides and has a diameter of 1 mm. It is attached to four double S-shaped actuators (Act_x^+, Act_y^+, Act_x^-, Act_y^-) as those ones shown in Fig. 2.11b. They are composed of bimorph cantilevers made of Al and SiO_2 with a layer of Pt in between that acts as the heater. The actuators maintain the mirror ≈ 300 μm over the plane of the frame that, at the same time, is supposed to be kept at 45° with respect to the silicon substrate (body) by a parallel bimorphs array that bends up due to the compresssive and tensile stress in the top (SiO_2) and bottom (Al) layers of the bimorphs, respectively. There are two stopper mechanisms that block this bending up movement at 45° by the contact between the hinge of the frame and the sidewalls of the cavities in the substrate (as in [93]). Finally, the scanner also has five electrical pads for driving each of the actuator plus one for the ground connection. The size of the chip substrate is 4 x 4 mm^2.

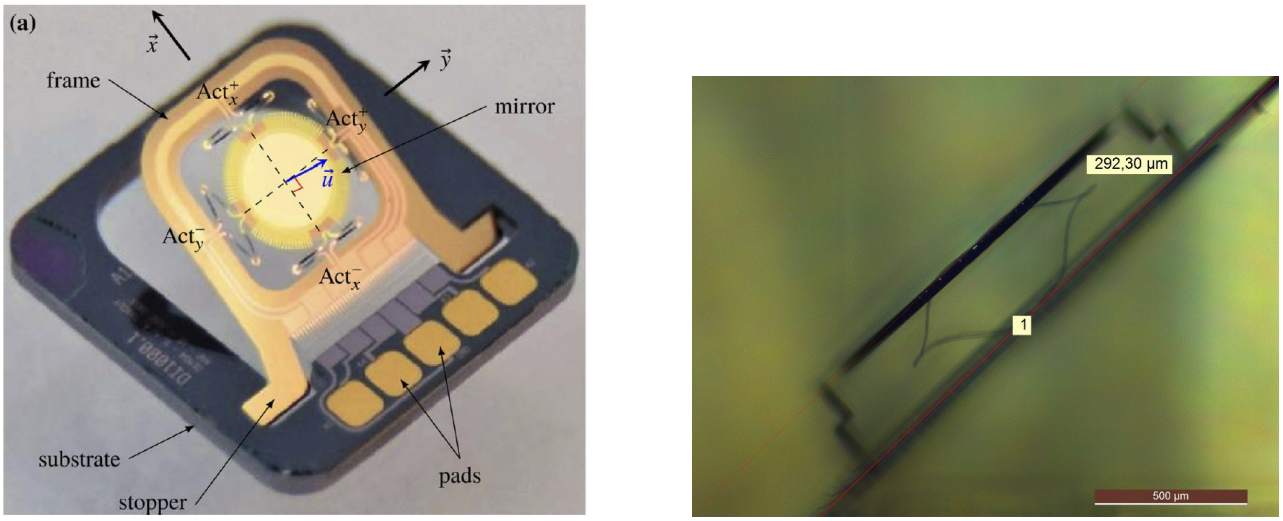

(a) (b)

Figure 2.15: (*a*) Electrothermal micro scanner. Image taken from [136]. (*b*) Sideview on suspended mirror.

One of the scanners of the batch was characterized and showed to be able to perform Lissajous scanning in real-time [136]. Some characteristics of this particular chip are presented in table 2.5. The scanning angles were achieved at the resonance frequencies driving the scanner with sinusoidal signals with a DC voltage of 3 V and an amplitude of 0.1 V. We integrated other scanner of the

same batch in the OCT probe and we performed a similar characterization that is presented in section 5.2.

Table 2.5: Scanner characteristics.

Size (mm)	**Driving V**	**Scan angle (°)**	**F_r (Hz)**
ⓜ 1 (D)	3 V_{DC}	3.67 (x-axis)	1186 (x-axis)
⊡ 4 x 4	0.1 V_{pp}	2.29 (y-axis)	1179 (y-axis)
ff: 4.9 %	(both)		

2.5 Conclusion

We revised the use of OCT endoscopic probes to visualize the internal layers of organs of the gastrointestinal tract such as the esophagus, stomach and colon. This technique allows to observe structural changes in cancered tissues that makes it a proper tool for non-invasive diagnosis. These endoscopic probes have been developed in the last years by coupling them inside balloons that flat the irregular lumen of the esophagus and improve the radial scanning and by integrating them in capsules that do not require the patient to be anesthetized. Other probes were integrated with MOEMS scanners that have proper characteristics for clinical applications such as small size, real-time scanning in 2-axis and low costs of fabrication. They are based on four types of actuation: electrostatic, electromagnetic, piezoelectric and electrothermal. The scanners with this last actuation principle own suitable features to perform endoscopy namely high fill factors, high scanning angles at low voltages and high scanning rates. At the end, we introduced the electrothermal micro scanner integrated in the OCT probe presented in this thesis. In the next chapter, the MOEMS interferometer is described.

3 OCT endoscopic probe based on a Mirau micro-interferometer

In this chapter, we present the Mirau micro-interferometer and the OCT images produced with it. This interferometer configuration has the sample and reference arms in the same optical path, making it more compact and fully compatible with wafer-level batch microfabrication process [115]. Besides, this common path (CP) optical setup compensates polarization and dispersion differences between both arms. Moreover, it is easier to align and has less sensitivity to external vibrations which makes it suitable for medical applications [116]. Popp *et al.* developed a CP FD-OCT system to scan a rabbit lung and obtain images of the volume changes of the alveoles during ventilation [117]. Other example is the development of a side-viewing CP probe of only 1 mm of diameter by Singh *et al.*, based on a spherical ball lens where the reference signal is obtained from the glass-air interface [118]. This probe was able to produce OCT images of the skin layers (startum corneum, epidermis and dermis) of an index finger. This type of CP probes are desirable for endoscopic applications since the reference mirror is at the near end of the probe. In this way, there is no need to match the length of the fibers (within 1 mm) of the long sample arm and the external reference arm. Besides, the bending and twisting of the sample arm fiber in these procedures distorts the optical path and the polarization state of the sample beam leading to a decrease in sensitivity. Other CP OCT probes are reported in [119], [120], [121].

3.1 Mirau micro-interferometer description

The Mirau micro-interferometer has five components: a silicon (Si) base, a micro lens, a silicon separator, a beam splitter and a reference mirror (Fig. 3.1). The silicon (Si) base was designed to couple a GRIN lens collimator that transmits the input light beam, with 1 mm diameter (d), to the interferometer. The base has a circular cavity with a diameter of 1.9 mm on the side of the micro lens and 1.8 mm for the side of the assembly port. The plano-convex micro lens (glass), with a diameter of 1.9 mm and a focal length (f_L) of 9.1 mm, focuses the input beam towards the beam splitter (BSP) made of TiO_2 and Borofloat 33 glass with a transmission/reflection ratio of 70:30. This last component reflects the light beam to the reference mirror (reference arm) and transmits it to the sample (sample arm). The reference mirror, made of Titanium (Ti), Nickel (Ni), and gold (Au), is fabricated on the planar side of the micro lens and has a diameter of 150 μm. The separator is a wafer of silicon with thickness of 4.8 mm that keeps the BSP at half of the distance between the lens and the focal point, fixing a working distance of the same length. In this way,

the sample reflects the beam back to the beam splitter where it interferes with the light beam reflected from the reference mirror. The interference is only produced if the difference between the reference and sample arms distances is small enough compared with the coherence length of the light source. Finally, the interference pattern is reflected back to the the micro lens and then to the input port.

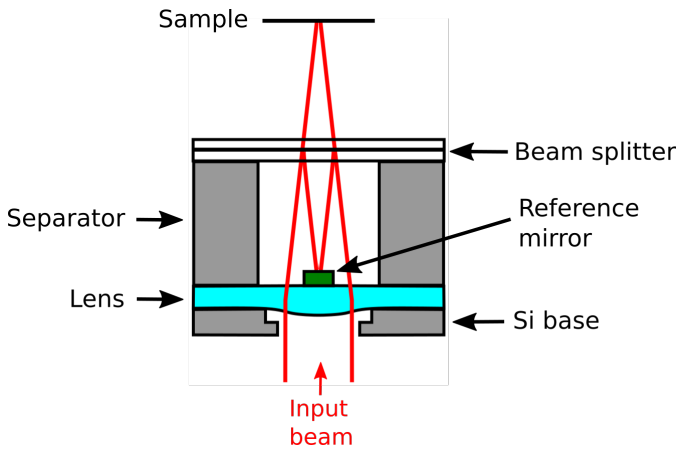

Figure 3.1: Diagram of the Mirau micro-interferometer.

The batch fabrication process of the Mirau micro-interferometer is presented in Fig. 3.2a and summarized as follows:

1. The process starts with the fabrication of the base that is a p-type, (100)-oriented Si wafer with a thickness of 500 μm.

2. To create the circular cavities for the GRIN lens assembly and the fabrication of the micro lens, the Si wafer is subjected to two deep reactive ion etching (DRIE) processes (one per each side of the wafer).

3. A Borofloat 33 glass wafer with a thickness of 500 μm and refractive index (n) of 1.465 (at λ = 850 nm) is joined to the Si base by anodic bondig in vacuum. Then, the assembled wafers are heated up in a furance at 700 °C causing the glass flow slightly towards the cavity because of the vacuum in it and producing the desired lens shape. The top layer of the glass wafer is polished horizontally to remove the downward deformation created by the thermal reflow and to make the planar side of the lens.

4. The Silicon membrane that created the cavity for the thermal reflow step is removed by a DRIE process.

5. The reference mirror is made by lift-off photolithography and e-beam evaporation of Ti, Ni and Au on the planar side of the micro lens.

6. The beam splitter is made of two wafers of Borofloat 33 glass with a single 100 nm-thick TiO_2 layer deposited by reactive magnetron sputtering.

Figure 3.2b shows the final wafer assembly with the Si base on the top. A total of 230 structures are obtained from a 4" wafer. Figure 3.2c shows one interferometer structure (after the dicing process) which size is 4.7 x 4.7 x 5.3 mm^3. The focal volume produced by the micro lens (when the

GRIN lens collimator is applied) is shown . A Full Width at Half Maximum (FWHM) of 5.8 μm was measured in a cross sectional view. The diameter of the micro lens is 1.9 mm but only the central part of 820 μm of diameter can be made spherical with the thermal reflow process. This is enough for the diameter of 1 mm of the input light beam.

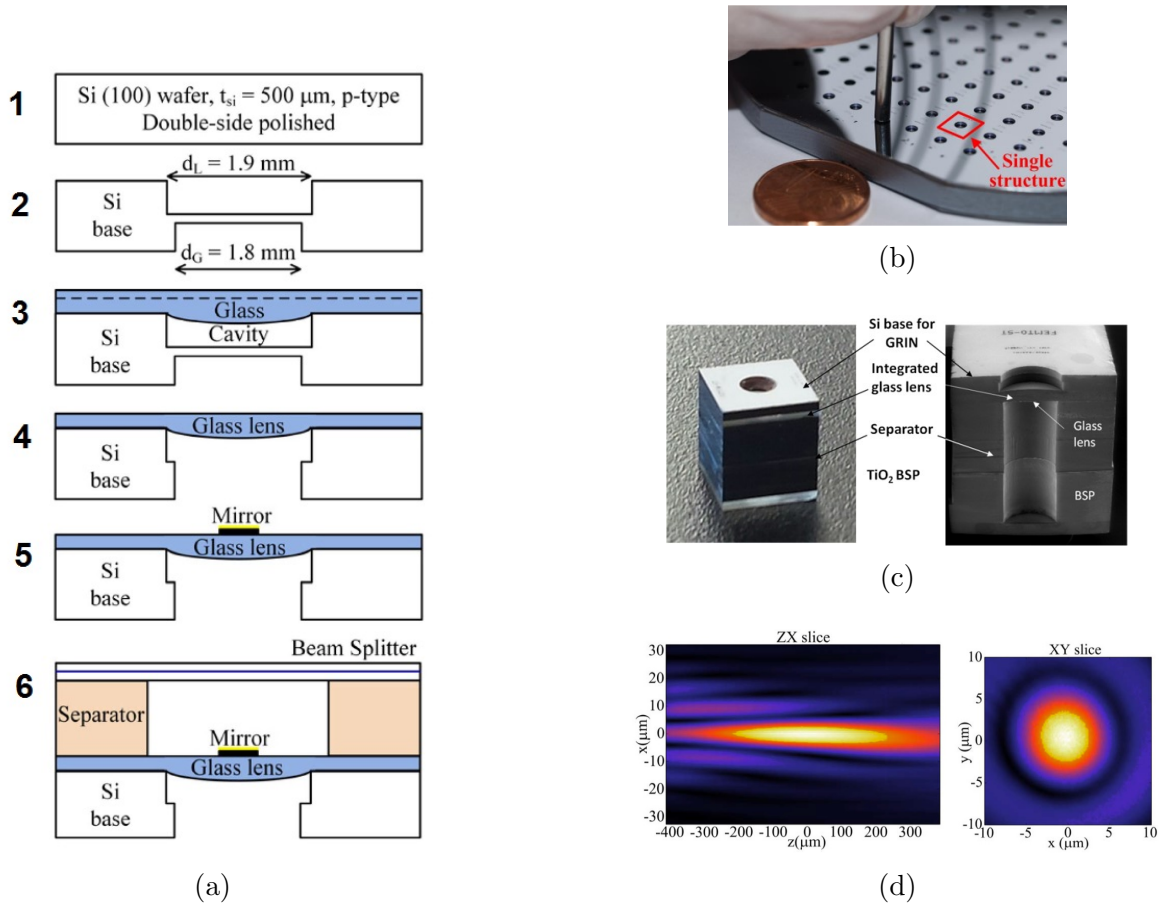

Figure 3.2: (a) Fabrication process of the Mirau micro-interferometer. Image adapted from [17]. (b) Interferometer at wafer level and (c) a single structure. (d) Focal volume produced by the microlens. The ZX slice is along the optical axis and the XY slice is perpendicular to it. Images taken from [17].

3.2 OCT imaging with the Mirau micro-interferometer

The capacity of the interferometer to produce OCT images was tested as a first step. We connected the Mirau interferometer to the optical fiber SS-OCT system shown in Fig. 3.3. We used a swept laser EXALOS ESS-840 with a central wavelength of $\lambda_0 = 840$ nm, a swept range of $\Delta\lambda = 60$ nm, an average output power of 8 mW and an A-scan rate of 110 kHz. The light beam passes first through a Mach-Zehnder interferometer clock box (Thorlabs INT-MZI-850) that takes 5 % of the input beam power to generate a k-clock signal that monitors the frequency variation of the swept source. This signal is used for the resampling of the interferograms produced by the Mirau interferometer and the layers of the sample in order to have equally spaced points in the frequency domain [122]. The k-clock signal is registered in the channel 2 (Ch 2) of a data acquisition card (GaGe CompuScope 12502) with a sampling rate of 500 MS/s. After, the swept beam goes to a polarization controller and then to an optical circulator that sends it to a GRIN lens collimator. This last component

directs the beam with a diameter (d) of 1 mm to the interferometer where the interference signal is produced and subsequently reflected back towards the optical circulator that, this time, transmits it to a photodiode (Thorlabs PDB430A). This device converts the optical signal to an electrical one which is registered in the channel 1 (Ch 1) of the GaGe DAQ at 500 MS/s as well. Figure 3.4a shows this signal that is produced by the reflection of the reference mirror without any sample. It corresponds to the intensity profile of the swept source where we can observe the temporal swept power profiles in the forward and backward directions. When a sample is placed in the focal point of the micro lens, fringes appear in this profile (see Fig. 3.6a). Notice that the GaGe DAQ is triggered by the swept source (channel Tr). Each rising edge of the pulses of the trigger signal corresponds to the beginning of one sweep cycle. Figure 3.4b shows the correspondent k-clock signal.

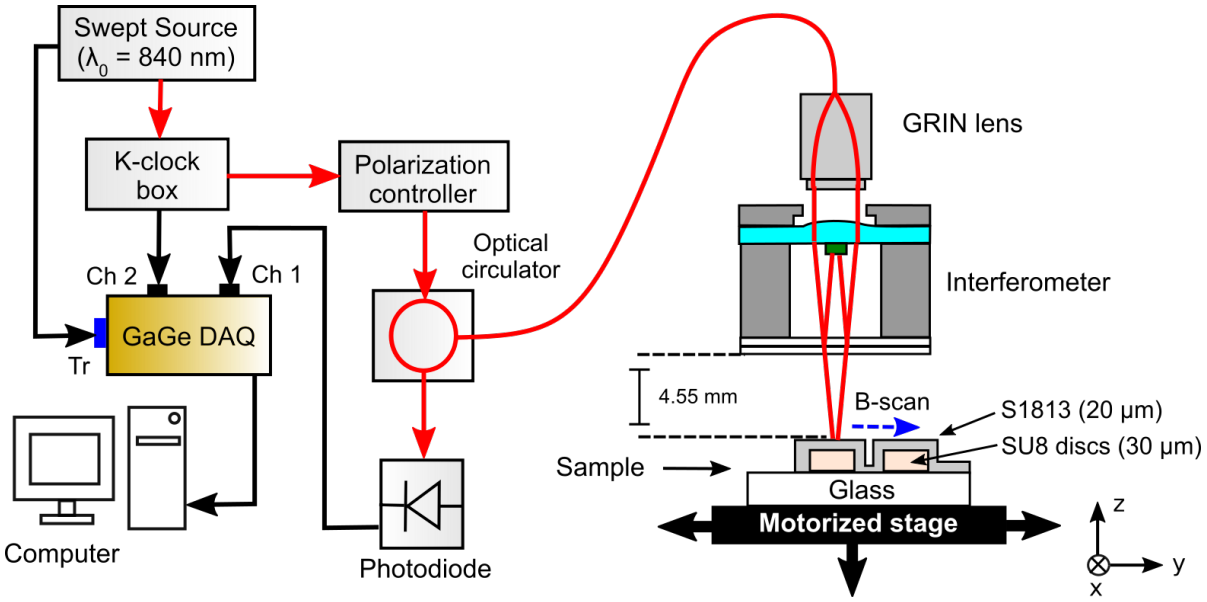

Figure 3.3: First version of the SS-OCT system. The red lines correspond to optical paths and the black lines to electronic paths.

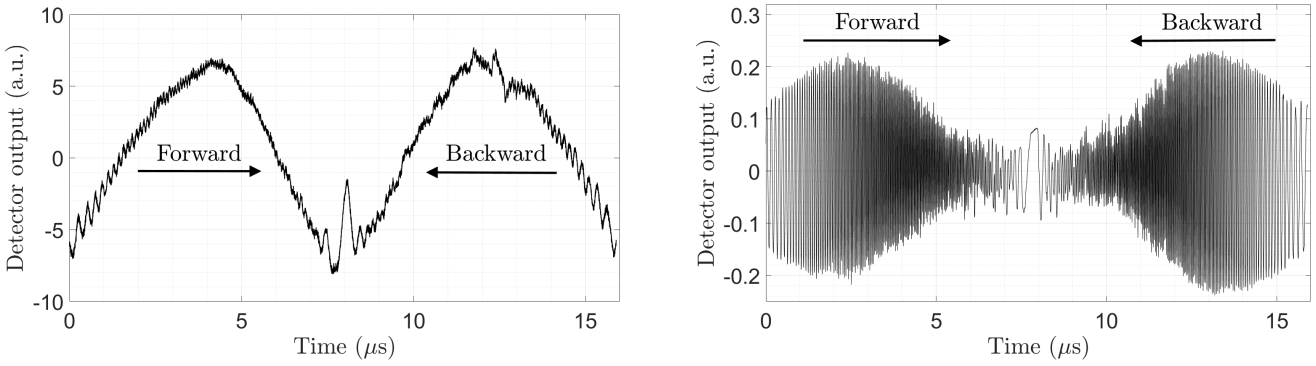

Figure 3.4: (a) Intensity profile of the swept source and (b) the correspondent k-clock signal.

In OCT, the axial resolution (Δz) is specified by the coherence length (l_c) of the light source

that is given by the equation 1.24 [123]. Therefore, we have:

$$\Delta z = l_c = \frac{2\ln(2)}{\pi}\left(\frac{\lambda_0^2}{\Delta\lambda}\right) \tag{3.1}$$

On the other hand, the lateral resolution (Δx) is determined by:

$$\Delta x = \frac{4\lambda_0}{\pi}\left(\frac{f_L}{d}\right) \tag{3.2}$$

where f_L is the focal length of the micro lens (9.1 mm) and d the diameter of the collimated beam on it (1 mm). The depth of focus (DOF) is given by:

$$\text{DOF} = \frac{\pi\,\Delta x^2}{2\,\lambda_0} \tag{3.3}$$

and the the numerical aperture of the micro lens is:

$$\text{NA} \approx n\,\frac{d}{2f_L} \tag{3.4}$$

where n is the index of refraction of air (1). The calculated parameters are summarized in table 3.1.

Table 3.1: Calculated optical parameters of the micro-interferometer

Δz	Δx	DOF	NA
5.18 μm	9.73 μm	177.13 μm	0.05

Regarding the sample, we fabricated one made of photoresist SU-8 discs with a thickness of 30 μm and a diameter of 2 mm separated by a distance of 20 μm on Borofloat 33 glass. Then, the discs were covered by a layer of photoresist S1813 with a thickness of 20 μm. The sample is placed in a 3D motorized stage (Thorlabs MT3-Z8) in order to move it laterally and perform the B-scans. The GaGe-DAQ has some supporing softwares in LabVIEW which were developed for different applications. We took the one that records the channels 1 and 2 (GageCoerce.vi) and modified it to add the code that moves the motorized stage in two directions (x and y axes) with a programable minimum step of 0.05 μm while recording the interferograms (Ch 1) and k-clock signals (Ch 2) at each position. With this sofware, we performed a B-scan of 4 mm of the sample in the y direction with a step of 10 μm (close to Δx).

Figure 3.5 presents a diagram that describes the steps to follow in order to obtain the depth profile of the sample (A-scan) for SS-OCT. We took this algorithm from [65]. All this data processing was performed in Matlab. The first step is to acquire the OCT signal (Fig. 3.6a). We have taken only the swept profile in the backward direction for this first test (acquisition time = 7.6 μs). The fringes produced in the intensity curve of Fig. 3.4a are clearly noticeable. The next step is to remove the background shape that is the interferogram measured without sample (Fig. 3.4a), in order to decrease the amplitude of the DC term in the following Fourier transform (see end of section 1.3). We measured (previously to this test) ten of these interferograms and averaged them to reduce noise, the resuling curve is shown in Fig. 3.6b. After, we remove it from the interferogram measured with sample (Fig. 3.6a) and the result is presented in Fig. 3.6c.

The next step is to resample the last curve at the positions where the k-clock signal crosses the zero axis. In this test, we averaged all the k-clock measurements (4000) of the B-scan to reduce noise and to peform the resampling of all the inteferograms with only one signal (Fig. 3.6d). We made an algoritm to detect the positions where it crosses the zero axis and to save them in one calibration vector. Then, we resample the interferogram of Fig. 3.6c at these positions and the resulting signal is shown in Fig. 3.6e that now it is equally spaced in the frequency domain. The total number of samples (M) is 349 that, according to equation 1.41 and 1.43, gives a maximum range in depth of $\pm z_{max} = \pm 1.02$ mm.

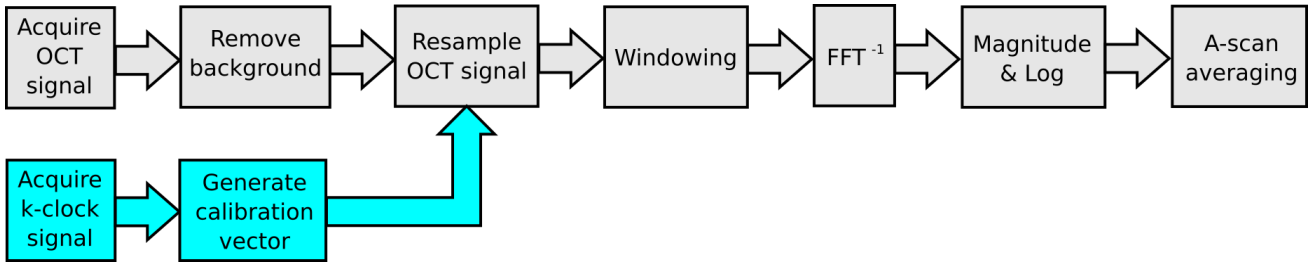

Figure 3.5: Diagram to obtain one A-scan from the OCT and k-clock signals. The diagram was taken from [65].

After the resampling, we can apply the fast fourier transform (FFT) and subsequently estimate the power spectrum (PS) that results from taking the absolute value of the complex numbers, given by the FFT (RMS spectrum) and then square them [124]. Since the spectrum is the same for the positive and negative frequencies (see Fig. 1.16), we only show the positive side. We used the function of Matlab called "periodogram" that makes all these last operations and also allows to perform windowing. We applied a hann window in all the images presented in this manuscript. Finally, we express the power spectrum in decibles (dB) using the next equation:

$$\mathrm{PS_{dB}} = 10 \log_{10}(\mathrm{PS}) \tag{3.5}$$

Figure 3.6f shows the resulting signal that corresponds to the depth profile of the sample in the position where there is only the layer of glass. For this first test, we took only one A-scan per position and averaging for noise reduction was not possible. We repeat the same data processing for all the A-scans and the obtained depth profiles are plotted together as an image in Fig. 3.7. The layers of glass and the photoresist S1813 are clearly visible. Even the space of 20 μm between the discs of the photoresist SU-8 could be resolved. We can also appreciate the presence of an artefact almost at the middle of the image that is produced by one of the reflective layers in the interferometer such as the beam splitter or the flat surface of the micro-lens [125]. Besides, a ghost image is observed at the bottom that is produced by the interference of the light beams reflected by the sample and one of these reflective layers that act as a reference mirror (as in [126]).

Other way to obtain the background shape is to average all the A-scans of the B-scan measured with the sample in place. Wang *et al.* showed that the artefacts can be removed by subtracting this last backgound signal from all the A-scans instead of the interferogram measured without sample as previously [127]. Figure 3.8a shows the curve that results from averaging all the A-scans and Fig. 3.8b presents the depth profile of the sample in the same position as before (Fig. 3.6f) where the artefact is removed by this method. Figure 3.8c shows the central part of the obtained OCT image where we can see that the artefact is attenuated along the B-scan. In consequence, we use the signal obtained from averaging all the A-scans of the correspondent B-scan for background

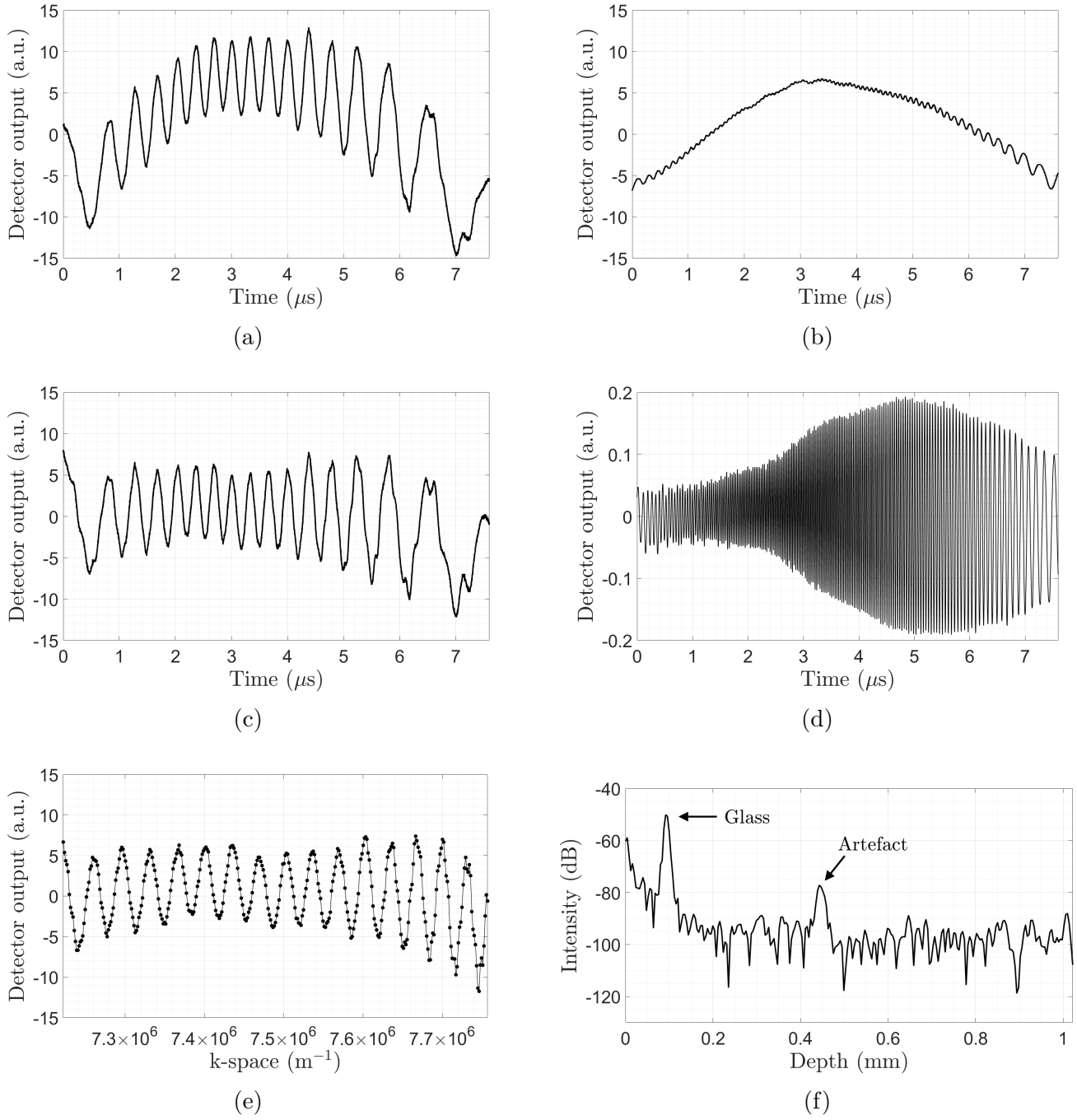

Figure 3.6: (a) The first interferogram of the B-scan, when the scanning beam is positioned on the glass. (b) Resulting signal of averaging ten interferograms without sample. (c) Interferogram after remotion of the background signal. (d) Resulting signal of averaging all the k-clock signals of the B-scan. (e) Resampled interferogram. (f) Depth profile of the sample (A-scan).

remotion in all the images presented in this work since, besides artefacts attenuation, there is no necessity to measure the interferogram without sample with this method.

Additionally, a C-scan of the sample (x and y directions) was performed using the software and the motorized stage with raster scanning. The scanned area was 2 x 4 mm. We processed all the interferograms acquired at each position of the sample and obtained the correspondent depth profiles. Figure 3.9a presents all the A-scans plotted as a 3D image. We show only the

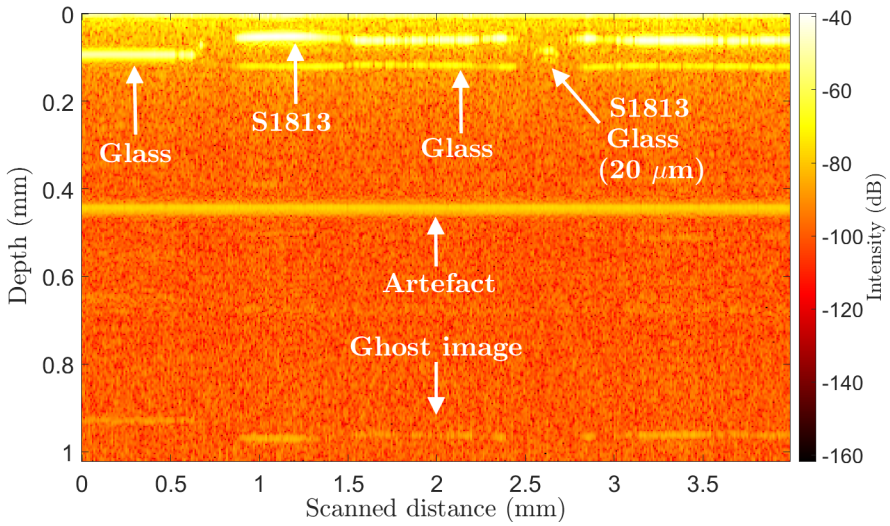

Figure 3.7: B-scan of the sample.

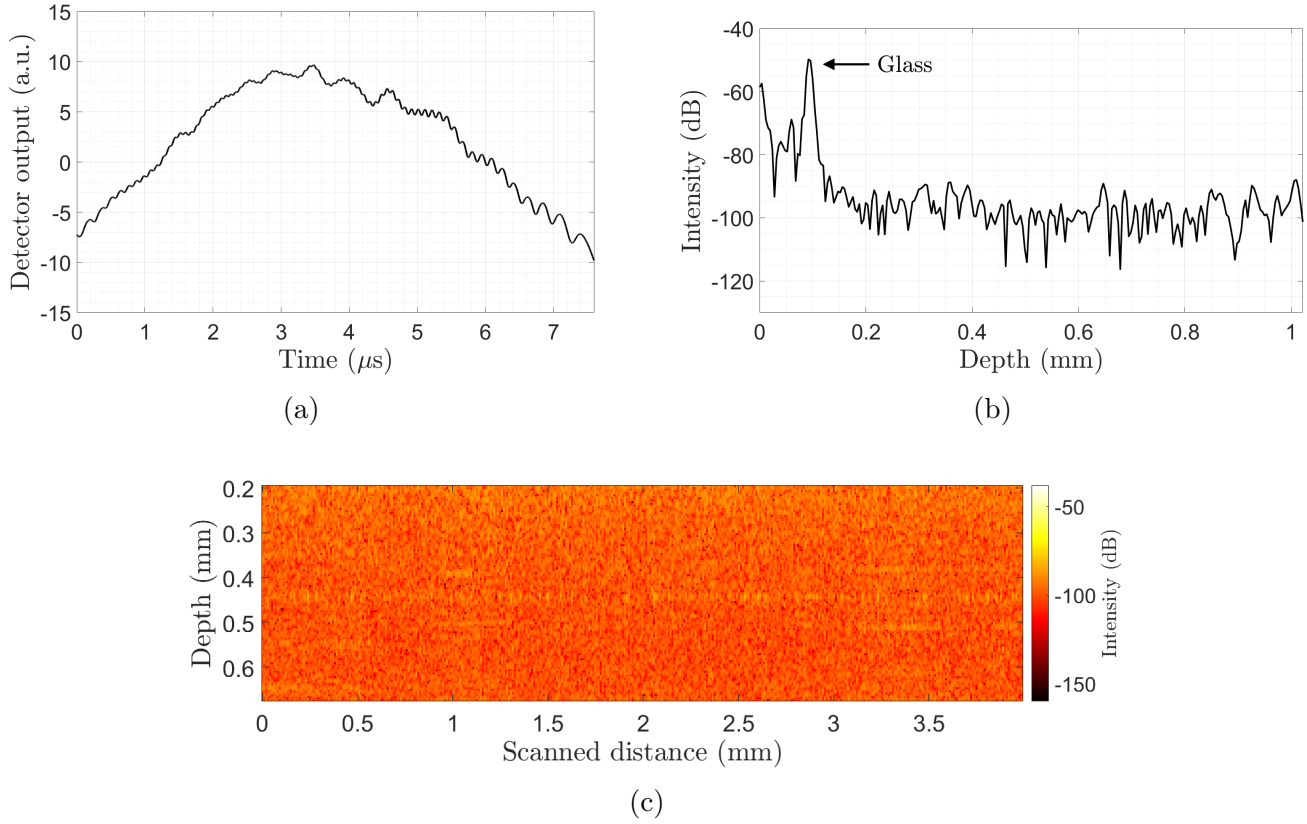

Figure 3.8: (*a*) Background signal obtained from averaging all the A-scans of the B-scan. (*b*) Depth profile of the sample where the artefact has been removed. (*c*) Central part of the OCT image with the artefact attenuated.

part until a depth of 180 μm, i.e. where the sample is placed. The DC term at zero position was also cropped. Figure 3.9b shows the top view of the image where the glass and the layer of the photoresist S1813, that covers the discs of SU-8, are seen. Besides, we noticed that one part of the sample was damaged and the break curve is also clearly visible.

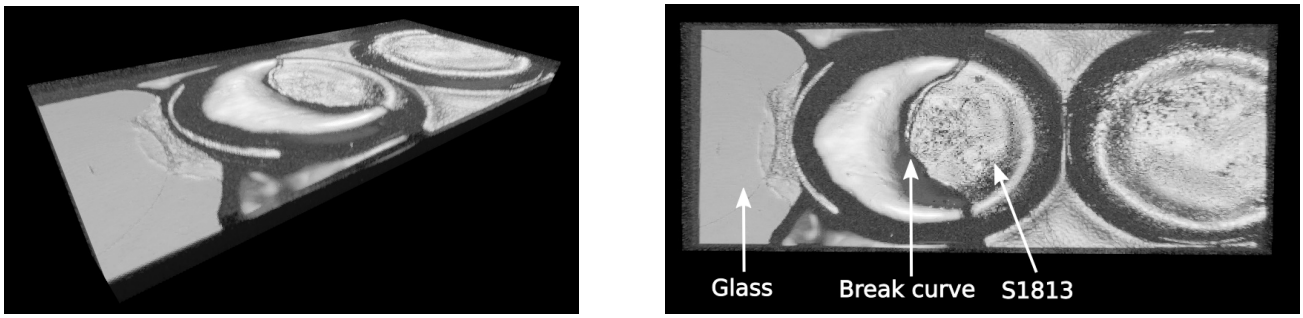

(a) (b)

Figure 3.9: (*a*) 3D OCT image of the sample (Area = 2 x 4 mm) (*b*) Top view. This 3D image was published in [147].

A sample made of three layers of tape with paper at the bottom that is more diffusive was also scanned (Fig. 3.10a). The obtained B-scan is shown in Fig. 3.10b where all the layers can be observed. The image is flipped with respect to the zero delay that is at the zero position of the z-axis (depth). Once more, we only show the part of the image where the sample is visible, i.e. until a depth of 268 μm in this case. Besides, the minimum value of the colorbar was set at -90 dB and the maximum at -45 dB in order to visualize only the reflective layers. Figures 3.10c and 3.10d (top view) show the correspondent C-scan whose scanned area is 3 x 2 mm with a step of 10 μm as well.

3.3 Implementation of the balanced differential detector in the Swept Source OCT system

Usually, the SS-OCT systems require a dual balanced detector in order to supress the noise caused by intensity fluctuations of the laser ([129], [78], [130]). Figure 3.11a shows the 2nd version of our SS-OCT system with the differential photodiode (Thorlabs PDB430A) added and also a fiber optic coupler with a split ratio of 90/10 (Thorlabs BXC42) and a variable optical attenuator (VOA, Thorlabs V800A). The coupler takes 90% of the input light beam and transmits it towards the optical circulator and the process described in the previous section is repeated. The other 10% of the beam goes to the variable optical attenuator (VOA) that decreases the quantity of light that is transmitted to the negative input of the photodiode and, at the same time, removes the DC component of the interference signal (see the final part of section 1.3). The level of attenuation of the VOA is controlled by a power supply (TENMA 72-2540, not shown in the diagram) applying DC voltages from 0 to 5V. We took this dual balanced optical configuration for common path OCT sytems from the intereferometer INT-COM-1300 manufactrured by Thorlabs. The wavelength range of this device is 1250 – 1350 nm, so, we had to implement a fiber coupler and a VOA compatibles with the range of our swept source (810 – 870 nm). Finally, the electrical signal of the photodiode (difference between the positive and negative inputs) is registered by the channel 1 of the GaGe DAQ with a sampling rate of 500 MS/s and then transmitted to the computer for processing. Figure 3.11b shows the intensity profile of the swept source (without a sample in place) where the DC component has been decreased with the VOA powered at 3 V. Again, the fringes are produced by parasitic internal reflections in the interferometer.

According to the diagram of Fig. 3.5, A-scan averaging should be done at the end of the data processing in order to decrease noise in the OCT image. With this new version of the SS-OCT

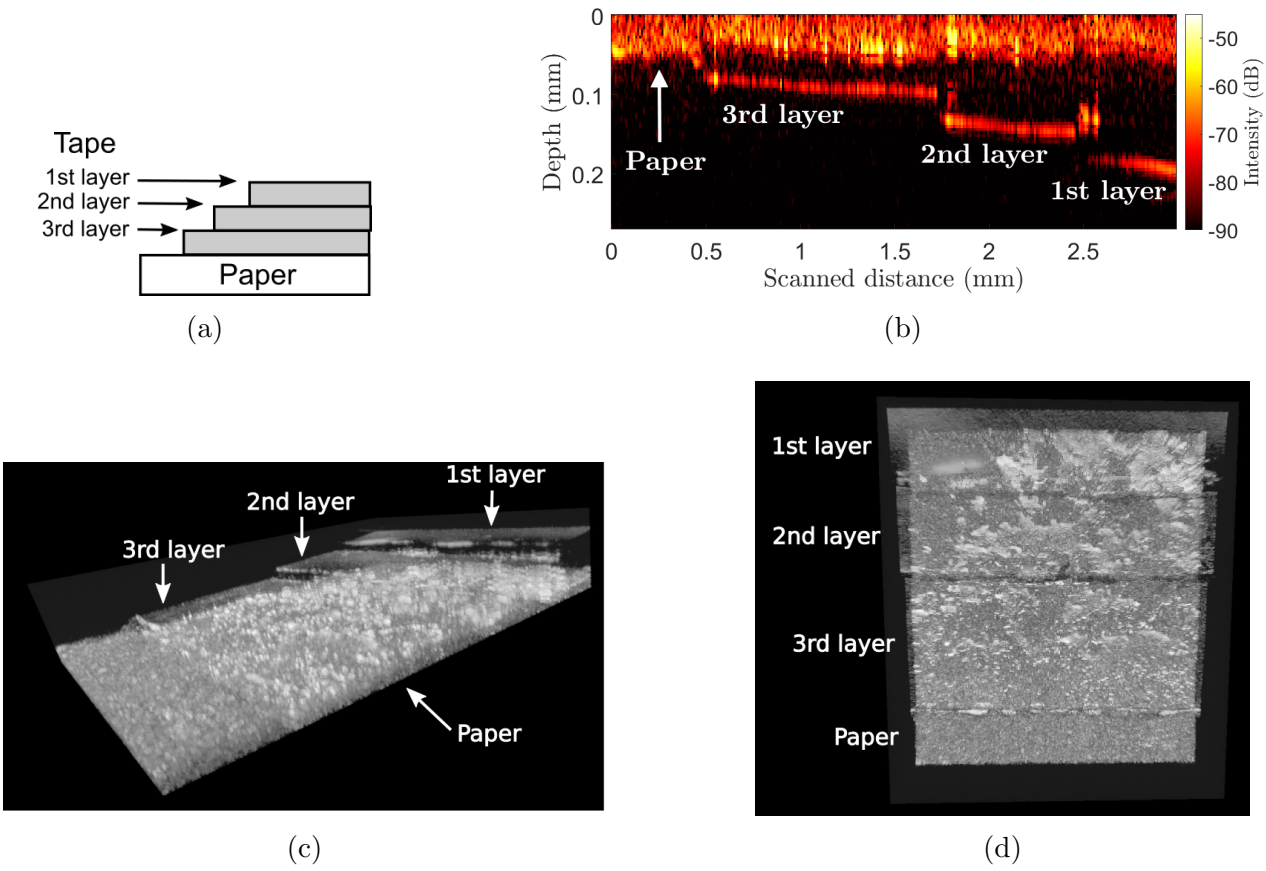

Figure 3.10: (a) Sample made of three layers of tape on paper. (b) B-scan of the sample. (c) C-scan of the sample (Area = 2 x 3 mm). (d) Top view.

system, we record ten sweep cycles (as in Fig. 3.11b) per A-scan to perform averaging and also to obtain images with the forward and backward sweeps. Since we need to know the beginning of each sweep cycle to separate them correctly, the trigger signal of the swept source must also be registered. The GaGe DAQ has only two input channels, so that, we disconnected the k-clock box from the channel 2 and connected the trigger instead. Previous to take this component off from the setup, we saved ten k-clock signals in one file and then we averaged them to perform the resampling step for the next OCT images with only one as before. Figure 3.12 shows one example of the signals that are registered in the channel 1 (up) and 2 (down). Notice that there is a delay of 2.8 μs between the rising edge of each pulse of the trigger signal and the beginning of the sweep that we had to compensate in the data post processing. The GaGe DAQ can also be triggered with the channel 2 that allows us to perform these measurements. The trigger port of the DAQ is not connected since it is needed for synchronization with the electrothermal micro scanner in the next and final version of the SS-OCT system that will be described in chapter 5.

To test this new setup and A-scan averaging, we scanned the middle part of the detector card shown in Fig. 3.13a (Thorlabs card VRC2) that has two surfaces: diffusive rough and reflective smooth. Figure 3.13b shows the respective B-scan obtained with the SD-OCT commercial system Thorlabs Callisto that it is used as a reference. This system has the characteristics presented in table 3.2.

We modified the algorithm used to produce the OCT images presented in the last section (Fig. 3.5) since, in this case, we register ten sweep cycles (acquistion time = 178 μs) and the

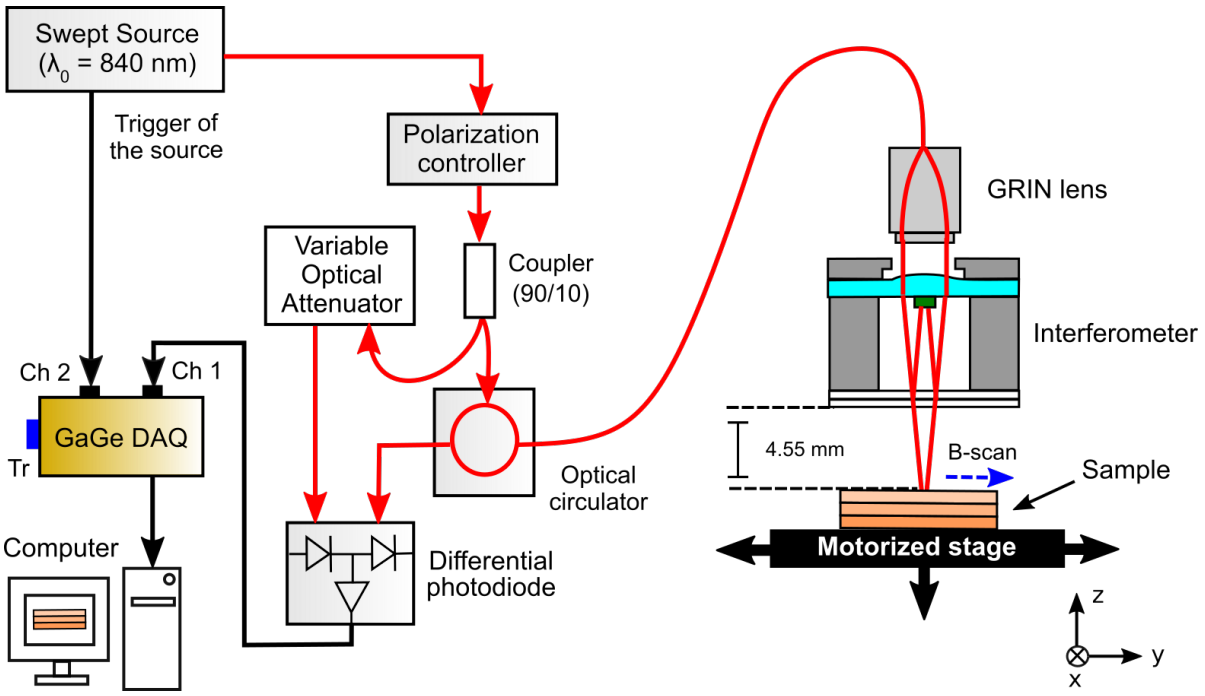

(a)

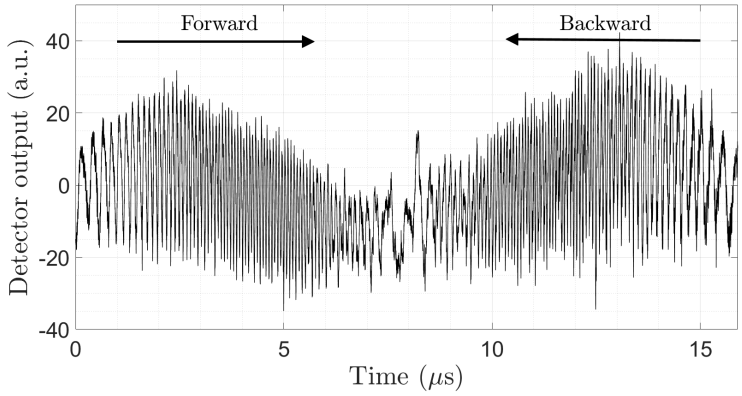

(b)

Figure 3.11: (a) Second version of the SS-OCT system with the dual balanced detector. (b) Intensity profile of the swept source with the DC component decreased.

Table 3.2: Characteristics of the SD-OCT commercial system Thorlabs Callisto.

λ_0	A-scan rate	Δz	Imaging depth	Sensitivity (Max)
930 nm	1.2 kHz	7 μm (in air)	1.7 mm	107 dB

trigger signal of the swept source. Figure 3.14 shows this new algorithm that we proposed and is compatible with this new SS-OCT setup. As a first step, the positions of the rising edges of the trigger signal are detected and then used in the long OCT one to separate each sweep (duration = 15.9 μs). We sum 2.8 μs to the positions of the edges to compensate the delay. After, the forward and backward segments (duration = 7.6 μs) are separated from each sweep cycle where the central part (marked inside red rectangles in Fig. 3.12, duration = 0.7 μs) correspond to the

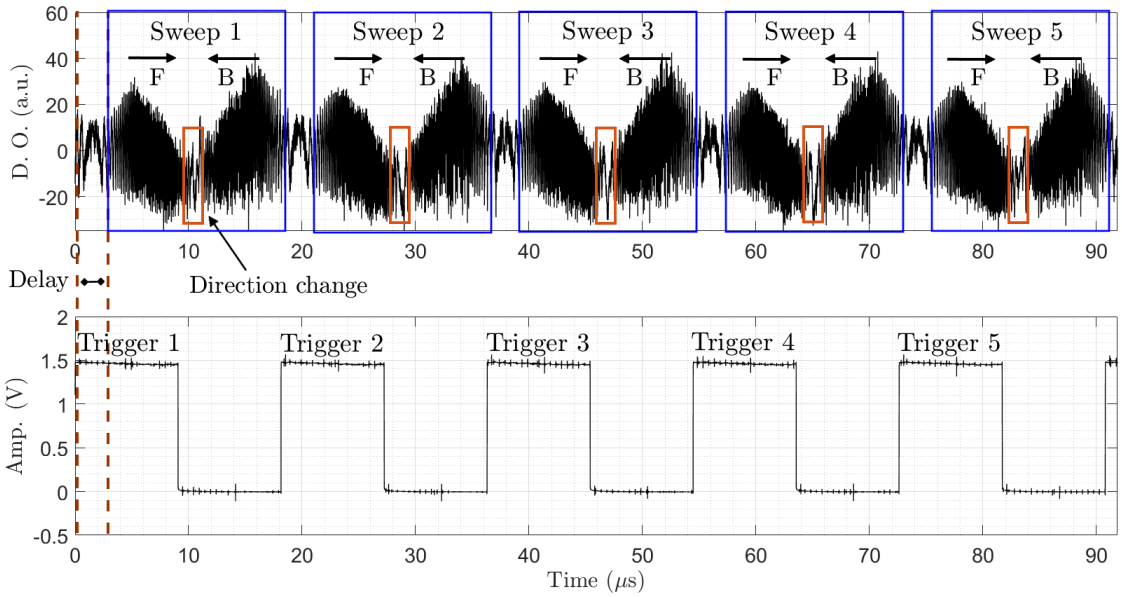

Figure 3.12: Signals registered in the channel 1 (up) and 2 (down) of the GaGe DAQ. Labels: detector output (D. O.), forward (F), backward (B), amplitude (Amp.). Each sweep cycle is in a blue rectangle. We take ten sweep cycles for OCT imaging but we show only five for clarity.

change of direction and must not be used for OCT imaging according to the specifications of the swept source. These segments are cut during this separation step. Then, the background signal is removed from all the sweeps that, once more, it is obtained from averaging all the interferograms (in the respective direction) of the B-scan in order to remove artefacts as in the last section. For the resampling step, the previous recorded and averaged k-clock signal is uploaded to the program and then separated in the forward and backward segments. One calibration vector per sweep direction is generated again by detecting the positions where the signal crosses the zero axis. Next, the resampling is performed with these vectors for each of the ten interferograms in each direction. Finally, the last steps of the diagram in Fig. 3.5 (windowing, FFT^{-1}, magnitude and log) are carried out for all the interferograms and twenty depth profiles (ten forward, ten backward) of the sample in one position are produced. Figures 3.15a and 3.15b show the B-scan for one frame obtained with the sweeps in the forward and backward directions respectively. The minimum value of the colorbar was set at -80 dB and the maximum at -37 dB. The scanning depth is ≈ 250 μm. Notice that the internal layer of the smooth surface is flipped over the zero delay. There is a decrease of signal to noise ratio (SNR) of 4.4 dB in the image produced with the backward sweeps. Figures 3.15c and 3.15d show the images that result from averaging the ten frames in both directions. Table 3.3 presents the values of SNR of each image that were calculated by taking the difference of the highest peak of the A-scan indicated in Fig. 3.15c with a dotted line, and the background noise obtained by averaging the values of the area inside the rectangle. We can see that averaging does not change the SNR significantly but improves the quality of the image. The SNR of one A-scan in the smooth surface of the image obtained with the commercial system without averaging (Fig. 3.13b) was calculated to be 80 dB (highest peak = 120 dB, background noise = 40 dB). There is a difference of SNR of 50.88 dB between this system and ours considering 1 frame of the image with the forward sweeps. This explains the decreased imaging depth and intensity in the images obtained with the Mirau interferometer.

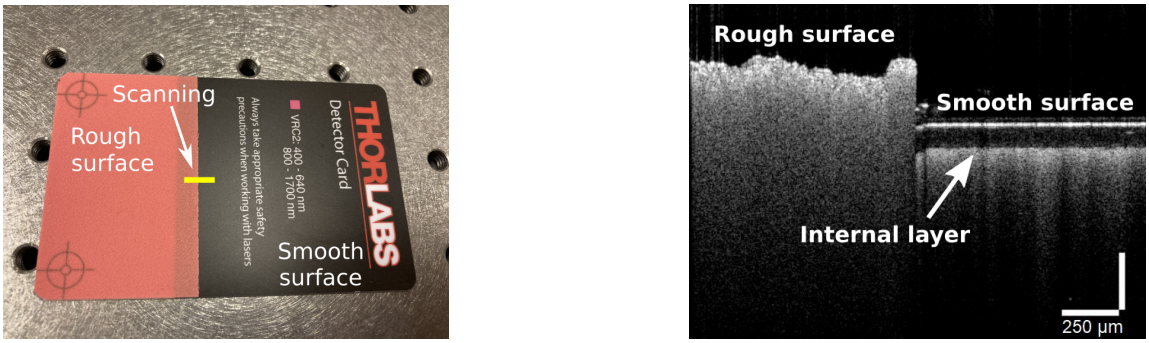

(a) (b)

Figure 3.13: (*a*) Scanned sample. Thorlabs card VRC2. (*b*) OCT image obtained with a commercial system.

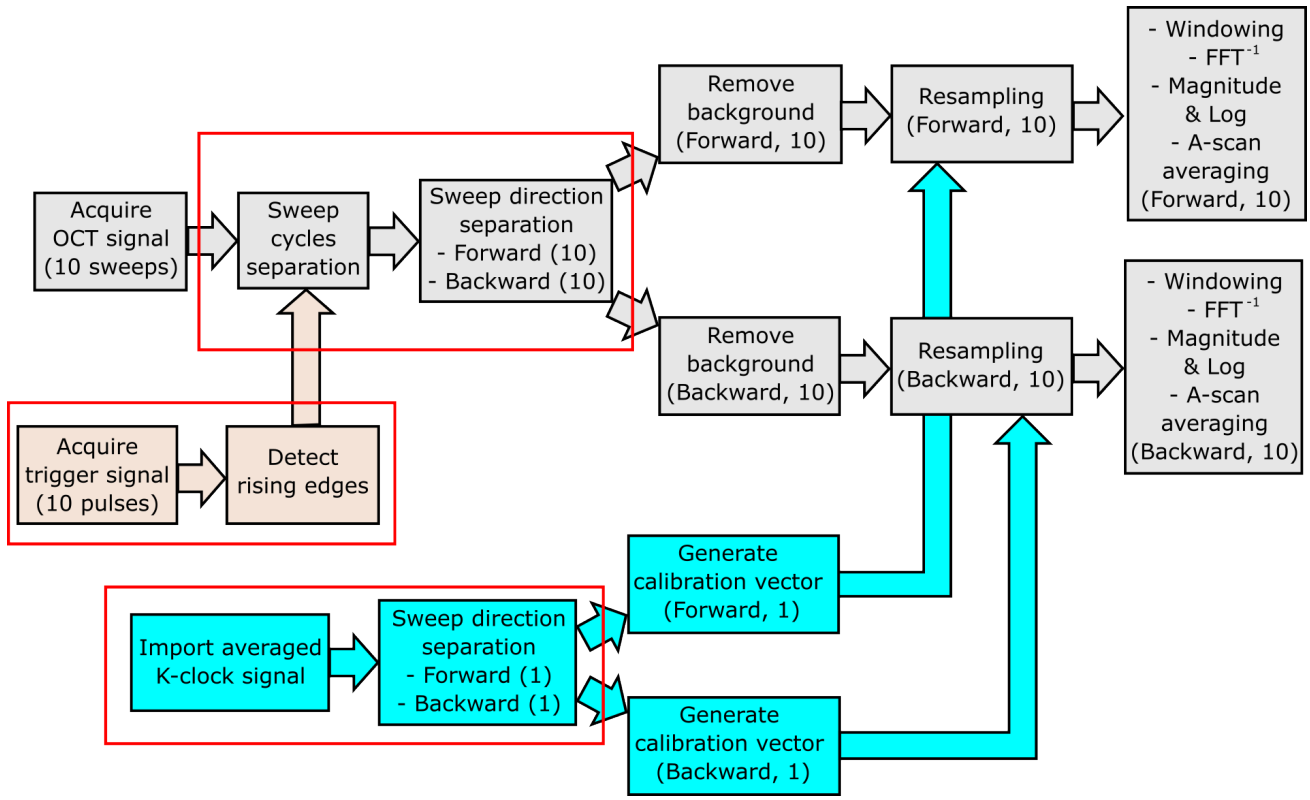

Figure 3.14: Modified algorithm to obtain one A-scan from ten sweep cycles and the trigger signal of the swept source. The steps that we add and modified from the original algorithm (Fig. 3.5) are inside the red rectangles. The numbers in parenthesis indicate the quantity of signals at each step.

Table 3.3: SNR of the images of Fig. 3.15. Label: averaged (av.).

Image	SNR
Forward sweeps (1 frame)	29.12 dB
Backward sweeps (1 frame)	24.7 dB
Forward sweeps (10 frames av.)	29.5 dB
Backward sweeps (10 frames av.)	24.1 dB

Averaging can also be performed before applying FFT as in [132]. The ten sweep cycles can be averaged after the separation (second step in Fig. 3.14) and then the next steps (sweep direction separation, remove background, etc.) are carried out with only one signal. Figures 3.16a and 3.16b show the resulting images obtained with the forward and backward sweeps respectively. The SNR of both images was calculated as before and it increases to 38.29 dB and 33.43 dB, respectively, compared with the images produced with the averaging step after FFT (29.5 dB and 24.1 dB). Finally, Fig. 3.16c shows the B-scan of the sample (averaging before FFT, forward sweeps) when it is moved 200 μm in the z direction towards the zero delay. The part of the image corresponding to the smooth surface flips and the internal layer can be appreciated.

We also scanned banana and onion peels to test the capacity of the micro-interferometer to produce OCT images of biological samples. Figure 3.17a and 3.17b show a B-scan of the banana peel obtained with the commercial and our system performing averaging before FFT and with the forward sweeps (image with the highest SNR) respectively. The scanned distance is 500 μm with a step of 3 μm in both cases. The internal structures of the sample can be seen in both images. Figure 3.17c and 3.17d show the corresponding B-scans for the onion peel. In this case, the internal layers are barely visible in the image produced with our system. The calculated SNR for the images of banana and onion obtained with our system were 37.7 dB and 48.6 dB, respectively. These values were estimated as previously with the indicated A-scans and background noise.

We succeeded in producing OCT images (B-scans and C-scans) with the micro-interferometer by scanning the sample with a motorized stage. For the onion peel, the internal layers could not almost be detected so that our system may not be optimum for imaging this type of biological samples. The next chapter presents the integration of the interferometer with the electrothermal micro-scanner described in section 2.4 and the other components of the probe.

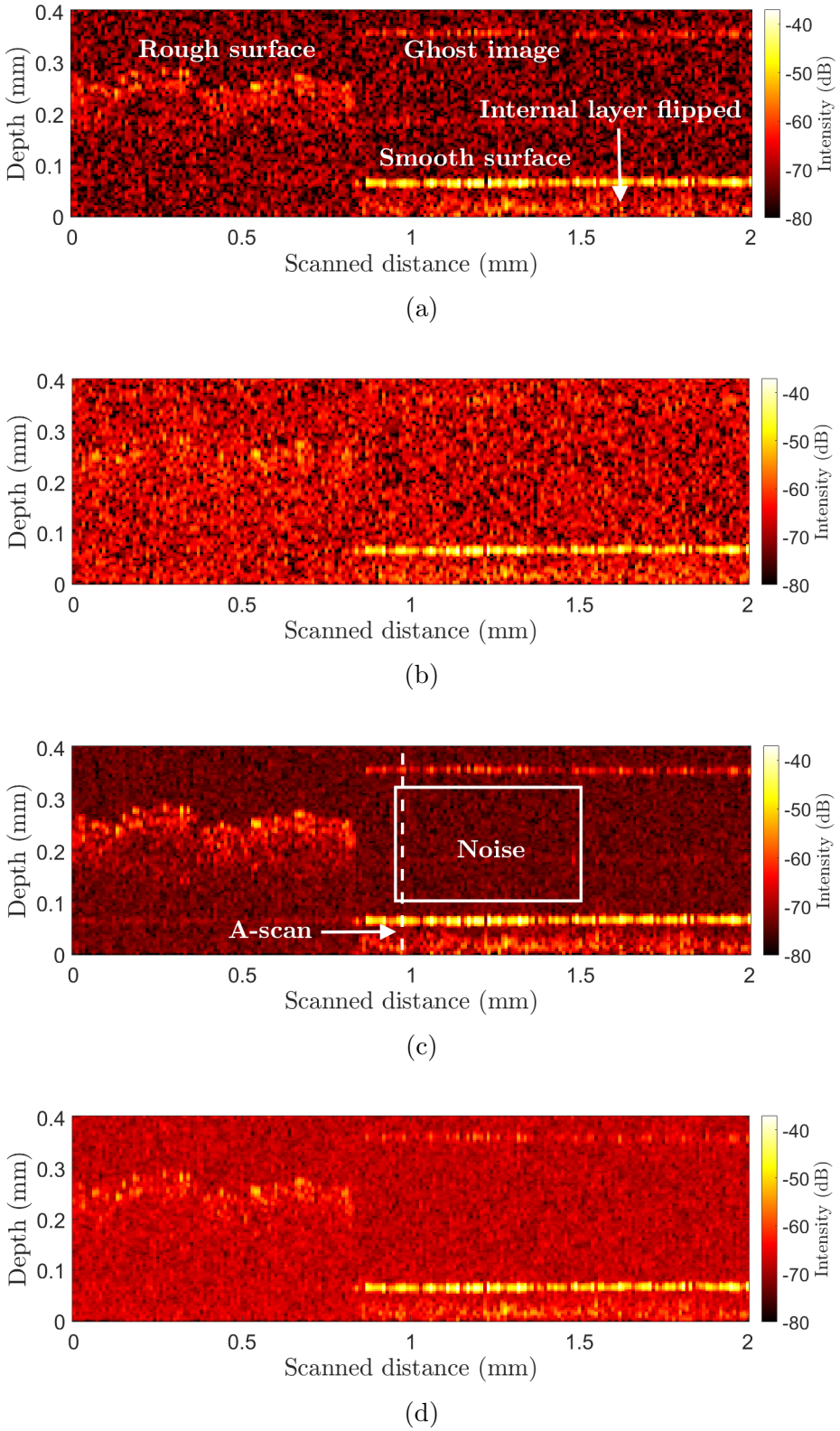

Figure 3.15: OCT images of the Thorlabs card VRC2 obtained with the Mirau micro-interferometer. (*a*) B-scan (1 frame) produced with the forward sweeps. (*b*) B-scan (1 frame) produced with the backward sweeps. (*c*) Ten frames with the forward sweeps averaged. (*d*) Ten frames with the backward sweeps averaged.

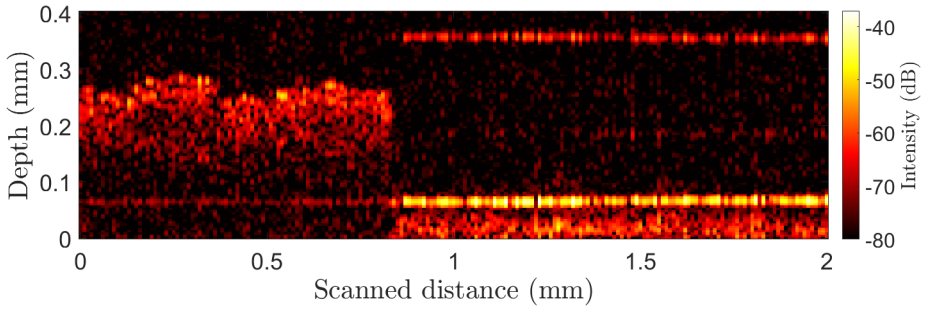

(a)

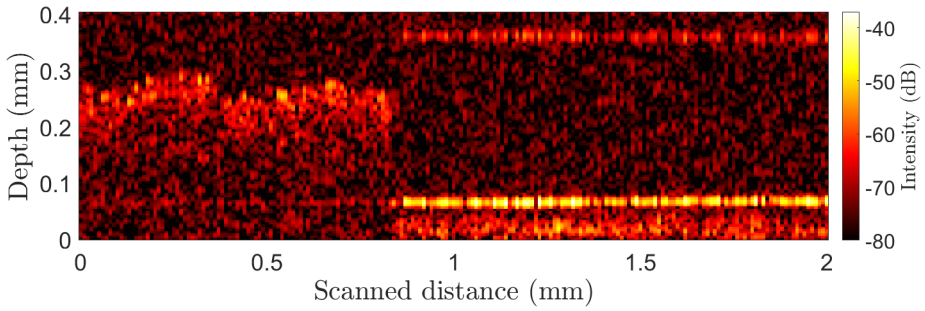

(b)

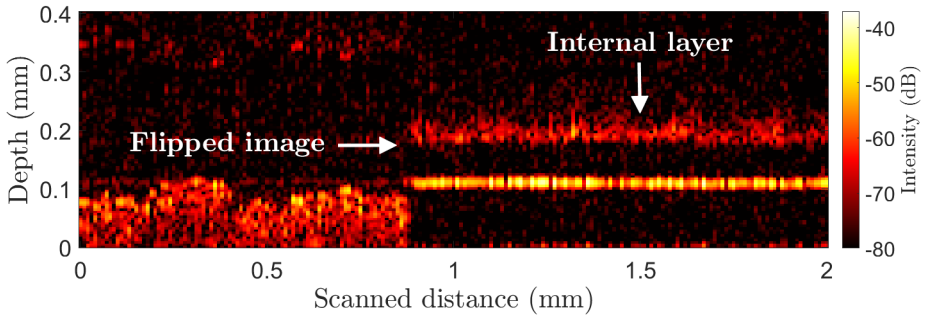

(c)

Figure 3.16: B-scans produced by performing averaging before FFT. (a) Forward sweeps. (b) Backward sweeps. (c) The sample was displaced 200 μm towards the zero delay (forward sweeps).

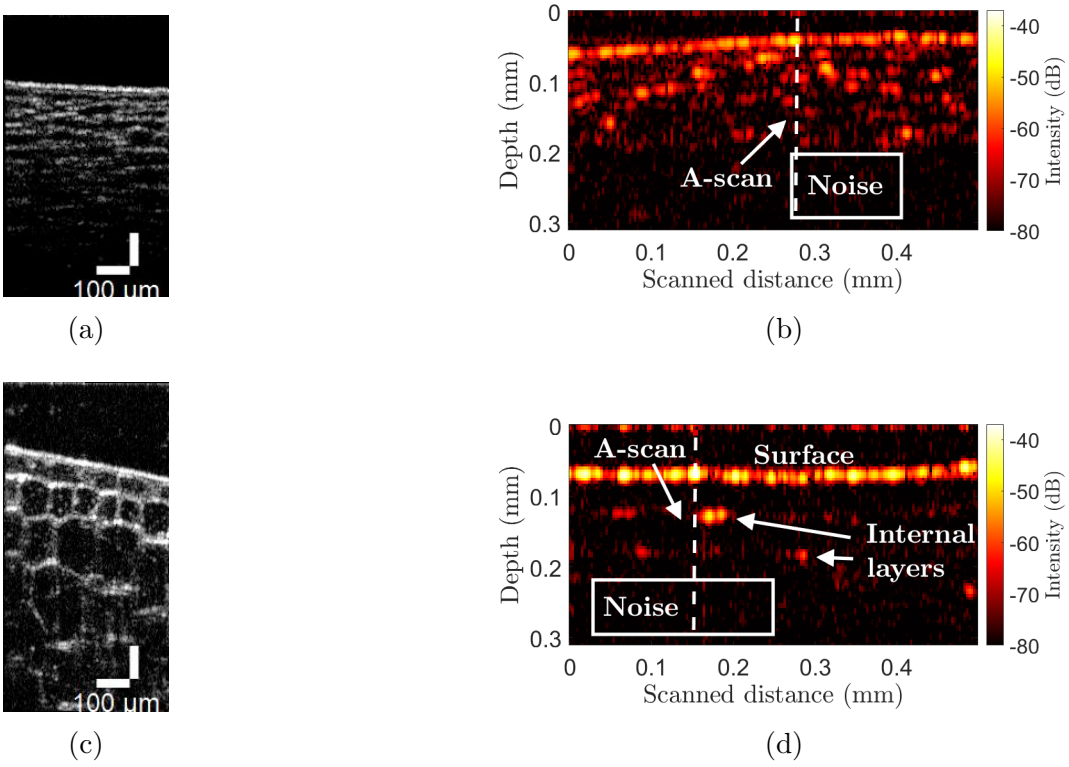

Figure 3.17: B-scan of a banana peel obtained with (a) the commercial and (b) our system. B-scan of an onion peel obtained with (c) the commercial and (d) our system.

3.4 Conclusion

The Mirau micro-interferometer and the SS-OCT setup were described in this chapter. Additionally, the process to obtain the depth profile of the sample in one position (A-scan) from the interference pattern was explained. 2D and 3D OCT images of a sample made of two layers of photoresist, and another made of three layers of tape were presented as well. A dual balanced detector was implemented in the setup to suppress the noise produced by the intensity fluctuations of the swept source. With this new setup configuration, we scanned a card with a diffusive rough and a reflective smooth surface taking ten sweep cycles of the laser to perform averaging. We found a scanning depth of ≈ 250 μm. There is a decrease of SNR of 4.4 dB in the images produced with the backward sweeps. Besides, averaging ten images do not change the SNR significantly but improves the quality of the image. Images of biological samples namely peels of banana and onion were also presented. For the onion peel, the internal layers could not almost be detected so that our system may not be optimum for imaging this type of biological samples. The next chapter presents the integration of the interferometer with the electrothermal micro-scanner described in section 2.4 and the other components of the probe.

4

Fabrication of the OCT probe with the 2-axis electrothermal micro-scanner

This chapter describes the fabrication process of the probe based on a micro-assembly and local adhesive bonding of its four building blocks: GRIN lens collimator, Mirau micro-interferometer, electrothermal micro-scanner and a flexible PCB. The complete procedure consists of five main steps and involves an active optical alignment between the micro-interferometer and the collimator as well as an electrical interconnection of the scanner with a flexible PCB.

4.1 Integration concept

The general integration concept, employed in this work, was imposed by the fact that the main building blocks of the probe were fabricated individually and delivered, at the current state of development, on the chip level. In those circumstances, the micro-assembly has been chosen as a convenient and natural approach for the fabrication of the probe where the individual components are aligned vertically along the optical axis and adhesive bonded according to the developed sequential bonding procedure [148]. Figure 4.1 presents schematically this integration concept.

Several general assumptions were made concerning the adhesive bonding:

- All adhesive bonding processes will be made at room temperature (no heating) to preserve the crucial alignment between the Mirau micro-interferometer and the GRIN lens collimator.
- Thermally conductive epoxy glue will be employed for bonding of the electro-thermal scanner chip on the Mirau interferometer. The goal is to help in heat dissipation (just in case) from the scanner towards the bulky Mirau.
- Electrically conductive epoxy glue will be used to form bumps on the scanner contact pads that are used in the subsequent adhesive bonding of the flexible PCB.

Most of the assembly steps were performed in a cleanroom environment using a chip-bonder tool HB70 (TPT, Germany), providing semi-automatic pick&place operations on small objects (i.e. microscanner chip, flexible PCB). The HB70 tool ensures basic alignment capability in three axis (in XY for the stage and in Z for the pick&place tool) and optical inspection with a high-resolution integrated camera. In the frame of this work, the machine has been equipped with additional components according to the specific requirements of each assembly step, e.g. home-made multi-axis micromanipulation stage, electrically-heated vacuum stage, optical microscope for

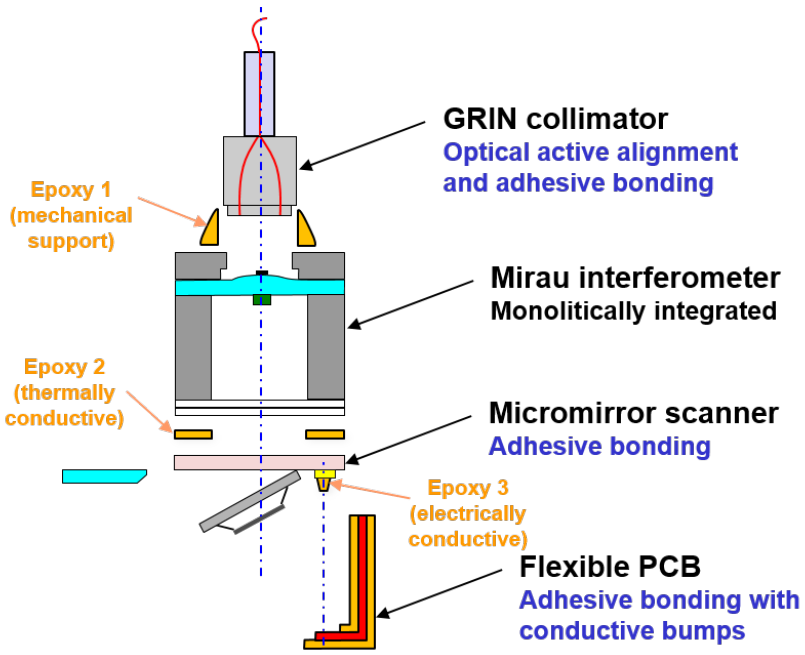

Figure 4.1: Schematic presentation of the integration concept of the probe.

side observation (Nikon SMZ 645). Different adaptations of the basic assembly setup (Fig. 4.2) will be presented in the following subsections.

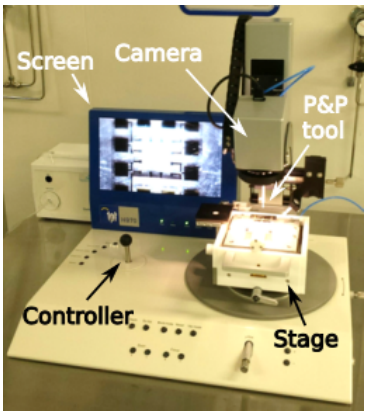

(a)

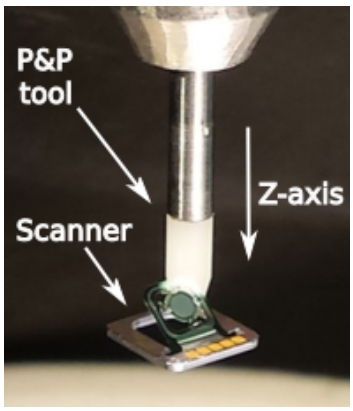

(b)

Figure 4.2: (*a*) Chip bonder machine HB70 (TPT, Germany). (*b*) Pick and place (P&P) capillary tool holding the scanner.

4.2 Steps of the assembly process

4.2.1 Assembly of the micro-interferometer with the GRIN lens collimator

In this subsection, the alignment procedure between the GRIN lens collimator and the Mirau interferometer as well as the posterior adhesive bonding are presented. The alignment is challenging

since the input light beam must hit the reference mirror of only 150 μm of diameter after reflection from the beam splitter. For this first task, we use the first version of the SS-OCT system (Fig. 3.3) without the dual balanced detector since we need to observe the signal of the intensity profile of the swept source without attenuation (Fig. 3.4a). The alignment procedure is as follows 4.3:

1. The light beam is directed to point towards the Si base of the interferometer. For this step, an infrared card is used to see where the beam is pointing when we move the GRIN collimator that is placed on a X,Y,Z translation stage. Once the light beam is in place, we tilt the holder of the interferometer in the yaw and pitch axis until getting the signal of intensity from the photodetector measured using a digital oscilloscope (Fig. 3.4a). This signal is detected only if the surface of the Si base reflects the light beam straight back towards the GRIN collimator meaning that both components have been properly aligned.

2. The GRIN lens is moved up (y-axis) towards the position of the reference mirror using a XYZ translation stage. Since the light beam is not reflected back anymore by the Si base, the signal disappears.

3. The GRIN lens is moved in the y and x directions until getting the signal again. This means that the light beam has been reflected back by the beam splitter and reached the reference mirror. The intensity of this signal is lower than when the light beam is reflected by the Si base. This is how we can know that the light beam was not carried there again.

4. Once the GRIN lens and the interferometer are aligned, the GRIN lens is gently insterted into the dedicated Si base port as shown in Fig. 4.4, checking that the signal does not change. Inspection optical microscope allows to observe that there is no any damage of the GRIN head or the Si port. A two-component epoxy glue (Poxypol) is applied manually around the GRIN/base interface and left for a few hours to be cured at the room temperature. Finally, the signal is checked again to confirm that the position of the GRIN lens has not been changed.

4.2.2 Correction of the angle of the scanner

The next step would be the integration of the scanner with the already assembled block of interferometer/GRIN. However, it has been found that the real tilt angle of the scanner frame is only 33° (Fig. 4.5a), much smaller than the desired value $\approx 45°$. This discrepancy is a result of a fabrication process, most probably due to small error in the design of the mechanical stopper or too small residual stresses in the parallel bimorphs array of the scanners. In this case, the light beam reflected by the mirror would be directed towards the surface of the probe itself instead of towards the sample (Fig. 4.5b). This problem may be solved in the next generation of scanners by an improved design of the stopper mechanism.

A temporary solution, proposed in this work, is based on a mechanical correction of the tilt angle by an adapted piece of glass, referred here as “angle corrector”. This component has to be placed on the surface of the silicon base of the scanner to push the frame and increase its angle. The angle corrector was designed with the exact measures to define the frame angle at $\approx 45°$ without any contact with the parallel bimorph array and without blocking the optical path (Fig. 4.6).

The angle corrector was fabricated in a Fused Silica (FS) substrate by a femtosecond laser-assisted wet etching (FLAE) method using a f100 aHead Enhanced machine (FEMTOprint, Switzerland) that is available at MIMENTO. The irradiation of the FS by the use of focused femtosecond

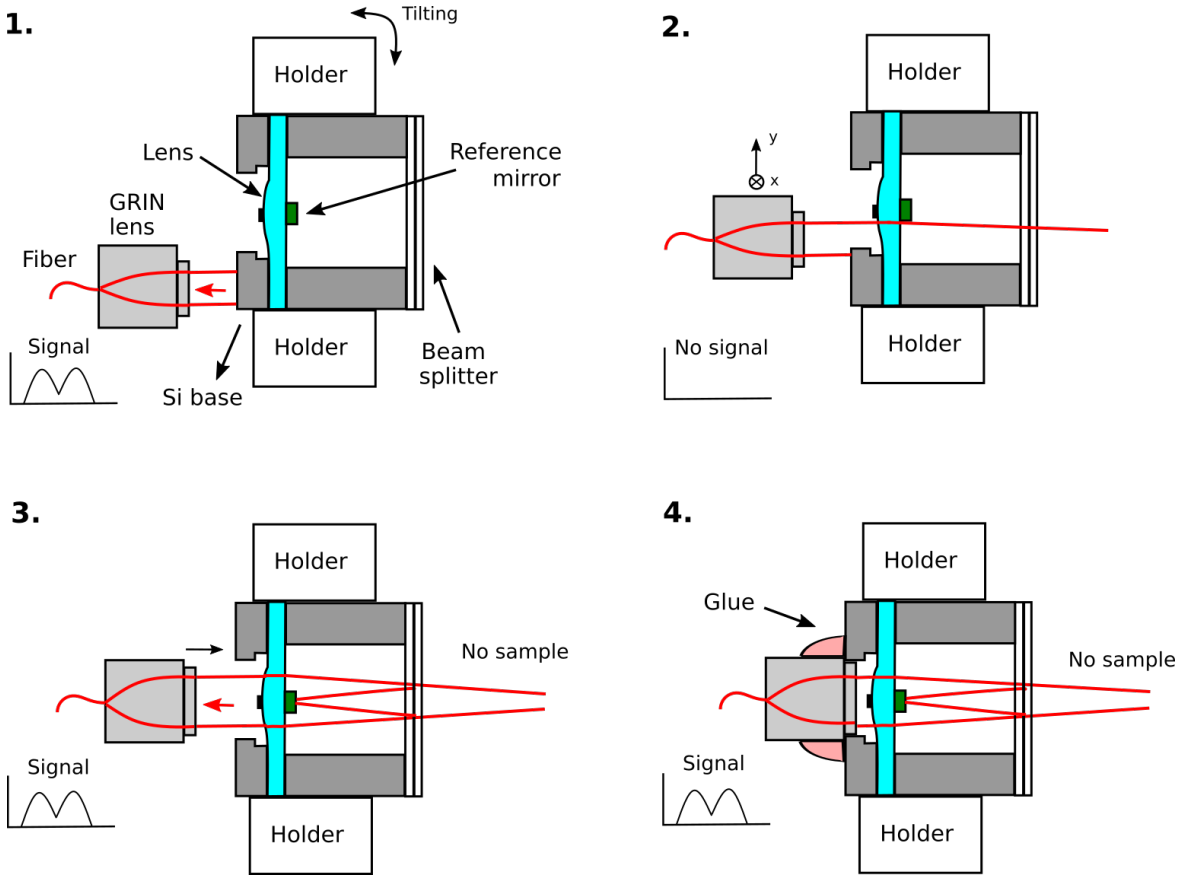

Figure 4.3: GRIN lens active alignment process.

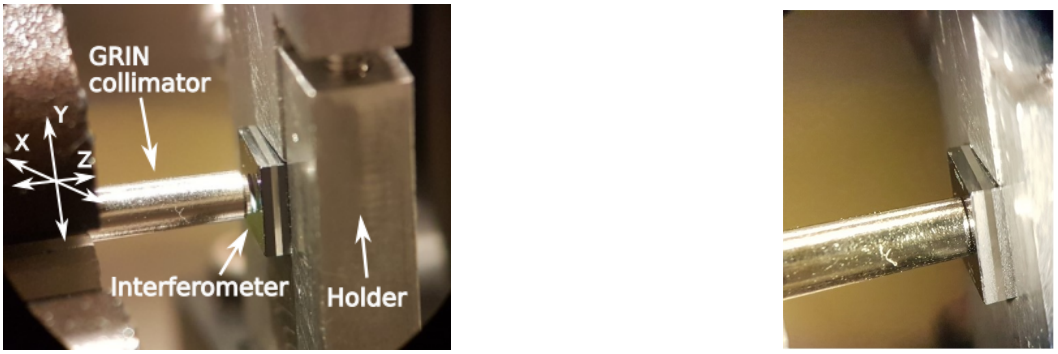

(a) (b)

Figure 4.4: GRIN lens collimator (a) aligned and (b) inserted into the Mirau micro-interferometer.

pulses with extremely high peak intensities (but below the ablation threshold) leads to a permanent modification of the FS in a very localized zone. The irradiation parameters are precisely tuned to achieve a significant increasing of the etch rate of the irradiated silica in wet etchants (e.g. HF, potassium hydroxide (KOH)) when compared to the etch rate of a non-irradiated material. The typical selectivity of etching is > 50 for HF and > 200 for KOH.

The fabrication process of the angle corrector included three main steps. First, a laser irradiation process was programmed in 3D in a dedicated software (Alphacam) that resulted in the generation of a machining code. Next, a 500-μm-thick 20 x 26mm^2 FS substrate was scanned

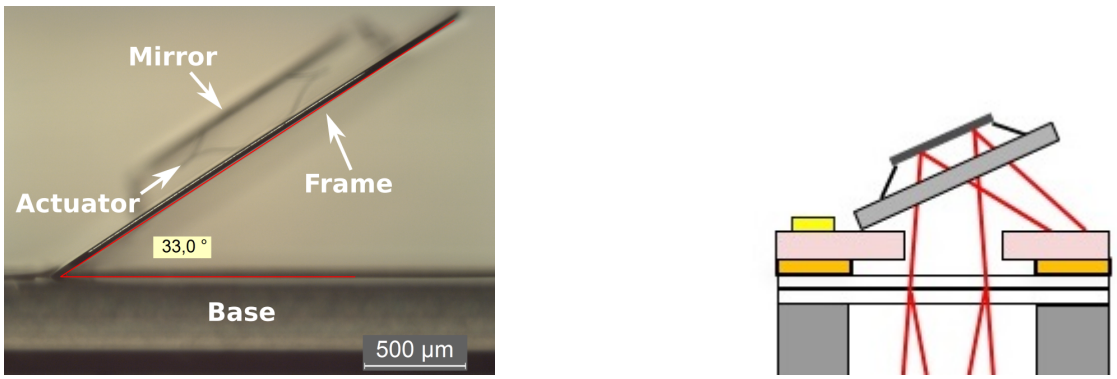

(a) (b)

Figure 4.5: (*a*) Lateral view of the scanner showing an angle of 33° between the frame of the scanner and the substrate. (*b*) Impact of the lower angle on the propagation of the beam.

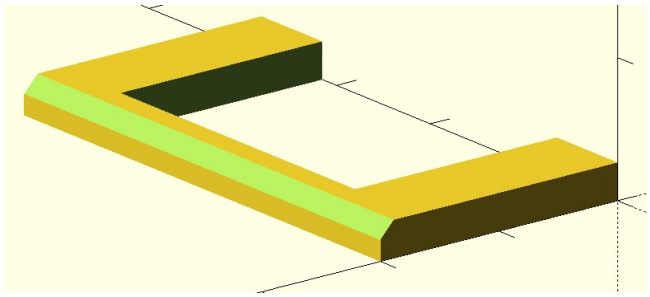

(a)

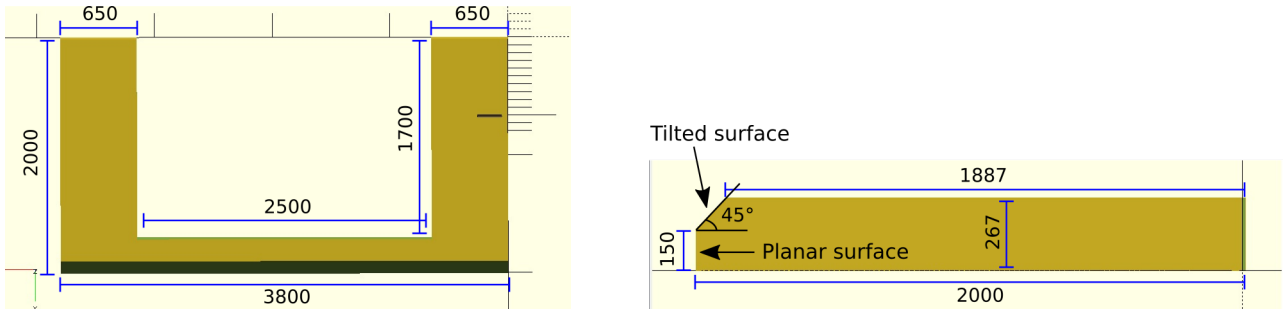

(b) (c)

Figure 4.6: (*a*) Design of the angle corrector made in OpenSCAD. (*b*) Top view (*c*) Lateral view. The units are in micrometers.

by the focused laser beam, according to the generated code, and the material was exposed to low-energy femtosecond pulses that accelerated locally the etching rate. Only very thin contours (2 - 2.5 μm wide) of the structure were exposed by the laser through the whole substrate thickness in sequential order (point by point). In the final step, the exposed silica was etched in a 10M KOH solution at 80°C during 16 hours resulting in the releasing of the corrector structure. Ultrasonic vibrations were generated periodically during the etching to enhance the penetration of KOH through this high aspect ratio structure and to stabilize the etching rate.

An 3 x 2 array of angle correctors could be fabricated in one process as shown in Fig. 4.7a. Small bridges were added to the design (Fig. 4.7b) in order to keep the correctors atached to the substrate during the KOH etching and the posterior rinsing and drying operations. Since

the corrector structure is too fragile to be detached from the substrate manually, e,g. with a tweezer, a programmable semi-automatic bondtester tool (Nordson DAGE 4000+) was used for this operation, working in the Shear Test configuration. The substrate was fixed on the motorized stage of the machine, as shown in Fig. 4.7c, and then, pushed slowly towards a immmobile shear blade tool (SHEAR-187-150: diameter = 4.75 mm, width = 3.81 mm) until breaking the bridges on both sides. The structure fell down and could be retreived it. Figures 4.7d shows a scanning electron microscope (SEM) image of one released component. The tilted and planar surfaces are shown in Fig. 4.7e and Fig. 4.7f.

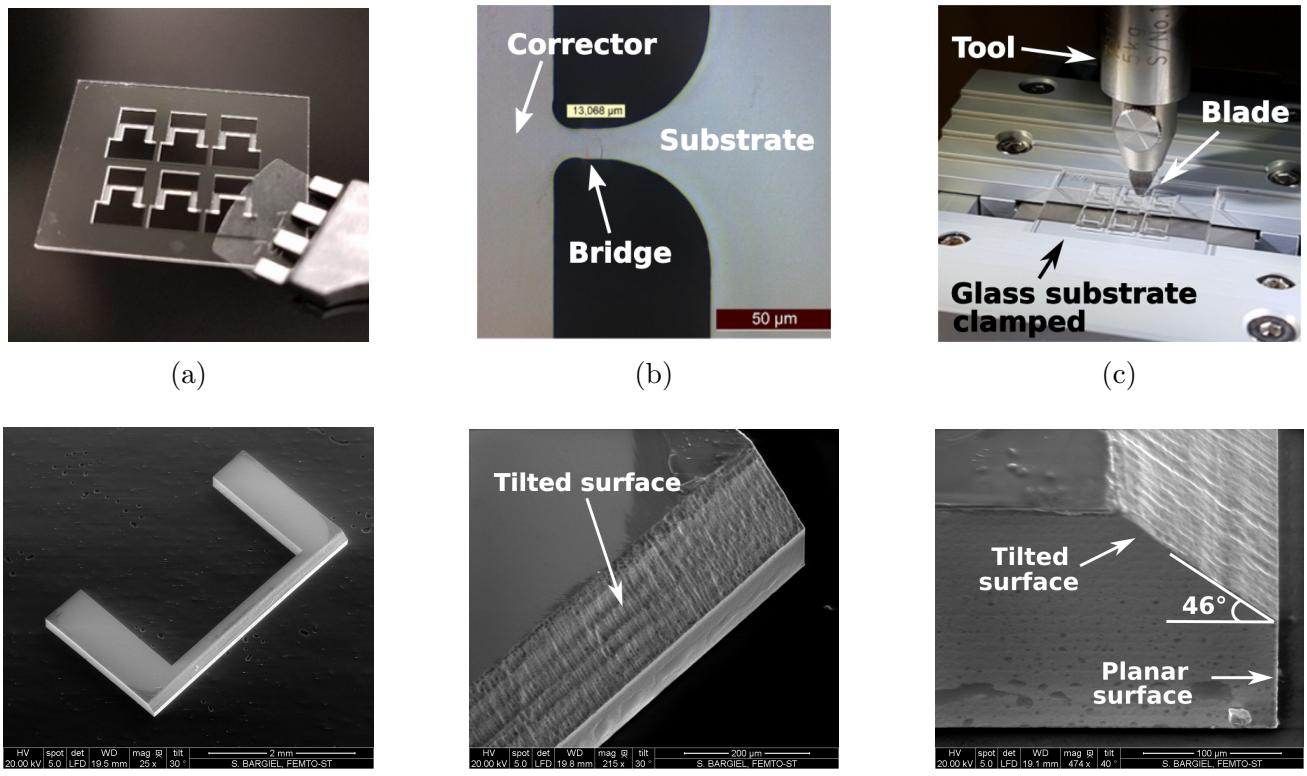

(a) (b) (c)

(d) (e) (f)

Figure 4.7: (*a*) Array of angle correctors after KOH etching. (*b*) Bridges joining the corrector to the substrate (thickness = 13 μm). (*c*) Release of one piece by pushing with a shear blade. (*d*) SEM image of one angle corrector. (*e*) Zoom on the tilted surface. (*f*) Lateral view.

The angle corrector was assembled on the scanner using the chip-bonder HB70 already introduced in section 4.1. The standard configuration of this machine was adapted specially for this task. The P&P tool moves in the z direction and the stage in the x and y directions (by the controller), giving three degrees of freedom. The chip bonder also has a high resolution camera that allows to observe precisely the manipulation of the micro components on the screen.

Besides positioning the angle corrector on the substrate of the scanner, it must also be pushed until making contact with the frame as shown in the diagram of Fig 4.8a. A blade is necessary to push it uniformly and also a piece of metal plate (or something else with linear shape) must be set behind the scanner to block its backward movement. Figure 4.8b shows the adapted setup mounted on the stage of the chip-bonder machine to place and push the angle corrector. The blade is attached to a X,Y,Z translation stage by a holder and the scanner is put on a rotatory mini-stage that allows to align it with the corrector. This component is placed on the substrate of the scanner using the P&P tool (H80-500, tip: 500 μm, hole 200 μm) and the camera of the

chip-bonder machine that is set in front of the setup. A stereomicroscope with long working distance was also installed in the setup to increase the range of observation as well as to provide side viewing.

Once the angle corrector is in the scanner (Fig. 4.8c), it is pushed with the blade using the X,Y,Z translation stage until making contact with the frame and then until increasing the angle to 46°. During this precise operation, the camera is set laterally to obtain a side-view of the scanner. A transparent sheet with the draw of two lines at an angle of 46° is attached on the screen of the chip-bonder machine as a visual reference (Fig 4.8d). In this way, the angle increasing can be performed with higher precision. Finally, a liquid instant glue (Loctite, Super Glue-3) dedicated for glass is applied on the back of the angle corrector (both sides) to maintain the angle. The application of the glue is made with a stamping system of the P&P tool using a needle (32G, DO/DI370/100) as shown in Fig. 4.8e. The glue penetrates easily under the corrector due to its low viscocity.

4.2.3 Assembly of the micro-scanner with the micro-interferometer

After the angle correction, the scanner is adhesive bonded to the block interferometer/collimator. For this purpose, a thin layer of thermally-conductive epoxy paste is formed on the beam splitter surface (BSP) by use of a simplified screen-printing method. The central part of the BSP cannot be covered, otherwise, the input light beam would be blocked. To protect this part, a mask of teflon adhesive tape is adhesive bonded on the BSP to let uncovered only a frame of the size of the scanner (4x4 mm) as shown in Fig. 4.9a. A small portion of silver-based adhesive paste (EPOTEC EJ2189-LV, mixing ration A:B /10:1) is applied on the mask, and then it is displaced and flattened with a blade. Then, the mask is retired and the frame of paste is printed on the BSP (Fig. 4.9b).

Once the layer of paste is ready, the block interferometer/collimator is installed vertically on the stage of the chip bonder machine to be bonded with the scanner. This last component is taken by the substrate with the P&P tool as shown in Fig. 4.2b and placed over the BSP without making contact. Then, the center of the mirror of the scanner is aligned with the optical axis of the interferometer moving it with the controller of the machine (stage displacement in the x and y axes). Once aligned, the scanner is brought down with the P&P tool (dsiplacement in the z-axis) until making contact with the frame of glue (Fig. 4.9c). Pressure is applied on several points of the substrate of the scanner using the P&P tool in order to uniformize the gluing. Finally, the glue is left to cure during 3 days (time recommended in the product specifications).

4.2.4 Assembly of the flexible PCB

It is necessary to apply electrical signals to the scanner pads to drive the actuators. For this purpose, a flexible printed circuit board (PCB) (shown in Fig 4.10a) is adhesive bonded to the pads and after connected with an external circuit. This PCB is composed of two layers of Kapton with five 200 μm-wide copper lines in between. The tip must be bent at 90° in order to bond this part with the pads and the rest of the planar shape must be extended along the interferometer as shown in the diagram of Fig 4.10b. To achieve this, the flexible PCB is placed on a glass plate and fixed with Teflon tape (Fig 4.10c). Then, a second glass plate is put over the PCB slightly down to define the edge of bending. Finally, the tip is bent using a blade until reaching an angle of 90° as shown in Fig 4.10d. All these manipulations are performed manually under a microscope.

The next step is to deposit small dots of electrically-conductive silver-based glue (EPOTEC EJ2189-LV, mixing ration A:B /10:1) on the pads of the scanner. The integrated probe is placed

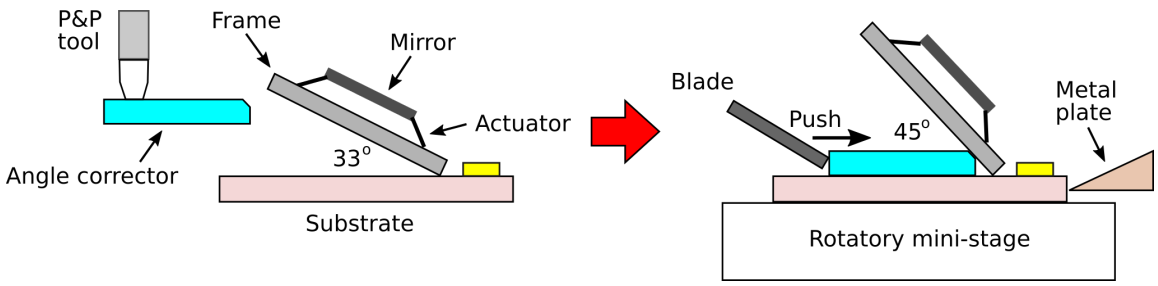

(a)

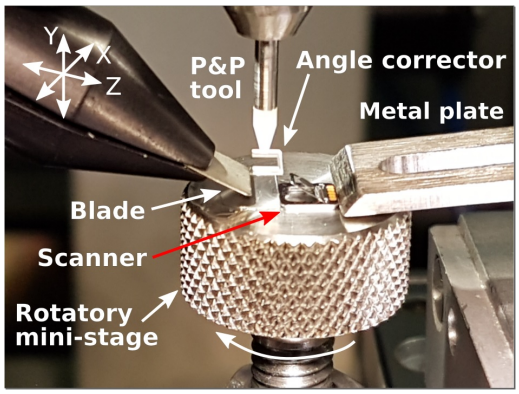

(b)

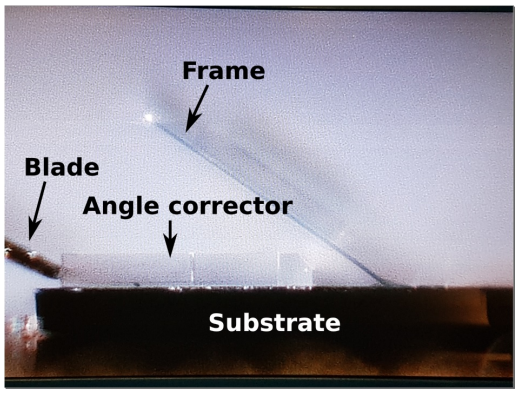

(c)

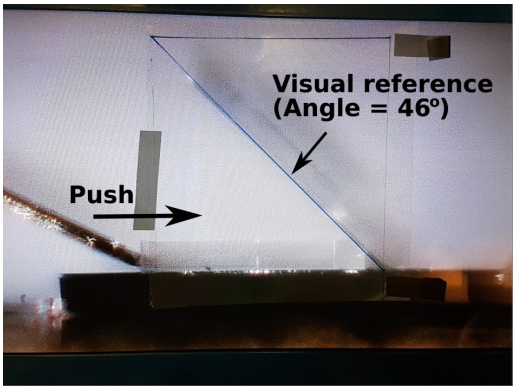

(d)

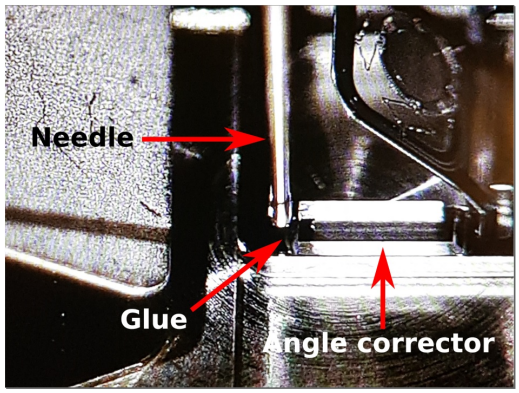

(e)

Figure 4.8: (*a*) Principle of the angle adjustment with the glass corrector using the P&P tool. (*b*) Setup mounted on the stage of the chip bonder machine. (*c*) Angle corrector placed on the substrate. (*d*) Reference lines at 46°. (*e*) Glue is applied on the backside of the angle corrector using a needle.

vertically in the aluminium holder (Fig 4.11a) that is also set in the chip bonder machine. A stamping capillary is installed in the P&P tool to deposit the glue on the pads with enough precision. The capillary is immersed in the paste (Fig. 4.11b) and then it is brought in contact with the pad. After, it is removed slowly to form a conical bump of glue as shown in Fig 4.11c. The same process is repeated for the five pads.

The bent flexible PCB can now be bonded on the pads of the scanner. For this last step of integration, a vacuum stage is placed on the stage of the chip bonder machine. The assembled probe (scanner, interferometer, GRIN lens) is placed and fixed horizontally on the vacuum port of the stage with the pads directed upwards as shown in Fig. 4.12a. Then, the P&P tool is used to

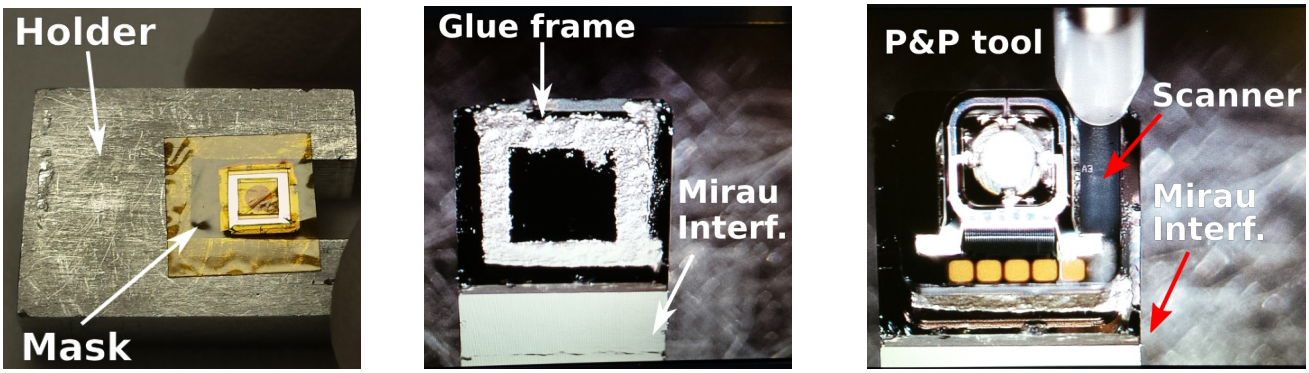

(a) (b) (c)

Figure 4.9: (*a*) Mask of Teflon tape on the BSP of the inteferometer. The block interferometer/collimator is kept vertical using an aluminium holder. (*b*) Frame of glue on the BSP. (*c*) Scanner placed on the interferometer with the P&P tool.

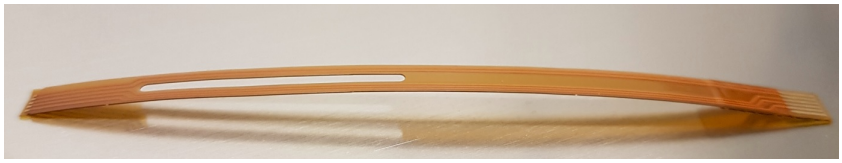

(a)

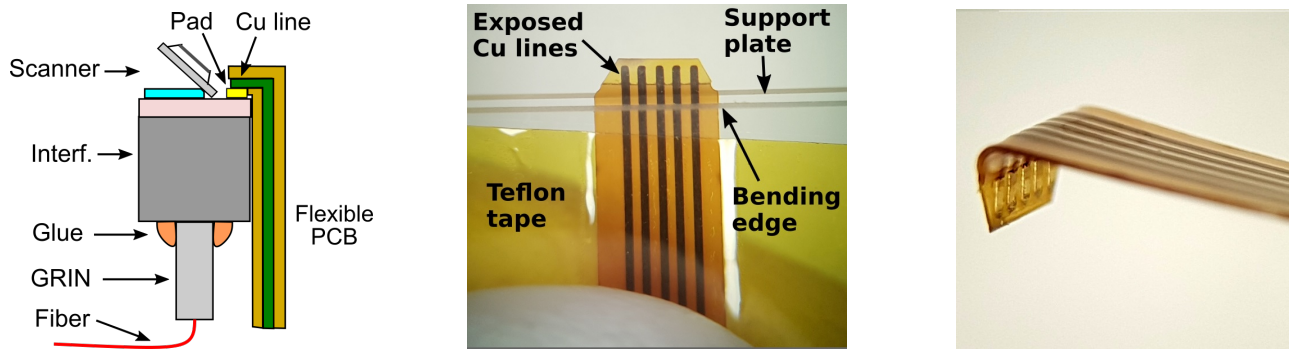

(b) (c) (d)

Figure 4.10: (*a*) Flexible PCB. (*b*) Diagram of the integration of the PCB on the pads of the scanner. (*c*) The PCB is placed between two glass plates for bending. (*d*) PCB bent at 90°.

bring the flexible PCB over the probe. For this handling, the biggest available capillary (H80-1016, tip 1016 μm, hole 508 μm, plastic tip) was coupled in the P&P tool and a flexible mini-suction pad was installed on its tip in order to lift the relative big PCB. The bent tip of the flexible PCB is placed very close (and aligned) to the electrical pads (Fig. 4.12b) and then, the probe is approached slowly moving the stage of the bonder machine until the glue on the pads make contact with the exposed Cu lines of the PCB. After, a blade is used (placed in a XYZ translation stage) to apply a small force in this connection (Fig. 4.12c). A blocking glass plate is placed behind the interferometer to avoid the backward movement of the probe when the force of the blade is applied. During the contact, the low-viscous adhesive bumps are slightly squeezed that is clearly visible through the semi-transparent PCB. Since now, the force must be carefully controlled to avoid an excessive increasing of the bumps diameter, and hence, a short circuit. The force can be

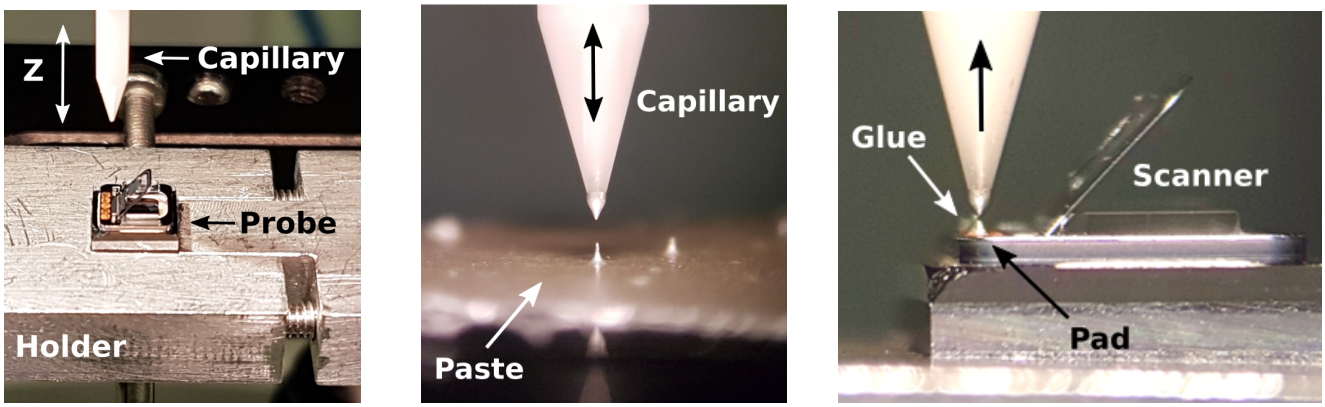

(a) (b) (c)

Figure 4.11: (*a*) Setup to deposit epoxy bumps on the pads. (*b*) The capillary is immersed in the silver paste. (*c*) Deposition of the glue on the pads.

removed after 1 day of curing at room temperature (full curing is achieved after $\approx$ 2 - 3 days).

The bonded interface is relatively week and it would not survive the pulling or bending of the PCB under normal operation of the probe. Therefore, liquid single-component instant glue (Loctite, Universal Super Glue) is applied on one part of the PCB with a needle to fix it to the interferometer and reinforce the bonding (Fig. 4.12d). All these manipulations are performed precisely using the camera of the chip bonder machine (top view) and a stereoscopic optical microscope (Nikon SMZ645, zoom range 0.8x-5.0x, total magnification 8x – 50x) (lateral view). Figure 4.13 shows the fully integrated OCT probe.

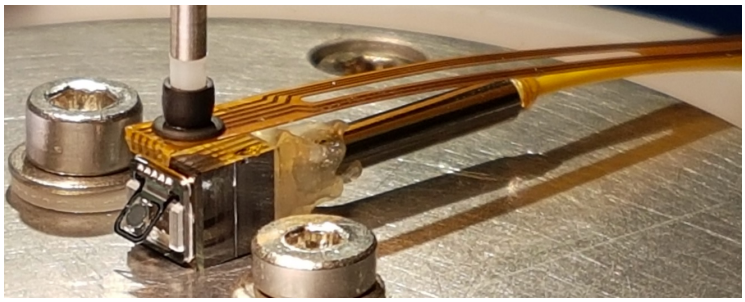

(a)

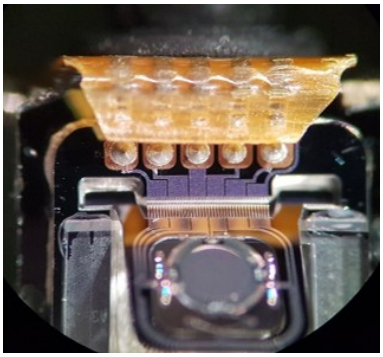

(b)

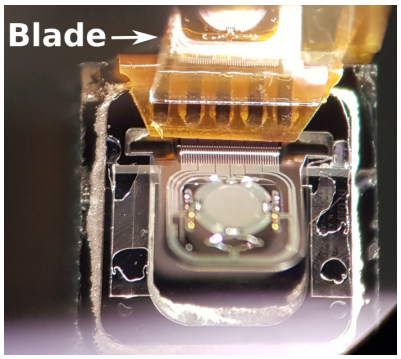

(c)

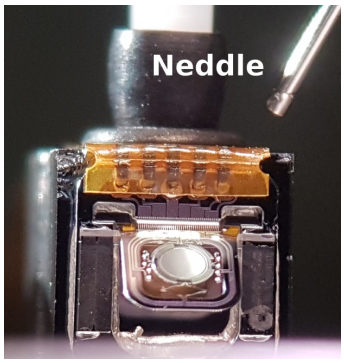

(d)

Figure 4.12: Assemby of the flexible PCB. (*a*) Positioning of the PCB over the vacuum Mirau/Scanner/GRIN. (*b*) Flexible PCB placed close to the pads. (*c*) A small force is applied on the PCB with a blade. (*d*) The flexible PCB is also glued to the interferometer to reinforce the bonding.

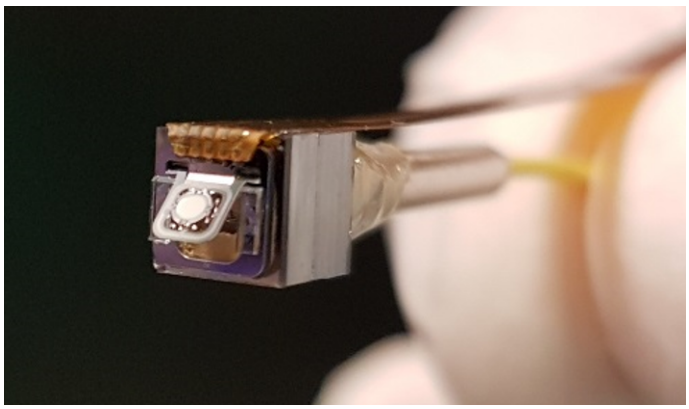

Figure 4.13: Fully integrated OCT probe.

4.3 Conclusion

All the components of the probe were successfully integrated. The angle of the frame of the micro scanner could be corrected by the fabrication and integration of an adapted piece of glass. The fully integrated probe is connected to the SS-OCT setup to perform imaging by scanning the sample with the micro scanner. This is detailed in the next chapter.

5 Performance analysis of the integrated OCT probe and 3D imaging

In this final chapter, the final SS-OCT setup that includes the components to drive the micro scanner is described. Besides, the frequency response of the scanner and the Lissajous pattern that we use to scan the samples are presented. This pattern is used for real-time imaging at low voltages in comparison with spiral scanning that is not adequate for MOEMS scanners and raster scanning that requires higher voltages for the slow axis and presents lower mechanical stability and scanning rates [16]. At the end, 3D OCT images obtained with the fully integrated probe are shown.

5.1 System for scanning characterization, control and SS-OCT imaging

Figure 5.1a presents the final version of the SS-OCT system with the correspondent components for imaging and scanning characterization. The fully integrated probe is connected to the SS-OCT system with the dual balance detector (Fig. 3.11a) described in section 3.3. A diagram of the MOEMS probe is shown in Fig. 5.1b where we can see that the scanner reflects the light beam out towards the sample. As already explained in section 2.2, the scanning in one direction (B-scan) is performed by driving two opposite actuators (A2 and A4 in the diagram) while the scanning in depth (A-scans) is carried out by the swept source [149], [150].

Regarding the control of the scanner, four sinusoidal signals (one per actuator) are generated by the computer and sent to the probe by a National instruments (NI) DAQ card (USB-6259). The resistances measured for each actuator were R1 = 418 Ω, R2 = 372 Ω, R3 = 407 Ω and R4 = 415 Ω (for A1 to A4 respectively, see Fig. 5.3). Previous tests in other scanners from the same batch showed that the actuators are damaged at driving voltages higher than 5 V. The voltage in each actuator is limited at 3.5 V to avoid damaging them, therefore, each actuator demands a current of I1 = 7.1 mA, I2 = 8 mA, I3 = 7.3 mA and I4 = 7.2 mA respectively. The maximum current provided by the output channels of the NI-DAQ card is 5 mA, therefore, a power circuit composed of four operational amplifiers (two integrated circuits LM358P, Texas Instruments) in the follower configuration (one per actuator) was built and it is connected to an external power supply (Aim TTi Pl PL303-P) at 10 V and 50 mA. In this way, each amplifier takes the signal from the NI-DAQ and transmits it to the correspondent actuator but with sufficient current taken from the power supply. To make the connection between the power circuit and the flexible PCB, the small PCB of

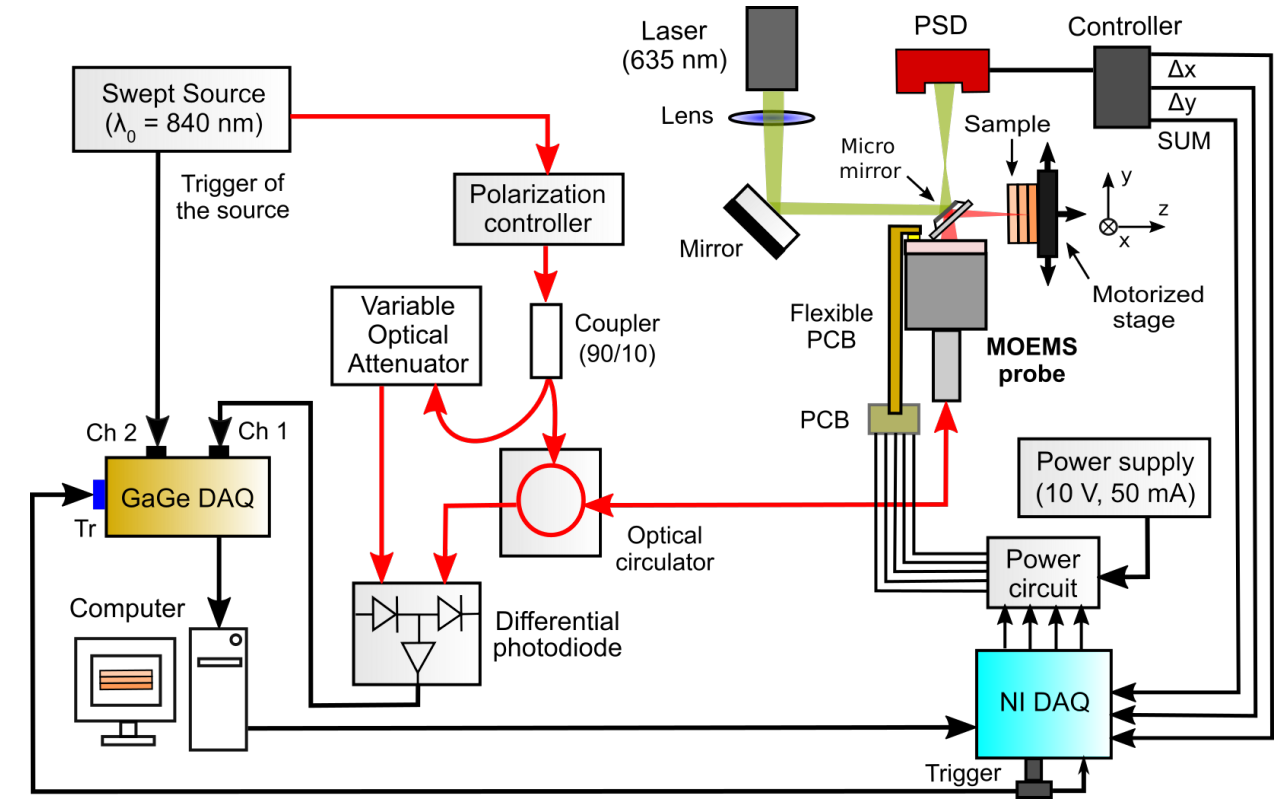

(a)

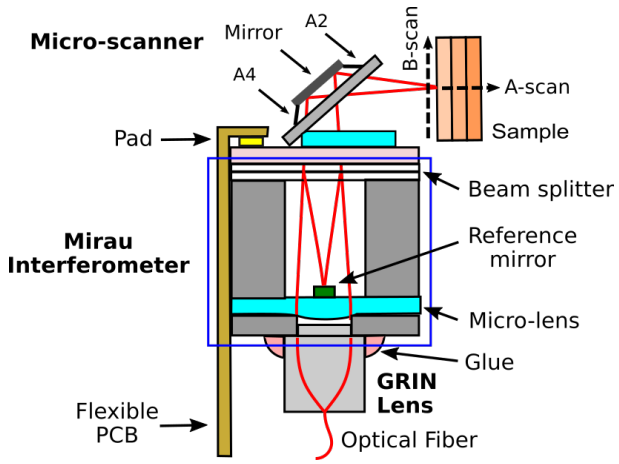

(b)

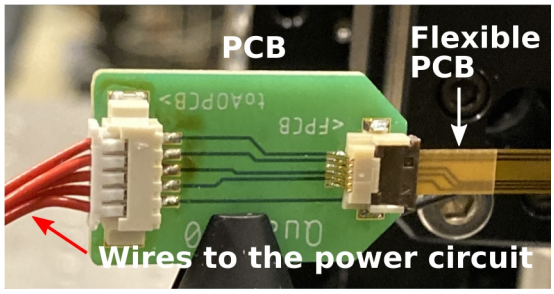

(c)

Figure 5.1: (a) Final version of the SS-OCT system with the components to drive the scanner (NI DAQ, power circuit and power supply) and a position sensing detector (PSD) to monitor the movement of the light scanning beam. (b) Diagram of the fully integrated MOEMS probe. (c) PCB that connects the OCT probe with the power circuit.

Fig. 5.1c was designed and fabricated. Please note that there are five wires in the connection, one per actuator plus the ground terminal. Finally, the flexible PCB transmits the electrical signals to the pads of the scanner that are connected to each actuator. The light beam is scanned in the x, y, or both axes depending on the actuators driven [151].

To monitor the position of the light beam on the sample while the scanner is driven, we take

advantage of the fact that the micro mirror has a reflective layer of Al on both sides. This allows to couple a position sensing detector (PSD) (Thorlabs PDP90A) behind, as shown in the diagram of the system (Fig. 5.1a). The light beam of a visible laser ($\lambda = 635$ nm, beam diameter (d) = 5 mm) (Thorlabs LDM635) with variable power is focused with a lens of focal length (f_L) of 150 mm towards the backside of the micro mirror. To facilitate the alignment of the visible beam with the micro mirror of only 1 mm of diameter, we use a mirror mounted in a holder that allowed precise tilting in the yaw and pitch axis. At last, the visible beam is reflected towards the PSD and repeats the scanning pattern of the infrared beam (from the swept source) on the sample.

To assure that the spot size of the visible light beam is smaller than the diameter of the micro mirror, we estimated the diameter of the visible beam along the optical path from the lens until the sensor of the PSD (3.05 mm inside the outer border) using the equation for a Gaussian beam:

$$D_{spot} = 2 * \left[\omega_0 \sqrt{1 + \left(\frac{Z}{z_R} \right)^2} \right] \tag{5.1}$$

where D_{spot} is the diameter of the beam along the optical axis Z and ω_0 is the radius of the spot at the focal point given by:

$$\omega_0 = \sqrt{\frac{\lambda \, z_R}{n \, \pi}} \tag{5.2}$$

being z_R the Rayleigh range:

$$z_R = \frac{\text{DOF}}{2} \tag{5.3}$$

and DOF the depth of focus given by the equation 3.3. With these equations and the parameters of the visible laser ($\lambda = 635$ nm, $f_L = 150$ nm, $d = 5$ mm), we calculated the diameter of the beam D_{spot} along the optical axis Z and it is shown in Fig. 5.2a. This curve allows to estimate the proper distances where to place the mirror and the probe to have a beam diameter of 500 μm on the surface of the micro mirror (diameter = 1 mm).

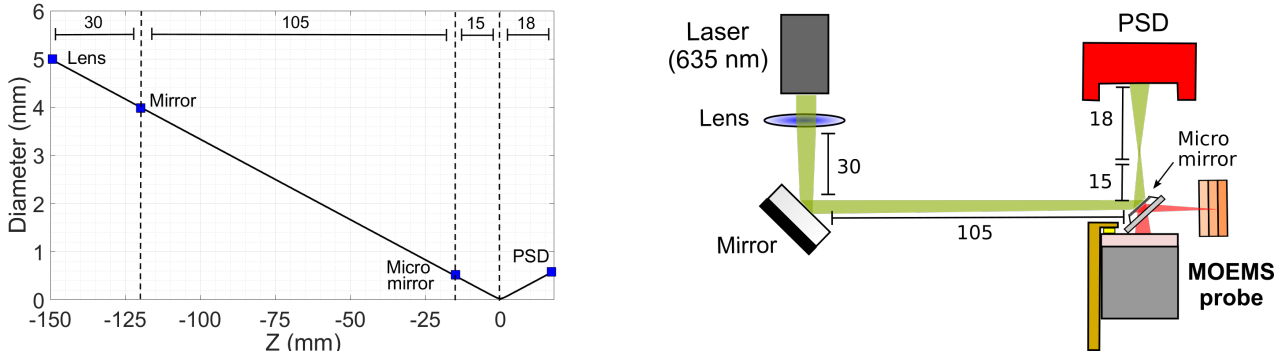

(a) (b)

Figure 5.2: (a) Diameter of the visible laser beam along the optical axis from the lens to the sensor of the PSD. (b) Chosen distances to assure a spot size of 500 μm on the micro mirror and 600 μm on the sensor.

The recommended spot size on the sensor of the PSD is from 0.2 to 7 mm. The sensor was placed at 18 mm from the focal point in order to have a beam diameter of 0.6 mm on it which is within the range and also because when the sensor is further away, the light beam goes out

of it (sensor size = 9 x 9 mm) if the scanner is driven at the resonance frequency. The PSD is connected to its correspondent controller (Thorlabs KPA101 K-Cube) that provides three signals: Δx, Δy and SUM that depend on differential voltages between a common cathode and an anode on each side of the sensor. The coordinates (x,y) that give the position of the beam on the sensor are given by:

$$x_{\mathrm{PSD}}(t) = \frac{L_x\,\Delta x(t)}{2\,[\mathrm{SUM}(t)]} \tag{5.4}$$

$$y_{\mathrm{PSD}}(t) = \frac{L_y\,\Delta y(t)}{2\,[\mathrm{SUM}(t)]} \tag{5.5}$$

where L_x and L_y are the lengths of the sides of a resistive layer in it (between the common cathode and the four anodes) which equals 10 mm in both cases ($L_x = L_y = 10$ mm) and t is the variable of time. The value of SUM equals the total voltage between all the four anodes and must be close and less than 4 V. Higher voltages saturate the system and leads to unreliable measurements. The value of SUM was fixed at 3.7 V by adjusting the optical power of the visible laser to avoid this saturation. The position resolution of the PSD is given by:

$$\Delta R = L_x \left(\frac{e_n}{\mathrm{SUM}}\right) \tag{5.6}$$

where e_n is the output noise voltage that equals 300 μV_{RMS}. For SUM = 3.7 V, the position resolution is 0.810 μm. The electrical signals (Δx, Δy and SUM) are registered by the NI-DAQ and post processed to obtain the position of the scanning beam using the equations 5.4 and 5.5.

A trigger signal is generated by the NI-DAQ towards the GaGe-DAQ card in order to synchronize the starting time of the acquisition of the interferograms (Ch1) and the trigger of the swept source (Ch2) and the starting time of the movement of the scanner (generation of the sinusoidal signals). The instrumentation of the SS-OCT system is made in LabVIEW (data acquisition, sinusoidal signals generation, scanning beam sensing and generation of the trigger signal) as the previous versions, presented in sections 3.2 and 3.3. In this case, the file "GageDeepAcqusition.vi" (of the supporting softwares of the GaGe-DAQ card) was taken and modified since it allows to make large data acquisitions and fill completely the memory of the DAQ (1 GS). Four function generators blocks were added to drive each actuator with sinusoidal signals. Figure 5.3 shows the system of reference used for the scanning beams on the sample and on the PSD. The actuators are refered as A1, A2, A3 and A4. As it was mentioned in section 2.2, two opposite actuators must be driven with two electrical signals with the same amplitude and frequency but dephased 180° to scan in one axis. First, a DC voltage (V_b) must be applied in the four actuators at the same time to contract them and bring the mirror down at the same plane of the frame. Once contracted, the actuators can be expanded or contracted more with the sinusodial signals and scan the micro mirror. To scan in the x-axis, the actuator A1 is driven with the signal:

$$U_x(t) = V_b + V_x \sin(2\pi f_x t + \phi_x) \tag{5.7}$$

where V_x and f_x are the amplitude and frequency of the signal respectively, ϕ_x the phase and t is the time variable. Consequently, the actuator A3 is driven with the same signal but with the phase delay of 180°. As a result, the micro mirror rotates around the y-axis and the optical angular displacement is given by:

$$O_x(t) = \theta_x^{opt} \sin(2\pi f_x t + \psi_x) \tag{5.8}$$

where θ_x^{opt} is the amplitude and ψ_x the phase. Similarly, the actuator A2 (and A4) is driven with other sinusoidal signal:

$$U_y(t) = V_b + V_y \sin(2\pi f_y t + \phi_y) \tag{5.9}$$

to scan in the y-axis. In this case, the micro mirror rotates around the x-axis and the angular displacement is given by:

$$O_y(t) = \theta_y^{opt} \sin(2\pi f_y t + \psi_y) \tag{5.10}$$

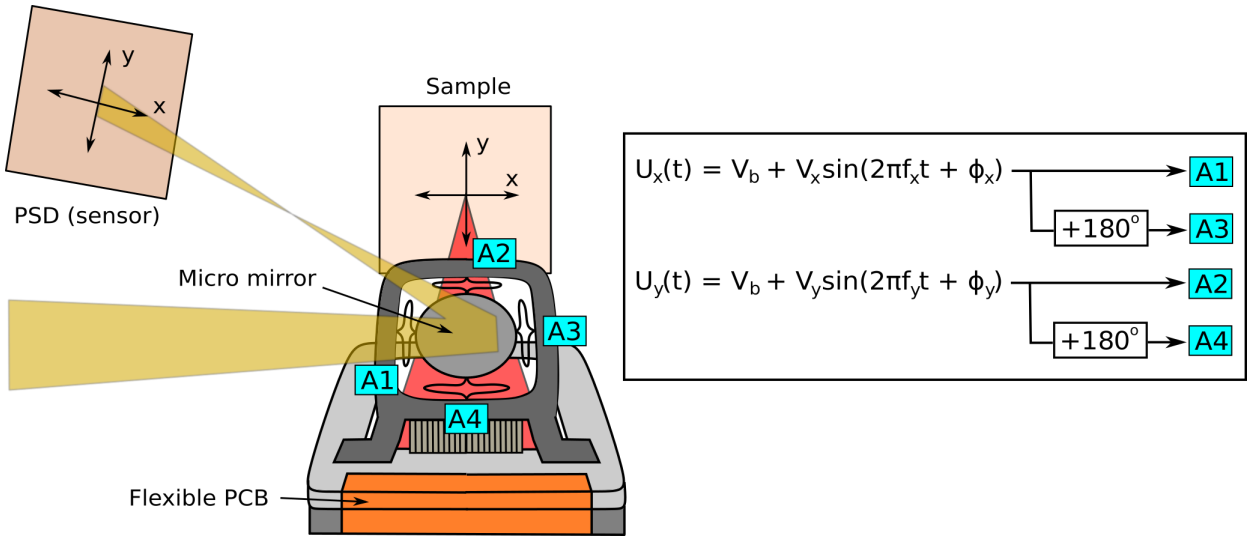

Figure 5.3: System of reference of the scanning beams on the sample and on the PSD. The actuators are driven with the sinusodial signals $U_x(t)$ (x-axis) and $U_y(t)$ where V_b is the DC voltage, V_x and V_y the amplitudes, f_x and f_y the frequencies, Φ_x and Φ_y the phases and t the time variable of the signals. The movement of the infrared beam from the swept source on the sample is mimicked on the PSD by the visible beam from the laser of 635 nm.

The correspondent blocks to configure three input channels of the NI-DAQ to register the signals from the PSD controller (Δx, Δy and SUM) were also added. Finally, the blocks that generate the trigger signal from the channel PFI 1 (output) of the NI-DAQ towards the trigger channel of the GaGe-DAQ to start the acquisition in the channels 1 and 2 and towards the channel PFI 0 (input) of the NI-DAQ (back again) to start the generation of the sinusoidal signals that control the scanner were also added. A "T" BNC connector was used to split the trigger signal in two. At the end, this software produces two files: one with the data from the channel 1 (interferograms) and channel 2 (trigger signal of the swept source) of the GaGe-DAQ and other with the signals from the PSD controller. The post-processing to obtain the OCT image and the position of the scanning beam is performed in Matlab. We present the scanning characterization in the next section.

5.2 Frequency response of the scanner

Two softwares in LabVIEW (different from the software described in the previous section) were developed to measure the resonance frequency of the scanner in each axis. Each of these softwares allows driving the scanner in one of the two axis at different frequencies using different iterations. To obtain the frequency response in the x-axis, the software sends the input driving signals:

$$U_x(t) = 2\,\text{V} + (0.1\,\text{V}) \sin(2\pi f_x t) \tag{5.11}$$

$$U_y(t) = 2\,\text{V} \tag{5.12}$$

In this way, the four actuators have the constant V_b of 2 V but the sinusoidal signals are only applied in the actuators A1 and A3 (Fig. 5.3). The voltage V_x was fixed at 0.1 V as in the characterization of other scanners of the same badge (see [136]), and V_b at 2 V to decrease even more the power required to drive the scanner ($V_b = 3$ V in previous scanners). In the first iteration, the software sends the signals during $t = 5$ s for an initial frequency f_x while the sinusoidal movement of the visible beam is registered by the PSD at 100 kHz and the signals Δx, Δy and SUM are saved in a file. In the next iterations, the value of f_x increases and the process is repeated. At the end, there is one file per frequency with the data Δx, Δy and SUM that are further processed in Matlab to calculate the position of the beam on the PSD with the equations 5.4 and 5.5. The sinusoidal movement in the x-axis is given by:

$$p_x(t) = M_x \sin(2\pi f_x t + \psi_x) \tag{5.13}$$

where M_x is the amplitude and ψ_x the phase. Figure 5.4 shows the interface of the above mentioned sofware where the starting frequency (Freq start), the frequency step (Freq step) and the number of steps (iterations) can be settled at the beginning. Also, the value of V_b (2 V) and the amplitude V_x (0.1 V) of the signal $U_x(t)$ can be specified (the signal $V_y(t)$ is kept at V_b without sinusoidal amplitude variations). Figure 5.5a shows the sinusoidal movement of the visible beam on the PSD at $f_x = 10$ Hz in the x-axis.

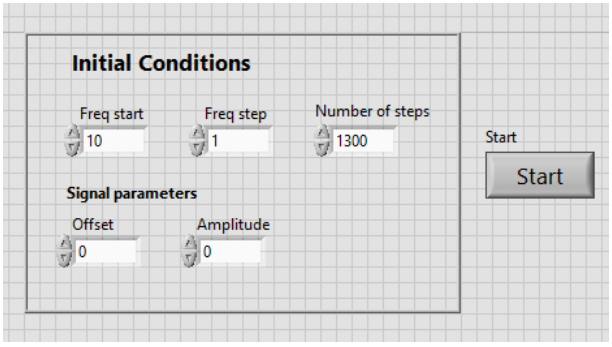

Figure 5.4: Interface of the software that gets the frequency response of the scanner.

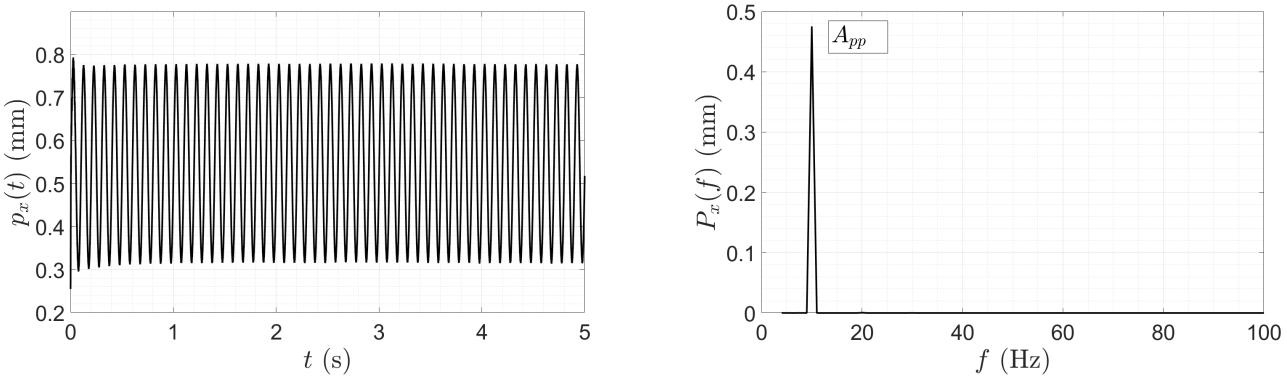

(a) (b)

Figure 5.5: (a) Movement of the scanning beam on the PSD in the x-axis at 10 Hz. (b) FFT of (a).

To find the resonance bandwidth, the starting frequency was set at 10 Hz, the step at 30 Hz to decrease the time of acquisition and the number of steps at 44 in order to have a final frequency of

1310 Hz. Previous scanners of the same badge (as in the scanner in [136]) had this range at lower frequencies. Once having all the files, the Fast Fourier Transform (FFT) of each $p_x(t)$ is estimated with Matlab at each frequency f_x but only during the second 2 ($t = 2$ s – 3 s, the middle of the measurement):

$$P_x(f) = |\mathcal{F}\{p_x(t)\}| \tag{5.14}$$

where f is the variable of the frequency domain. The absolute value of the transform must be calculated to get the magnitude since the FFT algorithm produces complex numbers. Figure 5.5b shows the FFT of $p_x(t)$ for $f_x = 10$ Hz (Fig. 5.5a) without the peak corresponding to the DC component. The maximum value of the peak corresponds to the amplitude peak-to-peak A_{pp} of the sinusoidal movement of the scanning beam. Figure 5.6a (dotted blue line) presents the plot between the amplitude ($A_{pp} = P_x(f_x)$) of the peak of each FFT and its correspondent frequency f_x. This graph is the magnitude frequency response of the scanner in the x-axis ($\vec{x} \cdot \vec{x}$) where we can see that the resonance bandwidth is between 800 Hz and 1080 Hz. When the scanner is driven in one axis (e.g. x-axis), there is also movement of the laser beam in the other one (e.g. y-axis) at the resonance. This is because both axes are coupled by the micro mirror. If the actuators of one axis are driven close to the resonance frequency, the actuators of the other axis are also excited by the same frequency making them to resonate as well. This effect is produced since both axes have almost the same resonance frequency. The black curve corresponds to this coupled y-axis ($\vec{x} \cdot \vec{y}$).

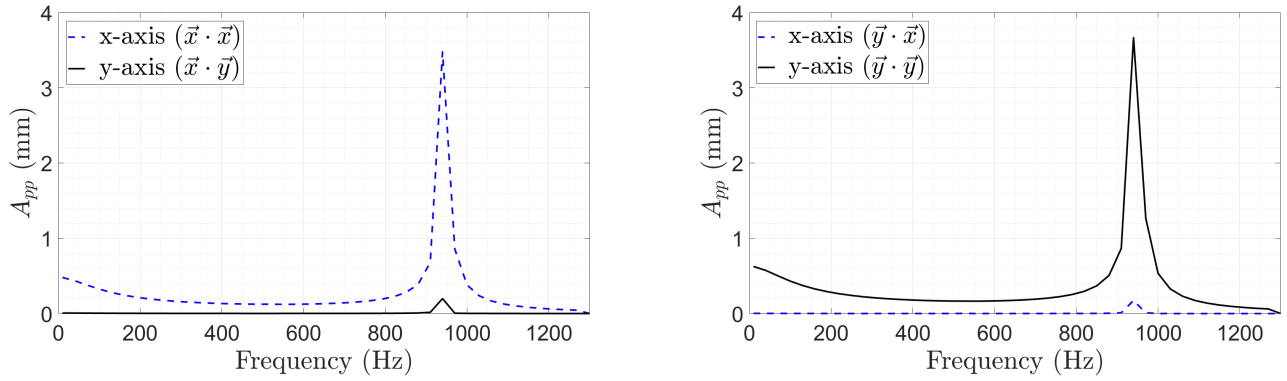

(a) (b)

Figure 5.6: (a) Frequency response of the MEMS scanner in the x-axis ($\vec{x} \cdot \vec{x}$, dotted blue line). (b) Frequency response in the y-axis ($\vec{y} \cdot \vec{y}$, black line).

The software that obtains the frequency response in the y-axis works in the same way but it sends the input signals:

$$U_x(t) = 2\,\text{V} \tag{5.15}$$

$$U_y(t) = 2\,\text{V} + (0.1\,\text{V})\sin(2\pi f_y t) \tag{5.16}$$

In this case, the actuators A2 and A4 are driven with sinusoidal signals. The movement of the beam on the PSD in the y-axis is given by:

$$p_y(t) = M_y \sin(2\pi f_y t + \psi_y) \tag{5.17}$$

and the corresponding FFT by:

$$P_y(f) = |\mathcal{F}\{p_y(t)\}| \tag{5.18}$$

Figure 5.6b shows the magnitude frequency response in the y-axis ($\vec{y} \cdot \vec{y}$, black line) and the coupled x-axis ($\vec{y} \cdot \vec{x}$, dotted blue line).

The magnitude frequency response of both axes ($\vec{x}\cdot\vec{x}$ and $\vec{y}\cdot\vec{y}$) in the resonance bandwidth with step of 1 Hz is shown in Fig. 5.7a where the amplitude peak-to-peak (A_{pp}) is expressed in optical angular displacement (θ_{pp}^{opt}). We can obtain these values with trigonometry knowing the distance from the micro mirror to the sensor of the PSD (D_1) which is 33 mm (Fig. 5.2b):

$$\theta_{pp}^{opt} = \tan^{-1}\left(\frac{A_{pp}}{D_1}\right) \tag{5.19}$$

This scanner has resonance frequencies of 943 Hz and 945 in the x-axis and y-axis respectively.

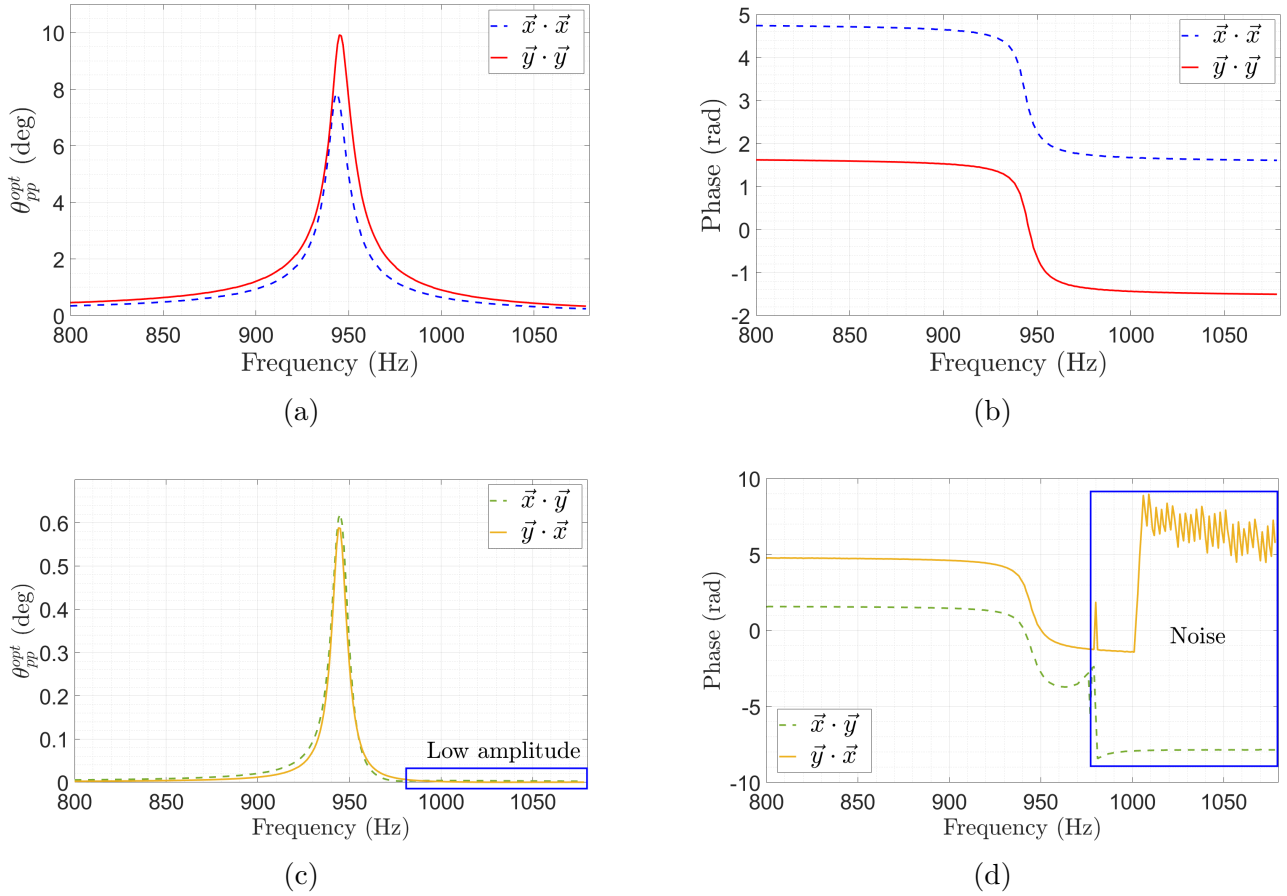

Figure 5.7: (a) Magnitude and (b) phase frequency response of the x-axis ($\vec{x}\cdot\vec{x}$) and the y-axis ($\vec{y}\cdot\vec{y}$). (c) Magnitude and (d) phase frequency response of the coupled axes ($\vec{x}\cdot\vec{y}$ and $\vec{y}\cdot\vec{x}$).

The phase frequency response of these driven axes is given in Fig. 5.7b that corresponds to the difference in phase between the electrical input signals ($U_x(t)$ and $U_y(t)$) and the laser beam displacement on the PSD ($O_x(t)$ and $O_y(t)$) in each axis. It is obtained from the FFTs as well with the method presented by Zhivomirov [142]. The author measures the phase difference between two signals with the function in Matlab "Angle" by:

$$\psi_x = \text{Angle}[\mathcal{F}\{p_x(t)\}_{f=f_x}] - \text{Angle}[\mathcal{F}\{U_x(t)\}_{f=f_x}] \tag{5.20}$$

for the case of the x-axis ($\vec{x}\cdot\vec{x}$). The term $\mathcal{F}\{U_x(t)\}_{f=f_x}$ is the FFT of the input signal U_x (equation 5.7) evaluated at the driving frequency $f = f_x$. The function "Angle" takes the complex number resulting from the FFT:

$$z = x + iy \tag{5.21}$$

and calculates the angle between the x axis (in the Cartesian plane) and the line from the origin to the point (x, y). For the case of the y-axis ($\vec{y} \cdot \vec{y}$):

$$\psi_y = \text{Angle}[\mathcal{F}\{p_y(t)\}_{f=f_y}] - \text{Angle}[\mathcal{F}\{U_y(t)\}_{f=f_y}] \tag{5.22}$$

The magnitude and phase frequency response of the coupled axes are shown in Fig. 5.7c and Fig. 5.7d respectively, where $\vec{x} \cdot \vec{y}$ is the curve of the angular displacement on the y-axis when the scanner is driven in the x-axis and $\vec{y} \cdot \vec{x}$ is the curve of the displacement on the x-axis when the scanner is driven in the y-axis. The amplitude in Fig. 5.7c after 980 Hz was too low to calculate the difference in phase in Fig. 5.7d. This is the reason why the behavior of the curves in this last figure is noisy after 980 Hz. To increase this amplitude, the input voltage must be increased. We prefered not to perform this last task to avoid a possible damage to the scanner since it would be resonating at higher voltages.

The angular gain with respect to θ_{pp}^{opt} at 10 Hz (θ_{DC}, quasi-static mode) is shown in Fig. 5.8a for the x and y axes. The frequency bandwidth where there is a gain higher than 0 dB is 894 Hz – 988 Hz for the x-axis and 894 Hz – 991 Hz for the y-axis. These ranges of frequencies will be used for the Lissajous trajectories in section 5.4. Figure 5.8b presents the linear increase of the angular amplitude peak-to-peak θ_{pp}^{opt} with the increase of the amplitudes V_x and V_y of the input signals (see equations 5.7 and 5.9) from 0.05 V to 0.5 V with a step of 0.05 V for both axes at 10 Hz (quasi-static mode). The angular amplitude θ_{pp}^{opt} at each V_x and V_y was also obtained applying the FFT to $p_x(t)$ and $p_y(t)$ during $t = 2$ s – 3 s and then measuring the amplitude of the peak at the driving frequency ($f = f_x$ and $f = f_y$), as with the frequency response of the scanner.

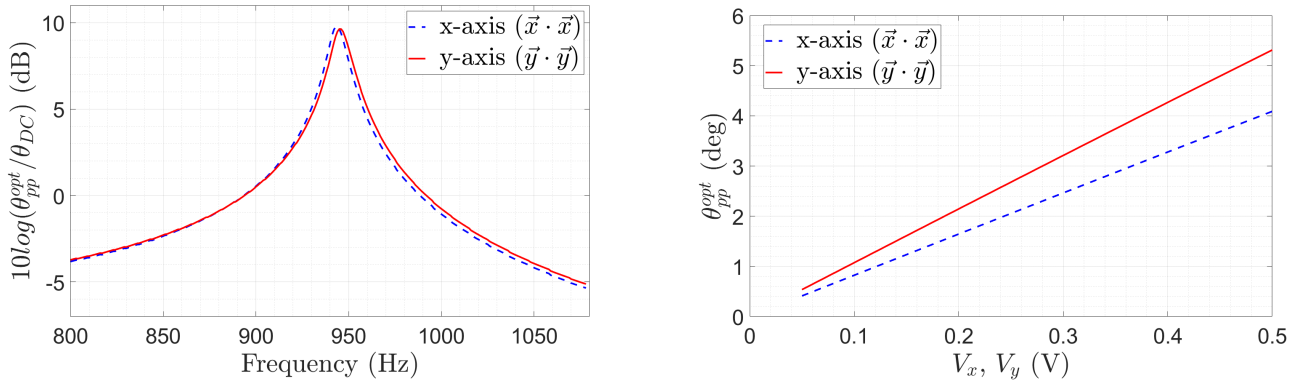

(a) (b)

Figure 5.8: (a) Angular gain of the scanner in both axes. (b) Angular amplitude peak to peak of the laser beam θ_{pp}^{opt} vs. amplitudes V_x and V_y of the input signals for both axes at 10 Hz (quasi-static mode).

For the scanning of the sample, we must calculate the scanned distance (DS) by the light beam of the swept source (back side of the micro mirror) at each frequency of the resonance bandwidth. Figure 5.9 shows this distance (in the y-axis) that is scanned by the focal spot on the sample and corresponds to the amplitude peak-to-peak of the sinusoidal movement of the infrared beam. We can estimate DS with trigonometry knowing the scanning angle of the micro mirror (Fig. 5.7a and Fig. 5.7c) and the distance from the micro mirror to the focal point of the probe (D_2). This distance was calculated to be $D_2 = 3.4$ mm knowing the focal length of the micro lens ($f_L = 9.1$ mm), and the measures of each part of the micro interferometer and the micro scanner. Hence, DS is given by:

$$DS = \tan(\theta_{pp}^{opt}) D_2 \tag{5.23}$$

The working distance (WD) of the probe is the distance from the edge of the interferometer to the focal point and was also estimated with trigonometry to be 1 mm. Figure 5.10a shows DS per amplitude $V_x = 1$ V (DS_{1V}) of the input signal for the driven x-axis ($\vec{x} \cdot \vec{x}$) and its correspondent coupled y-axis ($\vec{x} \cdot \vec{y}$) at each frequency of the resonance bandwidth. The values of DS were obtained for $V_x = 0.1$ but we can calculate the values for $V_x = 1$ V with a rule of three:

$$\frac{DS}{DS_{1V}} = \frac{0.1\,\text{V}}{1\,\text{V}} \tag{5.24}$$

$$DS_{1V} = \frac{(DS)(1\,\text{V})}{0.1\,\text{V}} \tag{5.25}$$

since the variation of θ_{pp}^{opt} with respect to the amplitude V_x (and V_y) is linear (Fig. 5.8b). Figure 5.10b shows DS_{1V} for the driven y-axis ($\vec{y}\cdot\vec{y}$) and its coupled x-axis ($\vec{y}\cdot\vec{x}$). The percentages of cross-coupling between the coupled and the driven axes were also estimated. Figure 5.10c presents these values for the driven x-axis (C_x) and Fig. 5.10d for the driven y-axis (C_y). Table 5.1 summarizes all the parameters of the scanner estimated in this section at the resonance frequencies.

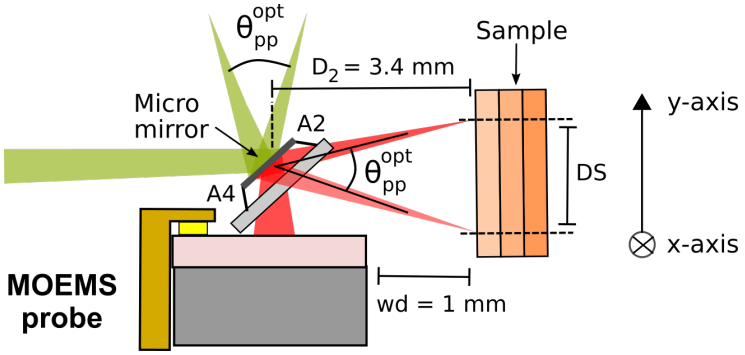

Figure 5.9: Distance DS in the y-axis scanned by the laser beam of the swept source.

Table 5.1: Parameters of the scanner at the resonance frequencies in both axes obtained with sinusoidal driving signals with $V_b = 2$ V, $V_x = V_y = 0.1$ V.

Axis	F_r (Hz)	θ_{pp}^{opt} (°)	Phase (rad)	Angular Gain (dB)
x	943	7.8	3.7	9.8
y	945	10	0	9.8

5.3 Impact of the micro mirror coating on the OCT images

We scanned again the samples already presented in section 3.3 (banana and onion) by moving them with the motorized stage, while keeping the scanner static, to see if the presence of the micro mirror affects the quality of the images. Figures 5.11c and 5.11d present the obtained images with the forward sweeps and averaging 10 signals before FFT (the best sensitivity). A decrease in intensity is observed when compared to the images obtained with the micro-interferometer before the micro scanner integration. Figures 5.11a and 5.11b show these images already presented in section 3.3 for comparison. The power of the laser at the output of one probe without scanner (after the beam splitter) was measured to be 2.18 mW. However, the power was decreased to

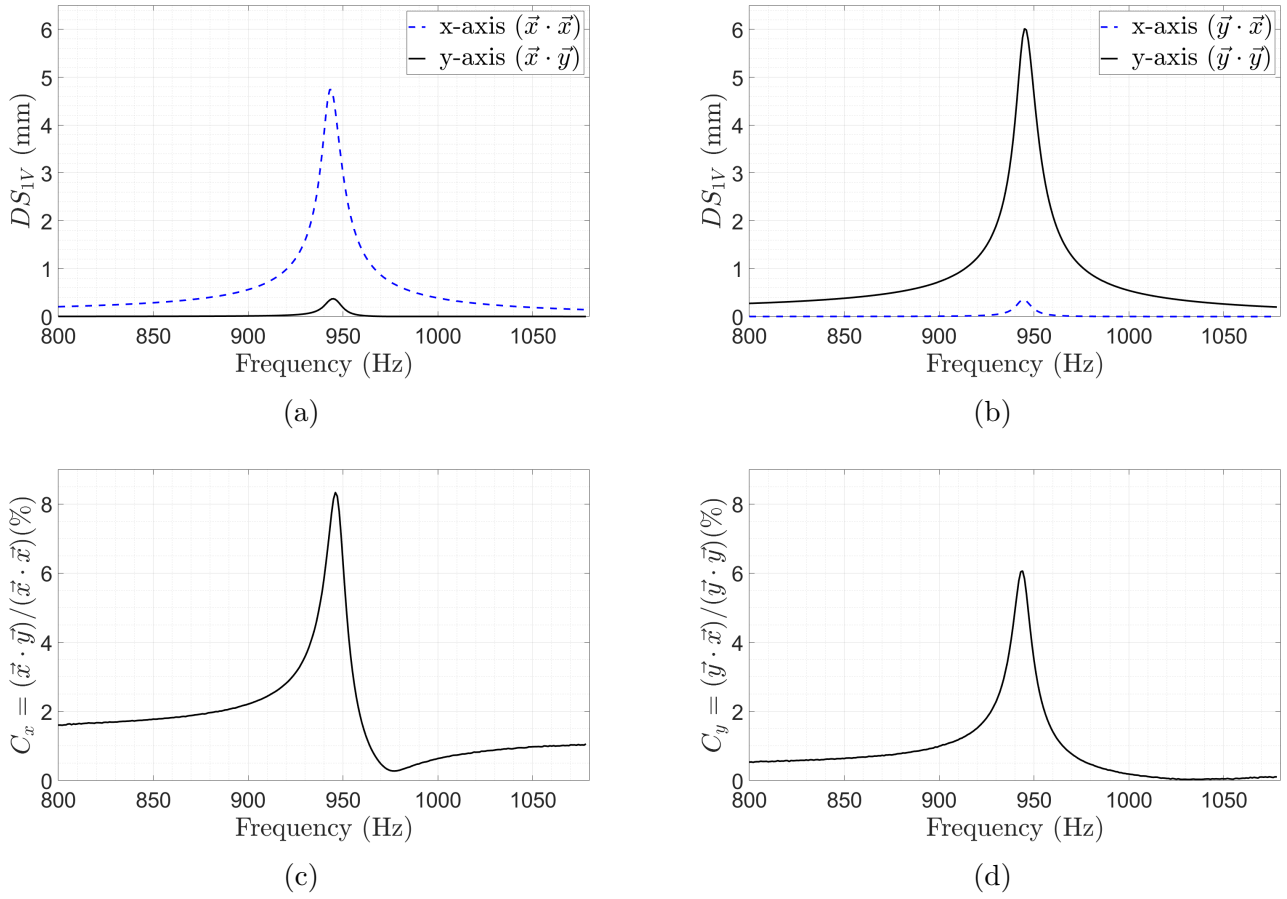

Figure 5.10: (a) Distance DS for $V_x = 1$ V when the scanner is driven in the x-axis. (b) Distance DS for $V_y = 1$ V when the scanner is driven in the y-axis. (c) Cross-coupling when the scanner is driven in the x-axis and in (d) the y-axis.

0.8 mW (drop of 63 %) in the probe with scanner after reflection from the mirror. The sensitivity in the images decreases since the mirror reflects poorly the infrared beam. The SNR in the images was calculated (see section 3.3) to be 21.9 dB and 32.2 dB for the image of the banana and onion, respectively. There is a decrease of 15.8 dB and 16.3 dB when compared to the images taken without the integrated scanner. This power drop was analyzed, taking into account the design of the micro mirror and its fabrication process, presented in [19].

The back-side of the mirror is composed of a thin-film multilayer of pure metals: 15 nm Cr (adhesion layer), 400 nm Al (main reflective layer) and 15 nm Cr (protection layer), deposited in a sequential process by ion assisted e-beam evaporation. Aluminum was chosen to simplify the technology of the Al-based electrothermal micro-actuators (i.e. one layer on the actuator is deposited at the same time as the micromirror coating) and also because of the good compromise between optical, thermal and mechanical properties, i.e. good reflectivity in a broad spectrum range, low stress, very good heat dissipation as well as low cost. A thin Cr layer was used as an additional coating to prevent, as explained in [19], an oxidation of the Al layer. Indeed, Cr is a mechanically robust and stable material that exhibits no tarnish when it is exposed to ordinary or even harsher atmospheric conditions. However, the native oxide present on the Al surface protects it from corrosion as well and has a small impact on the Al reflectance in the infrared range [133]. It seems that the role of Cr is rather the protection of the micro mirror surface during the releasing process that involves the plasma etching of the Si substrate. Moreover, this

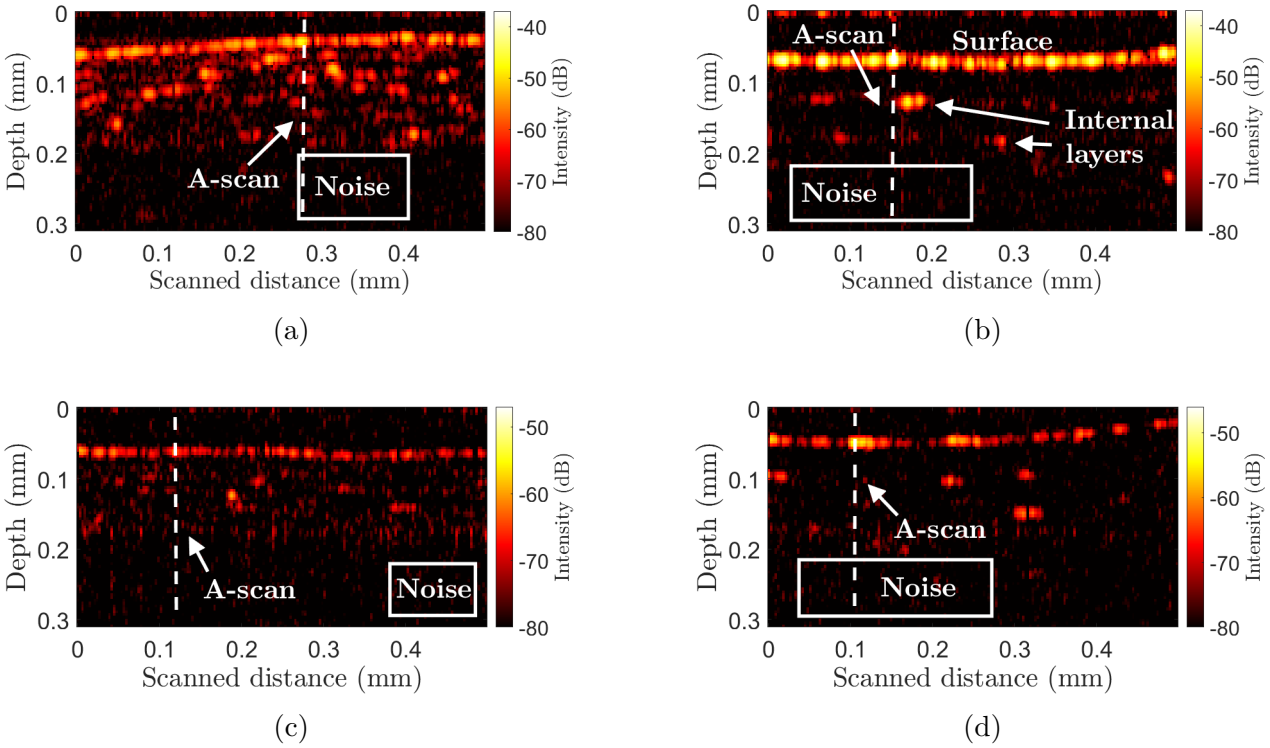

Figure 5.11: OCT images of biological samples scanned with the motorized stage: (a) banana and (b) onion obtained with probe without scanner, (c) banana and (d) onion obtained with the fully integrated probe (scanner static).

combination of materials has shown to be effective for long-term stability. The mirror coating does not show any symptoms of corrosion after 4-5 years from the fabrication, when stored in normal atmospheric conditions.

From the optical point of view, the reflectivity of the metal-coated mirror depends mainly on the wavelength of the incoming light and the optical constants of the used materials, which are also a function of their thickness. It may also be affected by the surface roughness and, to a much lesser extent, by the angle of beam incidence and the polarization state of the incoming light beam. Generally, aluminum has a fairly flat spectral reflectance in the UV-VIS-IR range, except around 820 nm where it exhibits a dip of reflectance to $\approx$ 86 % [133]. Unfortunately, this dip corresponds well to the operating wavelength range of the EXALOS swept source (840 nm) leading to a drop of the reflected optical power that is higher when compared to other popular metal coatings e.g. gold (R $>$ 95 %), as shown in Fig. 5.12a. Moreover, Cr is generally a bad reflector with a reflectance of only R $\approx$ 62 % in the considered swept range. On the other hand, the thickness of the evaporated layers was chosen to control their opacity level. The deposited layer of 400 nm of Al ensures a good opacity for coating (opaque point $\approx$ 100 nm), which determines an overall good reflectance. A deposition of 15 nm of Cr provides a semi-transparent protective layer which has $\approx$ 50 % of transmittance (Fig. 5.12b) and deteriorates the total reflectance slightly because of its absorption [134]. In short, the Cr/Al/Cr reflective coating configuration that was applied in the current version of micro scanner is not the best option for OCT imaging at a wavelength of 840 nm. This problem must be fixed in future versions of the scanner. Consequently, only samples with high reflectivity can be imaged with the fully integrated probe. The next section describes the Lissajous scanning pattern that was used to perform 3D imaging.

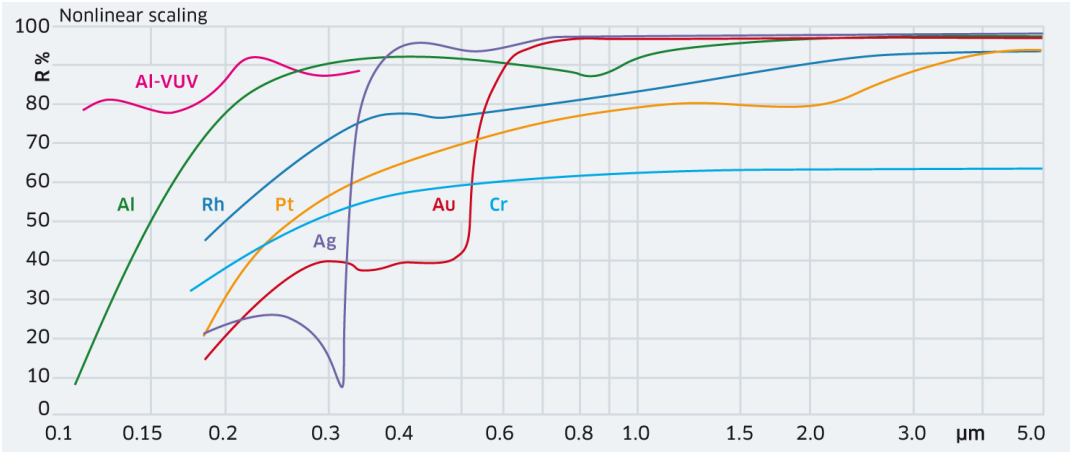

(a)

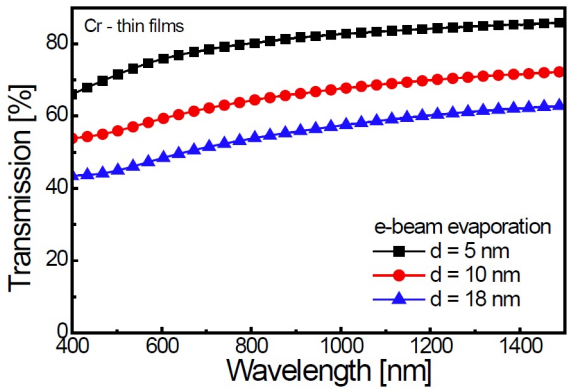

(b)

Figure 5.12: (*a*) Reflectivity of common metal coatings (e-beam evaporation) vs wavelength at normal incidence. Image taken from.[135] (*b*) Transmittance spectra of thin Cr layers deposited by e-beam evaporation. Image taken from [134].

5.4 Lissajous scanning

As shown elsewhere, the presented scanner has the ability to perform Lissajous scanning in real-time [136]. This scanning pattern (Fig. 5.13) is produced by driving the scanner on both axes at the same time with two sinusoidal signals:

$$u_x(t) = A_x \sin(2\pi f_x t + \psi) \tag{5.26}$$

$$u_y(t) = A_y \sin(2\pi f_y t) \tag{5.27}$$

where A_x and A_y denote the amplitudes and ψ is the phase difference between the two signals. The frame rate (FR) is given by:

$$FR = \mathrm{GCD}(f_x, f_y) \tag{5.28}$$

where GCD indicates the greatest common divisor and the number of lobes per frame is:

$$N = N_x + N_y = \frac{f_x}{FR} + \frac{f_y}{FR} \tag{5.29}$$

where N_x and N_y denote the number of lobes along the x and y axis, respectively.

The maximum distance between two scanning lines (h) is at the center of the pattern as shown in Fig. 5.13a and is given by:

$$h = \frac{2A_xA_y \sin\left(\frac{\pi}{2N_x}\right) \sin\left(\frac{\pi}{2N_y}\right)}{\sqrt{\left[A_x \sin\left(\frac{\pi}{2N_y}\right)\right]^2 + \left[A_y \sin\left(\frac{\pi}{2N_x}\right)\right]^2}} \tag{5.30}$$

That is obtained from the coordinates of the points P_0, P_1 and P_2:

$$P_0 = (0, 0) \tag{5.31}$$

$$P_1 = \left(A_x \sin\left(\frac{\pi}{2N_y}\right), A_y \sin\left(\frac{\pi}{2N_x}\right)\right) \tag{5.32}$$

$$P_2 = \left(A_x \sin\left(\frac{\pi}{2N_y}\right), -A_y \sin\left(\frac{\pi}{2N_x}\right)\right) \tag{5.33}$$

The distance h corresponds to the image resolution that is also given by the full width at half maximum (FWHM) of the scanning beam.

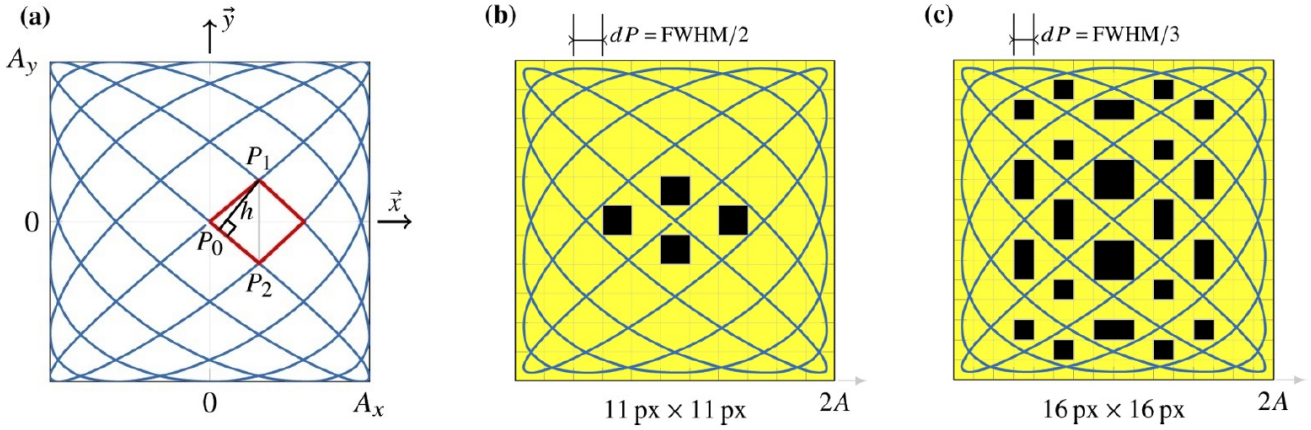

(a) (b) (c)

Figure 5.13: (a) Lissajous pattern. (b) The same pattern on a grid of 11 x 11 pixels (px) with a pixel size of dP = FWHM/2 and (c) on a grid of 16 px x 16 px with smaller pixel size of dP = FWHM/3. The pixels not reached by the scanning pattern were colored in black. Images taken from [136].

The squared scanned area ($A_x = A_y = A$) is given by:

$$A = \text{FWHM} \frac{\sqrt{\sin^2\left(\frac{\pi}{2N_x}\right) + \sin^2\left(\frac{\pi}{2N_y}\right)}}{2\sin\left(\frac{\pi}{2N_x}\right)\sin\left(\frac{\pi}{2N_y}\right)} \approx \frac{\text{FWHM}}{\pi}\sqrt{N_x^2 + N_y^2} \tag{5.34}$$

In the case of an image, it is composed of pixels that are filled out by the Lissajous trajectory as shown in Fig. 5.13b. Not all the pixels are reached by the scanning beam (black pixels). The field of view in pixels FOV_{px} is:

$$FOV_{px} = 2A = 2\left(\frac{\text{FWHM}}{dP}\right)\left[\frac{\sqrt{\sin^2\left(\frac{\pi}{2N_x}\right) + \sin^2\left(\frac{\pi}{2N_y}\right)}}{2\sin\left(\frac{\pi}{2N_x}\right)\sin\left(\frac{\pi}{2N_y}\right)}\right] \tag{5.35}$$

where dP is the size of one pixel and corresponds to the inverse of the sampling frequency. In order to resolve two adjacent focused beams (Gaussian beams) and achieve the maximum resolution of the system, this frequency must be at least the cutoff frequency of the modulation transfer function that, for a Gaussian beam, equals 1/FWHM. Following the Nyquist-Shannon sampling theorem, the sampling frequency should be twice this frequency (2/FWHM) in order to have two samples (pixels) per beam. Hence, the size of each pixel should be smaller than FWHM/2 at least. However, the pixelation of the beams reduces the contrast in the image (difference between the lowest and highest intensity in the image) since each pixel integrates the intensity values of the part of the Gaussian beam on it, making the maximum value to decrease and the minimum value to increase (Fig. 5.14a) [141]. Better samplings of the beam spots and higher contrasts are achieved by decreasing the size of the pixels (Fig. 5.14b). Figure 5.13c shows the Lissajous trajectory on a grid of 16 px x 16 px with dP = FWHM/3 where the maximum resolution in the image is maintained and the contrast increased but there are more pixels that are not reached by the scanning beam. The ratio between the pixels reached by the Lissajous pattern and the total number of pixels is the fill factor (FF) of the image and equals 86 % for the image with pixel size of dP = FWHM/3. On the other hand, the FF is 97 % for the image with dP = FWHM/2 meaning that there is a tradeoff between the contrast and the FF.

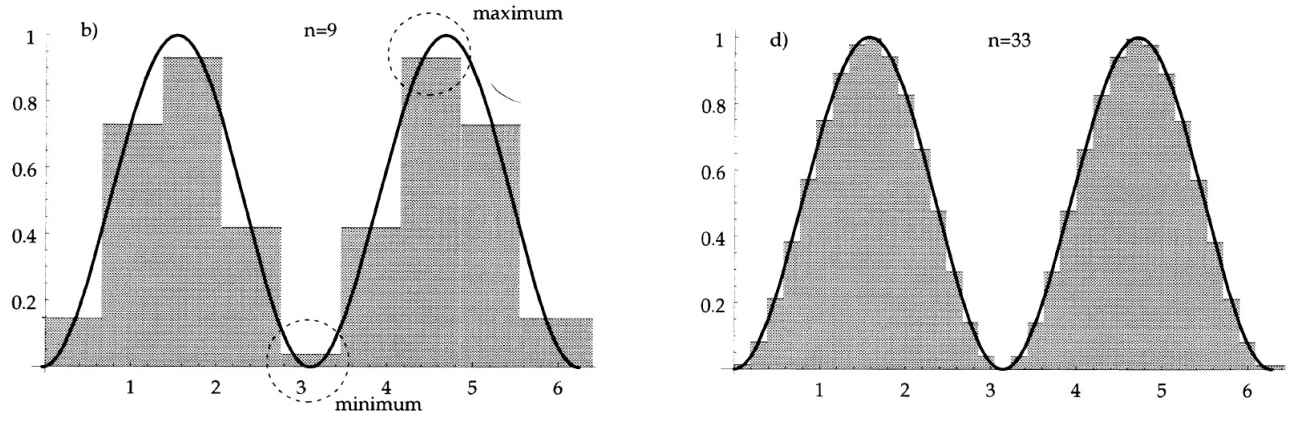

(a) (b)

Figure 5.14: (a) Pixelation of two Gaussian beams with 9 pixels (n = 9). Each value correspond to the intensity integrated over each pixel. (b) Pixelation of two Gaussian beams with 33 pixels (n = 33). Image taken from [141].

The frequency between two successive crossing points (F_{cp}) in the Lissajous pattern is given by:

$$F_{cp} = 4\, N_x N_y FR \tag{5.36}$$

To achieve FF higher than 80 %, the sampling frequency must be at least 6 times F_{cp} [136]. In OCT, the sampling frequency of the Lissajous trajectory is fixed by the A-scan rate that it is limited by the sweeping rate of the laser for SS-OCT, which is the fastest OCT mode. Usually, these frequencies are in the range from 20 kHz to 200 kHz but commercial swept sources with sweeping rates of even 3 MHz (OptoRes) have been developed in the last years.

The frequencies used for the Lissajous patterns are within the bandwidth 894 Hz – 988 Hz for the x-axis and within 894 Hz – 991 Hz for the y-axis, since in here, the angular gain is bigger than 0 dB (Fig. 5.8a). In other words, the angular displacement is greater than in the quasi-static mode (10 Hz) and there is an increase in scanning distance within this range at the same input voltage.

An algorithm made in Matlab calculates the FR, N_x, N_y, F_{cp} and the field of view in microns (FOV, equation 5.34) and in pixels (FOV_{px}, equation 5.35) of the Lissajous patterns produced with the 9310 combinations of f_x and f_y within the mentioned bandwidths. For the OCT probe, FWHM = 5.8 μm (spot on the sample given by the focusing lens of the interferometer, see section 3.1) and the pixel size was set to dP = FWHM/3. The number of combinations is reduced to 87 if we take into account only those ones that produce patterns with the next restrictions:

- $F_{cp} < 110$ kHz: The sampling rate of the Lissajous pattern is restricted to the A-scan rate of the swept source, employed in this setup, that is 110 kHz. Higher values of F_{cp} will not be sampled and the pattern will not be complete.
- $f_x \neq f_y$: When the frequencies are equal, the scanning pattern results in a tilted line.

Table 5.2 presents the parameters of 8 combinations of f_x and f_y with the highest values of $FOV_{\mu m}$ in descending order. We have prioritized to maximize this parameter over the others in order to scan the biggest possible area of the sample. Additionally, we present the percentages of cross coupling C_x and C_y at the corresponding frequencies f_x and f_y and the values of amplitude V_x and V_y of the input signals required to achieve the corresponding $FOV_{\mu m}$ on the plane of the sample (distance DS, Fig. 5.9). These last ones are also obtained with a rule of 3 having the values of DS_{1V} for the x ($\vec{x} \cdot \vec{x}$) and y ($\vec{y} \cdot \vec{y}$) axes (Figs. 5.10a and 5.10b, respectively):

$$V_{x,y} = \frac{(FOV_{mm})(1\,V)}{DS_{1V}} \tag{5.37}$$

Table 5.2: Scan parameters of the Lissajous patterns for the OCT probe.

No.	f_x **(Hz)**	f_y **(Hz)**	FR **(fps)**	N_x	N_y	$FOV_{\mu m}$ **(μm^2)**	V_x **(V)**	V_y **(V)**	C_x **(%)**	C_y **(%)**	FOV_{px} **(px^2)**	F_{cp} **(kHz)**
1	930	899	31	30	29	154 x 154	0.097	0.219	3.5	0.9	80 x 80	107.88
2	899	930	31	29	30	154 x 154	0.283	0.082	2.1	2.2	80 x 80	107.88
3	928	896	32	29	28	149 x 149	0.106	0.223	3.3	0.9	78 x 78	103.94
4	957	924	33	29	28	149 x 149	0.090	0.106	2.4	1.7	78 x 78	107.18
5	896	928	32	28	29	149 x 149	0.289	0.088	2.1	2	78 x 78	103.94
6	924	957	33	28	29	149 x 149	0.130	0.058	3	1.7	78 x 78	107.18
7	952	918	34	28	27	144 x 144	0.058	0.127	4.8	1.4	75 x 75	102.82
8	980	945	35	28	27	144 x 144	0.235	0.024	0.3	5.8	75 x 75	105.84

All the parameters are comparable between all these options. We choose the No. 4 (highlighted in blue) for scanning since the values of V_x and V_y are closer, we prefer to avoid a big difference of voltages between both axes as in option No. 8. Figure 5.15a shows a simulation of the resultant Lissajous pattern at t = 30.3 ms (1 frame) with a sampling rate of 110 kHz (A-scan rate of the swept source) and Fig. 5.15b shows the measured pattern (1 frame) when the scanner is driven with the correspondent sinusoidal signals:

$$U_x(t) = 2\,\text{V} + (0.09\,\text{V})\sin[2\pi(957\,\text{Hz})t] \tag{5.38}$$

$$U_y(t) = 2\,\text{V} + (0.1\,\text{V})\sin[2\pi(924\,\text{Hz})t] \tag{5.39}$$

As with the measurement of the frequency response, the signals are applied during $t = 5$ s and the trajectory is taken from $t = 2$ s to $t = 2.0303$ s (1 frame) that corresponds to the middle of the measurement where the amplitude variation is already stable. The sampling rate was fixed at 110 kHz as well. This Lissajous trajectory is measured on the PSD and then transferred to the plane of the sample by first calculating the angular displacement of the laser beams (visible laser and swept source) in both axes given by:

$$O_x(t) = \tan^{-1}\left(\frac{x_{\mathrm{PSD}}(t)}{D_1}\right) \tag{5.40}$$

$$O_y(t) = \tan^{-1}\left(\frac{y_{\mathrm{PSD}}(t)}{D_1}\right) \tag{5.41}$$

as with equation 5.19. After, the coordinates on the plane of the sample are estimated according to:

$$DS_x(t) = \tan[O_x(t)]D_2 \tag{5.42}$$

$$DS_y(t) = \tan[O_y(t)]D_2 \tag{5.43}$$

as with equation 5.23. In this case, the $FOV_{\mu m} = 169.7$ x 136.5 μm^2 approx. The tilt of the external frame is produced because of the cross-coupling between both axes. Notice that the crossing lines in one direction are overlapped. We believed that this phenomenon was caused because of the difference in phase presented in Fig. 5.7b that is 1.95 rad at $f_x = 957$ Hz ($\vec{x} \cdot \vec{x}$ curve) and 1.4 rad at $f_y = 924$ Hz ($\vec{y} \cdot \vec{y}$ curve). Figure 5.15c shows the simulation of the Lissajous pattern with an adjustement of these values of phase in the input signals in order to compensate this difference in phase at the output ($O_x(t)$ and $O_y(t)$):

$$U_x(t) = 2\,\mathrm{V} + (0.09\,\mathrm{V})\sin[2\pi(957\,\mathrm{Hz})t - 1.95\,\mathrm{rad}] \tag{5.44}$$

$$U_y(t) = 2\,\mathrm{V} + (0.1\,\mathrm{V})\sin[2\pi(924\,\mathrm{Hz})t - 1.4\,\mathrm{rad}] \tag{5.45}$$

In this case, the crossing lines in both directions overlap suggesting that this phenomenon is caused by a difference in phase between the input signals ($U_x(t)$ and U_y) and the laser beam displacement on the PSD ($O_x(t)$ and $O_y(t)$). Figure 5.15d shows the measured Lissajous trajectory on the plane of the sample with this phase adjustement. We observed that the crossing lines are still overlapped in one direction but not in the other one. More experiments concerning this phenomenon are still needed in future tasks of the project to understand its causes and correct the Lissajous trajectory adequately. For the 3D imaging tests of the probe, we used the scanning pattern without phase adjustement (Fig. 5.15b) and they are presented in the next section.

5.5 3D SS-OCT imaging based on Lissajous scanning

In this section, we present the OCT images obtained with the scanning performed by the electrothermal micro scanner. As it was mentioned in section 5.3, only samples with high reflectivity can be imaged with the fully integrated probe. A sample made of 3 layers of glass was scanned by driving the micro scanner and using the Lissajous trajectory presented in the last section (Fig. 5.15b). The obtained 3D image at $t = 30.3$ ms (1 frame) is shown in Fig. 5.16. The forward and backward sweeps were used, otherwise, half of the A-scans in the image would be lost. The 3 layers of glass are clearly visible due to its high reflectivity. One image of the smooth surface of the Thorlabs card could also be retrieved. Figure 5.17a shows the image corresponding to 1

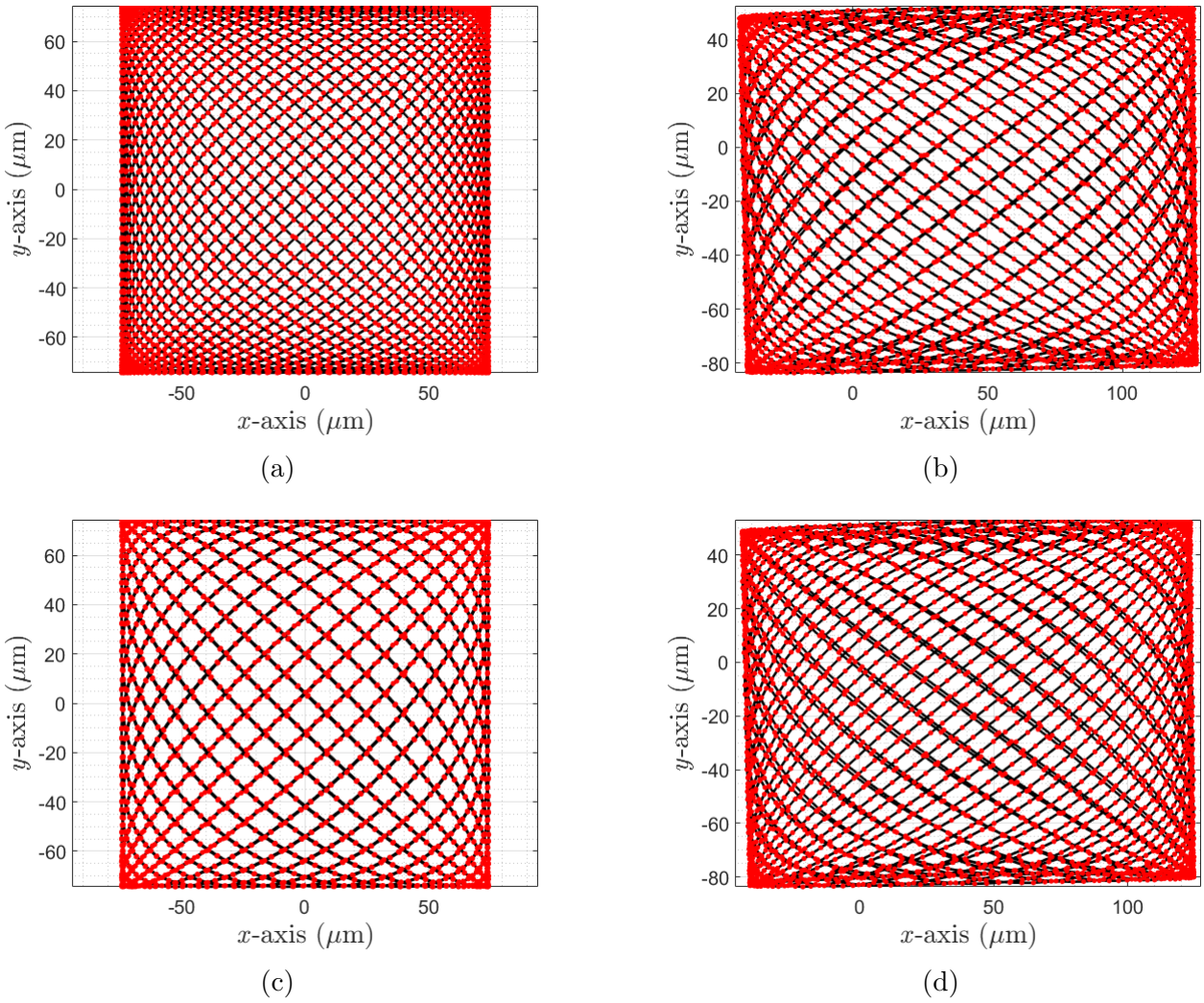

Figure 5.15: (*a*) Simulated Lissajous pattern produced with the amplitudes and frequencies of the option No. 4 of table 5.2 for $t = 30.3$ ms (1 frame). (*b*) Measured pattern when the scanner is driven with the same parameters during the same time. (*c*) Simulated and (*d*) measured Lissajous pattern with the phase adjustement (1 frame). The sampling points are colored in red.

frame ($t = 30.3$ ms) and Fig. 5.17b to 10 frames ($t = 303$ ms) averaged. Only the high reflective surface can be detected. Finally, the peel of an onion was scanned and the images are shown in Fig. 5.17c (1 frame) and 5.17d (10 frames averaged). In this case, one of the internal layers could be observed.

The previous scanned samples do not have spatial information that allows to know if the reconstruction of the 3D image is performed correctly. In order to confirm this, a pinhole of 300 μm of diameter was used as a sample (Fig. 5.18a). In this way, a lost of signal should be seen in the middle of the image. The $FOV_{\mu m}$ of 169.7 x 136.5 μm^2 of the Lisssajous pattern is not enough to cover the pinhole, therefore, the amplitude of the input signals was increased by a factor of 4:

$$U_x(t) = 2\,\mathrm{V} + (0.36\,\mathrm{V})\sin[2\pi(957\,\mathrm{Hz})t] \tag{5.46}$$

$$U_y(t) = 2\,\mathrm{V} + (0.4\,\mathrm{V})\sin[2\pi(924\,\mathrm{Hz})t] \tag{5.47}$$

The measured Lissajous pattern during $t = 30.3$ ms (1 frame) is shown in Fig. 5.18b where the

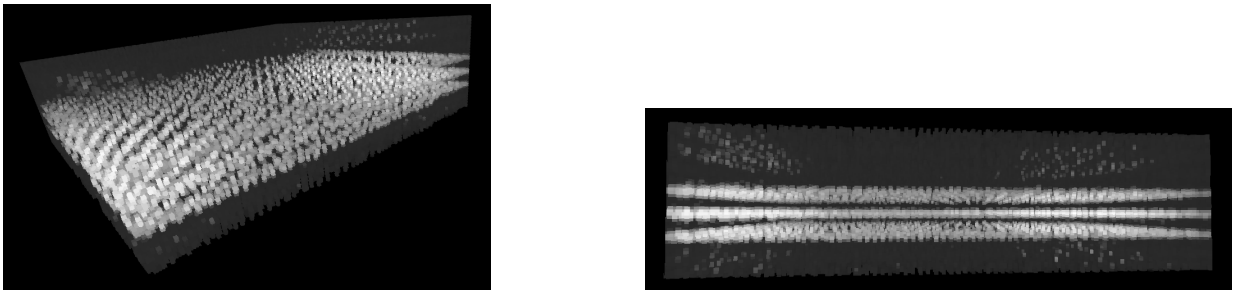

(a) (b)

Figure 5.16: (*a*) 3D OCT image of a sample made of 3 layers of cover glass. Measurement time $t = 30.3$ ms (1 frame). (*b*) Lateral view.

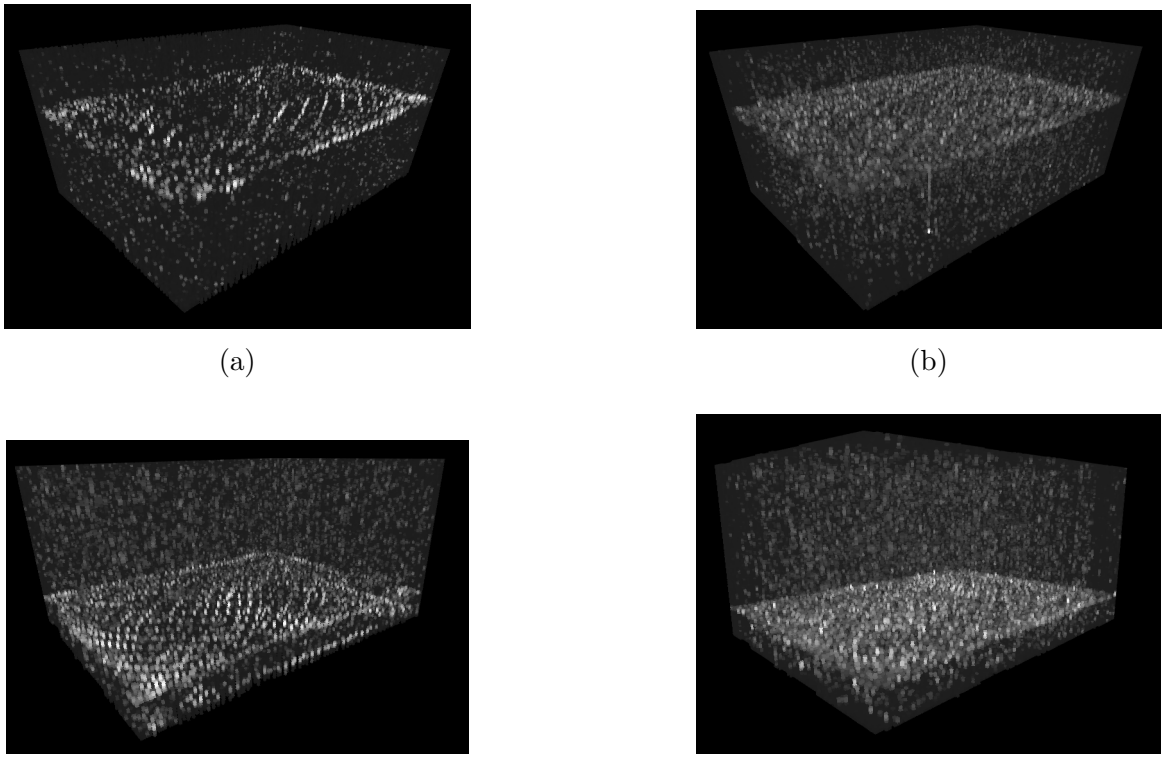

(a) (b)

(c) (d)

Figure 5.17: 3D image of the smooth surface of the Thorlabs card VRC2: (*a*) 1 frame (*b*) 10 frames averaged. Image of an onion peel: (*c*) 1 frame (*d*) 10 frames averaged.

$FOV_{\mu m} \approx$ 574.9 x 539.7 μm^2. The distorted trajectory close to the middle of the image and the modification of phase in both axes remained unexplained at this stage of the project. More tests are needed to understand the effect in the Lissajous trajectory caused by an increase in the amplitude of the input signals. The reconstructed 2D image of the plane where the pinhole is placed is presented in Fig. 5.18c. Since the external frame of the Lissajous pattern is tilted, a convex hull algorithm was applied to produce a squared FOV. All pixels in blue are not reached by the scanning trajectory. Notice that there are many of them in the middle of the image as a consequence of increasing the FOV since the crossing lines of the trajectory are more separated. In this image, it is difficult to see if the reconstruction has been made correctly. Interpolation of the data must be performed in order to fill the mising pixels and get the complete image. We used

the function in Matlab "inpaintExemplar" that makes this processing by the inpainting method. Figure 5.18d shows the resultant image where it can be seen that the image of the pinhole (a lost of signal in the middle) is not retrieved. However, some empty spaces are appreciated suggesting that there is a delay between the A-scans acquisition and the recording of the position of the laser beam on the PSD. We added several delays to the A-scans data with the respect to the first position of the Lissajous trajectory and found that for a delay of 318.18 μs (35 A-scans), the image of the pinhole can be reconstructed and is shown in Fig. 5.18e. The reconstruction in 3D is presented in Fig. 5.18f.

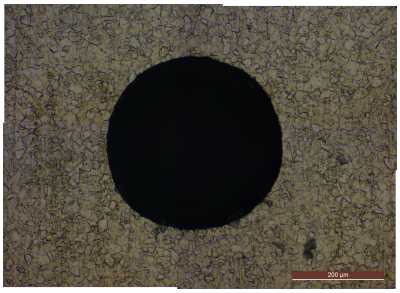

(a)

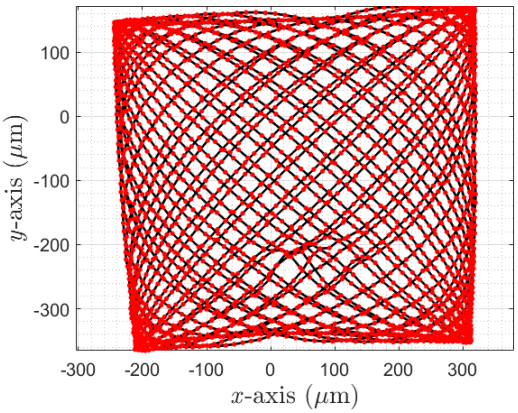

(b)

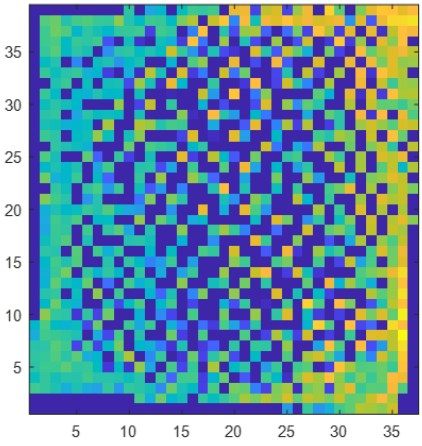

(c)

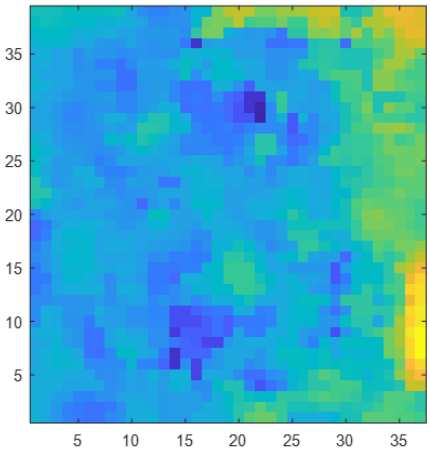

(d)

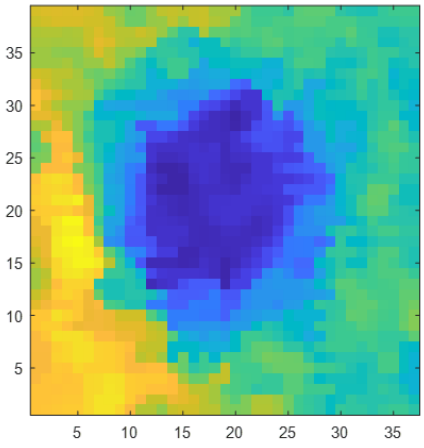

(e)

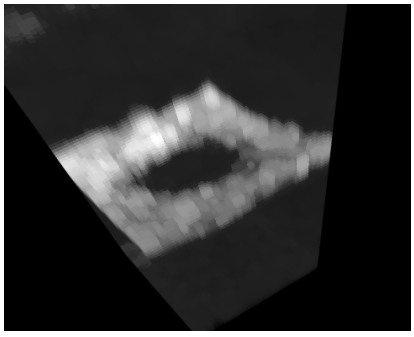

(f)

Figure 5.18: (a) Image of the pinhole obtained with an optical microscope (Leica DM8000). (b) Lissajous trajectory produced by increasing the amplitudes of the input signals by a factor of 4. (c) Reconstructed 2D image in the plane of the pinhole. The units in the x and y axes refer to pixels. (d) Image after interpolation. (e) Image with a delay of 318.18 μs in the A-scan acquisition. (f) Reconstructed 3D image of the pinhole.

5.6 Conclusion

The final version of the SS-OCT system, that includes the components to drive and characterize the micro scanner, was presented. Additionally, the characteristics of the electrical signals that should be applied in each actuator were explained. The measured resonance frequencies of the scanner were 943 Hz and 945 Hz for the x and y axis, respectively. Besides, a linear relation between the increase in the amplitude of the input signals (V_x and V_y) and the increase in the angular displacement peak-to-peak (θ_{pp}^{opt}) was observed in both axes.

Regarding OCT imaging with the fully integrated probe, the power of the laser beam at the output decreases from 2.18 mW to 0.8 mW (drop of 63 %) because of the presence of a not optimal metal coating of the micro mirror. Apparently, the micro mirror is absorbing 1.38 mW (37 %) and does not allow that an enough quantity of power is directed to the sample. This causes very weak back reflections from it producing almost no interference signals and images with very low intensity. There is a decrease of SNR of 16.3 dB in the image of the onion when compared to the image taken without the scanner integrated. This problem is related to a Cr layer of 15 nm that was used to coat the micro mirror to protect it from oxidation. This material is a bad reflector (R $\approx$ 62 %) in the range of the wavelength of the swept source (840 nm). Besides, this Cr layer has $\approx$ 50% of transmittance deteriorating the total reflectance of the Al micro mirror. As a consequence, only high reflective samples can be scanned with this probe.

For the Lissajous pattern used in this work, we selected the range of frequencies 894 Hz - 988 Hz for the x-axis and 894 Hz - 991 Hz for the y-axis, since there is a gain higher than 0 dB. We calculated the frame rate (FR) and the field of view (FOV) of the Lissajous trajectories produced with all the combinations of frequencies in these ranges, restricting those ones with a crossing point frequency (F_{cp}) less than 110 kHz (A-scan frequency of the swept source), that cannot be reconstructed completely. Between all these patterns, we choose one with $FR = 33$ fps and a $FOV = 149$ μm^2 (produced with the frequencies $f_x = 957$ Hz and $f_y = 924$ Hz) since the FOV is one of the largest possible allowing a broader scanned area of the sample and the values of the amplitude of the driving input signals are similar ($V_x = 0.090$ V and $V_y = 0.106$ V) avoiding a big difference of voltage in both axes that could result in the scanner damage. The measured Lissajous pattern has $FOV \approx 169.7$ x 136.5 μm^2 and the external frame is tilted because of the cross-coupling between both axes. Nevertheless, the crossing lines of this trajectory in one direction are overlapped because of a possible dephasing between the electrical input signals and the displacement of the laser on the PSD. We tried to correct this problem by adjusting the phase of the input signals but without success. This behaviour of the Lissajous trajectory remains unexplained at this stage of the project.

At the end, highly reflective samples (glass, Thorlabs card, onion) were scanned with this Lissajous pattern and 3D images could be reconstructed. When scanning a pinhole, we found a delay of 318.18 μs between the A-scan acquisition and the position of the laser beam on the PSD. This delay must be compensated to reconstruct a 3D OCT image.

Conclusions and perspectives

OCT has been successfully used in several fields of medicine, mainly in ophthalmology and dermatology, as a modern, high resolution and non-invasive optical diagnostic tool. The importance of this method will continue to increase with intense research and experimental development towards more performant OCT systems to support existing and new applications in oncology, cardiology, neurology, dentistry or cosmetics. According to the Future Market Insights (FMI) survey, the global OCT market worth has reached 912Mn US$ in 2021 and it is forecast to grow continuously to surpass 1349Mn US$ in 2031 with 6.7% CAGR (Compound Annual Growth Rate) [146].

In the gastroscopy field, the combination of OCT with endoscopic systems allowed the scanning of internal organs in the GI tract and performing pain-free optical biopsies. In particular, SS-OCT has gained special attention in the last years over other OCT modalities due to its capability of fast (real time) revealing microstructural abnormalities as small as < 10 μm in neoplastic tissue, despite the physiological movements of the human body. The obtained OCT images can be correlated with pathophysiology of various diseases of the GI tract, based on well observed non-uniformities of the internal layers of gastric tissues, as well as differences in their optical scattering properties. These features made the endoscopic SS-OCT technique a well suitable option for early diagnosis of GI cancers to increase significantly the chances of patient surviving. However, endoscopic SS-OCT is not a standard procedure and its promotion encounters various difficulties related to, among others, not-sufficient miniaturization of the endoscope to reach "remote" places, limited real-time control of the imaging probe in terms of stability and position accuracy, difficulties of analysis of OCT data (large amount of data, limited transfer speed) or existing limitations of OCT imaging performances (ghosts/motion artifacts).

We believe that breakthrough advances in this field can be achieved by an appropriate combination of two enabling technologies: MOEMS and Microrobotics. MOEMS technology allows high level miniaturization of endoscopic systems by strong size reduction of its passive/active components (i.e. lenses, scanning mirrors) that can be batch fabricated and smart integrated within heterogeneous systems. Microrobotics allows an improved maneuverability of endoscopic probes thanks to continuously bending robotic structures as well as an stable and accurate positioning of the probes by local microrobotic positioners, with compensation of physiological motions. These two technologies are complementary, e.g. a robot-assisted endoscope may improve the OCT imaging procedure (optical biopsy) or an OCT signal may be used to guide a robotic endoscope, for example, during a surgery procedure (determination of the borders of the lesion to be removed).

The overall goal of this work was to address the difficulties of early detection of cancer in the

human gastrointestinal tract and to develop a complete endoscopic-based solution for real-time, high-resolution and non-invasive OCT imaging (optical biopsy), using MOEMS technology.

Based on previous works carried out in the MOEMS Group of FEMTO-ST/MN2S, several technical solutions have been undertaken and further improved in this thesis to address various imaging difficulties, raised in the literature.

- The SS-OCT modality is employed as a modern and optical-fiber compatible solution in order to ensure a high A-scan frequency capability and a high axial optical resolution due to its short wavelength and relatively large sweep range. The employed EXALOS ESS-840 laser source (acquired in previous works) is characterized by an A-scan frequency of 110 kHz, a central wavelength of 840 nm and a sweep range of 60 nm, resulting in a theoretical axial resolution of 5.2 μm. It is worth to note that the selection of this sweep source advantages optical resolution at the expense of penetration depth.

- To address the overall miniaturization of the SS-OCT system, its core bulky component (optical fiber Michelson interferometer) is replaced by a Mirau micro-interferometer and integrated into the imaging probe. As a consequence, a common-path interferometric setup is created, in which a reference signal is generated within the sample arm. According to the bibliography revised here, the common-path configuration is appropriate to perform endoscopy since the reference mirror is placed in the probe itself. This makes the system insensitive to small optical path-length differences between the reference and sample arms generated typically by temperature variations of the environment or fiber bending by the robotic arm. Hence, common-path configuration addresses also some practical issues related to the usage of long optical fiber-based probes. Moreover, such Mirau-based probe performs 2D and 3D OCT imaging with ≈ 10 μm transversal resolution (as confirmed successfully in the proof-of-principle experiments by scanning the sample with the motorized stage) that is compatible with early-stage cancer detection specifications.

- MOEMS technology is used to address an improved manufacturability of advanced imaging probe at lower cost, in case of mass production. The two key building components of the OCT probe, i.e. Mirau micro-interferometer and micromirror scanner, demonstrate the great potential of MOEMS technology such as batch fabrication (229 Mirau micro-interferometers per 4" wafer), high level of integration due to vertical wafer-level bonding/stacking with precise lateral/axial optical alignment ($\approx 5/25$ μm, respectively), or possibility to perform a fast movement (in kHz range) of the Si-based micromirror at very low voltages.

- A 2-axis electrothermal scanning micromirror is employed to address the general need of a miniature but high-speed scanning component. It demonstrated real-time imaging based on Lissajous scanning at high resonance frequencies (0.9 - 1.2 kHz in both axes). Moreover, the very low driving voltages (< 5 V) meet the security requirements for endoscopic applications. It is noteworthy that the chip-level solution of the scanner releasing, employed in the technological process of this device, has imposed also a chip-level integration of the whole endoscopic probe.

In order to develop a complete endoscopic-based SS-OCT system, equipped with a operational MOEMS-based endoscopic probe, five main objectives have been defined in this work.

The first objective of this thesis concerned the fabrication of the probe by the integration of the existing MOEMS components and was achieved succesfully. The complete assembly procedure

consists of five steps and involves an active optical alignment between then micro-interferometer and the GRIN collimator, as well as the electrical interconnection of the scanner with a flexible PCB. An important complication discovered in this phase of integration was the low angle of the micromirror frame ($\approx 33°$) coming from an still not-optimized fabrication process of the scanner. This angle could be adjusted at 46° approx. (to avoid direct back reflections from the sample produced at 45°) by the design and fabrication of an adapted glass structure placed on the base of the scanner. Nevertheless, this integration method is time consuming and tedious making the fabrication of new probes a very slow process (1 week). This drawback can be addressed by the integration of the micro-interferometer and the micro scanner at wafer level rather than at chip level. In other words, the wafers where these components are fabricated should be aligned and bonded before the dicing process, integrating all the probes available on the wafers in only one step. Currently, there are 230 inteferometers in one wafer and 279 micro scanners in other one. The design of these components on the wafers must be modified and adapted to make them fit.

Another important disadvantage is the size of the integrated probe. The external frame of the micro-interferometer (4.7 x 4.7 mm^2) is too large to fit in the internal channel of a gastroscope which ranges from 2.8 to 3.8 mm in diameter. Although the size of micro-interferometer can be simply reduced by cutting smaller chips from the wafer stack (3.2b) to the limit of the glass lens diameter (1.9 mm), a further reduction of the existing scanner size (4 x 4 mm^2) is more difficult. An electrothermal micro scanner with a mirror frame size of only 1.2 x 1.2 mm^2 and the same type of double S-shaped actuators (Fig. 2.11b), was already reported in [93]. Furthermore, its mirror frame bends at 45° through a similar parallel bimorphs array and a stopper mechanism as the scanner utilized in this probe. This important quality would avoid the steps of fabrication and time consuming integration of the angle corrector. Hence, a modification of the design of this scanner could be considered for the fabrication of future probes making it adaptable for the integration with the micro-interferometer. Currently, this smaller scanner has a cavity for alignment with the GRIN lens that makes it big ($\approx$ 2.22 mm x 6.78 mm, table 2.4, Duan *et al.* 2016) and not compatible with our probe. After fixing all these issues, the encapsulation of the probes must be also carried out since presently, there is no any protection. Mu *et al.* propose a toroidal shape for encapsulation rather than a cylindrical one since this last structure produces astigmatism in the images [94]. These type of considerations must be also taken into account for final versions of the OCT probe.

The second objective concerned the characterization of the scanning performances of the probe. For this purpose, the SS-OCT system was successfully equipped with additional hardware modules to drive the scanner (NI DAQ card, small PCB, power circuit, power supply) and to characterize the movement of its micro mirror (PSD controller, laser at 635 nm). A control software was developed in LabView to measure the magnitude and phase of the frequency response of the scanner in both axes. These data were used to estimate various parameters, including the resonance frequencies, scanning angle and the scanned distance in the plane of the sample (Table 5.1). In general:

- The resonance frequencies are 943 Hz for the x-axis and 945 Hz for the y-axis. These frequencies are lower than those ones reported for other micro scanner of the same batch (1186 Hz and 1179 Hz) which was not integrated with a micro-interferometer (Table 2.5) [136]. The influence of the angle corrector and the integration with the micro-interferometer on the resonance frequencies of the micro scanner must be analyzed in future tasks of this project.

- The scanning angles are 7.8° for the x-axis and 10° for the y-axis at the resonance frequencies.

These angles were achieved with sinusoidal driving signals with $V_b = 2$ V, $V_x = V_y = 0.1$ V (low driving voltage chosen for security reasons).

- There is a linear relation between the amplitude of the driving input signals and the scanning angle in both axes. This simplifies the control of the scanning process.

The main issue of this probe is related to the very low reflectivity of the micro mirror, coated with Cr/Al/Cr thin-film multilayer, which is not well adapted for the wavelength range of the employed swept source (840 nm). The power of the laser beam decreases significantly to 37 % of its initial power after reflection from the bottom surface of the micro mirror. As a consequence, only highly reflective samples could be successfully scanned with the fully integrated probe. New scanners should be fabricated with gold thin-film coating on the silicon mirror in order to increase its reflectivity. Besides, the low scannning depth of ≈ 250 μm (Thorlabs card) of the probe is not enough to scan the mucosa of GI organs that, in the case of the stomach, ranges from 1030 to 1640 μm. We observed that the image of the sample was produced only in this small distance. The intensity of the OCT signal decreased significantly out of this scanning depth. This problem is related to the overall low sensitivity of the system. As we showed in section 3.3, there is a decrease in SNR of 50.88 dB when compared with a commercial system.

The measurement setup, presented in this work, can be used to drive and characterize future OCT probes. However, the power circuit needs to be improved since, sometimes, peaks of current damaged the actuators of the micro scanner, as shown in Fig. 5.19. We observed that these peaks are produced when, in the software, the amplitude of the input signals (V_x, V_y) is introduced before the DC voltage (V_b). This mistake is easy to make when working in the experimental setup but it can be avoided by the implementation of an electronic surge protection in the power circuit. Also, the algorithm should be improved in such a way that any amplitude signal (V_x, V_y) is sent to the scanner until the DC voltage (V_b) is already active. It is very important to implement these improvements in the setup since a new probe must be integrated again and characterized when one of the actuators of the scanner is damaged. As we showed in chapter 4, this process is very tedious and time consuming.

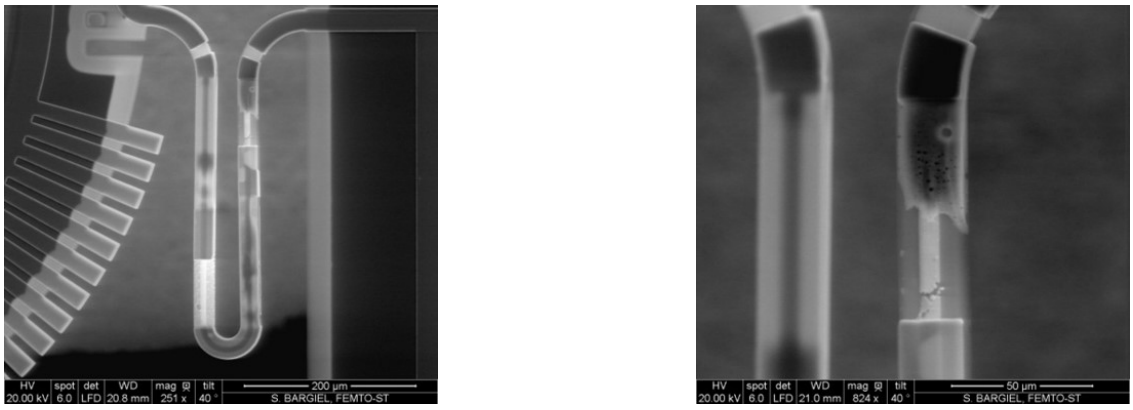

(a) (b)

Figure 5.19: (a) SEM image of a damaged electrothermal actuator. (b). Zoom in the burned part where the Pt heater line is exposed and interrupted.

The above mentioned issues lead us to the several recommendations for a new generation of the OCT probe from the design and technological point of view. The current device should be redesigned:

- To ensure a smaller size (≈ 2 mm) to be compatible with the internal channel of conventional gastroscopes while keeping a similar diameter of the micromirror.
- To increase the difference in the resonance frequencies between the x and y axis of the micro scanner in order to lower the mechanical coupling.
- To suppress back reflections in the probe, mainly in the glass layers inside the micro-interferometer to decrease artifacts in the OCT images.

The technological process should be modified:

- To adjust the inclined position of the micromirror frame at $\approx 46°$ (remove the angle corrector). Indeed, in the literature, angles of approximately 47° or 43° are chosen in order to deviate the specular reflexion from the optical axis.
- To improve the quality of the contact pads of the micro scanner in terms of adhesion.
- To replace the existing micromirror coating by a high quality Au-based in order to maximize the reflectivity.
- To perform the integration of the micro-interferometer with the microscanner at a wafer level rather than at chip level.

The third objective of this thesis, that concerned the implementation of the MOEMS OCT probe into the first generation of the SS-OCT experimental system, was achieved successfully. As a first step, the capacity of the simplified probe with the Mirau micro-interferometer (without the micro scanner integrated) to produce OCT images was tested. Then, the data processing to obtain an OCT image from this setup was explained and performed. A sample made of two layers of photoresist was scanned using a motorized translation stage and the different internal layers could be observed in the image. Some artifacts were observed because of parasitic reflections in the components of the SS-OCT setup. However, they could be removed by substracting the background shape obtained by averaging all the A-scans of the image. Due to these initial tests, the capacity of the Mirau micro-interfometer to perform OCT imaging was confirmed successfully. Additionally, 3D images of the sample of photoresist layers and other one made of 3 layers of tape with paper at the bottom were also obtained by scanning the sample with the motorized stage using raster scanning. This test allowed to visualize the type of 3D images that could be produced with the probe after the integration of the micro scanner. Further, the layer of paper could be observed in the image suggesting that the probe is able to detect diffusive samples such as biological tissues.

In order to enhance the OCT image quality, several devices were implemented in the first generation of the SS-OCT system to supress the noise produced by intensity fluctuations of the swept source (dual balanced detector) and decrease the contribution of the DC component in the interferograms (variable optical attenuator). Additionally, we scanned a Thorlabs card with a reflective and a difussive surface to produce and analyze the OCT images obtained with the forward and backward sweeps of the swept source. Both surfaces could be well appreciated but there was a decrease in SNR of 4.4 dB in the image created with the backward sweeps whose cause could not be explained. Furthermore, we found that averaging 10 frames after performing FFT does not increase the SNR notably compared with only one frame but improves the quality of the images in both sweep directions. Nevertheless, when averaging is carried out before applying FFT,

there is an increase in SNR of 8.79 dB (forward sweeps image) and 9.33 dB (backward sweeps image) in comparison with performing this step after FFT.

In addition to the decrease of SNR in the images produced with the backward sweeps, other issue related to the swept source was the trigger signal. It presents a delay of 2.8 μs with respect to the sweep cycles that could be compensated in the data post processing. However, we also observed a strange behaviour in this signal. In some tests, the rising edge of the pulses were found to be close to the beginning of the forward sweeps and, in other tests, to the beginning of the backward sweeps. Actually, this was other of the reasons why we decided to register the trigger signal in the CH2 of the GaGe DAQ, i.e. to ensure in the post processing that the pulses corresponded to the beginning of the sweep cycles. The swept source utilized in this work was specifically developed to work at a relatively short central wavelength of 840 nm and can be considered experimental since the quantity of swept sources for this wavelength was very limited at the time when it was acquired. We consider that rather than trying to fix these problems, the best solution would be to buy a new swept source as that this technology is more developed nowadays. For example, Axsun technologies has produced faster swept sources whose speed ranges from 1 to 400 kHz for central wavelengths of 1060, 1220 and 1330 nm. Using a laser with longer wavelengths will decrease the axial resolution (Eq. 3.2) but, on the other hand, it would increase the penetration depth allowing to scan innermost layers of the GI organs. Additionally, a more developed swept source will have a stable trigger signal that will not recquire a delay compensation.

The fourth objective concerned the software development to control the SS-OCT system and to produce OCT images. All the sofwares developed in this work were successfully finished and validated, namely:

1. Software that registers the Ch1 (interference signals) and Ch2 (k-clock signals) of the GaGe-DAQ card while moving the motorized stage to perform B-scans or C-scans.

2. Software in Matlab to process the OCT and the k-clock signals to produce an OCT image according to the diagram of Fig. 3.5 (section 3.2). This program also performs artefact remotion by the method presented by Wang *et al.* [127].

3. Software in Matlab to process the OCT and the trigger signals to produce an OCT image according to the diagram of Fig. 3.14 (section 3.3). This program compensates the delay between the sweep cycles and the pulses of the trigger signal, separates the sweep cycles in the forward and backward direction, removes artefacts, makes the resampling with a calibration vector measured in a previous test, applies FFT and performs averaging of 10 frames at the end.

4. Software in Matlab to process the OCT and the trigger signals to produce an OCT image. It works in a similar way that the program described in the last point but it performs averaging before applying FFT.

5. Software in LabVIEW that controls the final version of the SS-OCT system (Fig. 5.1a). It drives the scanner with electrical signals (see Fig. 5.3) using a NI-DAQ card, registers the Ch1 (OCT signal) and Ch2 (trigger signal) of the GaGe-DAQ card, monitors the scanning trajectory of the visible laser using the PSD, registers this position using the controller of the PSD and the NI-DAQ card and synchronizes the starting time of the acquisiton of Ch1 and Ch2 of the GaGe-DAQ and the starting time of the generation of the electrical driving signals of the scanner.

6. Softwares in LabVIEW to drive the scanner at different frequencies in order to obtain the data through the PSD and its controller to calculate the frequency response in both axes (see section 5.2).

7. Software in Matlab to analyze the data obtained by the program mentioned in the last point. This software estimates the magnitude and phase frequency response, optical angular displacement, angular gain, scanned distance in the plane of the sample and cross-coupling percentages between both axes (see section 5.2). From these data, the program calculates some parameters of the Lissajous patterns (see table 5.2) produced with all the combination of frequencies (f_x and f_y) that produce an angular gain bigger than 0 (see section 5.4).

8. Software in Matlab to process the data recorded by the program described in the point 5. It takes the data of the signals Δx, Δy and SUM from the controller of the PSD to calculate the scanning Lissajous pattern in the plane of the sample as explained in section 5.4. Then, it processes the OCT and trigger signals according to the diagram of Fig. 3.14 to obtain the A-scans for each sampled point of the Lissajous trajectory. At the end, a 3D matrix is created and all the A-scans are arranged in it according to the positions of this trajectory. When there is more than 1 frame, the program averages all the A-scans that have the same position. The resultant images are those ones that were shown in Figs. 5.16 and 5.17.

9. Software in Matlab to find and correct the delay between the A-scans acquisition and the recording of the position of the laser beam on the PSD, in 3D imaging. Interpolation is also performed in this program. (see Fig. 5.18).

As with the SS-OCT experimental setup, these softwares can be used to drive and characterize future improved probes as well as to produce 2D and 3D OCT images.

With respect to the final objective of this thesis, Lissajous scanning was successfully implemented from hardware and software point of view. The frequencies of the input signals were selected in the range where the angular gain is bigger than 0. In this resonance bandwidth, the optical angular displacement is increased more than at low frequencies (10 Hz), due to the resonance frequency of the scanner and not to an increase in amplitude of the input signals. This allows to scan bigger distances at low voltages. Nevertheless, the crossing lines in one direction in the resulting Lissajous pattern were overlapped because of, what we believe, a dephase issue between the input drving signals of the scanner and the response of the actuators. This strange behavior must be analyzed and corrected in future stages of the project. As it was shown at the end of section 5.5, there is a delay of 318.18 μs between the data recording of the A-scans and the movement of the visible laser on the PSD. However, this delay could be compensated in post processing. Although several issues have been identified to be solved in the future, real-time scaning at 33 fps was successfully demonstrated using highly reflective samples. Altough this very promising achievement could not be fully exploited with biological samples because of the mentioned problem regarding the low optical power, B-scans of peels of banana and onion were produced with external scanning (samples scanned by the motorized stage while keeping the micromirror static), revealing successfully some internal structures.

Additionally, we showed that the FOV can be increased by applying higher amplitudes in the driving input signals (V_x, V_y) but with the consequence of missing more pixels in the image. This characteristic would allow to scan bigger areas to locate the presence of a suspected tumor (preview at lower resolution) and then, the FOV can be decreased to scan a smaller area but with more pixels reached by the scanning beam (zoom at high resolution). Table 5.3 summarizes the main

problems found in this project and the proposed solutions and table 5.4 the characteristics of our system. The max. angles correspond to those ones achieved at the resonance frequency and the characteristics of the images, to those ones presented in section 5.5.

Table 5.3: Problems found during the project and proposed solutions.

Problem	**Solution**
1. Probe related issues	
Micro scanner	
The micro mirror has low reflectivity.	Coat with gold the surface of the micro mirror.
The quality of the contact pads is low (cracs, bad adhesion, higher resistance) due to inter-metallic thermal diffusion between Al-based contact and external Au coating during high temperature SiO_2 deposition (300°). Direct wire bonding with Au wires is not feasible.	To modify the fabrication process to assure high quality contact pads. Both Au and Al based pads are compatible with electrically conductive silver-based epoxy used in this work for adhesive bonding.
The micro mirror frame of the scanner is at very long angle 33°.	Optimize the fabrication process of the scanner to increase this angle at 46°.
Micro interferometer	
Some artifacts appear in the image because of the reflective layers of the beam splitter and the lens.	Use anti reflection coating in these reflective layers.
General	
The integration process is time consuming.	Integrate the micro interformeter and the scanner at wafer level (both designs must be modified).
The integrated probe is too big to fit in the internal channel of an endoscope.	Reduce the size of the components of the probe by new designs.
2. Laser source related issues	
There is a decrease of SNR in the images produced with the backward sweeps.	Buy a more modern and stable swept source.
There is instability and a delay in the trigger signal.	Buy a more modern and stable swept source.
3. Micro scanner power source related issues	
Peaks of current produced by the power circuit can damage the actuators.	Implement an electronic surge protection in the power circuit.
4. Lissajous control related issues	
The Lissajous pattern presents a deformation and overlapped crossed lines in one direction.	Study the effect of dephasing between the input signals and the response of the scanner.

This work was carried out in the context of the ROBOT project (INSERM, 2017-2021), targeting the development of a robotized OCT-based endoscope for optical biopsies in the GI tract. More precisely, it was part of the workpackage Wp2 (MOEMS design and experimental validation) but it supported partially other tasks of the project defined in WP3 (Compressed OCT scanning) and WP4 (OCT for robot-assisted optical biopsy). It is worth to mention the multidisciplinary aspect of this thesis work. Indeed, the realization of the objectives benefited from the wide collaboration

Table 5.4: Characteristics of our system.

1. OCT unit specifications
(a) OCT mode: Swept Source OCT
(b) Light source (EXALOS ESS-840) - Central wavelength: 840 nm - Swept range: 60 nm - A-scan rate: 110 kHz
2. Optical fiber scanning probe specifications
(a) Probe head size: 4.7 x 4.7 x 20 mm^3 (no housing)
(b) Electrothermal micromirror scanner - Scanner chip size: 4 x 4 mm^2 - Micromirror: Cr/Al/Cr (coating type), 1 mm / 15/400/15 nm (diameter / thickness) - Resonance frequency (measured): 943 Hz (x-axis), 945 Hz (y-axis) - Max driving voltage: 5 V (static), 3.1 V (resonance) - Max scan angle: 7.8° (x-axis), 10° (y-axis)
(c) Mirau micro interferometer - Mirau chip size: 4.7 x 4.7 x 5.3 mm^3 - Reference mirror: Ti/ Ni/Au (metal type), 150 μm (diameter) - Lens: Borofloat33 glass (material), 1.9 mm (diameter), no AR coating - Beamsplitter: TiO_2 (material), 70:30 (transmission/reflection ratio)
(d) GRIN single mode fiber collimator (GRIN Tech, Germany) - Lens GT-LFRL-180-025-20-NC - Lens diameter: 1.8 mm, 0.25 pitch@840nm, length 11.11 mm, NA 0.2, non-coated - Stainless steel tube: OD 2.3 mm, length 15mm, lens protrudes 0.2 mm - Diameter of light beam: 1 mm ($1/e^2$)
(e) Optical fiber SMF Nufern, length 1 m, 0.9 mm tubing, One side: FC/APC connector. Other side: glass ferrule 1.8 mm
3. Optical performances of the system
- Axial resolution (theoretical, in air): 5.2 μm - Lateral resolution (measured in static, in air): 9.7 μm
4. 3D OCT imaging performance
(a) Scanning type: Lissajous
b) Scanning object: glass, onion, banana, diffusive card
(c) Selected scanning parameters - Scanning rate: 33 fps - Scanning frequencies: 957 Hz (x-axis), 924 Hz (y-axis) - Corresponding FOV: 169.7 x 136.5 um^2 - Penetration depth: 250 μm

with the research groups involved in the ROBOT project i.e. MOEMS group of MN2S (microsystems), AS2M (robotics) and ICube (endoscopic robotics) and also from the Staff of the MIMENTO cleanroom and other PhD students/engineers of FEMTO-ST regarding the microfabrication technology and characterization methods. In particular, the fruitful discussions with Dr. Przemyslaw Struk from the Silesian University of Technology (Poland), author of the first generation of the

SS-OCT system at FEMTO-ST, resulted in several system improvements.

In the frame of the ROBOT project, a principle of combination of a flexible endoscope with the MOEMS OCT probe was experimentally tested. A standard endoscope was equipped with two LED illumination spots, a CCD camera and two instrument channels. Since the current version of the probe is too big to fit inside the operational channel, three integration strategies were verified. In the first strategy, the OCT probe is protruding directly from the instrument channel of the endoscope (Fig. 5.20b). The probe operates in a well illuminated zone within a field of view of the camera but with very limited movement capability. In the second strategy, the OCT probe is attached to a flexible manipulator, installed in the instrument channel of the endoscope, by the use of a 3D printed holder (Fig. 5.20c). This configuration is beneficial due to the 3D movement capability of the probe, that operates in an illuminated zone within the field of view of the camera (Fig. 5.20d). In the third strategy, the OCT probe is attached to the endoscope by the use of external 3D printed clips (Fig. 5.20e). This is the worst-case configuration since the probe increases the external diameter of the endoscopic system and operates out of the view of the camera (Fig. 5.20f). Various plastic components were fabricated in the ICube Laboratory by the use of a high-resolution (15 μm) 3D printing to support the integration tests. In particular, the plastic model of the MOEMS OCT probe was used to avoid an accidental damage of the original one. A first version of the plastic capsule to protect the probe has been fabricated as well.

(a)

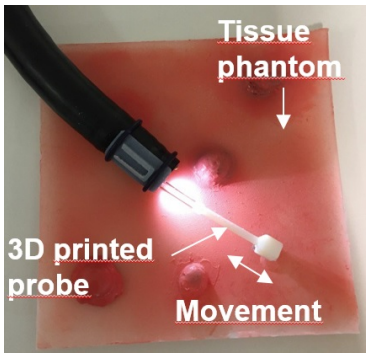

(b)

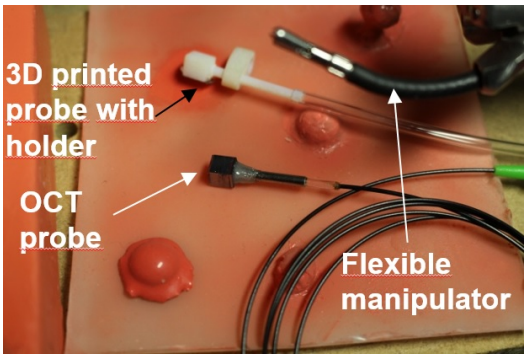

(c)

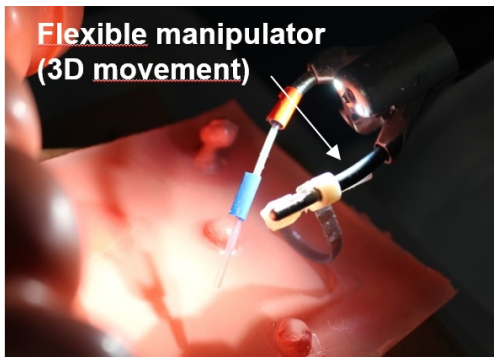

(d)

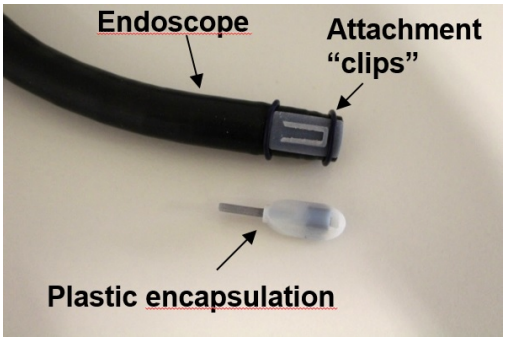

(e)

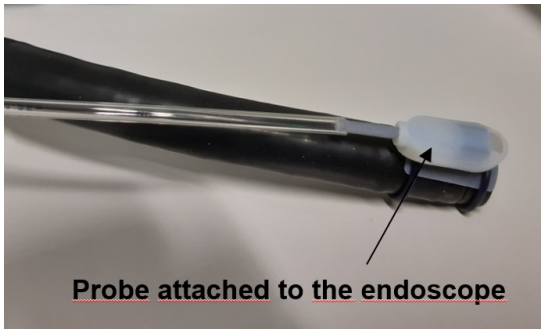

(f)

Figure 5.20: (*a*) From left to right: MOEMS OCT probe, 3D printed probe, 3D printed encapsulated probe, endoscope. (*b*) Strategy 1. 3D printed probe attached to the endoscope sumulating scanning in biological tissue. (*c*) and (*d*) Strategy 2. OCT probe attached to a flexible manipulator. (*e*) and (*f*) Strategy 3. OCT probe (encapsulated) attached to the endoscope by 3D printed clips

Bibliography

[1] M. Arnold *et al.*, "Global Burden of 5 Major Types Of Gastrointestinal Cancer," *Gastroenterology*, vol. 159, no. 1, pp. 335 - 349, 2020.

[2] N. Eleftheriadis *et al.*, "Definition and Staging of Early Esophageal , Gastric and Colorectal cancer," *J. Tumor*, vol. 2, no. 7, pp. 161 - 178, 2014.

[3] Rosen R. D., Sapra A. TNM Classification. [Updated 2021 Feb 23]. In: StatPearls [Internet]. Treasure Island (FL): StatPearls Publishing; 2022 Jan-. Available from: https://www.ncbi.nlm.nih.gov/books/NBK553187/

[4] A. Pennathur, M. K. Gibson, B. A. Jobe, and J. D. Luketich, "Oesophageal carcinoma," *Lancet*, vol. 381, pp. 400 - 412, 2013.

[5] S. Nagini, "Carcinoma of the stomach: A review of epidemiology, pathogenesis, molecular genetics and chemoprevention," *World J. Gastrointest. Oncol.*, vol. 4, no. 7, pp. 156 - 169, 2012.

[6] S. Bentley-hibbert and L. Schwartz, "Use of Imaging for GI Cancers," *J. Clin. Oncol.*, vol. 33, no. 16, pp. 1729 - 1736, 2015.

[7] R. S. Kwon, D. V. Sahani, and W. R. Brugge, "Gastrointestinal cancer imaging: Deeper than the eye can see," *Gastroenterology*, vol. 128, no. 6, pp. 1538 - 1553, 2005.

[8] T.-H. Tsai, J. Fujimoto, and H. Mashimo, "Endoscopic Optical Coherence Tomography for Clinical Gastroenterology," *Diagnostics*, vol. 4, pp. 57 - 93, 2014.

[9] F.-M. Lu and Z. Yuan, "PET/SPECT molecular imaging in clinical neuroscience: recent advances in the investigation of CNS diseases.," *Quant. Imaging Med. Surg.*, vol. 5, no. 3, pp. 433 - 447, 2015.

[10] C. H. Huh, M. S. Bhutani, E. B. Farfán, and W. E. Bolch, "Individual variations in mucosa and total wall thickness in the stomach and rectum assessed via endoscopic ultrasound," *Physiol. Meas.*, vol. 24, pp. N15 - N22, 2003.

[11] D. Huang *et al.*, "Optical coherence tomography," *Science*, vol. 254, no. 5035, 1178, 1991.

[12] T. -Tsai *et al.*, "Optical coherence tomography in gastroenterology : a review and future outlook," *J. Biomed. Opt.*, vol. 22, no. 12, 121716, 2017.

[13] J. Wang, Y. Xu, and S. A. Boppart, "Review of optical coherence tomography in oncology," *J. Biomed. Opt.*, vol. 22, no. 12, 121711, 2017.

[14] D. Panescu, "MEMS in medicine and biology," *IEEE Eng. Med. Biol. Mag.*, vol. 25, no. 5, pp. 19 - 28, 2006.

[15] C. Gorecki *et al.*, "Micromachined phase-shifted array-type Mirau interferometer for swept-source OCT imaging: design, microfabrication and experimental validation," *Biomed. Opt. Express*, vol. 10, no. 3, pp. 1111 - 1125, 2019.

[16] K. Hwang, Y. H. Seo, and K. H. Jeong, "Microscanners for optical endomicroscopic applications," *Micro Nano Syst. Lett.*, vol. 5, no. 1, pp. 1 - 11, 2017.

[17] P. Struk *et al.*, "Swept source optical coherence tomography endomicroscope based on vertically integrated mirau micro interferometer: Concept and technology," *IEEE Sens. J.*, vol. 15, no. 12, pp. 7061 - 7070, 2015.

[18] S. Bargiel *et al.* "Technological platform for vertical multi-wafer integration of miniature imaging instruments," *Proc. SPIE 9375, MOEMS and Miniaturized Systems XIV, 93750L*, 27/02/2015.

[19] Q. A. A. Tanguy, "Design and fabrication of a MEMS scanner for OCT imaging endo-microscopic probe," PhD manuscript, Université de Franche-Comté, Besançon, 9 Feb. 2018.

[20] Stifter *et al.*, "Advanced Optical Coherence Tomography techniques: novel and fast imaging tools for non-destructive testing" in *17th World Conference on Nondestructive Testing*, 25-28/10/2008.

[21] M. J. Gora *et al.*, "Tethered capsule endomicroscopy enables less-invasive imaging of gastrointestinal tract microstructure," *Nat. Med.*, vol. 19, no. 2, pp. 238 - 40, 2013.

[22] M. A. Duguay and A. T. Mattick, "Ultrahigh speed photography of picosecond light pulses and echoes," *Appl. Opt.*, vol. 10, no. 9, pp. 2162 - 2170, 1971.

[23] A. P. Bruckner, "Picosecond light scattering measurements of cataract microstructure.," *Appl. Opt.*, vol. 17, no. 19, pp. 3177 - 3183, 1978.

[24] H. Park, M. Chodorow, and R. Kompfner, "High resolution optical ranging system," *Appl. Opt.*, vol. 20, no. 14, pp. 2389 - 2394, 1981.

[25] J. G. Fujimoto *et al.*, "Femtosecond optical ranging in biological systems," *Opt. Lett.*, vol. 11, no. 3, pp. 150 - 152, 1986.

[26] R. C. Youngquist, S. Carr, and D. E. N. Davies, "Optical coherence-domain reflectometry: a new optical evaluation technique," *Opt. Lett.*, vol. 12, no. 3, pp. 158 - 160, 1987.

[27] A. F. Fercher, K. Mengedoht, and W. Werner, "Eye-length measurement by interferometry with partially coherent light," *Opt. Lett.*, vol. 13, no. 3, pp. 186 - 188, 1988.

[28] D. Huang, J. Wang, C. P. Lin, C. A. Puliafito, and J. G. Fujimoto, "Micron–resolution ranging of cornea anterior chamber by optical reflectometry," *Lasers Surg. Med.*, vol. 11, pp. 419 - 425, 1991.

[29] A. F. Fercher, C. K. Hitzenberger, W. Drexler, G. Kamp, and H. Sattmann, "In vivo optical coherence tomography," *Am. J. Ophthalmol.*, vol. 116, no. 1, pp. 113 - 114, 1993.

[30] E. A. Swanson *et al.*, "In vivo retinal imaging by optical coherence tomography," *Opt. Lett.*, vol. 18, no. 21, pp. 1864 - 1866, 1993.

[31] C. A. Puliafito *et al.*, "Imaging of macular diseases with optical coherence tomography," *Ophthalmology*, vol. 102, no. 2, pp. 217 - 229, 1995.

[32] M. E. Brezinski *et al.*, "Optical coherence tomography for optical biopsy. properties and demonstration of vascular pathology," *Circulation*, vol. 93, no. 6, pp. 1206 - 1213, 1996.

[33] G. J. Tearney *et al.*, "Scanning single-mode fiber optic catheter—endoscope for optical coherence tomography," *Opt. Lett.*, vol. 21, no. 12, pp. 543 - 545, 1996.

[34] J. Fujimoto and E. Swanson, "The development, commercialization, and impact of optical coherence tomography," *Investig. Ophthalmol. Vis. Sci.*, vol. 57, pp. 1 - 13, 2016.

[35] S. A. Boppart, M. E. Brezinski, C. Pitris, and J. G. Fujimoto, "Optical Coherence Tomography for Neurosurgical Imaging of Human Intracortical Melanoma," *Neurosurgery*, vol. 43, no. 4, pp. 834 - 841, 1998.

[36] Y. Pan and D. L. Farkas, "Noninvasive imaging of living human skin with dual-wavelenght optical coherence tomography in two and three dimensions," *J. Biomed. Opt.*, vol. 3, no. 4, pp. 446 - 455, 1998.

[37] J. M. Schmitt, "Optical coherence tomography (OCT): a review," *IEEE J. Sel. Top. Quantum Electron.*, vol. 5, no. 4, pp. 1205 - 1215, 1999.

[38] F. Fercher, K. Hitzenberger, G. Kamp, and S. Y. El-Zaiat, "Measurement of intraocular distances by backscattering spectral interferometry," *Opt. Commun.*, vol. 117, pp. 43 - 48, 1995.

[39] A. F. Fercher, "Optical Coherence Tomography," *J. Biomed. Opt.*, vol. 1, no. 2, pp. 157 - 173, 1996.

[40] M. Wojtkowski, "High-speed optical coherence tomography: Basics and applications," *Appl. Opt.*, vol. 49, no. 16, pp. D30 - D61, 2010.

[41] G. Häusler and W. M. Linder, "Coherence radar" and "spectral radar" - New tools for dermatological diagnosis," *J. Biomed. Opt.*, vol. 3, no. 1, pp. 21 - 31, 1998.

[42] M. Wojtkowski, R. Leitgeb, A. Kowalczyk, T. Bajraszewski, and A. F. Fercher, "In vivo human retinal imaging by Fourier domain optical coherence tomography," *J. Biomed. Opt.*, vol. 7, no. 3, pp. 457 - 463, 2002.

[43] S. Yun, G. Tearney, B. Bouma, B. Park, and J. de Boer, "High-speed spectral-domain optical coherence tomography at 1.3 μm wavelength," *Opt. Express*, vol. 11, no. 26, pp. 3598 - 3604, 2003.

[44] N. Nassif *et al.*, "In vivo human retinal imaging by ultrahigh-speed spectral domain optical coherence tomography," *Opt. Lett.*, vol. 29, no. 5, pp. 480 - 482, 2004.

[45] S. R. Chinn, E. A. Swanson, and J. G. Fujimoto, "Optical coherence tomography using a frequency-tunable optical source," *Opt. Lett.*, vol. 22, no. 5, pp. 340 - 342, 1997.

[46] F. Lexer, C. K. Hitzenberger, A. F. Fercher, and M. Kulhavy, "Wavelength-tuning interferometry of intraocular distances," *Appl. Opt.*, vol. 36, no. 25, pp. 6548 - 6553, 1997.

[47] B. Golubovic, B. E. Bouma, G. J. Tearney, and J. G. Fujimoto, "Optical frequency-domain reflectometry using rapid wavelength tuning of a Cr^{4+}: forsterite laser," *Opt. Lett.*, vol. 22, no. 22, pp. 1704 - 1706, 1997.

[48] S. H. Yun, G. J. Tearney, J. F. De Boer, N. Iftimia, and B. E. Bouma, "High-speed optical frequency-domain imaging," *Opt. Express*, vol. 11, no. 22, pp. 2953 - 2963, 2003.

[49] M. A. Choma, K. Hsu, and J. A. Izatt, "Swept source optical coherence tomography using an all-fiber 1300-nm ring laser source," *J. Biomed. Opt.*, vol. 10, no. 4, 044009, 2005.

[50] P. H. Tomlins and R. K. Wang, "Theory, developments and applications of optical coherence tomography," *J. Physicis D Appl. Phys.*, vol. 38, pp. 2519 - 2535, 2005.

[51] R. Huber, M. Wojtkowski, J. G. Fujimoto, J. Y. Jiang, and A. E. Cable, "Three-dimensional and C-mode OCT imaging with a compact, frequency swept laser source at 1300 nm," *Opt. Express*, vol. 13, no. 26, pp. 10523 - 10538, 2005.

[52] R. Huber, D. C. Adler, and J. G. Fujimoto, "Buffered Fourier domain mode locking: unidirectional swept laser sources for optical coherence tomography imaging at 370,000 lines/s," *Opt. Lett.*, vol. 31, no. 20, pp. 2975 - 2977, 2006.

[53] T. Klein, W. Wieser, C. M. Eigenwillig, B. R. Biedermann, and R. Huber, "Megahertz OCT for ultrawide-field retinal imaging with a 1050nm Fourier domain mode-locked laser," *Opt. Express*, vol. 19, no. 4, pp. 3044 - 3062, 2011.

[54] L. Schmitz, U. Reinhold, E. Bierhoff, and T. Dirschka, "Optical coherence tomography: Its role in daily dermatological practice", *JDDG - J. Ger. Soc. Dermatology*, vol. 11, no. 6, pp. 499 - 507, 2013.

[55] T. Wang *et al.*, "Heartbeat OCT: in vivo intravascular megahertz-optical coherence tomography," *Biomed. Opt. Express*, vol. 6, no. 12, pp. 5021 - 5032, 2015.

[56] G. J. Ughi *et al.*, "Clinical Characterization of Coronary Atherosclerosis With Dual-Modality OCT and Near-Infrared Autofluorescence Imaging," *JACC Cardiovasc. Imaging*, vol. 9, no. 11, pp. 1304 - 1314, 2016.

[57] S. P. Chong *et al.*, "Noninvasive, in vivo imaging of subcortical mouse brain regions with 1.7 μm optical coherence tomography," *Opt. Lett.*, vol. 40, no. 21, pp. 4911 - 4914, 2015.

[58] T. Akkin, D. Landowne, and A. Sivaprakasam, "Detection of neural action potentials using optical coherence tomography: intensity and phase measurements with and without dyes," *Front. Neuroenergetics*, vol. 2, no. 22, pp. 1 - 10, 2010.

[59] O. Assayag *et al.*, "Imaging of non-tumorous and tumorous human brain tissues with full-field optical coherence tomography," *NeuroImage Clin.*, vol. 2, pp. 549 - 557, 2013.

[60] D. Lorenser, X. Yang, R. W. Kirk, B. C. Quirk, R. A. McLaughlin, and D. D. Sampson, "Ultrathin side-viewing needle probe for optical coherence tomography," *Opt. Lett.*, vol. 36, no. 19, pp. 3894 - 3896, 2011.

[61] S. Lam *et al.*, "*In vivo* optical coherence tomography imaging of preinvasive bronchial lesions," *Clin. Cancer Res.*, vol. 14, no. 7, pp. 2006 - 2011, 2008.

[62] B. C. Quirk, R. A. McLaughlin, A. Curatolo, R. W. Kirk, P. B. Noble, and D. D. Sampson, "*In situ* imaging of lung alveoli with an optical coherence tomography needle probe," *J. Biomed. Opt.*, vol. 16, no. 3, 036009, 2011.

[63] H. Wang, W. Kang, H. Zhu, G. MacLennan, and A. M. Rollins, "Three-dimensional imaging of ureter with endoscopic optical coherence tomography," *Urology*, vol. 77, pp. 1254 - 1258, 2011.

[64] S. Kharchenko, J. Adamowicz, M. Wojtkowski, and T. Drewa, "Optical coherence tomography diagnostics for onco-urology. Review of clinical perspectives," *Cent. Eur. J. Urol.*, vol. 66, pp. 136 - 141, 2013.

[65] W. Drexler and J. G. Fujimoto, *Optical Coherence Tomography: Technology and Applications*, 2nd ed. Springer Reference, 2015.

[66] R. N. Bracewell, *The Fourier transform and its applications*, 3rd ed. McGraw-Hill, 2000.

[67] J. W. Goodman, *Introduction to Fourier Optics*, 2nd ed. The McGraw-Hill Companies, Inc., 1996.

[68] E. Hecht, *Optics*, 4th ed. Addison Wesley, 2002.

[69] R. Leitgeb, C. Hitzenberger, and A. Fercher, "Performance of fourier domain vs time domain optical coherence tomography," *Science*, vol. 11, no. 8, pp. 889 - 894, 2003.

[70] M. Choma, M. Sarunic, C. Yang, and J. Izatt, "Sensitivity advantage of swept source and Fourier domain optical coherence tomography," *Opt. Express*, vol. 11, no. 18, pp. 2183 - 2189, 2003.

[71] J. F. de Boer, B. Cense, B. H. Park, M. C. Pierce, G. J. Tearney, and B. E. Bouma, "Improved signal-to-noise ratio in spectral-domain compared with time-domain optical coherence tomography," *Opt. Lett.*, vol. 28, no. 21, pp. 2067 - 2069, 2003.

[72] J. F. de Boer, R. Leitgeb, and M. Wojtkowski, "Twenty-five years of optical coherence tomography: the paradigm shift in sensitivity and speed provided by Fourier domain OCT [Invited]," *Biomed. Opt. Express*, vol. 8, no. 7, pp. 3248 - 3280, 2017.

[73] M. J. Gora, M. J. Suter, G. J. Tearney, and X. Li, "Endoscopic optical coherence tomography: technologies and clinical applications [Invited]," *Biomed. Opt. Express*, vol. 8, no. 5, pp. 2405 - 2444, 2017.

[74] X. Liu, M. J. Cob, Y. Chen, M. B. Kimmey, and X. Li, "Rapid-scanning forward-imaging miniature endoscope for real-time optical coherence tomography," *Opt. Lett.*, vol. 29, no. 15, pp. 1763 - 1765, 2004.

[75] G. J. Tearney *et al.*, "In vivo endoscopic optical biopsy with optical coherence tomography," *Science*, vol. 276, pp. 2037 - 2039, 1997.

[76] A. Sergeev *et al.*, "In vivo endoscopic OCT imaging of precancer and cancer states of human mucosa," *Opt. Express*, vol. 1, no. 13, pp. 432 - 440, 1997.

[77] K. Kobayashi, J. A. Izatt, M. D. Kulkarni, J. Willis, and M. V Sivak, "High-resolution cross-sectional imaging of the gastrointestinal tract using optical coherence tomography: preliminary results," *Gastrointest. Endosc.*, vol. 47, no. 6, pp. 515 - 523, 1998.

[78] A. M. Rollins *et al.*, "Real-time in vivo imaging of human gastrointestinal ultrastructure by use of endoscopic optical coherence tomography with a novel efficient interferometer design," *Opt. Lett.*, vol. 24, no. 19, pp. 1358 - 1360, 1999.

[79] C. Pitris, C. Jesser, S. A. Boppart, D. Stamper, M. E. Brezinski, and J. G. Fujimoto, "Feasibility of optical coherence tomography for high-resolution imaging of human gastrointestinal tract malignancies," *J. Gastroenterol.*, vol. 35, pp. 87 - 92, 2000.

[80] H. L. Fu, Y. Leng, M. J. Cobb, K. Hsu, J. H. Hwang, and X. Li, "Flexible miniature compound lens design for high-resolution optical coherence tomography balloon imaging catheter," *J. Biomed. Opt.*, vol. 13, no. 6, 060502, 2008.

[81] K. Liang *et al.*, "Ultrahigh speed *en face* OCT capsule for endoscopic imaging," *Biomed. Opt. Express*, vol. 6, no. 4, pp. 1146 - 1163, 2015.

[82] H.-C. Lee *et al.*, "Circumferential optical coherence tomography angiography imaging of the swine esophagus using a micromotor balloon catheter," *Biomed. Opt. Express*, vol. 7, no. 8, pp. 2927 - 2942, 2016.

[83] Y. Pan, H. Xie, and G. K. Fedder, "Endoscopic optical coherence tomography based on a microelectromechanical mirror," *Opt. Lett.*, vol. 26, no. 24, pp. 1966 - 1968, 2001.

[84] L. Liu, L. Wu, J. Sun, E. Lin, and H. Xie, "Miniature endoscopic optical coherence tomography probe employing a two-axis microelectromechanical scanning mirror with through-silicon vias," *J. Biomed. Opt.*, vol. 16, no. 2, 026006, 2011.

[85] J. Sun *et al.*, "3D In Vivo optical coherence tomography based on a low-voltage, large-scan-range 2D MEMS mirror," *Opt. Express*, vol. 18, no. 12, pp. 12065 - 12075, 2010.

[86] Y. Xu *et al.*, "Design and development of a 3D scanning MEMS OCT probe using a novel SiOB package assembly," *J. Micromechanics Microengineering*, vol. 18, 125005, 2008.

[87] K. H. Kim *et al.*, "Two-axis magnetically-driven MEMS scanning catheter for endoscopic high-speed optical coherence tomography," *Opt. Express*, vol. 15, no. 26, pp. 18130 - 18140, 2007.

[88] W. Jung *et al.*, "Three-dimensional optical coherence tomography employing a 2-Axis Microelectromechanical Scanning Mirror," *IEEE J. Sel. Top. quantum Electron.*, vol. 11, no. 4, pp. 806 - 810, 2005.

[89] C. Chong, I. Keiji, J. Evans, and H. Toshiyoshi, "Optically-modulated MEMS Scanning Endoscope for Optical Coherence Tomography," in *Biomedical Optics*, Technical Digest (CD) (Optical Society of America, 2006), paper WE7.

[90] Q. A. A. Tanguy et al., "Design and fabrication of a 2-axis electrothermal MEMS micro-scanner for optical coherence tomography," *Micromachines*, vol. 8, no. 146, pp. 1 - 11, 2017.

[91] J. Singh *et al.*, "A two axes scanning SOI MEMS micromirror for endoscopic bioimaging," *J. Micromechanics Microengineering*, vol. 18, 025001, 2008.

[92] T. Xie, H. Xie, G. K. Fedder, and Y. Pan, "Endoscopic optical coherence tomography with new MEMS mirror," *Electron. Lett.*, vol. 39, no. 21, pp. 1535 - 1536, 2003.

[93] C. Duan, W. Wang, X. Zhang, L. Zhou, A. Pozzi, and H. Xie, "A self-aligned 45°-tilted two-axis scanning micromirror for side-view imaging," *J. Microelectromechanical Syst.*, vol. 25, no. 4, pp. 799 - 811, 2016.

[94] X. Mu *et al.*, "MEMS micromirror integrated endoscopic probe for optical coherence tomography bioimaging," *Sensors Actuators A Phys.*, vol. 168, pp. 202 - 212, 2011.

[95] T. Xie, H. Xie, G. K. Fedder, and Y. Pan, "Endoscopic optical coherence tomography with a modified microelectromechanical systems mirror for detection of bladder cancers," *Appl. Opt.*, vol. 42, no. 31, pp. 6422 - 6426, 2003.

[96] A. Jain, A. Kopa, Y. Pan, G. K. Fedder, and H. Xie, "A two-Axis Electrothermal Micromirror for Endoscopic Optical Coherence Tomograhpy," *IEEE J. Sel. Top. Quantum Electron.*, vol. 10, no. 3, pp. 636 - 642, 2004.

[97] J. Singh *et al.*, "Optical coherent tomography (OCT) bio-imaging using 3D scanning micromirror," in *Proc. SPIE* 6432, *Endoscopic Microscopy II*, 64320C (13 February 2007).

[98] H. Xie, J. Sun, and L. Wu, "Optical micro-endoscopes for 3D in-vivo imaging," SPIE Newsroom, 2010, pp. 1 - 2.

[99] S. Samuelson *et al.*, "A 2.8-mm imaging probe based on a high-fill-factor MEMS mirror and wire-bonding-free packaging for endoscopic optical coherence tomography," *J. Microelectromechanical Syst.*, vol. 21, no. 6, pp. 1291-–1302, 2012.

[100] D. Wang *et al.*, "Endoscopic swept-source optical coherence tomography based on a two-axis microelectromechanical system mirror," *J. Biomed. Opt.*, vol. 18, no. 8, 086005, 2013.

[101] C. Duan, Q. Tanguy, A. Pozzi, and H. Xie, "Optical coherence tomography endoscopic probe based on a tilted MEMS mirror," *Biomed. Opt. Express*, vol. 7, no. 9, pp. 3345 - 3354, 2016.

[102] J. T. W. Yeow *et al.*, "Micromachined 2-D scanner for 3-D optical coherence tomography," *Sensors Actuators, A Phys.*, vol. 117, pp. 331 - 340, 2005.

[103] W. Jung *et al.*, "In vivo three-dimensional spectral domain endoscopic optical coherence tomography using a microelectromechanical system mirror," *Opt. Lett.*, vol. 32, no. 22, pp. 3239 - 3241, 2007.

[104] K. Kumar *et al.*, "Fast 3D in vivo swept-source optical coherence tomography using a two-axis MEMS scanning micromirror," *J. Opt. A Pure Appl. Opt.*, vol. 10, 044013, 2008.

[105] J. M. Zara, S. Yazdanfar, K. D. Rao, J. A. Izatt, and S. W. Smith, "Electrostatic micromachine scanning mirror for optical coherence tomography," *Opt. Lett.*, vol. 28, no. 8, pp. 628 - 630, 2003.

[106] J. M. Zara and S. W. Smith, "Optical scanner using a MEMS actuator," *Sensors Actuators, A Phys.*, vol. 102, pp. 176 - 184, 2002.

[107] W. Piyawattanametha *et al.*, "Two-Dimensional Endoscopic MEMS Scanner for High Resolution Optical Coherence Tomography," in *Conference on Lasers and Electro-Optics/International Quantum Electronics Conference and Photonic Applications Systems Technologies*, Technical Digest (CD) (Optical Society of America, 2004), paper CWS2.

[108] W. Jung, D. T. McCormick, J. Zhang, L. Wang, N. C. Tien, and Z. Chen, "Three-dimensional endoscopic optical coherence tomography by use of a two-axis microelectromechanical scanning mirror," *Appl. Phys. Lett.*, vol. 88, 163901, 2006.

[109] A. D. Aguirre *et al.*, "Two-axis MEMS Scanning Catheter for Ultrahigh Resolution Three-dimensional and *En Face* Imaging," *Opt. Express*, vol. 15, no. 5, pp. 2445 - 2453, 2007.

[110] M. Strathman *et al.*, "MEMS scanning micromirror for optical coherence tomography," *Biomed. Opt. Express*, vol. 6, no. 1, pp. 211 - 224, 2014.

[111] T. Mitsui, Y. Takahashi, and Y. Watanabe, "A 2-axis optical scanner driven nonresonantly by electromagnetic force for OCT imaging," *J. Micromechanics Microengineering*, vol. 16, pp. 2482 - 2487, 2006.

[112] Y. Watanabe, Y. Abe, S. Iwamatsu, S. Kobayashi, Y. Takahashi, and T. Sato, "Electromagnetically driven two-axis optical beam steering MEMS mirror and its dependence of actuation on magnetic field," *Electron. Commun. Japan*, vol. 94, no. 11, pp. 107 - 112, 2011.

[113] K. H. Gilchrist, R. P. McNabb, J. A. Izatt, and S. Grego, "Piezoelectric scanning mirrors for endoscopic optical coherence tomography," *J. Micromechanics Microengineering*, vol. 19, 095012, 2009.

[114] J. Sun and H. Xie, "MEMS-based endoscopic optical coherence tomography," *Int. J. Opt.*, vol. 2011, pp. 1 - 12, 2011.

[115] J. Albero *et al.*, "Micromachined array-type Mirau interferometer for parallel inspection of MEMS," *J. Micromechanics Microengineering*, vol. 21, 065005, 2011.

[116] A. B. Vakhtin, D. J. Kane, W. R. Wood, and K. A. Peterson, "Common-path interferometer for frequency-domain optical coherence tomography," *Appl. Opt.*, vol. 42, no. 34, pp. 6953 - 6958, 2003.

[117] A. Popp *et al.*, "Common-Path Fourier Domain Optical Coherence Tomography of Irradiated Human Skin and Ventilated Isolated Rabbit Lungs," in *Optical Coherence Tomography and Coherence Techniques* II, W. Drexler, ed., Vol. 5861 of Proc. SPIE (Optical Society of America, 2005), paper TuB2.

[118] K. Singh, D. Yamada, and G. J. Tearney, "Common Path Side Viewing Monolithic Ball Lens Probe for Optical Coherence Tomography," *Improv. Methodol.*, vol. 7, no. 1, pp. 29 - 33, 2015.

[119] A. R. Tumlinson *et al.*, "Endoscope-tip interferometer for ultrahigh resolution frequency domain optical coherence tomography in mouse colon," *Opt. Express*, vol. 14, no. 5, pp. 1878 - 1887, 2006.

[120] M. Marrese, H. Offerhaus, E. Paardekam, and D. Iannuzzi, "70 μm Diameter Optical Probe for Common-Path Optical Coherence Tomography in Air and Liquids," *Opt. Lett.*, vol. 43, no. 24, pp. 5929 - 5932, 2018.

[121] S. Lee, C. Lee, R. Verkade, G. W. Cheon, and J. U. Kang, "Common-path all-fiber optical coherence tomography probe based on high-index elliptical epoxy-lensed fiber," *Opt. Eng.*, vol. 58, no. 02, 026116, 2019.

[122] C. Dorrer, N. Belabas, J.-P. Likforman, and M. Joffre, "Spectral resolution and sampling issues in Fourier-transform spectral interferometry," *J. Opt. Soc. Am. B*, vol. 17, no. 10, pp. 1795 - 1802, 2000.

[123] B. E. Bouma and G. J. Tearney, *Handbook of Optical Coherence Tomography*. New York: Marcel Dekker, 2002.

[124] M. Cerna and A. F. Harvey, "The Fundamentals of FFT-Based Signal Analysis and Measurement," *National Instruments, Application Note 041*, 2000.

[125] S. Moon, S.-W. Lee, and Z. Chen, "Reference spectrum extraction and fixed-pattern noise removal in optical coherence tomography," *Opt. Express*, vol. 18, no. 23, pp. 24395 - 24404, 2010.

[126] D. Wang, C. Duan, X. Zhang, Z. Yun, A. Pozzi, and H. Xie, "Common-path optical coherence tomography using a microelectromechanical-system-based endoscopic probe," *Appl. Opt.*, vol. 55, no. 25, pp. 6930 - 6935, 2016.

[127] R. K. Wang and Z. Ma, "A practical approach to eliminate autocorrelation artefacts for volume-rate spectral domain optical coherence tomography," *Phys. Med. Biol.*, vol. 51, no. 12, pp. 3231 - 3239, 2006.

[128] B. Hofer *et al.*, "Artefact reduction for cell migration visualization using spectral domain optical coherence tomography," *J. Biophotonics*, vol. 4, no. 5, pp. 355 - 367, 2011.

[129] M. R. Hee, J. A. Izatt, J. M. Jacobson, and J. G. Fujimoto, "Femtosecond transillumination optical coherence tomography," *Opt. Lett.*, vol. 18, no. 12, pp. 950 - 952, 1993.

[130] A. M. Rollins and J. A. Izatt, "Optimal interferometer designs for optical coherence tomography," *Opt. Lett.*, vol. 24, no. 21, pp. 1484 - 1486, 1999.

[131] Y. Chen, D. M. de Bruin, C. Kerbage, and J. F. de Boer, "Spectrally balanced detection for optical frequency domain imaging," *Opt. Express*, vol. 15, no. 25, pp. 16390 - 16399, 2007.

[132] A. H. Bachmann, R. Michaely, T. Lasser, and R. A. Leitgeb, "Dual beam heterodyne Fourier domain optical coherence tomography," *Opt. Express*, vol. 15, no. 15, pp. 9254 - 9266, 2007.

[133] H. E. Bennett, J. M. Bennett, and E. J. Ashley, "Infrared Reflectance of Evaporated Aluminum Films," *J. Opt. Soc. Am.*, vol. 52, no. 11, pp. 1245 - 1250, 1962.

[134] V. Lozanova, A. Lalova, L. Soserov, and R. Todorov, "Optical and electrical properties of very thin chromium films for optoelectronic devices," *J. Phys. Conf. Ser.*, vol. 514, 2014.

[135] www.laseroptik.com. 2022. Metal coatings. [online] Available from: https://www.laseroptik.com/en/coatings/metal-coatings.

[136] Q. A. A. Tanguy *et al.*, "Real-time Lissajous imaging with a low-voltage 2-axis MEMS scanner based on electrothermal actuation," *Opt. Express*, vol. 28, no. 6, pp. 8512 - 8527, 2020.

[137] W. Du, G. Zhang, and L. Ye, "Image quality analysis and optical performance requirement for Micromirror-Based Lissajous scanning displays," *Sensors*, vol. 16, no. 5, 675, 2016.

[138] K. Hwang, Y. H. Seo, J. Ahn, P. Kim, and K. H. Jeong, "Frequency selection rule for high definition and high frame rate Lissajous scanning," *Sci. Rep.*, vol. 7, no. 1, 14075, 2017.

[139] A. Bazaei, Y. K. Yong, and S. O. R. Moheimani, "High-speed Lissajous-scan atomic force microscopy: Scan pattern planning and control design issues," *Rev. Sci. Instrum.*, vol. 83, 063701, 2012.

[140] J. Wang, G. Zhang, and Z. You, "Design rules for dense and rapid Lissajous scanning," *Microsystems Nanoeng.*, vol. 6, 101, 2020.

[141] E. H. K. Stelzer, "Contrast, resolution, pixelation, dynamic range and signal-to-noise ratio: Fundamental limits to resolution in fluorescence light microscopy," *J. Microsc.*, vol. 189, no. 1, pp. 15 - 24, 1998.

[142] Hristo Zhivomirov (2021). Phase Difference Measurement with Matlab (https://www.mathworks.com/matlabcentral/fileexchange/48025-phase-difference-measurement-with-matlab), MATLAB Central File Exchange. Retrieved September 3, 2021.

[143] M. Sedlacek. "Digital Measurement of Phase Difference of LF Signals A Comparison of DSP Algorithms'. *Proceedings of XVII IMEKO World Congress*, pp. 639 - 644, 2003.

[144] M. Sedlacek, M. Krumpholc. "Digital measurement of phase difference – a comparative study of DSP algorithms". *Metrology and Measurement Systems*, Vol. 12, No. 4, pp. 427 - 448, 2005.

[145] E. A. Swanson and J. G. Fujimoto, "The ecosystem that powered the translation of OCT from fundamental research to clinical and commercial impact [Invited]," *Biomed. Opt. Express*, vol. 8, no. 3, pp. 1638 - 1664, 2017.

[146] Optical Coherence Tomography Market By Product Type (Spectral Domain-OCT, Swept Source-OCT), Application (Ophthalmology, Dermatology, Cardiovascular, Dental), End User & Region - Forecast to 2021 - 2031, Optical Coherence Tomography Market - Analysis, Outlook, Growth, Trends, Forecasts, Report, June 2021.

My publications

[147] P. Struk, S. Bargiel, Q. A. A. Tanguy, F. E. Garcia Ramirez, N. Passilly, P. Lutz, O. Gaiffe, H. Xie and G. Gorecki, "Swept-source optical coherence tomography microsystem with an integrated Mirau interferometer and electrothermal microscanner," *Opt. Lett.*, vol. 43, no. 19, pp. 4847 - 4850, 2018.

[148] S. Bargiel, F. E. García - Ramírez, P. Struk, J. - L. Skora, Q. A. A. Tanguy, O. Gaiffe, P. Lutz, J - M Cote, H. Xie, C. Gorecki, "3 - D micro-assembly approach to fabrication of a scanning MOEMS - based endoscopic probe for Optical Coherence Tomography imaging," in *Intern. Symposium on Optomechatronic Technology ISOT* 2021, 2 - 5/11/2021, Besançon, France

[149] F. E. García-Ramírez, S. Bargiel, O. Gaiffe, Q. A. A. Tanguy, P. Struk, J-M Cote, P. Lutz, H. Xie and C. Gorecki, "SS-OCT probe with a Mirau micro interferometer

and a 2-axis electrothermal micro-mirror scanner for endoscopic applications", *Conf. International Industrialization Potential of Optics in Biomedicine (i-POB)*, Poland, 07-08/10/2020

[150] F. E. García-Ramírez, S. Bargiel, O. Gaiffe, Q. A. A. Tanguy, P. Struk, J-M Cote, N. Passilly, P. Lutz, C. Gorecki and H. Xie, "Characterization of an integrated MOEMS scanning probe towards real-time Lissajous-based SS-OCT imaging for endoscopic applications", *Conf. International Biophotonics Congress: Biomedical Optics* 2020 (Translational, Microscopy, OCT, OTS, BRAIN), 20-23/04/2020, Fort Lauderdale, USA (virtual).

[151] F. E. García-Ramírez, S. Bargiel, O. Gaiffe, Q. Tanguy, P. Struk, J-M, Cote, J-L. Skora, P. Lutz, C. Gorecki, H. Xie, "Optical Coherence Tomography endoscopic probe based on MOEMS technology for early stomach cancer detection", *20th Intern. Symposium on Optomechatronic Technology ISOT* 2019, India

[152] S. Bargiel, F. E. García-Ramírez, Q. A. A. Tanguy, P. Struk, O. Gaiffe, J-M Cote, N. Passilly, J-L. Skora, P. Lutz, C. Gorecki and H. Xie, "Swept-source optical coherence tomography microsystem with an integrated Mirau interferometer and electrothermal micro-scanner for gastrointestinal endomicroscopy", Workshop NAMIS, 22-24/11/2019, Mumbai, India